Proton Radioactivity Measurements Using A Double–Sided Silicon Strip Detector

Paul Jonathan Sellin, B.Sc.

Thesis submitted for the degree of Doctor of Philosophy

Department of Physics

University of Edinburgh

1992

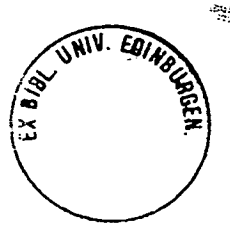

Abstract

Proton radioactivity measurements have been carried out using a new double–sided silicon strip detector. Highly proton rich fusion–evaporation reaction products are velocity and mass separated using the Daresbury recoil separator before being implanted into the strip detector located at the separator's focal plane. The strip detector records the energy and position of charged particles emitted from the implanted residues, allowing the identification of very low cross section decay events with microsecond half–lives. The double–sided silicon strip detector contains 48 strips on each face, orthogonally crossed to provide x,y position information with a strip pitch of ± 335 μm. This first use of such a detector has used new high density microelectronics to instrument up to 120 channels of data.

A commissioning experiment was carried out using the reaction $^{58}\mathrm{Ni} + {}^{54}\mathrm{Fe} \rightarrow {}^{112}\mathrm{Xe}^{*}$ which successfully tested the performance of the detection system by observing proton emission from ^{109}I. The subsequent production experiment investigated proton radioactivity from nuclei around ^{147}Tm and ^{151}Lu, produced using the reactions $^{58}\mathrm{Ni} + {}^{92}\mathrm{Mo} \rightarrow {}^{150}\mathrm{Yb}^{*}$ and $^{58}\mathrm{Ni} + {}^{96}\mathrm{Ru} \rightarrow {}^{154}\mathrm{Hf}^{*}$. The first unambiguous identification of the proton emitter ^{150}Lu is reported, with a measured half–life of 30 ± 5 ms. An additional four proton transition half–lives have been re–measured with substantially improved accuracies, and explicit mass assignments are made for the first time for the proton transitions from ^{151}Lu, ^{147m}Tm and ^{109}I. In addition a new proton transition has been observed with an energy of 947 ± 5 MeV and a half–life of 5 ± 3 ms, which is tentatively assigned to the decay of an isomeric state in ^{147}Tm.

Declaration

The data presented in this thesis was obtained by myself and fellow collaborators. The data analysis and interpretation is all my own work, and the thesis has been composed by myself.

Acknowledgments

I am extremely grateful for the help and encouragement which so many people have provided during this work, and without which the success of this project would not have been possible. My particular thanks go to my supervisor Dr. Phil Woods for his constant enthusiasm and encouragement. I would also like to thank Professor Alan Shotter and all my colleagues in the Edinburgh University Nuclear Physics group for their help and support, especially my 'predecessor' Robert Page for many hours of helpful discussion, and Tom Davinson for essential help with the vagaries of strip detectors. My thanks go to the additional members of the experimental collaboration for their support and essential practical skills, particularly Arthur James and Sigurd Hofmann. Various technical problems encountered in this project were only solved with expert help, and I am especially grateful to Dick Hunt for giving me a glimpse into the workings of Charissa, and for his many hours spent modifying the system to our ever-varied specification. Thanks go also to Archie Howett of the Computer Science Department for invaluable tuition with the printed circuit board design system. I am grateful for financial support from the S.E.R.C., which provided a three year research studentship. Special thanks go to Debbie, my parents and friends for their essential encouragement and support.

Contents

List of Figures

Chapter 1

The phenomenon of direct proton emission

1.1 Introduction

Decay by direct proton emission occurs from nuclei at the very edge of nuclear stability. Indeed the onset of proton emission from a nucleus indicates the most fundamental hadronic limit of nuclear stability. Figure 1.1 shows the extent of the known nuclear chart, which contains a narrow diagonal band of stable nuclei. At higher masses these nuclei exhibit an increasing neutron excess, due to the repulsive coulomb force acting between the constituent protons. Nuclei lying on either side of this region of stability decay by β–emission, which is energetically allowed with only small differences in parent and daughter binding energy.

For nuclei further from stability the difference between parent and daughter binding energies increases, opening up the Q–value available for other decay modes. Initially β–decay gives way in favour of β–delayed particle emission, in which the initial β–decay populates excited levels in the daughter nucleus. These daughter states are unbound with respect to nucleon emission and exhibit decay modes such

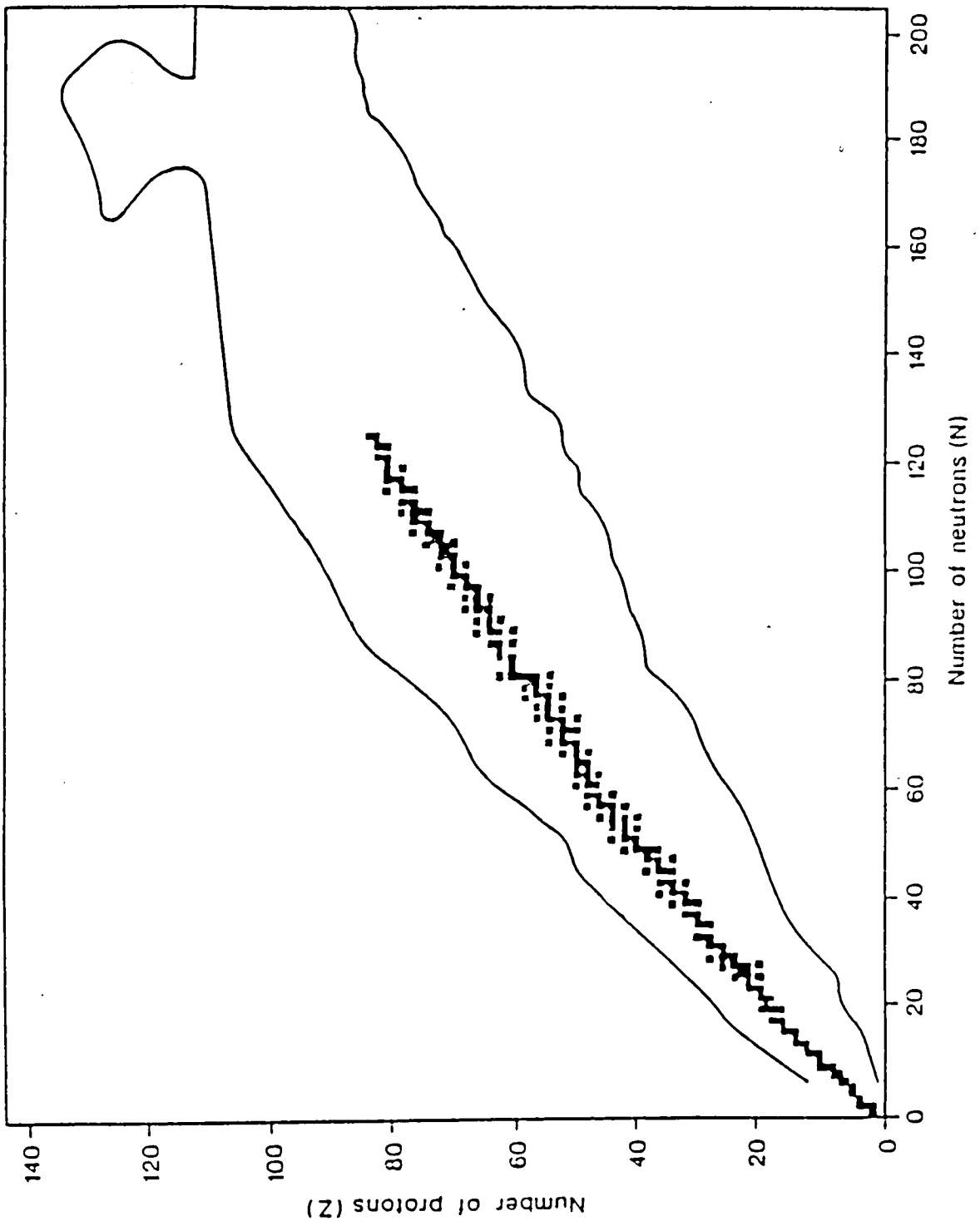

Figure 1.1: *The chart of the nuclides, showing the diagonal valley of stability, and the drip lines which mark the edge of nuclear stability*

as βp, βn, $\beta\alpha$ etc. Such decays occur via a characteristic two step mechanism, involving a slow β–decaying precursor followed by fast nucleon emission from the daughter state. Examples of various β–delayed mechanisms have been observed in many regions of the nuclear chart, from both neutron rich and proton rich nuclei.

Amongst heavier mass proton rich nuclei, the increasing Q–value far from stability makes direct alpha emission energetically allowed. For such nuclei the competing β partial half–life only increases gradually on moving further from stability, whereas the alpha decay partial half–life quickly drops reflecting the strong energy dependence of the decay mode. In this way alpha emission becomes the dominant decay mode for highly proton rich nuclei above N=83.

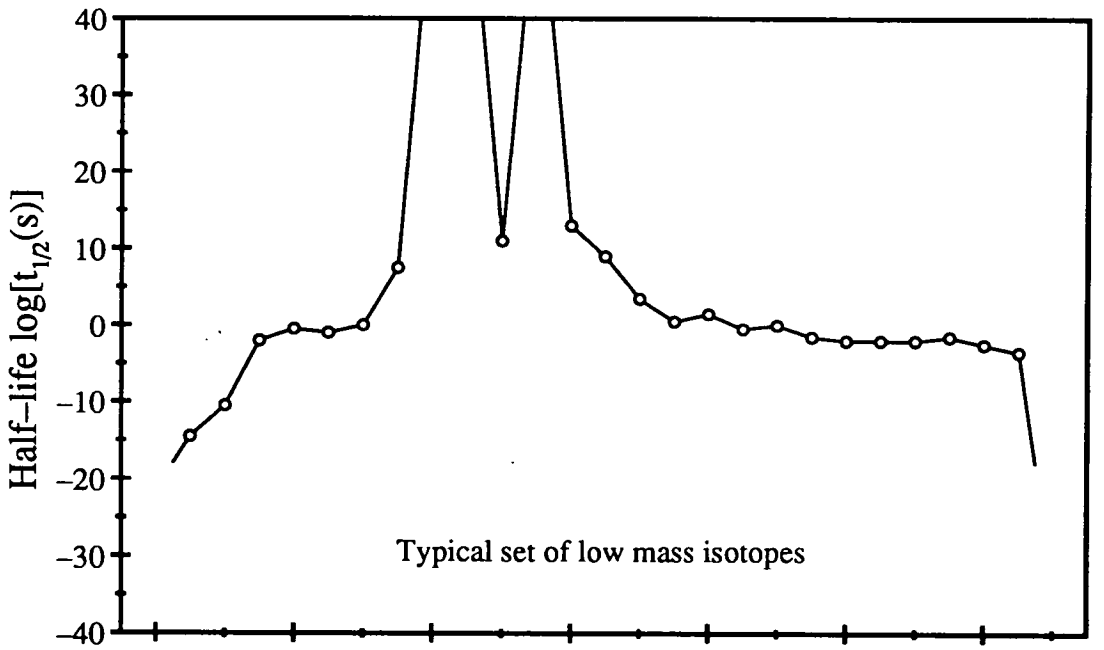

Figure 1.2: *Typical variation of half–life for isotopes as a function of neutron number. The half–life drops much more abruptly on crossing the neutron drip line compared to crossing the proton drip line (from [Dét86])*

The onset of direct single nucleon emission occurs after crossing either the proton

or neutron drip lines, which represent the locii of nuclei where $Q_p = 0$ or $Q_n = 0$. The position of the proton drip line runs considerably closer to the valley of stability than that of the neutron drip line, due to the repulsive coulomb force which tends to reduce the stability of highly proton rich nuclei. The extra distance of the neutron drip line from stability is an additional factor which hinders the experimental production of nuclei on or close to the neutron drip line for all but light masses. The present limit of observation for nuclei on the neutron drip line is at $^{35}_{11}$Na [Gui89], whereas the proton drip line has been completely mapped up to $^{39}_{22}$Ti [Dét90].

Beyond the drip lines the partial half–lives for both proton and neutron emission drop rapidly, and quickly dominate over other decay modes. In the case of proton emission, the coulomb force provides an additional contribution to the potential barrier, which is not present for neutron emission, and so softens the abrupt drop in half–life which is seen when crossing the neutron drip line (see figure 1.2).

For regions where proton and alpha emission are competing decay modes, proton emission quickly dominates for isotopes a few nuclei from the drip line. This is due to the relatively higher coulomb contribution to the barrier for alpha emission, which causes the proton partial half–life to drop more rapidly with increasing Q–value than the alpha partial half–life. Figure 1.3 indicates this rapid change of proton and alpha partial half–life for thallium (Z=81) isotopes, illustrating the dominance of proton emission in nuclei only 1 or 2 isotopes beyond the Q_p=0 limit.

The rarity of experimentally observed cases of direct proton emission arises because of the combination of a narrow range of nuclei with observable half–lives, plus the experimental difficulties in accessing such proton rich species. Recent advances in production and separation techniques are now opening up more regions of the proton drip line, and are discussed in chapter 2. In general no more than two isotopes of each element possess a Q_p value suitable for observable proton

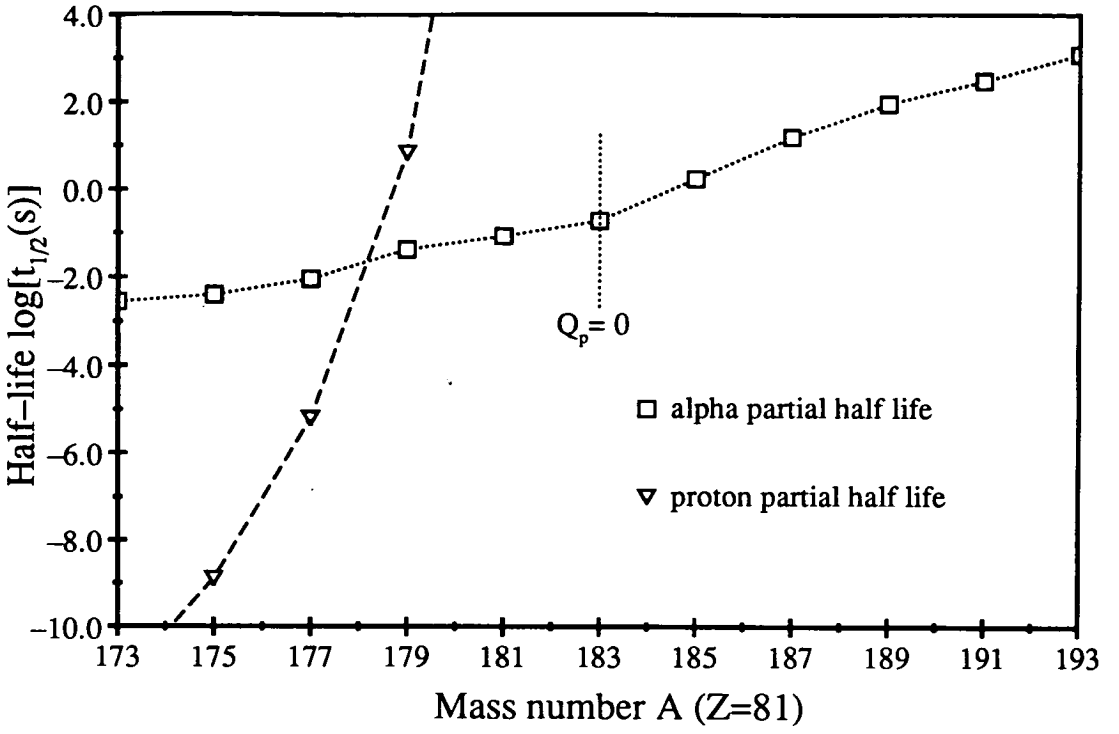

Figure 1.3: *Plot of partial half–life for proton and alpha decay of Z=81 even–N isotopes (Data for A≤183 are extrapolated from predicted Q-value systematics [Wap88])*

emission. Nuclei with a small positive Q_p value tend to exhibit a very low proton branching ratio, whereas those with a large Q_p value decay with an unobservably short half–life ($\lesssim$ 100 ns). This limits the choice of observable proton emission candidates in the heavy mass regions to nuclei with Q_p values in the approximate range of 0.5 – 1.5 MeV.

The observation and measurement of direct proton emission reveals much useful nuclear structure information on nuclei at the limit of the known nuclear chart. At the simplest level, the occurrence of direct proton emission indicates the crossing of the proton drip line, and so fixes the limit of nuclear stability. Proton emission is an extremely clean decay mode and can be treated in an analogous but simpler way to that of alpha decay. It will be shown in section 1.2 that the partial proton

half–life has an extremely strong dependence on the orbital angular momentum l of the emitted proton, as well as on its energy. For this reason half–life measurements can give precise information on the level ordering of low–lying states in proton unstable nuclei. At the same time, Q_p values derived from measured proton transition energies provide a stringent test of competing mass models in regions far from the known mass surface.

The numerous experimental programmes which have searched for examples of direct proton emission have only observed to date four examples of ground state proton emission from drip line nuclei, around mass regions 151 and 109. The first observed case of direct proton emission was from a high–lying isomeric state in ^{53}Co [Jac70, Cer70]. This nucleus is relatively close to stability, and has a ground state which is strongly bound with respect to proton emission. No further examples of this type of isomeric proton decay were found, and experimental efforts have since concentrated on drip line nuclei. The discussion in this thesis will concentrate solely on proton emission from nuclei beyond the proton drip line.

So far no examples of direct proton emission have been seen in light mass regions below tin ($A \lesssim 100$) where the predicted Q_p values are generally below 500 keV, and β–delayed modes dominate around the proton drip line. However the smaller differences in binding energies present in such light mass nuclei open up the possibility of observing direct two–proton emission. This mode is predicted to arise when pairing effects make the binding energy for even–Z nuclei stable with respect to one–proton emission, but unbound to two–proton emission. Below $Z \simeq 40$ a variety of such nuclei are predicted to exhibit the necessary Q_{2p} values required for observable two–proton half–lives. No examples of this potentially interesting decay mode have yet been observed, although cases have been seen in this region of the similar β–delayed two–proton decay.

In the heavier mass regions ground state proton emission was first observed from ^{151}Lu, followed by ^{147}Tm, and later from ^{109}I and ^{113}Cs. These examples are dis-

cussed in more detail in section 2.2. Elsewhere the exact position of the proton drip line remains unknown, although at least one observable proton emitting isotope is predicted for each odd-Z element. The prospect of making systematic measurements of direct proton transitions over a substantial region of the drip line has become a real possibility using the technique developed within this thesis work. Such a set of measured Q_p values could be used to look for systematic deviations of the measured masses of nuclei beyond the drip line, compared to their predicted values. Any such effect would give evidence for the proposed Thomas–Ehrmann shift [Com88, Dét90], which predicts a reduced Q_p value for nuclei with an unbound proton compared to the equivalent bound nucleus.

1.2 Theory of direct proton emission

1.2.1 The barrier penetration model

The process of proton emission can be treated theoretically in an analogous way to that of alpha emission, however with two particular differences. Firstly since a single nucleon is emitted rather than a four nucleon cluster, the problems associated with determining a cluster preformation probability are alleviated. Secondly the proton has a spin $\sigma = \frac{1}{2}$, as opposed to zero for the alpha particle, requiring the inclusion of the spin–orbit interaction for a complete model of the proton–core system.

Protons are emitted with an orbital angular momentum l, selected by the conservation of total spin and parity such that

$$\vec{J}_i = \vec{J}_f + \vec{l} + \vec{\sigma} \tag{1.1}$$

$$\Pi_i = \Pi_f(-1)^l \tag{1.2}$$

where $\vec{J}_i$, $\vec{J}_f$ are the parent and daughter state total spins, Π_i, Π_f are the parent and daughter state parities.

Treating this system in analogy to alpha decay, a nucleus of charge $Z+1$ is considered to consist of a proton confined within the potential arising from the daughter nucleus of charge Z. The resulting potential barrier $V(r)$ is made up of a superposition of terms,

$$V(r) = V_{nuc}(r) + V_c(r) + V_l(r) + V_{so}(r) \tag{1.3}$$

consisting of the nuclear potential $V_{nuc}(r)$, the coulomb potential $V_c(r)$, the centrifugal potential $V_l(r)$ and the spin–orbit potential $V_{so}(r)$.

An essential requirement for proton emission is that the transition has a positive Q_p value, which is defined as the difference between initial and final masses of parent and daughter system. In this way

$$Q_p = M_{(Z+1)} - M_{(Z)} - m_p - m_e \tag{1.4}$$

where M is the atomic mass including electrons, m_p is the proton mass and m_e is the mass of an electron. Conservation of linear momentum requires that the total kinetic energy is divided between the two products in inverse proportion to their masses. Therefore in terms of the energy of the proton E_p and of the daughter nucleus $E_{(Z)}$

$$Q_p = E_p + E_{(Z)} \tag{1.5}$$

and

$$E_p = Q_p \left(\frac{M_{(Z)}}{M_{(Z)} + m_p} \right) \tag{1.6}$$

$$E_{(Z)} = E_p \frac{m_p}{M_{(Z)}} \tag{1.7}$$

Q_p can be more conveniently expressed in terms of binding energies, that is the energy required to break the nucleus into its constituent nucleons. Hence

$$B_{(Z)} = ZM_H + Nm_n - M_{(Z)} \tag{1.8}$$

where M_H is the atomic mass of hydrogen and m_n is the mass of a neutron. Q_p is then simply the difference between parent and daughter binding energies, giving

$$Q_p = B_{(Z)} - B_{(Z+1)} \tag{1.9}$$

The experimentally measured Q_p value is slightly less than the $Q_{p,nuc}$ 'nuclear' value which is required for the theoretical treatment of proton decay rates. The corrected value compensates for the small loss in energy of the proton as it passes through the electron cloud. This screening correction E_{SC} arises from the difference in binding energies of the electrons in the parent and daughter atoms. In this way

$$Q_{p,nuc} = Q_p + E_{SC} \tag{1.10}$$

In general the kinetic energy of the proton in the fermi level of the parent nucleus is far smaller than the maximum barrier height, and so spontaneous proton emission is only possible by quantum mechanical tunnelling of the proton through the barrier. The first treatments of spontaneous alpha emission due to quantum mechanical tunnelling were published simultaneously by Gamow [Gam28] and Gurney and Condon [Gur28]. In this one–body model the alpha particle is assigned a decay constant λ equal to the product of the particle's oscillation frequency in the well ν and the transmission coefficient T_{jl}, hence

$$\lambda = \nu\, T_{jl} \tag{1.11}$$

Various similar treatments have been used for calculating the proton partial half–life (eg. references summarised in [Hof88]) based on the simple one–body model of alpha decay [Bet37, Ras59]. In this way ν can be expressed as

$$\nu = \frac{\sqrt{2}\ \pi^2\hbar^2}{m^{\frac{3}{2}} {R_o}^3 (\frac{2Ze^2}{R_o} - Q_p)^{\frac{1}{2}}} \tag{1.12}$$

where m is the proton mass and R_o is the inner radial turning point (see figure 1.4). A typical value for the oscillation frequency is $\nu \simeq 6 \times 10^{21}$ Hz for the proton decay of ^{151}Lu [Hof88].

The transmission coefficient T_{jl} is derived by solving the radial part of the Schrödinger equation using the WKB (Wentzel–Kramers–Brillouin) approximation. This gives an exponential form for T_{jl} expressed as

$$T_{jl} \;=\; e^{-2\int_{R_o}^{R_1} k(r)dr} \tag{1.13}$$

$$k(r) = \frac{1}{\hbar}(2\mu[V(r) - Q_p])^{\frac{1}{2}} \tag{1.14}$$

where R_1 is the outer radial turning point and μ is the reduced mass of the proton–daughter system defined in terms of the daughter mass number A as

$$\mu = \frac{A}{A+1} m_\mu \tag{1.15}$$

where $m_\mu = 931.501$ MeV/c^2.

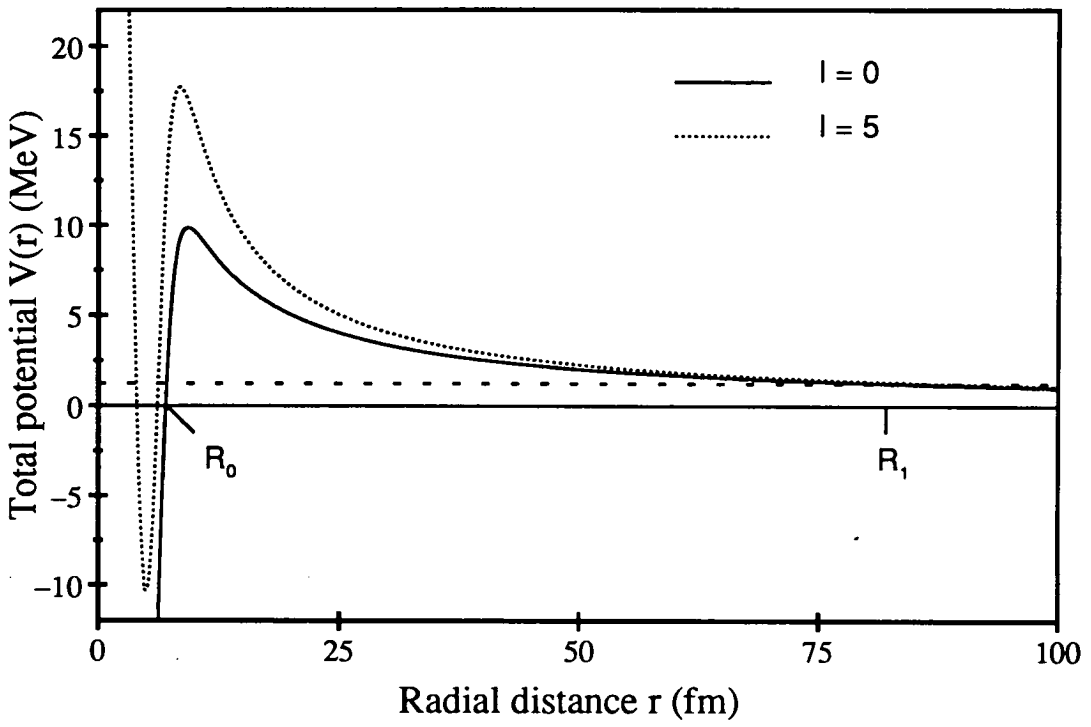

Figure 1.4: *Total potential $V(r)$ as a function of radial distance for ^{151}Lu, using the optical model potential of Bechetti and Greenlees*

Generally it is the choice of nuclear potential within $V(r)$ which most strongly affects the calculated decay widths. The accuracy of such calculations is governed by the difficulty in choosing a suitable potential which accurately describes the behaviour of low energy ($\simeq$ 1 MeV) protons. The real part of an optical model potential is often used, such as the potentials of Bechetti and Greenlees [Bec69], and Perey and Perey [Per72], derived from the scattering of $10 - 40$ MeV protons.

These experimentally produced potentials are fitted to many proton reactions in an attempt to generalise their parameters for a range of nuclei. An alternative approach is to use a theoretical potential derived from the droplet model [Mye70]. The droplet model of Myers is parameterised in terms of the neutron excess $N-Z$ and has been shown to reproduce well the systematics of nuclear radii in nuclei away from stability. This approach should therefore produce a potential which is applicable to proton emitting nuclei at the proton drip line.

Hofmann and others (see for example [Hof88, Pag90]) have performed barrier penetration calculations using an optical model nuclear potential within $V(r)$, with the form

$$V_{nuc}(r) = -V^{o}_{nuc}\, f(r, R_{nuc}, a_{nuc}) \tag{1.16}$$

where

$$f(r,R,a) = [1 + exp\frac{r-R}{a}]^{-1} \tag{1.17}$$

$$V^{o}_{nuc} = 54.0 - 0.32E_p + 0.4\frac{Z}{A^{\frac{1}{3}}} + 24.0\frac{N-Z}{A}\ \text{MeV} \tag{1.18}$$

$$R_{nuc} = 1.17\ \text{fm} \times A^{\frac{1}{3}} \tag{1.19}$$

$$a_{nuc} = 0.75\ \text{fm} \tag{1.20}$$

The coulomb potential $V_c(r)$ assumes a point-like proton moving within the uniform charge distribution of the daughter nucleus. In this way

$$V_c(r) = \left(\frac{Ze^2}{8\pi\varepsilon_o R_c}\right)\left(3 - \frac{r^2}{R_c^2}\right) \tag{1.21}$$

for $r \leq R_c$ where $R_c = 1.21\ \text{fm} \times A^{\frac{1}{3}}$, and

$$V_c(r) = \frac{Ze^2}{4\pi\varepsilon_o R_c} \tag{1.22}$$

for $r > R_c$.

The centrifugal barrier term is strongly dependent on the proton's orbital angular momentum l, and has the form

$$V_l(r) = \frac{l(l+1)\hbar^2}{2\mu r^2} \tag{1.23}$$

The spin–orbit potential has a strength and sign which is dependent on the product of the proton spin σ and l, and is written

$$V_{so}(r) = \vec{\sigma}.\vec{l}\lambda_{\pi}^{2}\frac{1}{r}\left(\frac{d}{dr}(f(r, R_{so}, a_{so})\right) \tag{1.24}$$

where $f(r, R, a)$ is the function of equation 1.17, and

$$\vec{\sigma}.\vec{l} = l \qquad \text{for } j = l + \frac{1}{2} \tag{1.25}$$

$$\vec{\sigma}.\vec{l} = -(l+1) \quad \text{for } j = l - \frac{1}{2}\ (l > 0) \tag{1.26}$$

$$R_{so} = 1.01 \text{ fm} \times A^{\frac{1}{3}} \tag{1.27}$$

$$a_{so} = 0.75 \text{ fm} \tag{1.28}$$

and λ_{π} is the pion Compton wavelength ($\simeq \sqrt{2}$ fm).

Various authors have used this WKB approach to calculate half–lives for predicted proton emitters over the length of the proton drip line. Hofmann has performed calculations [Hof82] using both optical model and liquid drop potentials to calculate the proton half–life for ^{151}Lu. He concluded that the values obtained using the different potentials varied by only about 25% for the low spin ($s_{\frac{1}{2}}$, $d_{\frac{3}{2}}$) states, and by about 50% for the $h_{\frac{11}{2}}$ state. As will be discussed in section 1.2.2, the predicted half–life is altered so dramatically by a change of only one unit of l, that uncertainties in the calculated half–life due to the choice of nuclear potential are not usually critical.

The straight forward nature of these barrier penetration calculations allows them to be performed using relatively simple computer codes. Such calculations provide a reasonably accurate way to predict half–lives and so deduce proton spin assignments. Gillitzer *et al.* [Gil87] refined these single–particle half–life estimates by introducing an explicit spectroscopic factor S_{jl}. For a pure shell model parent state $(jl)^n$ containing n protons, the spectroscopic factor is given by

$$S_{jl} = \frac{2j + 2 - n}{2j + 1} \tag{1.29}$$

assuming a transition into a seniority zero daughter state. The decay constant λ now has the form

$$\lambda = \nu \, T_{jl} \, S_{jl} \tag{1.30}$$

S_{jl} is unity for nuclei close to a closed shell, and 0.5 for those in the middle of a subshell.

Various other more complex theoretical techniques have been used to model direct proton emission in a more generalised way. Feix and Hilf [Fei83] used a direct integration of the Schrödinger equation within a spherical potential to calculate single–proton decay widths using a 'cold–core plus nucleon' model. Their calculations are in agreement with WKB half–lives for ^{151}Lu and ^{147}Tm, and they predict half–lives for proton emitters over the region of prolate deformed light rare earth nuclei either side of Z=64. Bugrov *et al.* [Bug85] have developed a generalised approach to proton decay incorporating multi–particle effects, following a similar treatment of alpha decay [Kad75]. Further calculations [Bug89] have extended this technique to include a proton spectroscopic factor for nuclei away from closed shells, and to consider nucleons within a non–spherical potential. This powerful technique reproduces well the half–lives of the deformed proton emitters ^{109}I and ^{113}Cs [Bug89], and would appear to offer the best predictive ability for new regions of deformed proton emitters.

1.2.2 Sensitivity of the decay mode

The exponential dependence of the transmission coefficient on the width of the barrier causes a dramatic change in proton half–life for a small change in barrier height. For this reason the proton half–life is extremely sensitive to the orbital angular momentum of the emitted proton, due to the strong l dependence of the centrifugal potential term. In the case of alpha decay the variation of the barrier height with changing l is reduced due to the the larger reduced mass of the alpha–daughter system.

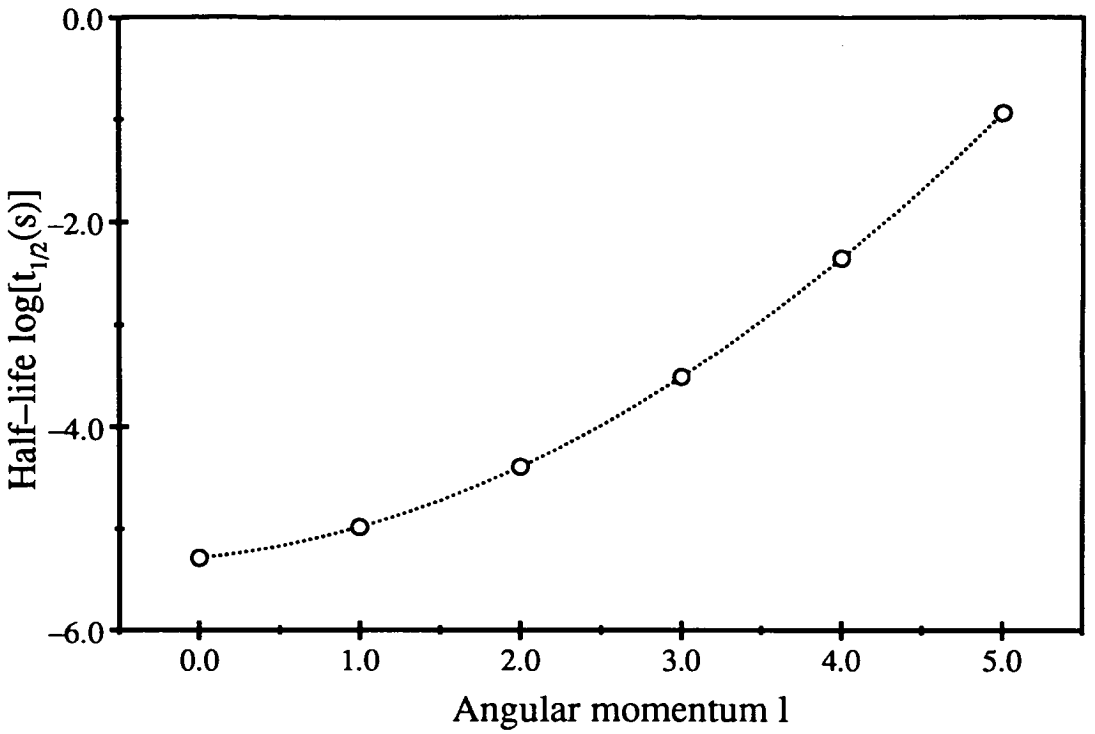

Figure 1.5: *Predicted proton decay partial half-life of ^{151}Lu calculated from a WKB model, as a function of possible proton angular momentum*

For the simplest case of proton decay, from the ground state of an even–odd parent nucleus to the 0^+ ground state of an even–even daughter (eg. $^{151}_{71}Lu_{80}$ to $^{150}_{70}Yb_{80}$), the angular momentum of the emitted proton is determined by the spin of the parent fermi–level proton orbital. Figure 1.5 shows predicted proton partial half–lives for ^{151}Lu over a hypothetical range of l–values from l=0 to l=5, calculated using the spherical potential WKB approach discussed above. In this shell model nucleus the $s_{\frac{1}{2}}$, $d_{\frac{3}{2}}$ and $h_{\frac{11}{2}}$ single–particle proton levels are predicted to be only finely separated around the fermi level. However the measured proton half–life of 85 ± 10 ms for this nucleus [Hof82] clearly identifies the l=5 orbital in preference to the l=0 and l=2 orbitals.

The proton partial half–life is also extremely dependent on the decay Q_p value, due to the variation in barrier width which must be tunnelled through by the proton

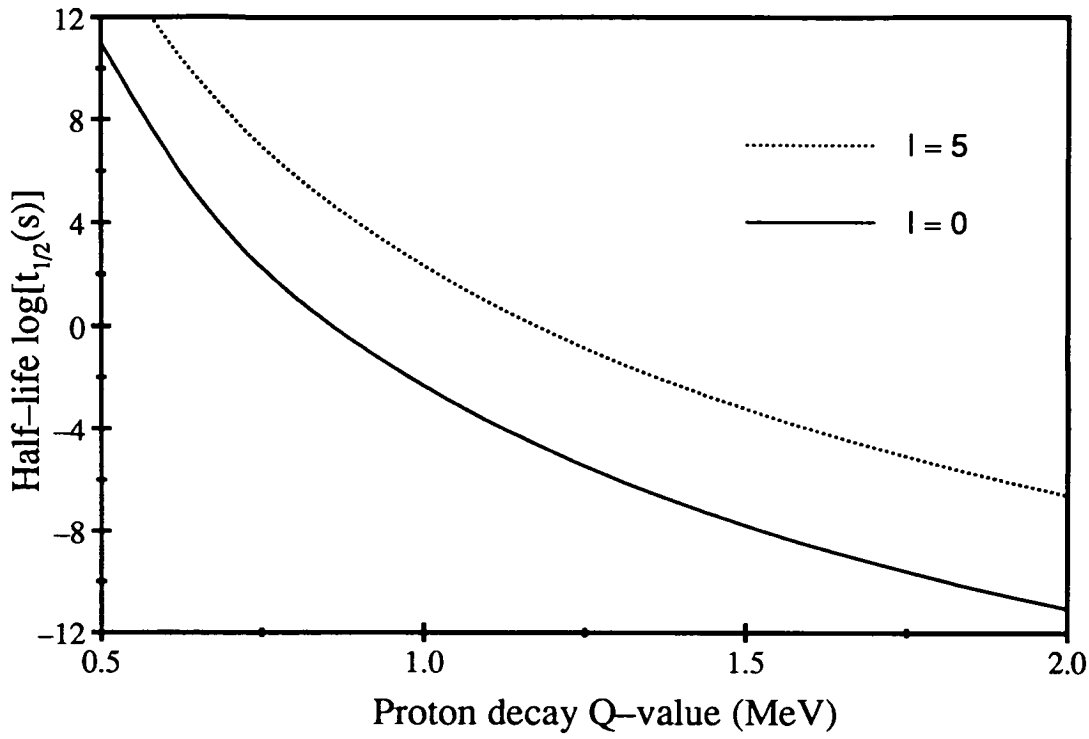

Figure 1.6: *Predicted proton decay partial half-lives of* ^{151}Lu *calculated from a WKB model, as a function of hypothetical Q-value* Q_p

at different energies within the potential well. This strong energy dependence of the half-life is shown in figure 1.6, where changes in Q_p of less than 100 keV can affect the partial half-life by an order of magnitude.

Since Q_p is obtained from the difference in parent and daughter binding energies, systematic trends in Q_p over a set of isotopes are strongly affected by local and systematic nuclear structure effects. The upper plot in figure 1.7 shows the calculated trend in Q_p for Z=71 lutetium isotopes [Mol88], which exhibit strong odd-even staggering due to proton-neutron pairing. The lower plot shows the resulting variation in proton partial half-life, which changes by fifteen orders of magnitude within six isotopes beyond the drip line. The dashed lines indicate the approximate limits of measurable proton half-lives, and demonstrate why observable examples of this type of decay are so scarce.

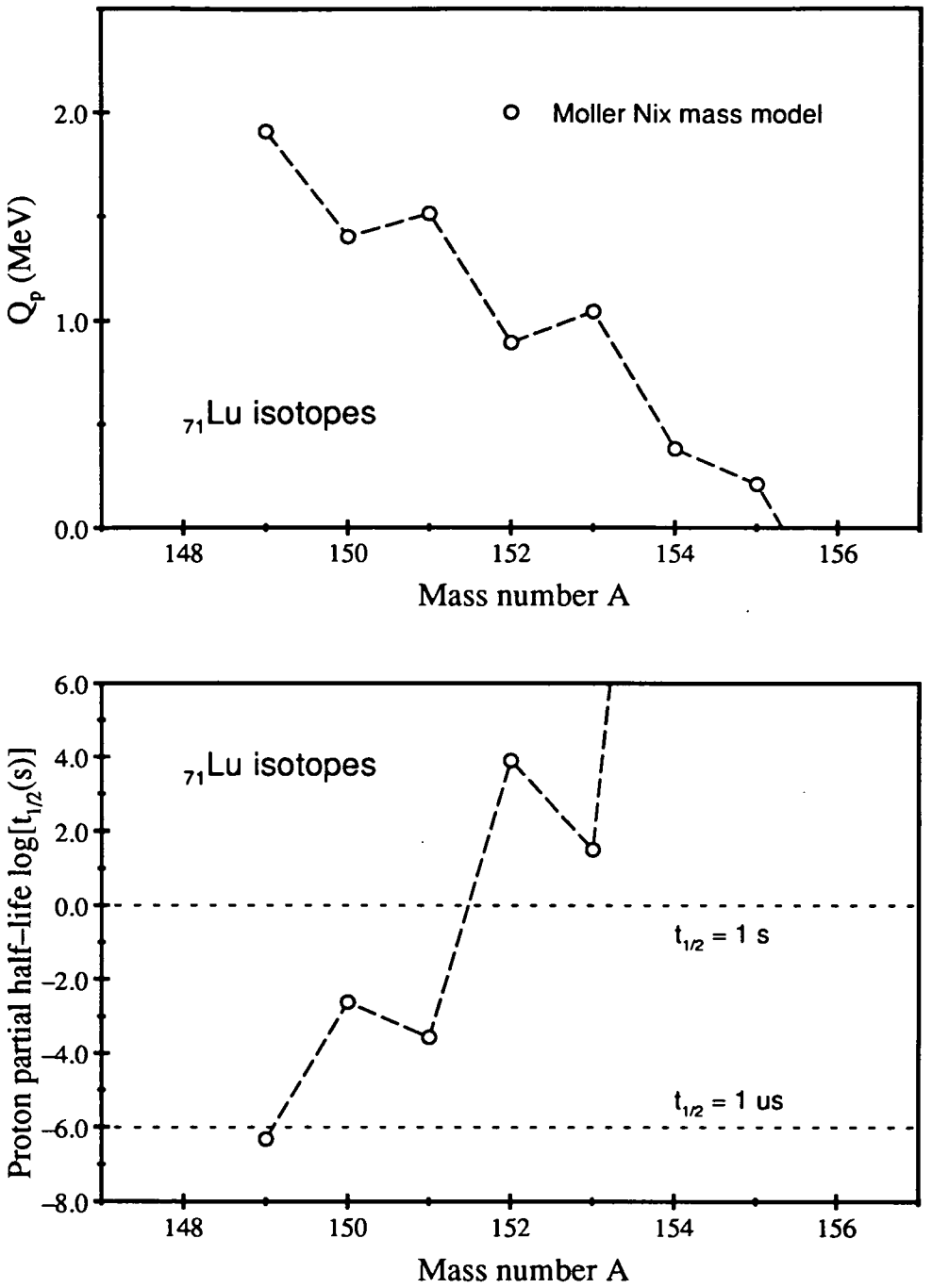

Figure 1.7: *Q_p values and proton partial half-lives for Z=71 lutetium isotopes, calculated from the Möller Nix mass model [Mol88].*

a) the upper plot shows the variation in Q_p for proton unbound isotopes,

b) the lower plot shows the resulting proton partial half-lives, which vary by more than six orders of magnitude within 3 isotopes

1.3 The shell model description of the nucleus

1.3.1 The spherical shell model

Since proton emission decay widths are highly sensitive to the emitted proton's orbital angular momentum, the observed proton half–life is dependent on the spin of the proton fermi level state within the parent nucleus. A proper understanding of proton partial half–lives therefore requires a knowledge of the ordering of proton states around the fermi level.

The spherical shell model of the nucleus has been found to successfully describe the level ordering of nucleons, and reproduces the experimentally observed shell closures. The model considers the independent motion of each nucleon within an average field, where each nucleon follows a largely unperturbed orbit with a mean free path approximately equal to the nuclear diameter. The average potential arises from the summation of each nucleon–nucleon interaction, and can be represented in the first instance by a spherically symmetric potential.

In principle a self–consistent average potential can be determined using a Hartree–Fock type method, based on the sum of two–body interactions. However suitable one–body potentials can be constructed from a knowledge of basic properties of the nucleus, such as the charge density. One such potential is the Woods–Saxon [Woo54], which is derived from the fermi function charge distribution, and gives a potential in terms of the radial distance r with the form

$$V_{ws}(r) = -V_0 \left[1 + e^{\frac{r-R_o}{a_{ws}}}\right]^{-1} \tag{1.31}$$

where $R_o \simeq 1.2$ fm $\times A^{\frac{1}{3}}$, $V_0 \simeq 50$ MeV and $a_{ws} \simeq 0.5$ fm. This choice of potential function has zero gradient (no overall force) close to the centre, and an increasingly attractive force for nucleons nearer to the nuclear surface ($r = R_o$). The potential drops quickly to zero beyond the nuclear surface, correctly reproducing the finite

range of the nuclear force.

In general the energy levels of the single–particle orbitals generated by the shell model are the eigenvalue solutions of the time–independent Schrödinger equation with eigenfunctions ϕ_i

$$\left\{-\frac{\hbar^2}{2m}\nabla^2 + V(\vec{r})\right\}\phi_i(\vec{r}) = \epsilon_i\phi_i(\vec{r}) \tag{1.32}$$

where the hamiltonian includes some form of average potential $V(\vec{r})$, and m is the mass of the nucleon. As a first estimate an infinite square well potential can be used, which gives analytically complete eigenfunctions. The resulting energy levels are shown on the left side of figure 1.8 labelled by the principle quantum number n and the orbital angular momentum l (s,p,d etc). Each shell model level (eg. 2d) can accommodate $2(2l+1)$ of either protons or neutrons.

The use of a more realistic potential, such as the Woods–Saxon type, plus the introduction of proton spin–orbit coupling [Hax49], produces a more realistic single–particle level scheme, as shown on the right of figure 1.8. The spin–orbit interaction splits the two–fold degeneracy of each level, and the total angular momentum j can take two values (provided $j > 0$), namely

$$j = l \pm \frac{1}{2} \tag{1.33}$$

The resulting levels contain a maximum of $2j+1$ nucleons, with an energy separation between level pairs which increases with higher l.

In principle for a shell model nucleus in its ground state, the single–particle orbitals are filled in order of ascending energy with the fermi level holding the last nucleon. The orbital angular momentum of the proton occupying the fermi level in such a shell model nucleus is simply taken from the l value of the highest occupied level.

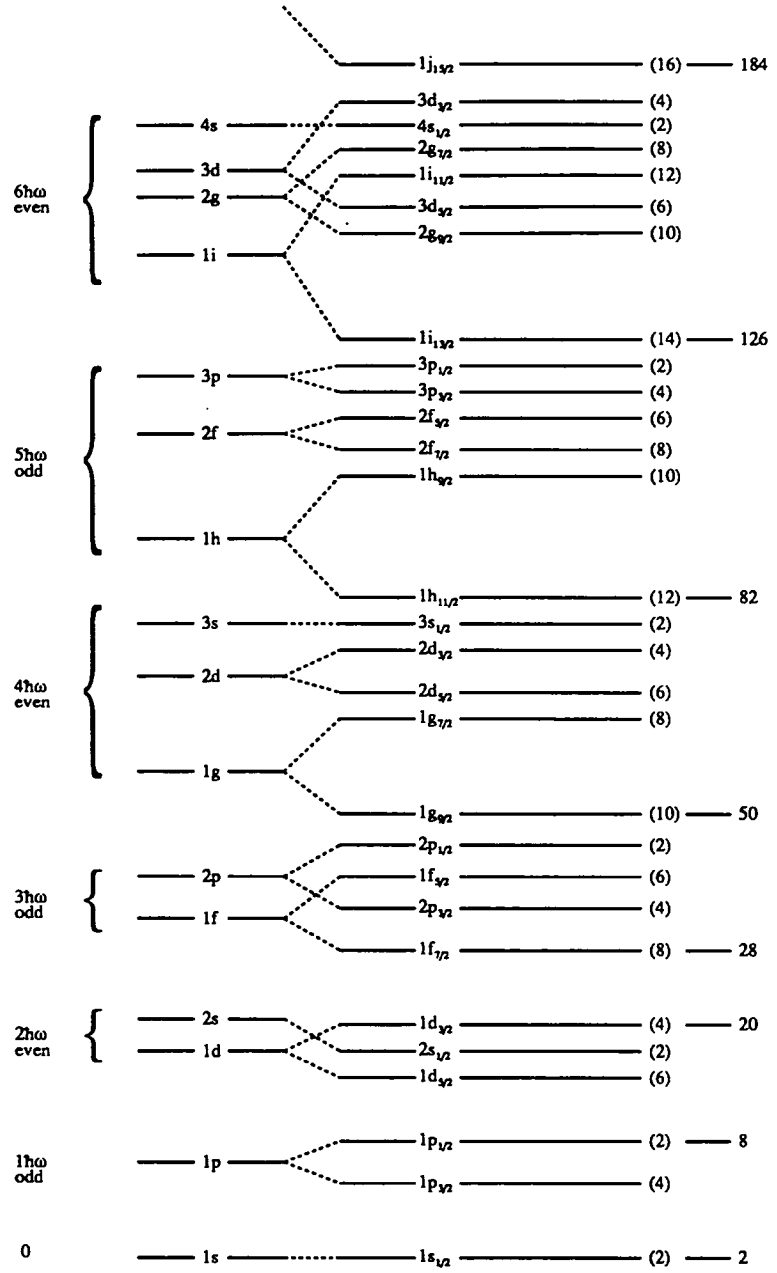

Figure 1.8: *Single–particle orbitals calculated from a spherical potential. Levels on the left are generated using a spin independent potential, whilst those on the right use a potential which includes a spin–orbit interaction*

1.3.2 The deformed shell model and Nilsson orbitals

In general it is incorrect to consider the nucleus as spherical and so the simple shell model picture cannot accurately describe the nuclear level scheme. Particularly in nuclei away from the major closed shells, the states can exhibit large quadrupole moments, and the self–consistent average potential is non spherical.

The application of the Schrödinger equation within the one–body model for non–spherical nuclei was first developed by Nilsson [Nil55], using an assumed spheroidal potential. The resulting single–particle eigenvalues are functions of the nuclear deformation, often parameterised in terms of the quadrupole deformation β_2. The harmonic oscillator hamiltonion is used in the form

$$H_o + H_\delta = -\frac{\hbar^2}{2m}\nabla^2 + \frac{1}{2}m\omega_o^2 r^2 + -\frac{4}{3}\sqrt{\frac{\pi}{5}}\delta m\omega_o^2 r^2 Y_{20} \tag{1.34}$$

where ω_o is the harmonic oscillator frequency, and the deformation parameter δ describes deviations from a spherical shape along the symmetry axis.

The wave functions in the Nilsson scheme are the eigenfunction solutions of the operator

$$H = H_o + H_\delta + C\vec{l}.\vec{s} + D\vec{l}^2 \tag{1.35}$$

where the last two terms describe the spin–orbit and centrifugal contributions respectively. The resulting wave functions are quantised along the symmetry axis, and are described by the quantum numbers

$$Nl\Lambda\Sigma \tag{1.36}$$

where N is the principle quantum number (the total number of nodes in the wave function), l is the orbital angular momentum quantum number , and Λ, Σ are the projections onto the symmetry axis of l and σ respectively.

The projection of the total angular momentum onto the symmetry axis is Ω, such that

$$\Omega = m_l \pm \frac{1}{2} \tag{1.37}$$

and the parity Π of each state is

$$\Pi = (-1)^l = (-1)^N \tag{1.38}$$

For non–zero deformations neither the orbital angular momentum l nor the total angular momentum j of the nucleon is conserved. At large axially symmetric deformations the last two terms in equation 1.35 become negligible, and the states are well defined by the asymptotic quantum numbers

$$[Nn_z\Lambda\Omega] \tag{1.39}$$

which are good quantum numbers at infinite deformation. The new quantum number n_z represents the number of nodal planes in the axial direction, and splits the degeneracy of the shell model state at non–zero deformation into $\frac{2j+1}{2}$ subshells. Each level is two–fold degenerate and is characterised by $|\Omega|$ and the parity. In this way the levels are uniquely described by the labelling convention

$$\Omega\Pi[Nn_z\Lambda] \tag{1.40}$$

Figure 1.9 shows the level scheme from a recent Nilsson–type calculation [Naz90] for rare earth nuclei using a deformed Woods–Saxon potential. The single–particle energies are plotted as functions of quadrupole deformation β_2, with positive parity states shown by a solid line. Such a deformed single–particle level scheme can be used to determine the orbital angular momentum of fermi level protons as a function of deformation in a similar way to the spherical shell model diagram. In this way an odd–Z deformed nucleus has a ground state spin $j = \Omega_o$ where Ω_o takes its value from the Nilsson level occupied by the last nucleon after filling the orbitals at the appropriate deformation. The presence of intruder states of opposite parity to the surrounding levels can lead to dramatic changes in the level ordering compared to the equivalent shell model scheme.

This deformed level scheme can also be used to calculate the ground state deformation, by summing the single–particle energies at each value of β_2 and minimising

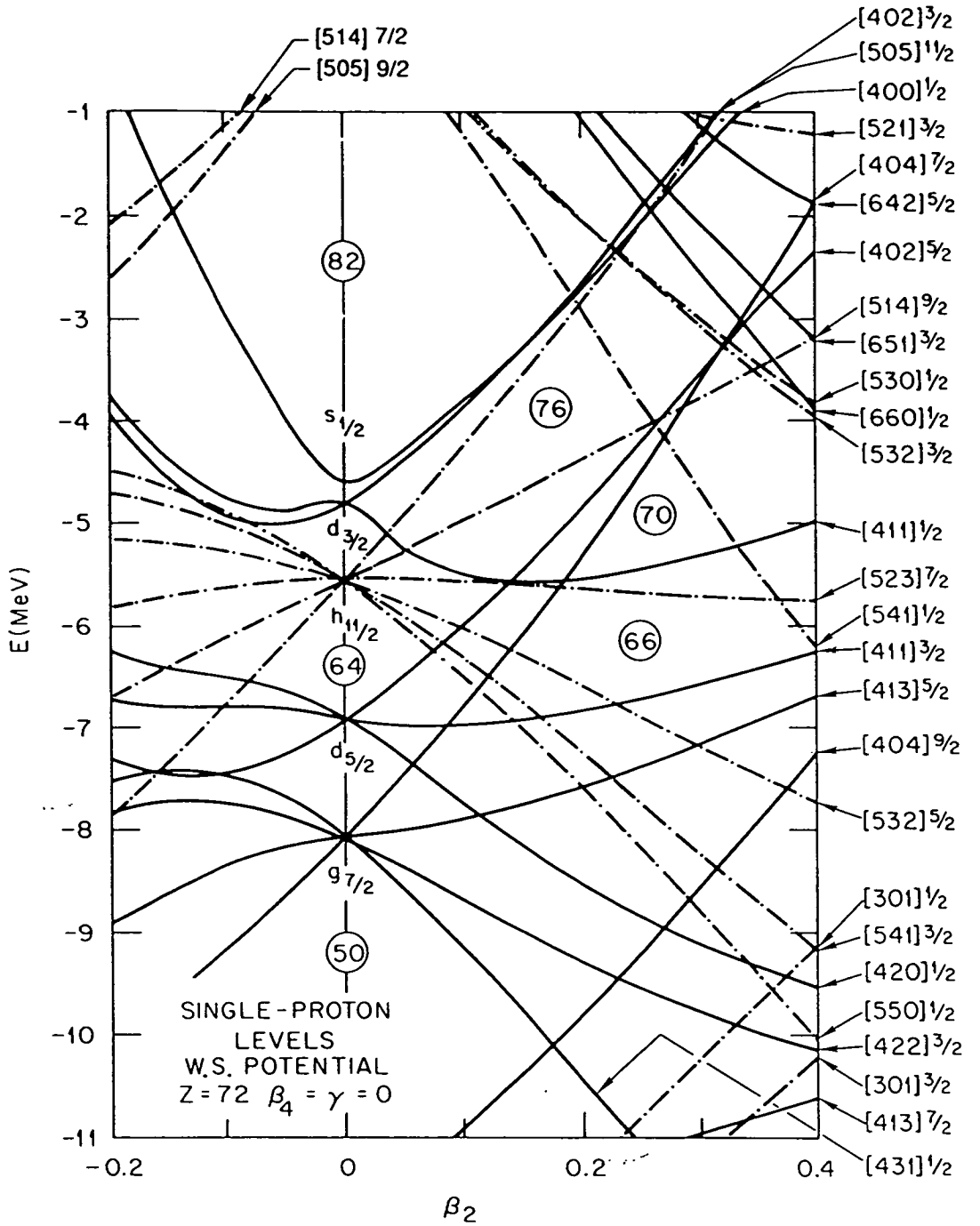

Figure 1.9: *Proton single–particle levels for deformed nuclei in the rare earth region, as a function of quadrupole deformation β_2. From calculations by W. Nazarewicz et al. [Naz90] using a deformed Woods–Saxon potential*

the total energy as a function of deformation. However the resulting energy does not accurately give an absolute ground state binding energy, since this must include additional contributing energy terms such as the nuclear collective motion. The following section describes a deformation dependent mass model based on the macroscopic properties of the nucleus, which can be used to calculate ground state deformations and nuclear masses.

1.4 The Möller Nix mass model

1.4.1 The macroscopic and microscopic terms

The extreme sensitivity of the proton emission decay width to changes in decay energy requires the accurate prediction of Q–values for nuclei far from stability, as well as a knowledge of the ordering of single–particle levels close to the fermi surface. Since in general nuclei are deformed, it is necessary to use a mass model for Q–value predictions which can determine the nuclear ground state deformation. The Möller Nix mass formula is a good example of such a model which can be used both in regions of shell model and transitional nuclei. The model calculates the total nuclear potential energy as a function of deformation, and so locates the ground state deformation as that corresponding to the minimum total energy.

The Möller Nix mass formula uses a 'macroscopic–microscopic' model, consisting of a semi–empirical energy term varying smoothly over a wide range of Z and N, plus a rapidly fluctuating correction describing the shell structure around the fermi level. General descriptions of this type of model can be found in review articles by J.R. Nix *et al.* [Nix72] and S. Bjørnholm *et al.* [Bjø80]. In general the total nuclear potential energy is formed from the sum of these two contributions, each as a function of particle number and nuclear deformation

$$E(Z, N, shape) = E_{macr}(Z, N, shape) + E_{micr}(Z, N, shape) \qquad (1.41)$$

A detailed description of the original form of the Möller Nix model is given in [Mol81].

The macroscopic energy is calculated from a shape dependent volume integral describing the surface and volume nuclear energies [Kra79]. Up to eight additional correction terms are included to model physical effects such as the coulomb energy, charge asymmetry and nucleon pairing. These correction terms have been gradually refined during the development of the model (see [Mol81, Mol81a, Mol88]). The macroscopic term contains a total of nineteen constants, fourteen of which are given fixed values deduced without direct reference to known masses. The remaining five constants are varied in order to produce a best fit between a set of calculated and known mass values.

The microscopic energy term models the fluctuations in the total energy arising from the non–uniform distribution of single–particle levels in the nucleus. The microscopic correction term is the sum of a shell–correction energy and a pairing energy

$$E_{micr}(Z, N, shape) = E_{shell}(Z, N, shape) + E_{pair}(Z, N, shape) \qquad (1.42)$$

The microscopic energy is calculated as described by Bolsterli *et al.* [Bol72] using Strutinsky's shell correction method [Str67, Str68]. The first step is to calculate the single–particle levels for protons and neutrons by solving the Schrödinger equation for some form of single nucleon shape–dependent potential [Tal56].

Having obtained the energies of the occupied single–particle Nilsson orbitals, Strutinsky's method is used to obtain the shell correction $E_{shell}(Z, N, shape)$. This is performed by essentially summing the energy of the occupied levels and subtracting from this the energy calculated by integrating over a smoothed single–particle level density. The resulting shell correction term smoothes out local fluctuations in the single–particle level density, particularly around the major closed shells.

The pairing correction $E_{pair}(Z, N, shape)$ arises due to the short–range interaction of correlated pairs of nucleons, which tends to lower the total potential energy relative to the energy without pairing. The BCS approximation is used [Pra73] to calculate the energy lowering expected for both the actual level distribution and for the smoothed level distribution. The difference in the two lowering terms gives the pairing correction.

1.4.2 Calculation of ground state masses

The total energy formula is initially used to calculate ground state masses for nuclei with experimentally known masses. The first step in calculating the nuclear ground state masses is to minimise the total energy for each nucleus with respect to the two deformation parameters β_2 and β_4. A two dimensional grid in β_2 and β_4 is constructed, and the single–particle levels, macroscopic energy, shell correction energy and pairing energy are calculated for each grid point. The parameters of the single particle potential are dependent on Z and N, however in order to minimise the computing time the same values are used for groups of neighbouring nuclei. It is found that the macroscopic energy term constants, which are varied when fitting to the known mass surface, are virtually independent of shape deformation. This allows the ground state deformation to be found for each nucleus, corresponding to an energy minimum on the ε_2, ε_4 parameter surface, with the five constants within the macroscopic term held fixed for each value of Z and N.

Once the ground state deformations are calculated, the total energy formula is used to calculate the ground state mass of each nucleus. These values are compared to the known masses, taken from either the 1977 mass data set [Wap77] or from recent measurements of new masses far from stability. The most recent adjustment [Mol88] calculates the root–mean–square deviation between experimental and calculated masses as 0.832 MeV for 1593 nuclei between ^{16}O and ^{263}106. In this calculation the most significant change to the energy formula com-

pared to previous evaluations is in the macroscopic energy pairing term, which is described in detail in [Mad88]. The model is used to calculate masses for a total of 4678 nuclei ranging up to $^{318}122$.

1.5 Using mass models for Q_p predictions

In order to make accurate predictions of Q_p values a mass model must possess good predictive qualities for nuclei a long way from the known mass data. In general it is found [Hau88] that those models which can achieve a good fit to the known mass data by using a large number of free parameters have poor predictive abilities far from stability. Conversely the Möller Nix mass model, with only five free parameters, produces a below average fit to the known mass data, yet has particularly good predictive qualities.

An alternative type of mass model is the empirical shell model formula of Liran and Zeldes [Lir76]. This adopts a more fundamental approach by summing the strong pairing interactions between nucleons within each major shell. Additional contributions are included to model breaking of nucleon pairs, and single nucleon excitations between shells. The range of Z and N values are divided into separate shell regions, each with five related parameters. The mass values are calculated separately for nuclei within each shell region, and then matched across each shell boundary to form a continuous mass surface.

Figure 1.10 shows the Q_p values for Z=71 lutetium isotopes, calculated by the mass models of Möller Nix, Liran and Zeldes, and the simple droplet model of Myers [Mye70]. The figure also shows for comparison the known Q_p value of ^{151}Lu, and data from the 1988 atomic mass evaluation of Wapstra *et al.* [Wap88]. These Q_p values are deduced from known mass systematics, and only values with an error of less than approximately 500 keV have been included.

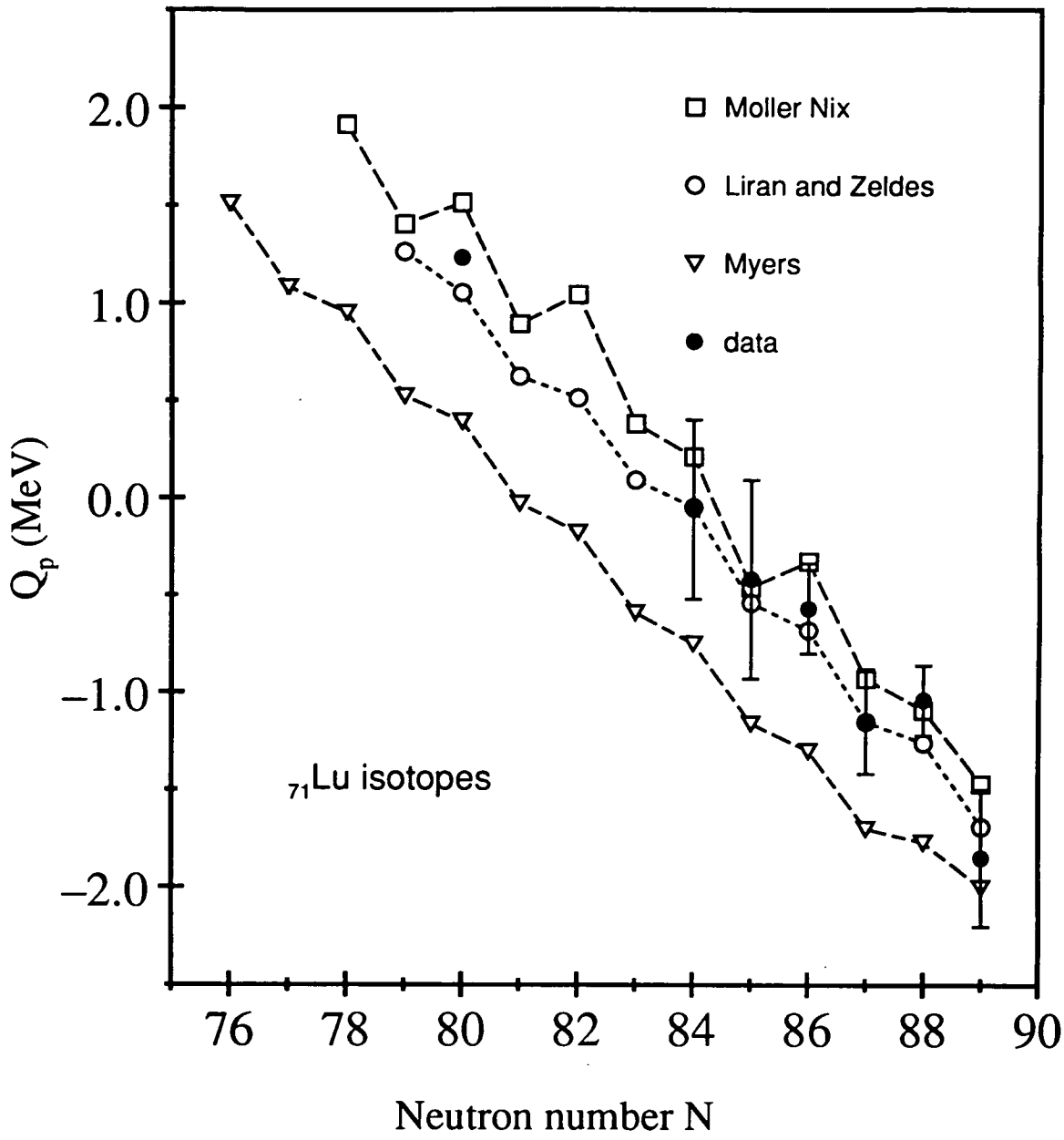

Figure 1.10: *Calculated Q_p values for Z=71 lutetium isotopes, including the known proton transition ^{151}Lu. Other data points are from Wapstra mass systematics, restricted to Q_p values with an error less than 500 keV*

The 1988 Möller Nix calculation includes a revised treatment of the proton–neutron pairing interaction, and tends to over calculate the odd–even staggering. The Liran and Zeldes shell model calculations show a reduced staggering effect, which produces Q_p values close to the Möller Nix figures for the odd–N isotopes only.

The droplet model of Myers predicts Q_p values which both neglect the odd–even staggering, and are consistently lower than the experimental values by up to 800 keV. This effect, which is discussed by Hofmann *et al.* [Hof81], is surprising since the model calculates Q_α values for isotopes of Re–Hf which are in good agreement with experiment. The weaker odd–even staggering in Q_p values indicates that the Myers model underestimates the strength of the neutron–proton pairing.

The regions of the drip line of immediate interest for new examples of direct proton emission lie immediately above and below the known proton emitters at masses 147 and 151. Consideration of odd–Z candidates in the range $73 \leq Z \leq 77$ suggests that ^{165}Ir, ^{160}Re and ^{156}Ta offer the best chance of observing direct proton emission. Q_p values would need to be sufficiently large in this region to prevent significant competition from alpha decay. Table 1.1 summarises the Möller Nix Q_p value predictions for these nuclei between Z=61 and Z=77. At the time of writing recent experiments from the group have confirmed proton emission from ^{156}Ta, ^{160}Re, and also from ^{146}Tm. These latest results will be discussed briefly in section 5.4.

At lower masses the light rare earth region between Z=61 and Z=67 provide a region of possible new proton emitters, which have no competing alpha decay mode. The predicted position of the proton drip line in this region lies so far from the known mass data that Q_p estimates from mass models are extremely unreliable. By drawing a line between the known emitters around A=109 and A=147, a simple interpolation suggests that the deformed nuclei ^{128}Pm, ^{132}Eu,^{138}Tb and

Nucleus	Q_p	$t_{\frac{1}{2}}^{calc}$		
	MeV	Δl=0	Δl=2	Δl=5
^{165}Ir	1.15	2.3 ms	19 ms	18 s
^{160}Re	1.30	38 μs	300 μs	280 ms
^{156}Ta	1.39	4.5 μs	35 μs	31 ms

Table 1.1: *Möller Nix Q_p predictions and proton partial half-life estimates for prospective proton emitting isotopes with $73 \leq Z \leq 77$. Half-lives are calculated using a WKB model [Pag90] with a real optical potential [Per72]*

^{142}Ho have predicted Q_p values within the necessary approximate range.

Chapter 2

Experimental observations of direct proton emission

2.1 Accessing the proton drip line

The development of the experimental techniques required to access the proton drip line at intermediate and heavy masses has continued throughout the last few decades. During the mid sixties Macfarlane *et al.* [Mac65] carried out a study of neutron deficient nuclei around $N = 82$ using light–ion projectile fusion reactions at the Berkeley linear accelerator. The resulting new alpha emitting isotopes of lutetium (^{155,156}Lu) and hafnium (^{157,158}Hf) were produced by bombarding a target of ^{144}Sm with beams of ^{19}Fe and ^{20}Ne. The helium–jet transport system limited the sensitivity of the technique to nuclei with half–lives $\geq$ 1 ms, giving collection efficiencies of approximately 5%. The restricted range of light–ion beams available from this type of accelerator prevented the production of neutron deficient isotopes far enough beyond the drip line to exhibit proton emission (eg. ^{151}Lu).

An alternative approach to exotic nucleus production uses proton–induced spallation reactions. This technique has the potential advantage of large production

cross sections, and uses chemical selectivity to separate the desired ion species from the large range of reaction products. The ISOLDE facility at CERN has been used to study highly neutron–deficient alpha emitting mercury isotopes by Hagberg *et al.* [Hag79] using 600 MeV protons incident on a molten lead target. The relatively long release times of the ions from the liquid target restricts the use of this technique to nuclei with half–lives $\gtrsim$ 100 ms.

The proton drip line has now been successfully reached at light masses using projectile fragmentation reactions, notably at GANIL and at MSU (see for example Borrel *et al.* [Bor91] and Mohar *et al.* [Moh91]). This technique uses beams of highly proton rich nuclei at high energy ($\simeq 50-65$ MeV/u) which fragment to produce a strongly forward focused cone of reaction products containing a wide range of nuclei of proton number up to that of the projectile species. Fragment separators such as LISE at GANIL and the new A1200 at MSU are used in conjunction with time–of–flight and energy loss measurements to identify the fragments. Recent experiments at MSU have reached the proton drip line at Z=37 [Moh91] using beams of $^{78}_{36}$Kr on a $^{58}_{28}$Ni target. However the beam energies available at these facilities in the near future restricts the accessible region of the proton drip line to light nuclei. The imminent completion of the SIS accelerator at GSI, together with its associated fragment recoil separator, will allow beam energies up to about 2 GeV/u, and will make possible the production of many new nuclei using extremely heavy beam fragmentation reactions.

Compound nucleus production using heavy ion fusion–evaporation reactions has long been used to produce proton rich nuclei in regions of intermediate and heavy masses. With the advent of heavy ion accelerators such as UNILAC at GSI, it has been possible to choose proton rich combinations of stable beam and target nuclei in order to produce the required highly proton rich compound nuclei. Typical reactions using ^{58}Ni and ^{40}Ca beams on targets of isotopically enriched ^{92}Mo, ^{96}Ru and ^{54}Fe have accessed the proton drip line in regions around mass 151 and 109. Usually the three nucleon evaporation channels are used, with compound nucleus

excitation energies in the range 30−80 MeV. Fast efficient on–line separation of the evaporation residues from both the projectile nuclei and other reaction products is essential to prevent the low yield decay lines being swamped by background events. The lower limit on the observable half–life is usually imposed by the detection system and instrumentation rather than the separator flight time, which for SHIP at GSI and the Daresbury recoil separator is typically 1 μs.

2.2 Known examples of direct proton emission

To date all the observations of direct proton emission have been at heavy masses above tin. In each case the drip line has been accessed using heavy ion fusion–evaporation reactions with a combination of proton rich stable beams and targets.

The first example of direct ground state proton emission was recorded by Hofmann *et al.* in 1982 [Hof82] using the SHIP in–flight velocity separator at the GSI UNILAC accelerator. A ^{58}Ni beam was used on a target of isotopically enriched ^{96}Ru to produce the compound nucleus ^{154}Hf* at an excitation energy of 47 MeV. The evaporation residues were separated from the beam–like particles using SHIP, before being implanted into the silicon detector system. A discrete transition was seen at an energy well below that of the observed alpha lines, which was subsequently measured with an energy of 1233 keV. The measured transition was attributed to the direct proton decay of ^{151}Lu using excitation function and Q–value systematics. The half–life was subsequently measured as 85 $\pm$ 10 ms, which clearly identified the origin of the transition as the $h_{\frac{11}{2}}$ proton level in ^{151}Lu.

Shortly after the observation of proton emission from ^{151}Lu, Klepper *et al.* [Kle82, Lar83] reported strong evidence for direct proton emission from the nucleus ^{147}Tm. The observations were made with the GSI on–line mass separator using the reaction ^{58}Ni + ^{92}Mo $\rightarrow$ ^{150}Yb*. In this mass separator technique (see [Bru81, Kir81]) the recoiling products are stopped in a tantalum catcher foil inside the thermal

ion source, from where the mass separated ion beams are implanted into carbon foils positioned in front of a pair of ΔE–E silicon detector telescopes. The finite release time of the ions from the catcher foil limits the sensitivity of this technique to half–lives greater than about 100 ms. A discrete transition was seen at 1059 ± 10 keV corresponding to A=147 isobars, which was assigned to the direct proton decay of ^{147}Tm. A measured half–life of 560 ± 40 ms indicated an l=5 proton transition from an $h_{\frac{11}{2}}$ ground state.

In 1984 two further examples of proton radioactivity were reported from ^{113}Cs and ^{109}I by Faestermann *et al.* [Fae84]. Using the Munich MP tandem and linear post–accelerator, targets of ^{58}Ni and ^{54}Ni were irradiated with a pulsed beam of ^{58}Ni. A discrete line was seen in each case, with energies of 980 ± 80 keV and 830 ± 80 keV respectively. The half–lives for each line were subsequently measured [Gil87] as 33 ± 7 μs and 109 ± 17 μs respectively. The Munich technique separated the residues from the beam–like particles using a catcher foil within an annular gas detector, see [Gil87]. The technique was sensitive to half–lives as low as 10 ns, so overcoming the time–of–flight limitation inherent in large in–flight separators.

Extensive searches were carried out using SHIP during the period 1981 to 1987 to locate further examples of direct proton emission in the light rare earth region located between the two existing groups of proton emitters. Production of the desired evaporation residues was generally attempted via the p2n channel, with a detection sensitivity to half–lives of typically > 20 μs and cross sections $\gtrsim$ 25 μb. No further examples of proton emission were observed, which was most probably due to the p2n residues not being sufficiently far beyond the proton drip line to exhibit a significant proton decay branch. The sensitivity of the SHIP technique was not sufficient to look for the more promising candidates produced via p3n channels, which have predicted cross sections about an order of magnitude less than the p2n channel.

2.3 Proton radioactivity measurements using SHIP

The unique technique provided by the in-flight velocity separation of SHIP allowed the group at GSI to remeasure each of the four direct proton lines discussed in the previous section, and record improved values for the decay energies and half-lives. In addition the SHIP experiments recorded two further weak proton transitions, again using the reactions ^{58}Ni + ^{92}Mo $\rightarrow$ ^{150}Yb* and ^{58}Ni + ^{96}Ru $\rightarrow$ ^{154}Hf* . A 1118 keV line produced from ^{150}Yb* was preliminarily assigned to proton emission from a low spin excited state in ^{147}Tm, and a very weak line at 1263 keV was seen from ^{154}Hf* which is most probably due to the decay of ^{150}Lu. Table 2.1 lists the six major transitions which were measured at SHIP during this period, which are summarised in [Hof88].

Nucleus	Energy E_p keV	$t_{\frac{1}{2}}$	Compound nucleus	E_x MeV	σ_{peak} μb
^{151}Lu	1233 ± 3	85 ± 10 ms	^{154}Hf*	49	70
^{147}Tm	1051 ± 4	560 ± 40 ms	^{150}Yb*	51	30
(^{150}Lu)	1263 ± 4	> 10 ms	^{154}Hf*	74	10
(^{147}Tm)	1118 ± 6	360 ± 80 μs	^{150}Yb*	42	3
^{113}Cs	959 ± 4	33 ± 7 μs	^{116}Ba*	48	50
^{109}I	813 ± 5	109 ± 17 μs	^{112}Xe*	52	50

Table 2.1: *Summary of direct proton transitions measured at SHIP (from [Hof88]), with tentative assignments given in brackets*

The GSI UNILAC accelerator was used to accelerate proton-rich heavy ion beams (such as ^{40}Ca and ^{58}Ni) with typical beam energies of up to 6 MeV/u. A variety of target materials were bombarded during the systematic program of search experiments, using a range of isotopically enriched neutron deficient isotopes from ^{50}Cr to ^{106}Cd, with thicknesses in the range $500 - 1000$ μg cm^{-2}.

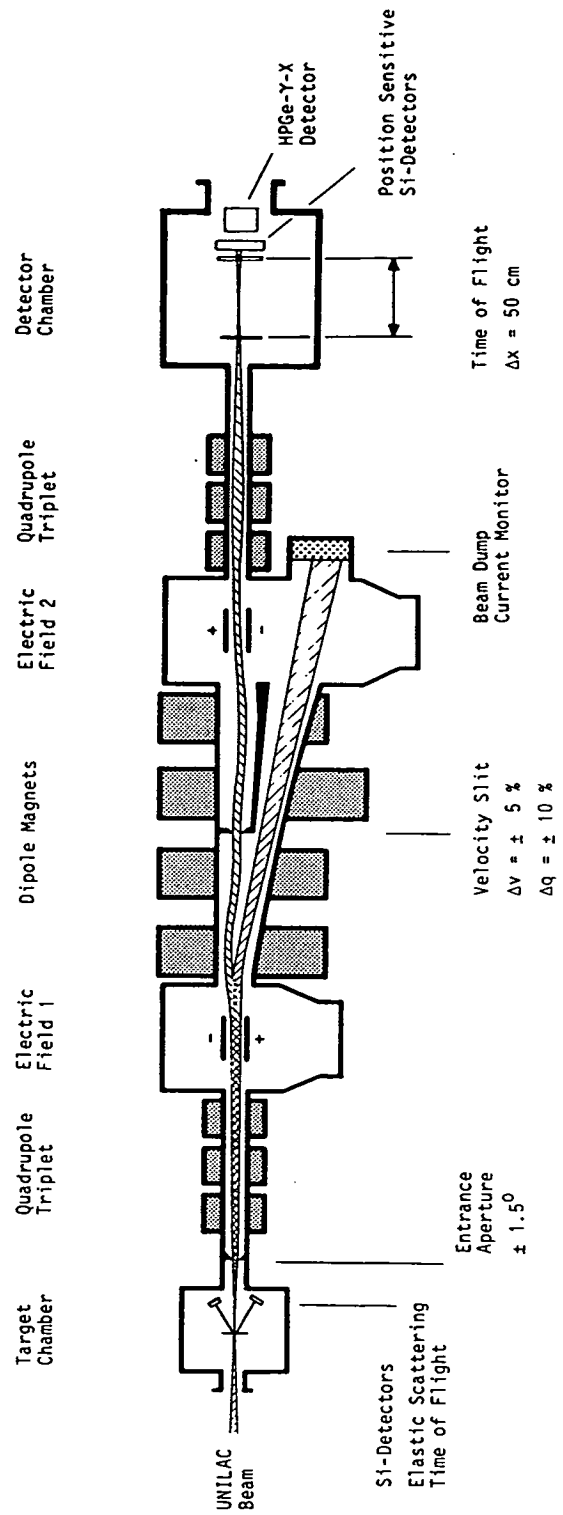

Figure 2.1: *The velocity filter SHIP at GSI*

The recoiling evaporation residues were separated from the projectiles and other fusion reaction products by the velocity separator SHIP, which is shown schematically in figure 2.1. The separator uses a combination of electric fields and dipole magnets to separate the residues, which travel through the 11 m long device with flight times in the range $0.6 - 1.1$ μs. The separator's design and operation is described in detail by Münzenberg *et al.* [Mun79]. The overall separation and transmission efficiency for residues arriving at the focal plane varied between 10% and 40% for the various evaporation channels.

At the separator focal plane the evaporation residues were implanted into an array of seven one–dimensional position sensitive detectors, which recorded the energy, time and vertical position for each implantation event. The energy of the implanted nuclei's subsequent decays were measured by the detectors, together with their position and time. During analysis correlated event chains could be identified by extracting a sequence of events in the same vertical position in the detector, and which occurred within a predetermined time window. In this way decay half–lives of the parent nucleus could be measured up to several milliseconds, with an implantation rate of several hundred residues per second [Hof81].

Sensitivity to half–lives in the millisecond range was improved by using a chopped beam, with a 'macro' structure of a 5 ms beam pulse followed by a 15 ms beam–off period. Half–lives in the range of 10 ms to several seconds were measured using a rotating cylinder to chop the evaporation residues upstream of the detector array.

Assignment of the observed low energy transitions to proton emission was confirmed by replacing the position sensitive detectors with a solid state ΔE–E telescope [Hof82]. Evaporation residues were implanted and stopped within the ΔE detector, which was approximately 25 μm thick. Protons and alpha particles emitted in a forward direction during the subsequent decay events were stopped by the thick detector located 15 mm downstream. The resulting particle identification plot could clearly separate events from the two different particle types. The

absence of coincident γ or X–rays was confirmed using a 12% efficient germanium detector located behind the particle detectors.

Due to the absence of internal low energy calibration lines, the energy of the proton transition from ^{151}Lu was measured accurately at SHIP using a thick silicon detector calibrated with alpha particles and conversion electrons from laboratory sources. Subsequent SHIP measurements of the other proton lines used an internal energy calibration based on the ^{151}Lu line and alpha lines from implanted evaporation residues.

2.4 Proton emitters produced from ^{150}Yb* and ^{154}Hf*

2.4.1 The proton decay of ^{147}Tm and ^{151}Lu

The two strong proton transitions seen previously from the compound nuclei ^{150}Yb* (E_p = 1051 keV) and ^{154}Hf* (E_p = 1233 keV) have been convincingly assigned to ground state proton emission from ^{147}Tm and ^{151}Lu respectively [Hof88].

The strong 1051 keV line from ^{147}Tm is the only prompt proton emitter for which there is a direct mass assignment, measured during the mass separator experiments of Klepper *et al.* [Kle82]. It was fortunate that both the half–life and yield of this transition were within the sensitivity range of this technique. In general direct proton decays will be either too fast or too weak (or possibly both) to be observed in this way. For proton emitters with alpha-decaying daughter nuclei (such as ^{113}Cs and ^{109}I) a mass assignment can be made in principle if the daughter nucleus can be unambiguously identified from its alpha decay.

In general proton transitions identified using SHIP cannot be directly mass assigned, and so are identified from the excitation function systematics of the com-

pound nucleus evaporation channels. The 49 MeV excitation energy of $^{154}Hf^*$, which corresponded to the maximum proton yield, identified the source of the 1233 keV line as ^{151}Lu, produced via the p2n channel [Hof82]. A direct mass assignment using the on–line mass separator was not possible due to the relatively quick half–life of the decay.

Parent	^{147}Tm $\frac{11}{2}^-$	^{151}Lu $\frac{11}{2}^-$
Daughter	^{146}Er 0^+	^{150}Yb 0^+
Δl	5	5
Compound nucleus	$^{150}Yb^*$	$^{154}Hf^*$
Excitation energy	51 MeV	49 MeV
σ_{peak}	30 μb	70 μb
E_p	1051±4 keV	1233±3 keV
experimental half–life $t_{1/2}^{exp}$	560±40 ms	85±10 ms
proton branching ratio b_p	21±10 %	70±35 %
proton partial half–life $t_{1/2,p}^{exp}$	$2.7^{+2.5}_{-0.9}$ s	120^{+120}_{-40} ms
calc. partial half–life $t_{1/2,p}^{WKB}$		
l=0	97 μs	2.9 μs
l=1	200 μs	5.9 μs
l=2	820 μs	26 μs
l=3	6.7 ms	185 μs
l=4	110 ms	2.7 ms
l=5	3.3 s	81 ms

Table 2.2: *Summary of the SHIP measurements of ^{147}Tm and ^{151}Lu (from [Hof88])*

Comparison of the measured half–lives for the two lines with calculated WKB estimates are shown in table 2.2. Allowing for the approximate factor of two uncertainty in these calculations, it is clear that both decays can be described by an l=5 transition without the need for additional hindrance. This suggests that the $h_{\frac{11}{2}}$ proton orbital is the ground state level in each case.

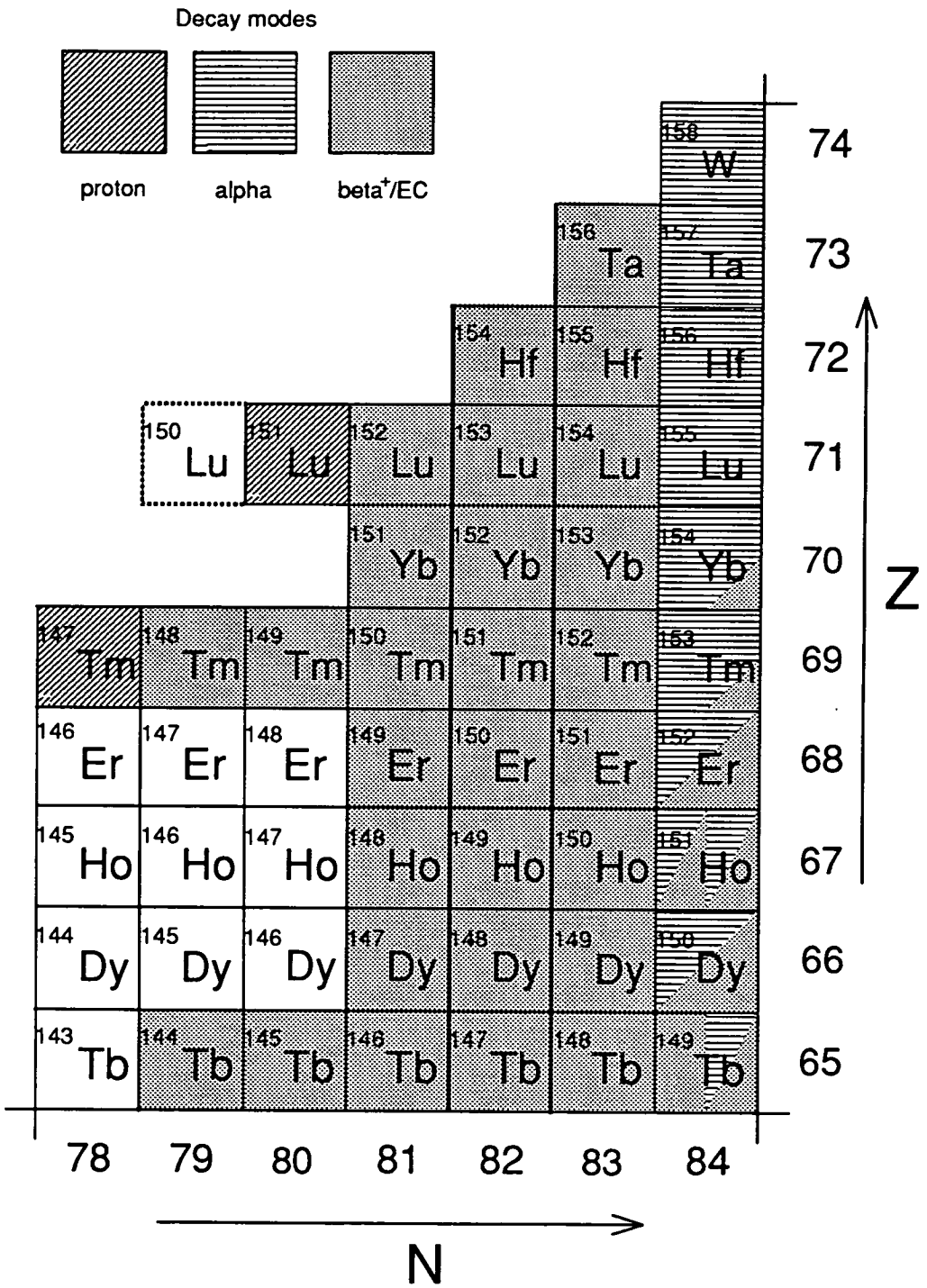

Figure 2.2: *Decay modes of proton rich nuclei in the region* $Z > 64$, $N \leq 84$

The decay modes of drip line nuclei in this region are influenced by the presence of the neutron major shell closure at N=82. As is shown in figure 2.2, isotopes near the drip line with $N \geq 84$ tend to exhibit alpha decay, whereas those with $N \leq 83$ decay by β^+ emission. The proton emitters around ^{147}Tm and ^{151}Lu lie in the quadrant $Z \geq 64$, $N \leq 82$ and exhibit pure shell model states where the proton levels $1h_{\frac{11}{2}}$, $3s_{\frac{1}{2}}$ and $2d_{\frac{3}{2}}$ are around the fermi surface.

The low-lying single-particle level scheme is known for nuclei reasonably far from stability in this region, due mainly to γ-spectroscopy from daughter nuclei fed by β^+ decay (see [Tot87] for a recent summary). Amongst the odd-Z even-N isotopes in this region, partial single-particle level schemes are known as far as $^{147}_{65}$Tb, $^{149}_{67}$Ho, $^{151}_{69}$Tm and $^{155}_{71}$Lu. In general in the region $65 \leq Z \leq 71$ $N \leq 86$, the $h_{\frac{11}{2}}$ and $s_{\frac{1}{2}}$ states are separated by approximately 50 keV, with the $d_{\frac{3}{2}}$ level forming the second excited state at an energy typically less than 250 keV above the ground state. Figure 2.3 shows the relative positions of single proton states in odd-Z N=82 isotones, where the crossing of the $h_{\frac{11}{2}}$ with the $s_{\frac{1}{2}}$ level is seen between ^{147}Tb ($s_{\frac{1}{2}}$ ground state) and ^{149}Ho ($h_{\frac{11}{2}}$ ground state).

2.4.2 Weaker proton lines seen around ^{147}Tm and ^{151}Lu

During the SHIP experiments using the reactions ^{58}Ni + ^{92}Mo $\rightarrow$ ^{150}Yb* and ^{58}Ni + ^{96}Ru $\rightarrow$ ^{154}Hf* a number of weaker proton transitions were also observed. Two lines were clearly observed, one at an energy of 1118 keV from ^{150}Yb* and the other at 1263 keV from ^{154}Hf*. An additional five very weak lines were observed, listed in table 2.3.

The two lines at 1118 keV and 1263 keV were preliminarily assigned to direct proton emission from a low spin excited state in ^{147}Tm and from the ground state of ^{150}Lu respectively. However the low cross section and occurrence within a narrow range of excitation energies prevented a full excitation function study.

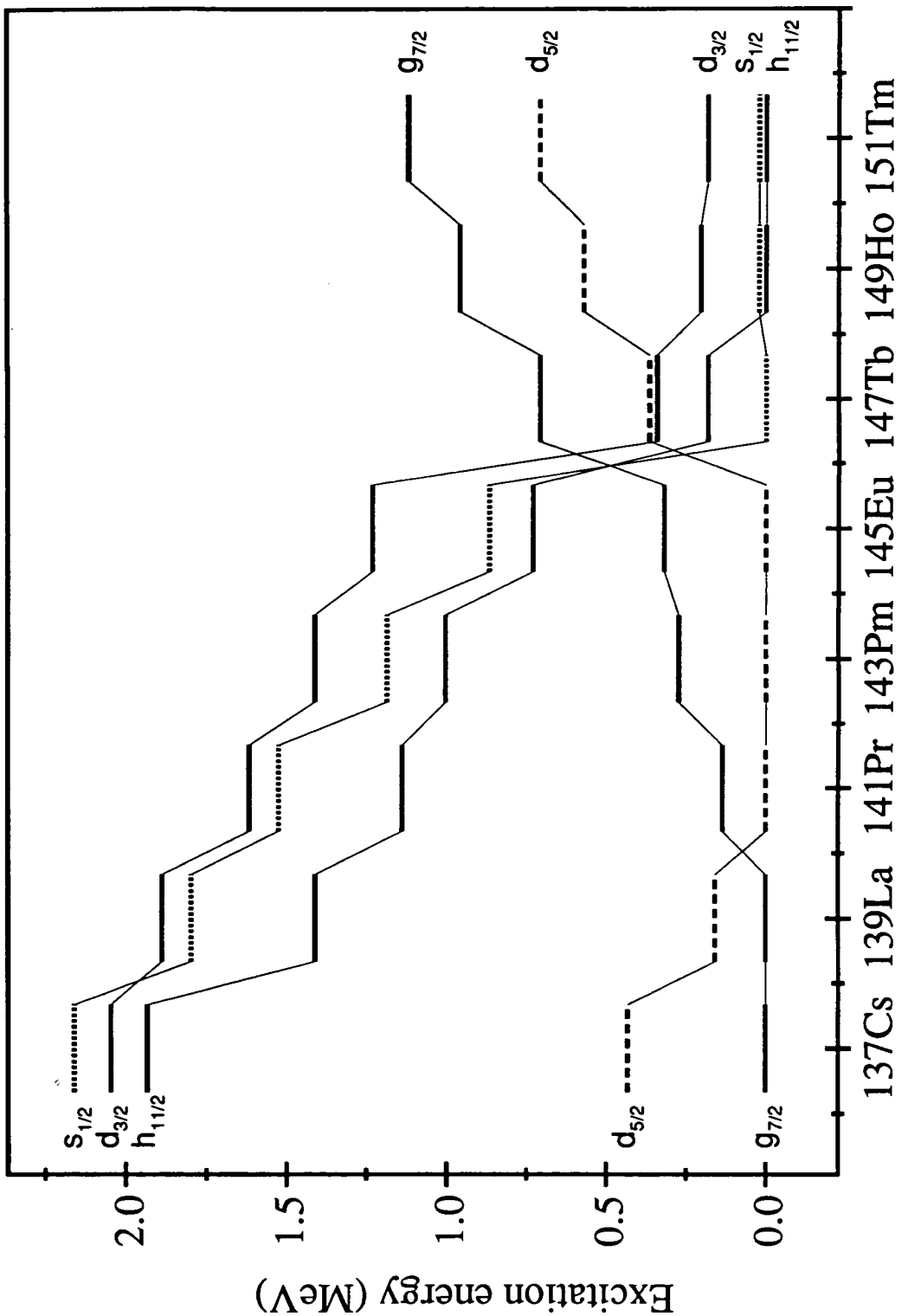

Figure 2.3: *Experimental systematics of proton levels in light rare earth odd-Z N=82 isotones. Beyond the the Z=64 closure (between ^{145}Eu and ^{147}Tb) both the $g_{\frac{7}{2}}$ and $d_{\frac{5}{2}}$ levels are proton hole states*

Compound nucleus	Excitation energy MeV	Decay energy keV	Measured half-life	Measured proton σ μb	Assignment
^{150}Yb*	51	1051 ± 4	560 ± 40 ms	30	^{147}Tm
^{154}Hf*	49	1233 ± 3	85 ± 10 ms	70	^{151}Lu
^{150}Yb*	42	1118 ± 6	360 ± 80 μs	<3	(^{147}Tm)
	50	2467 ± 20	10^{-3}–10 ms	10	?
	50	2851 ± 15	10^{-3}–10 ms	20	?
	50	2935	10^{-3}–10 ms	5	?
	50	3277	10^{-3}–10 ms	5	?
^{154}Hf*	72–78	1263 ± 4	>10 ms	2–10	(^{150}Lu)
	68	1360 ± 10	>2 ms	1	?

Table 2.3: *Summary of proton transitions arising from SHIP experiments on ^{150}Yb* and ^{154}Hf*, tentative assignments are in brackets (from [Hof88, Hof91])*

In the case of the 1118 keV line the excitation energy of 42 MeV corresponds to the maximum cross section of both the two nucleon channels (^{148}Er, ^{148}Tm and ^{148}Yb) and the low-lying excited states of the three nucleon channels. Since the $s_{\frac{1}{2}}$ and $d_{\frac{3}{2}}$ levels are predicted to have a very narrow separation energy in this region, it is unclear which level would be occupied in the first excited state. Figure 2.4 shows the calculated Q_p value predictions for nuclei produced via the two nucleon evaporation channels, and for transitions from 50 keV excited states for nuclei via the three nucleon channels. From the two nucleon channels, only ^{148}Tm has a positive predicted Q_p value which is approximately 500 keV less than the required value. The possibility of the transition originating from a low-lying isomeric state in ^{148}Tm cannot be ruled out since odd–odd nuclei below N=81 are known to form low spin states by coupling the $s_{\frac{1}{2}}$ or $d_{\frac{3}{2}}$ proton with neutron holes. Decay schemes by Nolte *et al.* [Nol82] identify excited states at a few hundred keV in

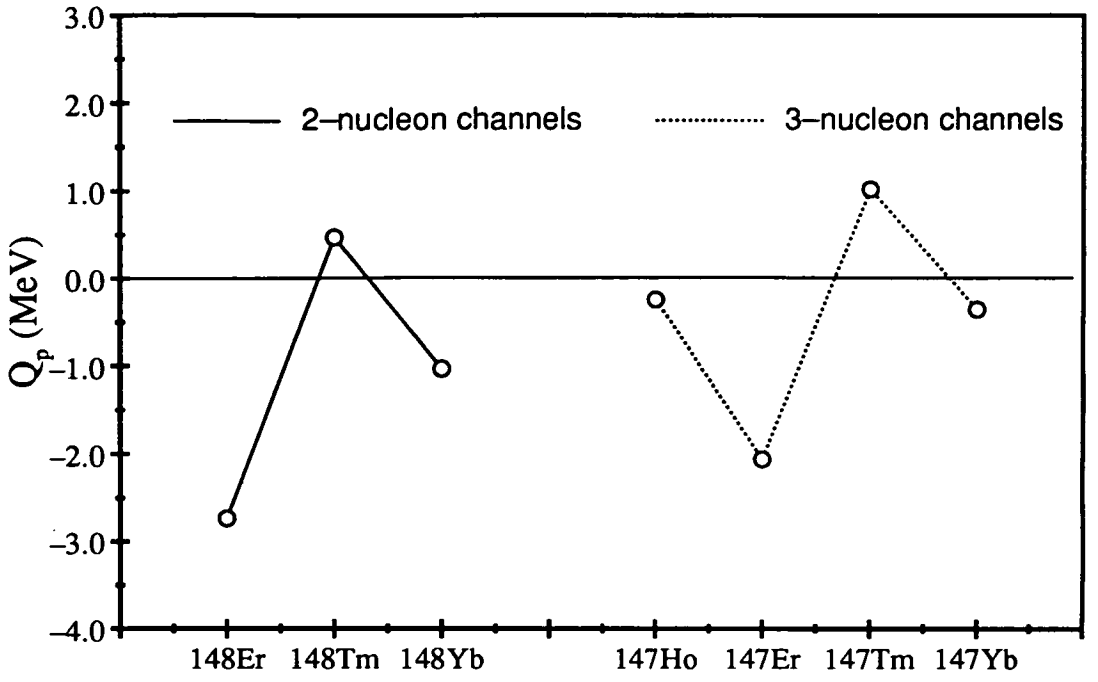

Figure 2.4: *Calculated Q_p values for nuclei produced via the 2 and 3 nucleon channels from $^{150}Yb^*$ (from [Mol88]). Q_p values for 3 nucleon residues assume a transition from a 50 keV low–lying proton level*

$^{148}_{67}Ho_{81}$ and a $J \geq 6$ ground state in $^{148}_{69}Tm_{79}$. From the three nucleon channels no candidate apart from ^{147}Tm has a positive Q_p value.

The measured half–life of 360 ± 80 μs would suggest an l=2 transition (calculated $t_{\frac{1}{2},p} = 140$ μs) rather than an l=0 transition (calculated $t_{\frac{1}{2},p} = 14$ μs). Based on a combination of half–life and Q_p value arguments, Hofmann [Hof84] suggests that the decay is from the $d_{\frac{3}{2}}$ level, which would imply a swap in the ordering of the $s_{\frac{1}{2}}$ and $d_{\frac{3}{2}}$ levels compared to the $N \geq 84$ Tm isotopes.

The 1263 keV line from $^{154}Hf^*$ was observed with a cross section in the range $2 - 10$ μb at excitation energies in the range $72 - 78$ MeV. The most likely source of this transition is from a high spin $l \geq 5$ level (assumed to be the ground state) in ^{150}Lu to a low spin level in ^{149}Yb. The excitation energy of approximately

75 MeV for this line is higher than that for the peak cross section of the ^{151}Lu transition, consistent with moving from a 3 nucleon (p2n) to a 4 nucleon (p3n) evaporation channel. The nucleus ^{150}Hf, produced via the 4n channel, can be excluded due to its predicted negative Q–value (Q_p= −3.7 MeV).

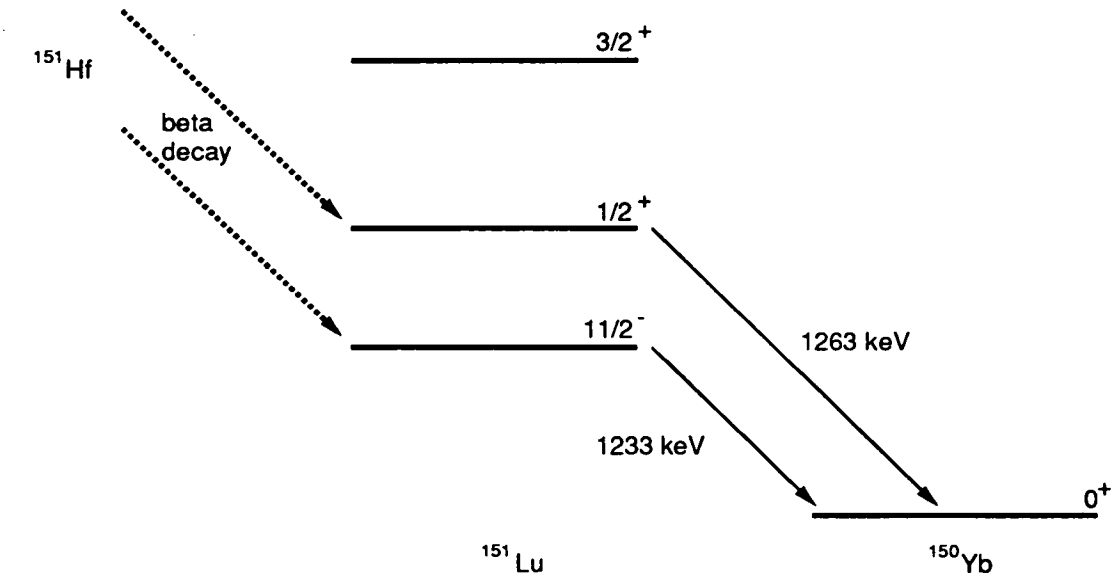

Figure 2.5: *Proposed feeding of ^{151}Lu by β^+–decay from ^{151}Hf*

An alternative explanation suggested by Hofmann [Hof88] is shown in figure 2.5. In this mechanism the 1263 keV line originates from a low spin isomeric state in ^{151}Lu, fed via β^+–decay from ^{151}Hf. Production of ^{151}Hf via the 3n channel would explain the higher excitation energy required, relative to direct production of ^{151}Lu via the p2n channel. As the ground state of ^{151}Lu would also be populated in the same way from ^{151}Hf, this would explain the observation at SHIP of both the 1263 keV line and the ^{151}Lu line at the higher excitation energy.

The calculated WKB proton half–life for a 1.26 MeV transition is 40 ms for a Δl=5 transition from ^{150}Lu, whereas the β^+ half–life of ^{151}Hf is calculated in the range 100–300 ms. The low statistics of the SHIP measurement prevented a half–life from being obtained, giving only an experimentally deduced lower limit of 10 ms, so leaving either mechanism as a possibility.

The remaining weak lines observed from ^{150}Yb* are shown in table 2.3, with energies of 2467 ± 20 keV, 2851 ± 15 keV [Hof83, Hof88], 2935 and 3277 keV [Hof91]. No half–life measurements could be made since the peaks were barely above background, but experimental limits could be deduced of 1 μs −10 ms in each case. This upper limit on the half–life rules out β^+–delayed proton emission as a source of these lines.

In addition a further weak line was seen from ^{154}Hf* (E_x=68 MeV) by Hofmann with an energy of 1360 ± 10 keV. Decay energy spectra from this experiment [Hof91] show a weak line at a cross section of about 1 μb barely identifiable above background with an experimentally deduced lower half–life limit of 2 ms. No assignments for any of these five very weak lines were made by Hofmann, and until now no further experiments had been performed to reproduce them.

2.5 The Daresbury experiments

The development of the residue implantation detection system (RIDS) at the Daresbury recoil separator uses a technique based on that of the successful SHIP experiments. The RIDS technique, which is described in section 3.1, uses the combination of the recoil separator and a new detection system to improve on the sensitivity of measurements which were possible using SHIP. The experiments that make up this project exploited these improved features of the RIDS technique in order to study proton emission from the reactions ^{58}Ni + ^{92}Mo → ^{150}Yb* and ^{58}Ni + ^{96}Ru → ^{154}Hf*. The aim of the work was to clarify all of the unresolved questions concerning the proton transitions listed in table 2.3.

At the simplest level it would be possible to give a direct mass assignment to each observed proton transition, making use of the explicit mass separation of the recoil separator. This removes the need for excitation function studies which are not practicable for Daresbury experiments with a limited amount of beam time.

Apart from the ground state proton transition from ^{147}Tm, none of the remaining proton lines have a suitable half–life or yield to be studied at the GSI on–line mass separator and so have not had a direct mass assignment.

In the cases of the 1118 keV line from ^{150}Yb* and the 1263 keV line from ^{154}Hf*, a direct mass assignment would immediately select one of the alternative origins discussed in section 2.4.2. In addition the greater sensitivity of RIDS should allow a half–life measurement for the 1263 keV line.

It would be of particular interest to either confirm of deny the existence of the additional five weaker lines. Apart from these SHIP measurements, no other direct proton transitions have been observed at energies over 2 MeV, and such lines would have to be attributed to decays from high–lying proton states.

In the longer term beyond the immediate scope of this thesis project, the RIDS technique should now be able to identify new regions of direct proton emission. The improved sensitivity allows the search for candidates produced via p3n evaporation channels, allowing access to a range of extremely promising nuclei in the light rare earth regions and at higher masses up to Z=82.

Chapter 3

Experimental Technique

3.1 Summary of the technique

3.1.1 Introduction

The residue implantation detection system (RIDS) has been developed on the Daresbury recoil separator as a highly sensitive technique for the measurement of short-lived (≥ 1 μs) low cross section proton emitting nuclei. The technique uses the recoil separator to provide in-flight separation of the evaporation residues from the beam and other reaction particles. The evaporation residues are implanted into a silicon detector located at the focal plane of the recoil separator . In previous work a two-dimensionally position sensitive silicon surface barrier detector was used to study alpha emission [Woo89], which recorded both the energy and x,y position of the implantation and decay events. The mass separation of the recoil separator disperses the residues horizontally at the focal plane in proportion to their $^{A}/_{Q}$ (mass to ionic charge ratio), so that an explicit mass identification is obtained directly from an event's horizontal position in the detector. This technique has been used to successfully measure alpha radioactivity from extremely

proton rich nuclei around A=109 [Pag90].

A major part of this thesis work has been to replace the position sensitive detector with a completely new double–sided silicon strip detector, representing the first ever use of such a detector in a nuclear physics application. The double–sided strip detector, which is described in section 3.2.3, provides two–dimensional position information with an improved position and energy resolution compared to the previous surface barrier silicon detector. The improved position resolution greatly increases the correlation efficiency between implanted residues and their subsequent decays, and so increases the sensitivity to low cross section correlated decay chains. This effectively lengthens the range of observable decay half–lives, allowing the clean separation of decay peaks from background events for even longer lived nuclei. In the case of short–lived transitions an improved correlation efficiency further suppresses the long–lived background so that extremely low yield correlated events can be seen against a virtually zero level of background.

The resulting high performance of this new strip detector has made possible the measurement and identification of the weak proton transitions outlined in section 2.5. In the longer term the technique provides the necessary sensitivity to search for new proton emitting candidates. However the large number of individual strips within the strip detector has required a completely new approach to the detector instrumentation and signal processing. The development of a new multi–channel system of electronics has formed a large part of the technical work for this thesis project, and the various components are described in detail in the following sections.

3.1.2 In–flight separation using the Recoil Separator

Heavy ion beams accelerated using the Daresbury tandem accelerator are brought into the target chamber which is positioned immediately upstream of the recoil separator. The beam is steered onto the target with an image size of approxi-

mately ±3.5 mm vertically by ±0.5 mm horizontally. The resulting fusion reaction produces evaporation residues which are ejected out of the target in a forward direction. The recoil separator is designed to accept the reaction products ejected in a forward focused cone about the beam axis, and separate the evaporation residues from the primary beam particles and other reaction products.

Figure 3.1 shows a schematic diagram of the main components of the recoil separator , which consist of three magnetic quadrupole triplet lenses, two crossed–field (Wien filter) devices, a 50° sector magnet and two sextuple magnets. The crossed field devices introduce a velocity dispersion which separates recoiling nuclei from the beam particles. The sector magnet imposes a momentum dispersion resulting in a velocity–independent focus at the focal plane, with horizontal dispersion in $^{A}/_{Q}$. A full description of the design and performance of the recoil separator is given by A.N. James *et al.* [Jam88].

Setting up the recoil separator fields by the experimenter is extremely straight forward, requiring only the selection of the two parameters $^{A}/_{Q}$ and velocity ($^{V}/_{C}$) of the required residues. The recoil separator is controlled by a dedicated mini–computer, running the control program LXIO which calculates the required field settings for the $^{A}/_{Q}$ and $^{V}/_{C}$ values input by the user. The computer system sets a total of eighteen currents to achieve the correct field settings, and automatically maintains them at the desired value.

The final quadrupole triplet focuses the residues onto the separator's focal plane with a mass resolution of $\frac{\Delta A}{A} \simeq \frac{1}{300}$. The ellipsoidal image has a size typically 10 mm FWHM vertically by 3 mm FWHM horizontally. The separator's $^{A}/_{Q}$ acceptance of ±1.2% provides about four mass groups at $A \simeq 147$ over a width of about 15 mm. The overall transmission efficiency of the recoil separator is typically $\simeq 2 - 10\%$, whilst the optimum target thickness for maximum yields is typically 500 $\mu g\,cm^{-2}$. The yield for residues produced via a particular evaporation channel is a function of the ionic charge state Q, and an appropriate value of $^{A}/_{Q}$ is used

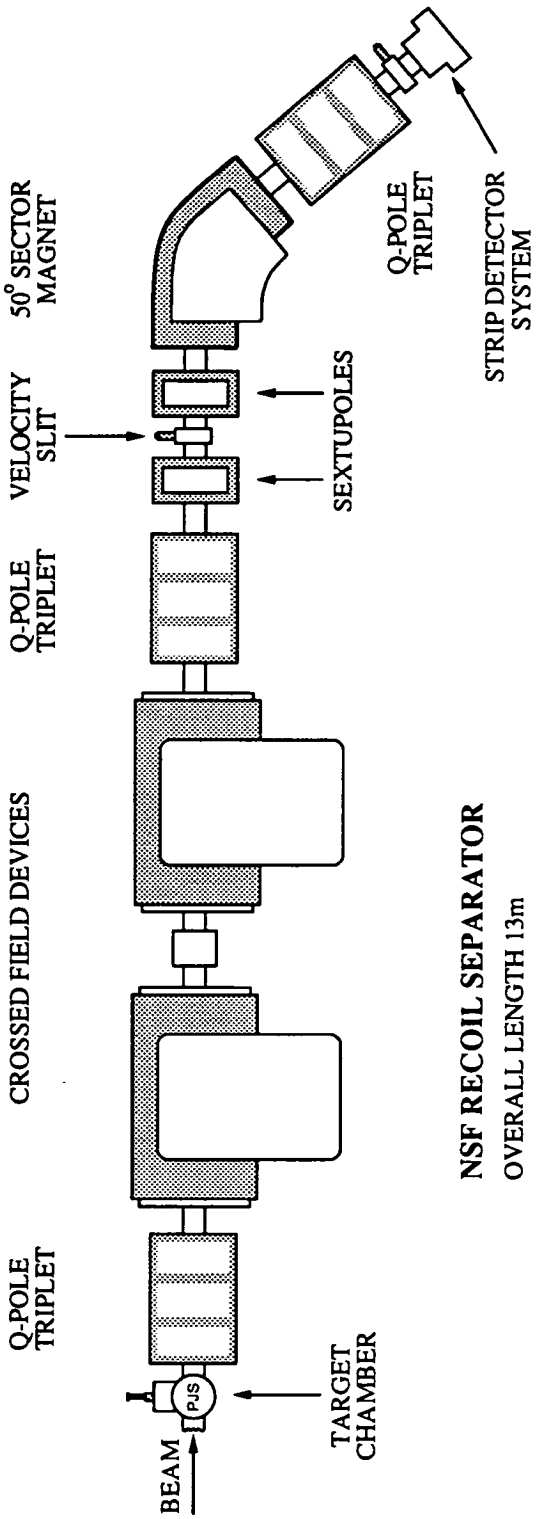

Figure 3.1: *Schematic diagram of the Daresbury recoil separator*

to select the charge state with the highest yield. The computer program RECSET calculates the optimum $^{A}/_{Q}$ and $^{V}/_{C}$ for the main evaporation channel required, which are then used as first estimates for the separator's settings. The beam rejection factor is dependent on both the kinematics of the particular reaction and on the selected charge state, and is consistently better than 10^{8}.

In order to superimpose the separator's focal plane onto the silicon detector, the control parameter VECTOR 2 is used to shift the plane up or down the local beam axis. For this work a new end plate was built to hold the strip detector assembly, which required the focal plane to be moved a few centimetres further downstream, using the setting VECTOR 2,3. The initial stages in setting up the separator use the x vs y implantation position spectrum to look for distinct mass groups. The calculated values of $^{A}/_{Q}$ and $^{V}/_{C}$ are used as a first estimate, and these are then adjusted to maximise the ratio of residues to other beam–like events. In general residue events have a well defined horizontal mass structure which shows evenly spaced peaks of constant width. Contamination from other reaction products which pass through the separator produce a background continuum which tends to wash out the mass structure of the residues. Scans in $^{A}/_{Q}$ and $^{V}/_{C}$ about their initial values are used to choose settings with the best combination of the maximum residue yield and minimum background. At various charge states strong contamination from scattered beam particles tends to reach the focal plane, producing a characteristically very intense region of events within the x, y plot. In order to prevent local detector damage and an unacceptably high implantation trigger rate these $^{A}/_{Q}$ settings must be avoided. Figure 3.2 shows two sample x vs y recoil implantation distributions; the upper is optimised on charge state $Q = 28^{+}$ and $^{V}/_{C} = 3.7\%$ whilst the lower shows strong contamination from beam–like particles due to the beam being steered too low onto the target frame.

Once the recoil separator is set to maximise the residue–to–background ratio, it is necessary to identify the mass groups reaching the detector. In principle the

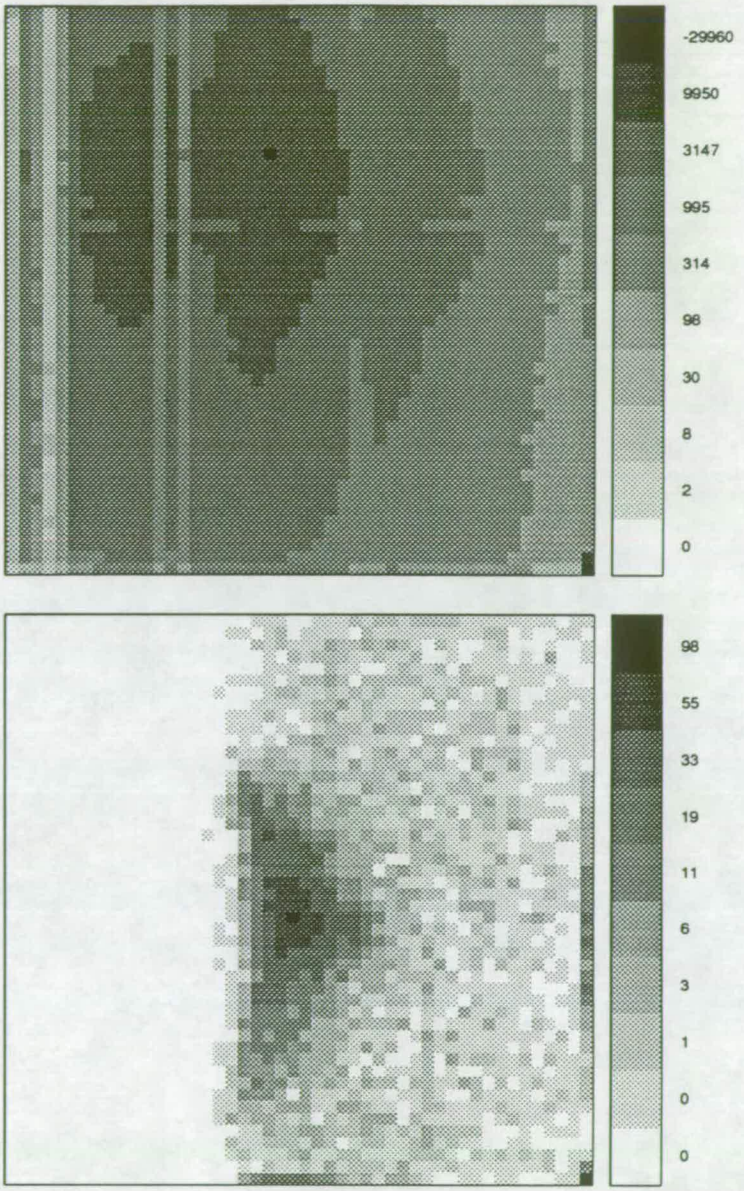

Figure 3.2: *Plots of implantation x vs y distributions obtained from the strip detector whilst setting up the recoil separator. The upper plot shows the separator optimised with A=151, $Q = 28^{+}$. The lower plot shows severe contamination due to beam like particles scattering off the target frame. The rectangular corner of the frame can be clearly seen, this was corrected by steering the beam higher onto the target*

central mass group is identified from the separator's $^{A}/_{Q}$ value and an estimate of the highest yield charge state. However other evaporation channels of different charge state will also reach the detector and may well have an observable yield. These 'charge state ambiguities' can considerably complicate the observed mass distribution, especially if they are positioned with their mass peaks directly overlapping those of the main mass distribution. In the reactions studied around A=147 and A=151 it was possible to identify the mass groups by the strong alpha lines produced with both the main $Q = 28^{+}$ charge state and from target contaminants with $Q = 29^{+}$ charge state. In regions without known neighbouring alpha decays it can be more difficult to identify initially the observed mass groups.

3.1.3 The focal plane detection system

Figure 3.3 shows a schematic diagram of the focal plane detection system. The silicon detectors forming the residue implantation detection system are mounted on a new dedicated end plate, which replaces the gas ionisation chamber used during γ–ray studies. The carbon foil detector assembly [Con82] is standard for all separator experiments.

The carbon foil is positioned across the path of the separated residues, at an angle of 30° to the perpendicular. Secondary electrons emitted from the carbon foil are detected by the microchannel plate assembly, which records the energy loss of the particle through the carbon foil. The plate assembly also generates a position signal locating the horizontal position of the carbon foil event. In this application the focal plane is moved onto the strip detector, and the carbon foil position information is not used directly. The energy loss signal is used to produce a logic pulse which tags any particle passing through the foil. The energy loss signal is sensitive to particles passing through the foil with low kinetic energy ($<$ 10 MeV) and has a high detection efficiency ($>$ 99%). It is of vital importance to mark such low energy implantation events, which would otherwise appear as a

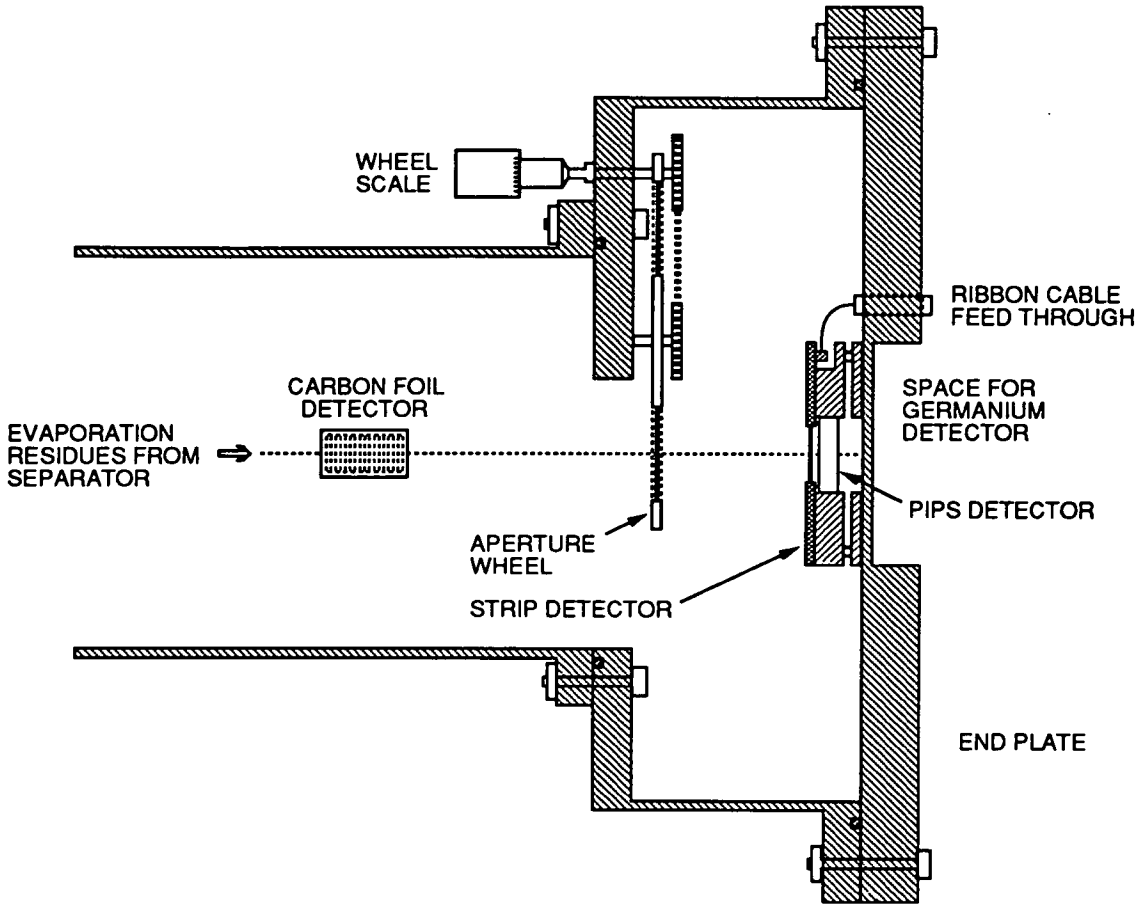

Figure 3.3: *Diagram of the detection system layout at the focal plane of the recoil separator*

background continuum in the strip detector decay energy spectra.

Immediately in front of the strip detector is positioned an aperture wheel, which can be rotated by hand via an external scale. The wheel is geared so that a 180° turn on the scale moves the wheel by one position (45°). The wheel has eight positions, used to contain calibration sources, collimating masks and degrading foils. Table 3.1 shows the contents of each wheel position used during the main experiment. The ^{241}Am alpha source is used to calibrate the strip detector, providing a set of alpha peaks in each strip which can be used as a calibration check during strip gain matching. The resolution of these alpha spectra also provide a useful monitor of radiation damage during the experiment in different regions of

Position	Angle	Collimation	Al Foil
1	0°	^{241}Am α–source	none
2	45°	offset cross	600μg cm^{-2}
3	90°	segment	none
4	135°	segment	600μg cm^{-2}
5	180°	segment	780μg cm^{-2}
6	225°	segment	800μg cm^{-2}
7	270°	segment	1000μg cm^{-2}
8	315°	central cross	600μg cm^{-2}

Table 3.1: *List of collimators and foils mounted on the aperture wheel for the main experiment*

the strip detector.

The cross–hair collimators are used during initial setting up, principally whilst setting the pole zero adjustments on each strip amplifier. The pole zeros are adjusted on the high gain amplifiers during overload conditions from implantation events, and so can only be set when beam is on the target. The cross–hair apertures prevent an excessive implantation rate on the detector and so limit unnecessary radiation damage during the hour or two which is needed for these adjustments.

The majority of the wheel positions contain a segment–shaped aperture plus an aluminium degrader foil. The wedge shape of the aperture makes a vertical mask over half of the detector face when positioned approximately 5° off centre. This is used to extend the detector life time where there is a high implantation rate, by masking off each half of the detector in turn and restricting the implantations to a smaller number of mass groups. The aluminium foils are of varying thickness to control the degree of energy loss experienced by the residues. In this way the implantation energy can be reduced (typically by a factor of 2) to limit the saturation in the high gain decay amplifiers. A reduction in the amplifier overload

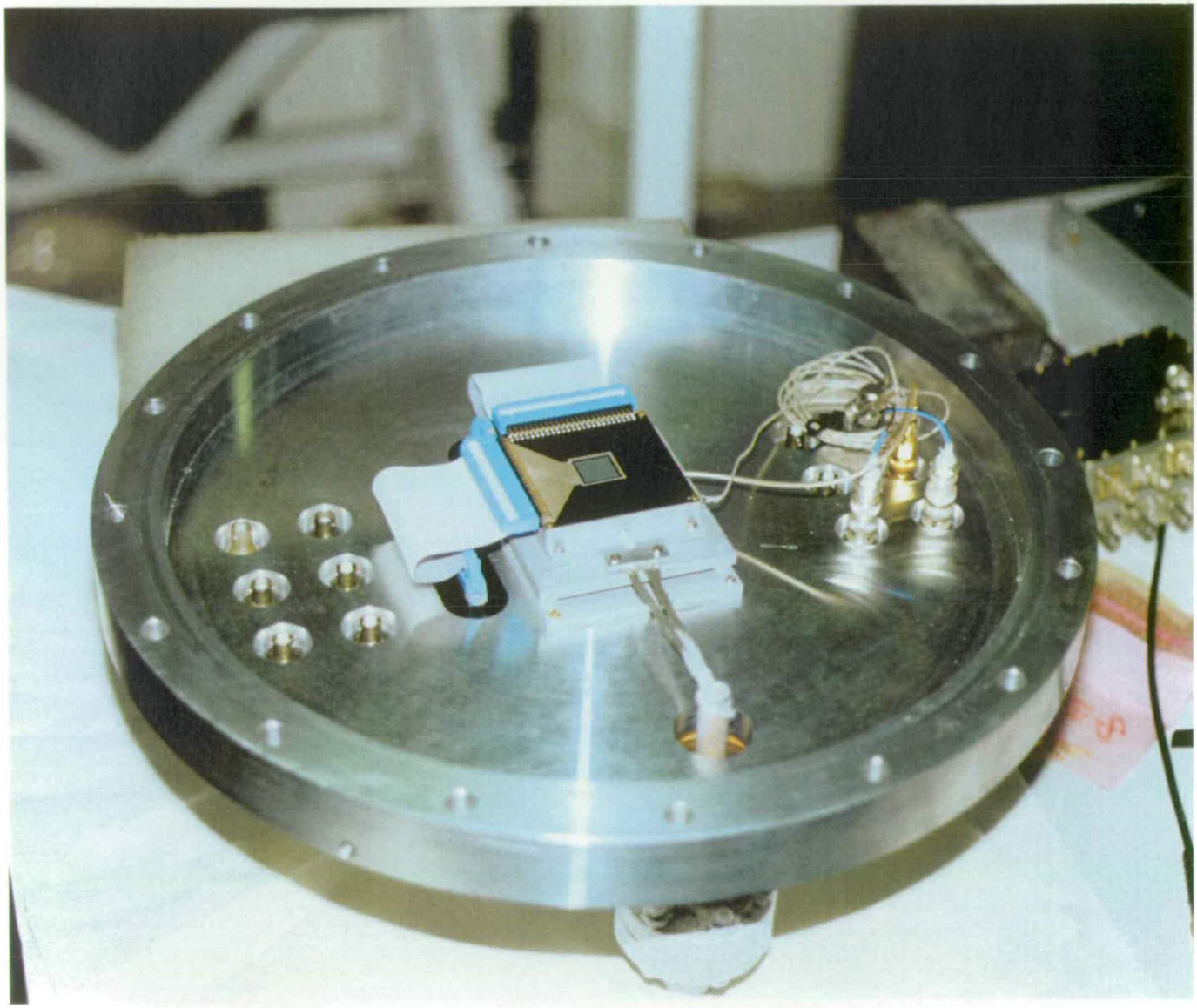

Figure 3.4: *Photograph of the double–sided strip detector mounted on the vacuum end plate. The PIPS detector is out of sight, mounted immediately behind the strip detector*

decreases the amplifier base line recovery time and shortens the effective dead time following an implantation event. However excessive energy degradation will cause a smearing of the implantation energy down to energies comparable to that of decay events. For this reason it is important that the carbon foil energy loss signal is efficiently tagging implantation events, particularly those with a low energy prior to passing through the degrading foil.

The silicon detector assembly is mounted on the separator's end plate (see figure 3.4) and contains the silicon strip detector and a thick PIPS (passivated implanted planar silicon) detector. The combined detector mount is thermally isolated from the end plate and is connected via copper braid to a cold finger, immersed externally in liquid nitrogen. Thermocouples are used to monitor the mount temperature which is held at approximately 0°C. The strip detector provides energy signals from each of its 96 strips, with the signal sent to external preamplifiers via two short lengths of 48–way ribbon cable. Position information is deduced from the strip hit pattern, with the vertically alligned strips on the front face giving the event's $^{A}/_{Q}$ value directly. The thick PIPS detector is mounted immediately behind the strip detector and measures the energy of β^{+}–delayed protons, annihilation radiation , X–rays and low energy γ–rays originating from decay events within the strip detector. A hyperpure germanium detector is positioned just behind the end plate in line with the beam axis to measure any higher energy γ–rays in coincidence with strip detector events.

3.2 Strip detectors

3.2.1 Introduction

Silicon strip detectors have found an increasing use in nuclear physics experiments in recent years, following their development as particle tracking detectors in high

energy physics experiments. The silicon strip detector provides many individual detector elements within a single silicon wafer, and combines the advantages of conventional silicon junction detectors with the flexibility of semiconductor production techniques. The detectors are manufactured using a photolithographic planar process, making possible complex detector geometries using precision photomasks.

The most common layout of elements in a strip detector is many finely spaced parallel strips. The small inter–strip separation minimises the dead area on the detector surface, whilst the strip width can be chosen to suit each specific application. The use of surface passivation during the production process minimises surface leakage currents between strips, leading to significantly reduced electronic noise compared to surface barrier detectors of comparable geometry.

As a continuation of the Edinburgh group's development of strip detectors for nuclear physics applications, this work made the first use of a new double–sided strip detector. This type of strip detector contains strips on both front and rear faces, positioned orthogonally to provide two–dimensional position information. The detector surface is effectively divided into many individual pixels, where the strip pitch defines the position resolution along each axis. The specification for these detectors was chosen specifically for this application, and is discussed in section 3.2.3.

3.2.2 Manufacture of strip detectors

Silicon strip detectors are operated as reverse–biased p^+–n semiconductor junctions. Silicon exhibits a small band gap (1.1 eV at room temperature) and very high charged carrier life times and mobilities, producing low noise detectors even at room temperature. Figure 3.5 shows an outline of a simple p^+–n junction detector with a layer of p^+ donor impurities (eg. boron ions) implanted into the front surface region of the n–type silicon. Negative bias is applied to each p^+

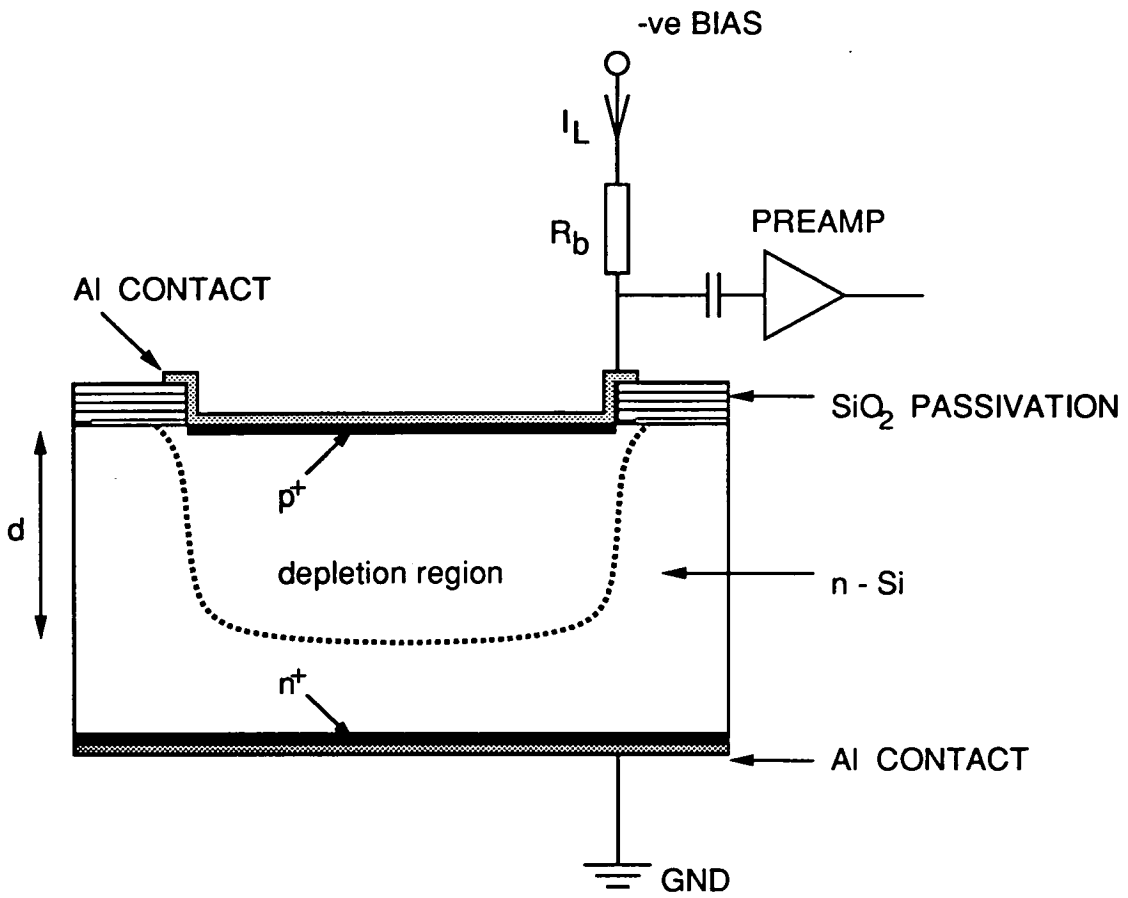

Figure 3.5: *Details of a basic p^+–n junction silicon detector*

region via aluminium contacts, which produces a depletion region in the bulk of the silicon. The depth of the depletion region d is a function of the reverse bias V given by

$$d \propto \sqrt{\rho V} \tag{3.1}$$

where ρ is the resistivity of the silicon. The capacitance of the junction C is similarly dependent on the bias voltage and the junction area A, given by

$$C \propto \frac{A}{\sqrt{\rho V}} \tag{3.2}$$

Silicon detectors are often operated at several times their full–depletion bias to ensure that full depletion is maintained during any fluctuations in leakage current.

Generally in silicon junction detectors the reverse leakage current I_L is due to a combination of processes which are dominated by the bulk generation current

and the surface leakage current. The planar process used to manufacture silicon strip detectors produces a high resistivity inter–strip surface layer of silicon oxide which suppresses the surface current. Strip detectors produced by the planar process exhibit much lower reverse leakage currents than comparable surface barrier silicon detectors, with bulk generation being the dominant cause. Bulk generation currents are generally due to either thermal generation of electron–hole pairs in the depletion region, or less importantly from the diffusion of minority charge carriers across the junction.

The main steps involved in the planar production process are shown schematically in figure 3.6 [Kem80, Kem84]. The process exploits technology developed for the manufacture of integrated circuits and uses photolithographic masks to define the strip patterns on the wafer surfaces. Initially passivation of the silicon wafer is achieved by depositing a layer of silicon oxide using thermal oxidation at around 1000°C. Masks are then used to etch windows corresponding to the strip layout into the silicon oxide. Double sided detectors are produced using front and rear photomasks to etch the strip pattern onto each face. The p^+ and n^+ layers are then added into the silicon using ion implantation, typically with boron ions to form the p^+ layer and arsenic ions for the rear n^+ layer. The implanted ions are annealed before the aluminium contacts are added.

3.2.3 The double–sided silicon strip detector

The double–sided silicon strip detectors are supplied to a specification designed for this application. The devices are capable of providing high resolution energy signals with a sub–millimetre position resolution in each axis. The strips on front and rear face are orthogonally crossed to provide two–dimensional 'pixels' over the detector surface, with a position resolution defined by the strip pitch. The active area of the silicon wafer must be sufficiently large to cover the image region at the separator's focal plane, which is approximately 20 mm by 20 mm. The thickness

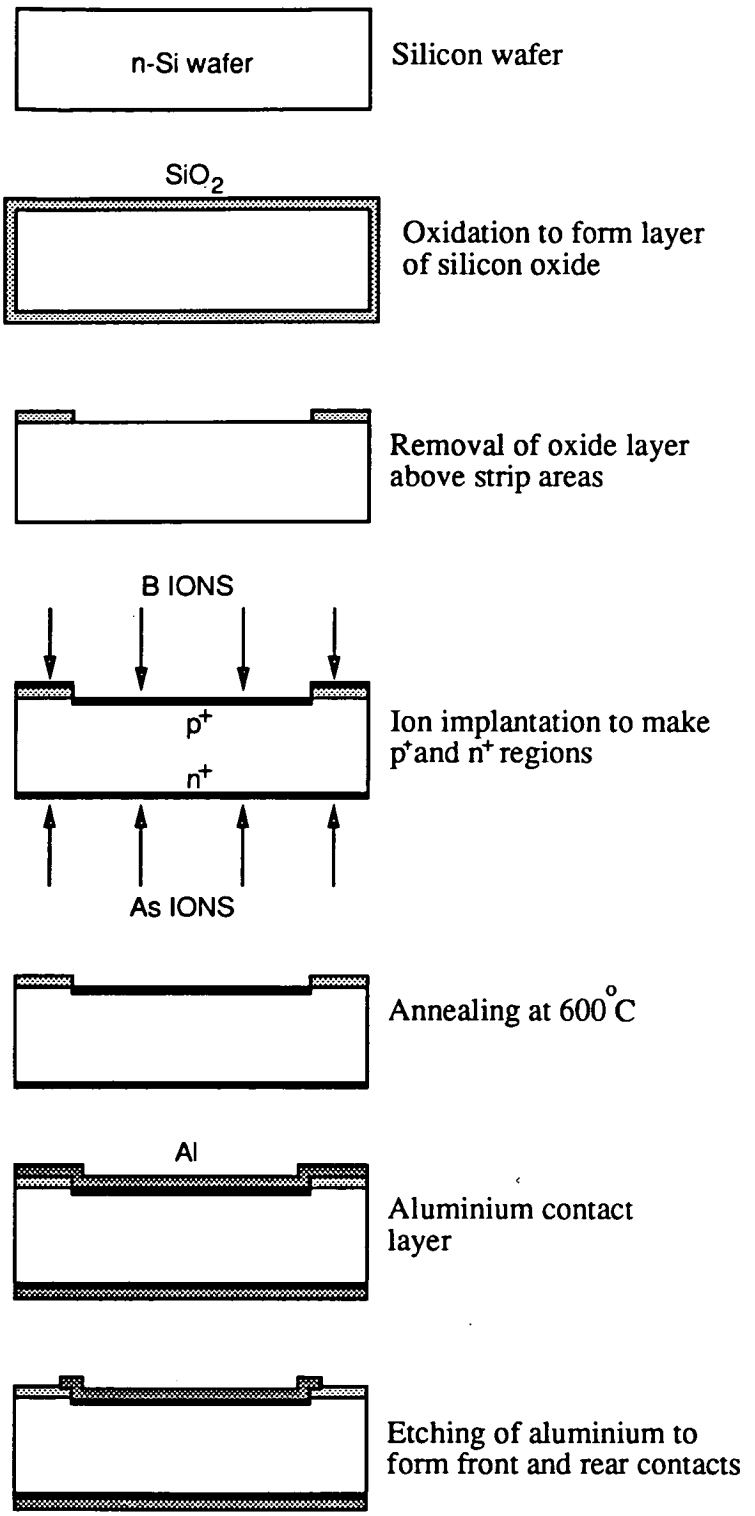

Figure 3.6: *The main steps involved in the planar process for manufacturing silicon strip detectors*

of the wafer is chosen to provide sufficient depth to stop forward–emitted alpha particles and low energy (direct) protons, whilst remaining effectively transparent to the low energy β^+ tail.

Active area	256 mm^2
Thickness	65 – 110 μm
Front face	48 p^+ strips, horizontal
Back face	48 n^+ strips, vertical
Strip width	300 μm
Strip pitch	335 μm
Strip length	16 mm
Depletion voltage	−5−−10 V
Leakage current per strip	< 4 nA (25°C)
(3× depletion voltage)	< 0.7 nA (7°C)

Table 3.2: *Summary of double–sided strip detector specification, MSL type PP*

Figure 3.7 shows a photograph of thefront face of a double–sided strip detector. The specification of the detector, which contains 48 strips on each face,is listed in table 3.2 . The detector is mounted at the focal plane so that the front strips (denoted type 'B') are orientated vertically and so provide the x–position information, and the rear strips (type 'A') are orientated horizontally for y–position information. Provided that an event produces a valid signal in only one strip per face, the pair of strips define the event's location within an effective pixel on the detector surface.

Each strip is 300 μm wide with a 35 μm inter–strip separation, giving a strip pitch of 335 μm. The strip pitch must be large relative to the typical ranges of decay particles in silicon, which are approximately 15 μm for 1 MeV protons and 30 μm for 5 MeV alpha particles. Particles which cross under the inter–strip region can cause clusters of strips to fire and produce ambiguous position coordinates.

The active area of the silicon wafer is 16 mm by 16 mm, which is sufficient to

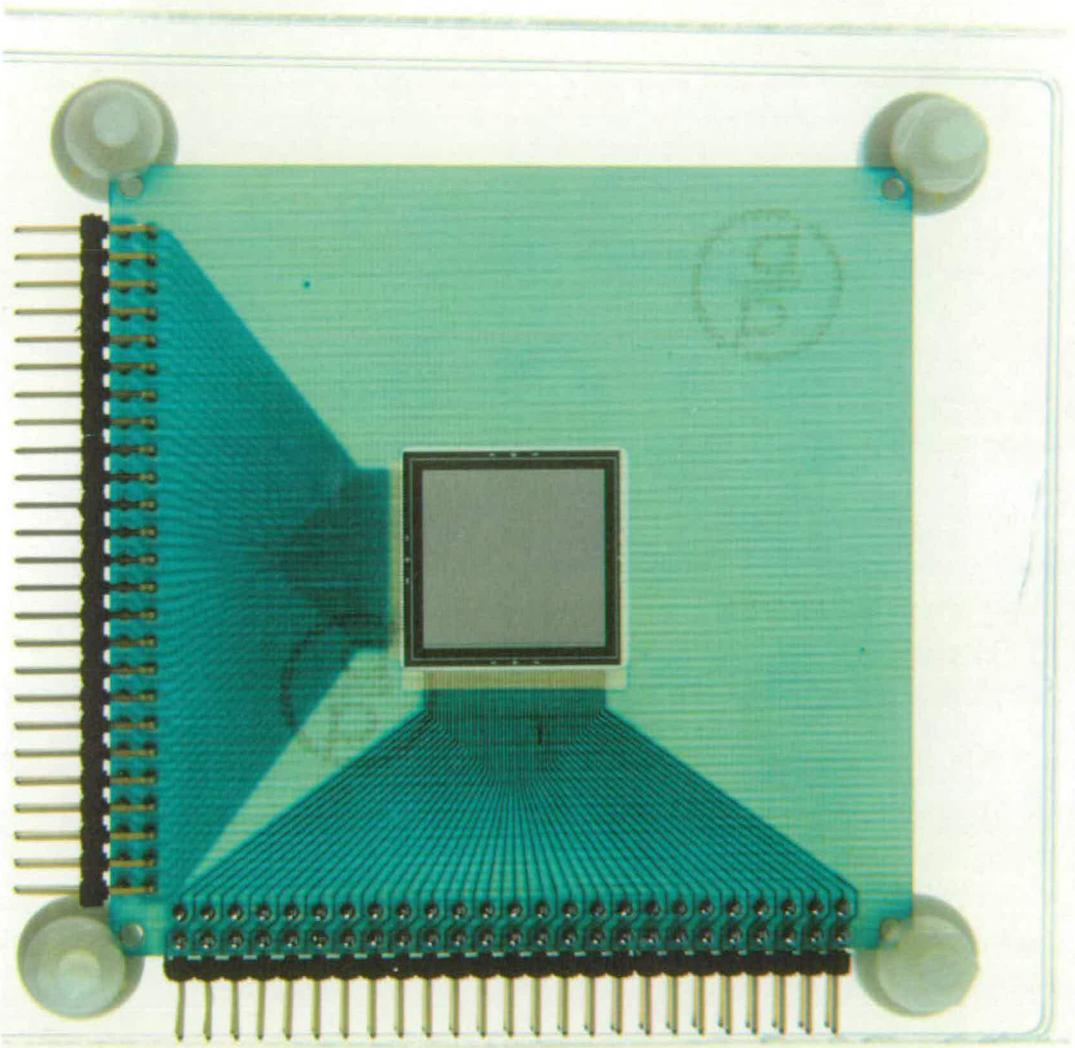

Figure 3.7: *Photograph of the front face of a double–sided strip detector, showing the silicon wafer mounted on the printed circuit board*

accommodate most of the ellipsoidal beam image at the focal plane. In principle larger wafers could be used but the production costs escalate rapidly with increased active area. In addition to maintain the strip pitch, a larger wafer would require the instrumentation of more strips which would demand more electronics.

A variety of wafer thicknesses were supplied by Micron, ranging from 67 μm to 110 μm. Typical implantation depths of the residues into the detector are $\lesssim$ 10 μm, so that alphas and low energy protons emitted in the forward direction are fully stopped. Backward emitted particles escape out of the detector's front face, depositing a proportion of their energy in the detector so causing a characteristic escape peak in the decay energy spectra. β^+–delayed protons with energies between $\simeq 2-5$ MeV have ranges of up to approximately 200 μm and so are not stopped within the strip detector in even the forward direction. A proportion of these events are stopped by the rear PIPS detector and their total energy can be reconstructed by summing the PIPS signal and the strip detector energy loss signal. Using these two signals a $\Delta E/E$ particle identification plot can be used to distinguish PIPS events as originating from either protons or positrons.

Two variations of the detector specification were supplied by Micron Semiconductor Ltd, as prototype and production detectors (see figure 3.7). The strip geometry was the same for both types of detectors, except that the six production detectors had a ground plane added to the printed circuit boards to reduce pickup in the edge strip signals. Negative bias is supplied to each front face strip from the preamplifier unit, with connections made to the wafer using fine wires ultrasonically bonded onto each strip. Rear strips are connected similarly, with the preamplifier channels connecting each rear strip to ground. Figure 3.8 shows details of the connections to each face of the detector, with positive polarity signals coming from the front p^+ strips and negative polarity signals from the rear n^+ strips. Each preamplifier inverts the polarity of the signals it receives at the input.

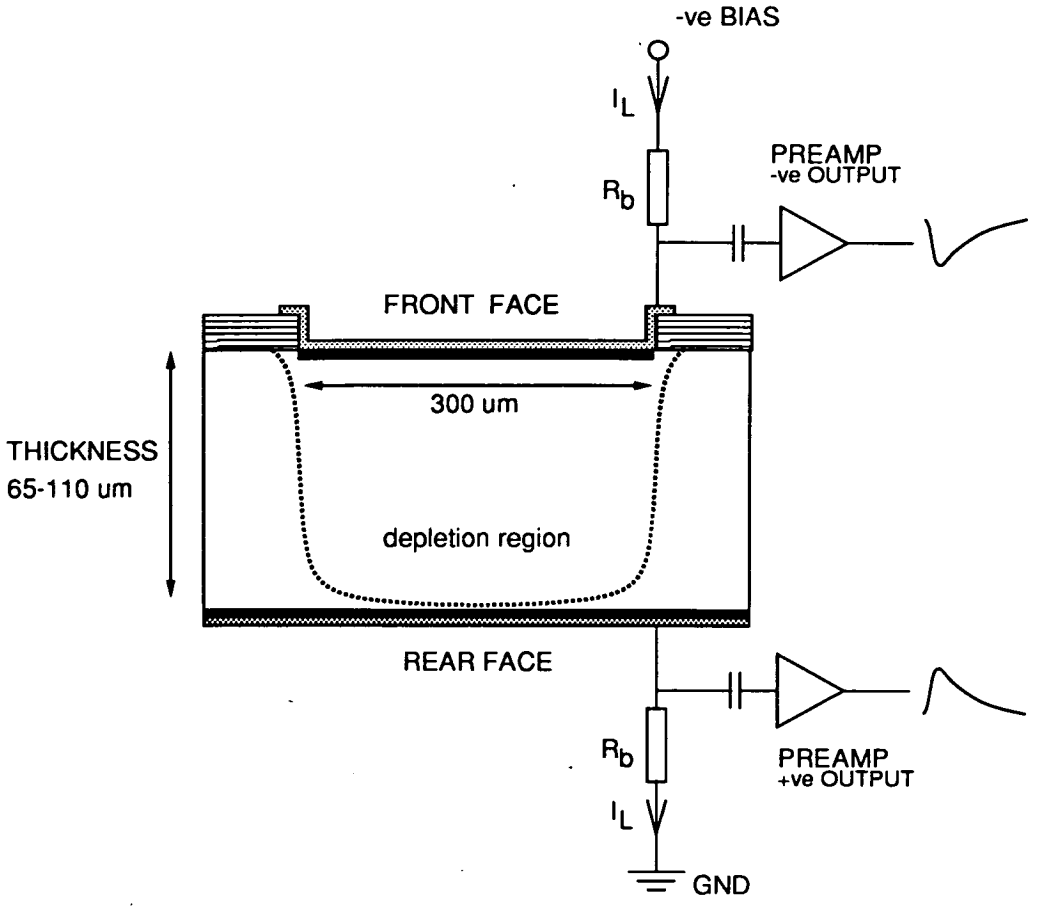

Figure 3.8: *Details of the preamplifier connections to a double–sided strip detector*

The two prototype detectors were first used in March 1990 for the commissioning experiment, followed in April 1991 by the main run in April 1991 which used a further two production detectors. A description of their performance and the results obtained is given in chapter 4, and has been published separately in Nuclear Instrumentation and Methods [Sel92].

3.3 Signal processing electronics

3.3.1 Strip detector electronics

The strip detector records the energy and position of both the implantation subsequent decay events. The electronics associated with the strip detector are divided into two parallel branches in order to process separately the signals from each event type. Figure 3.9 shows a block diagram of the strip detector electronics. One set of amplifiers has a high gain suitable for the decay event signals, and the other has a low gain suitable for the implantation (recoil) signals. However each type of signal passes simultaneously into both branches of amplifiers with the effect that implantation events momentarily saturate the high gain amplifiers. In order to minimise the time which these amplifiers are dead following saturation, they must have a good overload recovery performance and carefully adjusted pole zeros.

The preamplifier signals are split equally into each of the parallel sets of shaping amplifiers. A total of 96 preamplifier signals are brought up to the control room through six 100 m 34–way twisted pair cables, which are T'd into two pairs of 'splitter' boxes. Each splitter box accepts three 34–way twisted pair cables, outputting the signals through six 16–way sockets.. The 48 signals from the front face preamplifiers (ADC channels 1–48) are negative polarity and so are inverted in two of the splitter boxes. 16–way ribbon cables connect the signals from the boxes to the shaping amplifiers, each amplifier card producing eight analogue signals and eight ECL logic signals.

The analogue signals from each of the high gain amplifiers are sent to individual ADCs which record the energy of decay events in each strip separately. The gains are set so that a 10 V full scale output is equivalent to $\simeq$ 22 MeV. Therefore decay energies in the range $0 - 10$ MeV produce signals $\leq$ 5 V in the ADCs. Energy signals from the low gain amplifiers are combined into two groups of 48 producing a

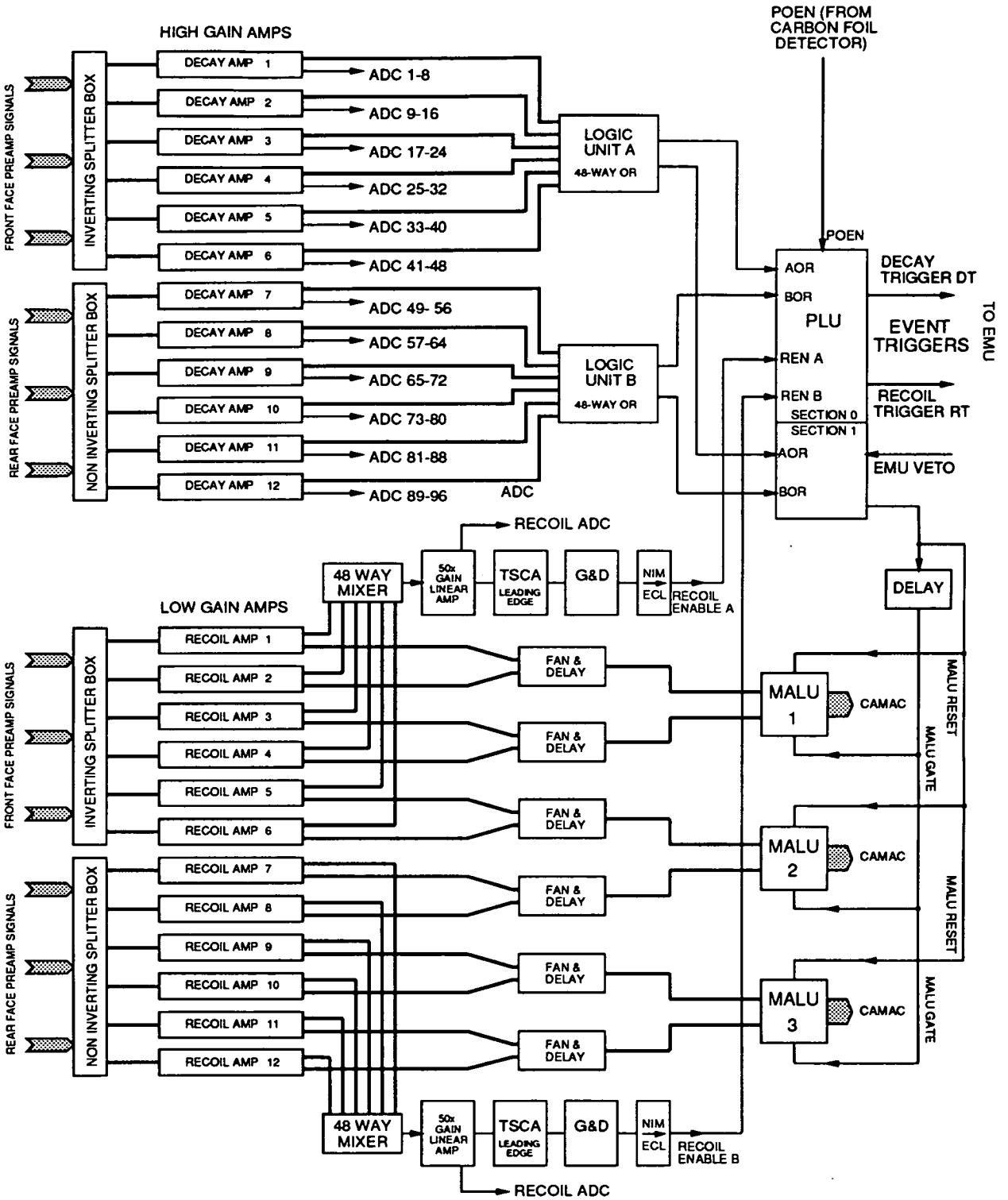

Figure 3.9: *Block diagram of the strip detector electronics (final version)*

pair of signals for the implantation energy, one from each face of the detector. The signals are primarily used to generate logic signals (denoted RECOIL ENABLE A/B) which indicate when the event exceeds a preset energy threshold, typically 10 MeV. These amplifiers have gains set equivalent to 220 MeV full scale, designed to handle energies in the range 50 – 100 MeV.

Each amplifier module also contains a leading–edge discriminator circuit and produces a logic signal output. The logic signals from each set of amplifiers are used in different ways and require different energy thresholds. Logic signals from the decay amplifiers are passed through two 48–way OR units to generate the signals AOR and BOR. Each signal indicates when at least one strip has fired on that face of the detector, and is used by the programmable logic unit (PLU) to produce a trigger signal. The sensitivity of the detection system to low energy decay events is dependent on the decay amplifier threshold levels, which are kept as low as the amplifier noise allows (< 0.5 MeV). Details of the trigger logic and control signals are discussed in section 3.6.

The logic signals from the recoil amplifiers are used to reconstruct the implantation x,y position information from the hit pattern of those strip signals which exceed the recoil amplifier thresholds. The discriminator levels for each amplifier are set at $\simeq 15$ MeV which is sufficiently high to exclude decay events and cross talk from neighbouring strips. The resulting hit pattern is read by the three majority logic units (MALU) each acting as a 32 bit CAMAC readable pattern register. The fan and delay units correct any timing differences between the strips and delay the logic signals until after the MALU gate pulse arrives. The units have a maximum delay of 500 ns adjustable in 50 ns steps.

The commissioning experiment used a simpler form of this circuit, the main difference being the use of only one set of amplifiers to process both types of signal. This caused various problems due to the large difference in the dynamic ranges of the two types of signals, and the circuit was modified for the main experiment to

the form given above.

3.3.2 Clock circuitry and carbon foil signals

The clock circuitry records the time of the implantation and decay events in a form which is read by the event manager and incorporated into the event–by–event data. The circuit is shown in figure 3.10, which uses a 10 MHz crystal oscillator via a 10× rate divider to produce 1 MHz clock pulses. A dedicated 32–bit scaler counts the pulses and outputs the accumulated total as two 16–bit data words. Four Daresbury pattern registers are needed to read these words, since one pair is read for decay events and the other pair for implantation events. Each pair of pattern registers is read by the event manager via a CAMAC dual input register. Separate pairs of registers are required for each event type to prevent dead time problems in those cases where the decay trigger follows quickly ($\lesssim$ 50 μs) after the recoil trigger. The pattern registers were originally designed to be used with the alternative Daresbury event manager system, and they closely follow the operation of a Daresbury ADC. In the Charissa event manager environment some of these features, such as rise time protect (RTP) and the inspect pulse are not used.

The layout of the carbon foil electronics is also shown in figure 3.10. The main signal is the energy loss signal POEN which is used to produce the logic pulse sent to the PLU. The analogue POEN is also sent to both a recoil and decay ADC. The horizontal left and right position signals POSIL and POSIR are used as TAC start and stops to produce the square–topped position signal POSI, which is read by a recoil ADC. POSIL and POSIR logic signals are also read by a pair of recoil ADCs to provide additional boolean values for use in the offline analysis. These could be later used to provide an additional tag of implantation events if it were found that the POEN efficiency was inadequate. The fixed–amplitude TAC signal is connected to a rate meter and scaler to give a measure of the total detector

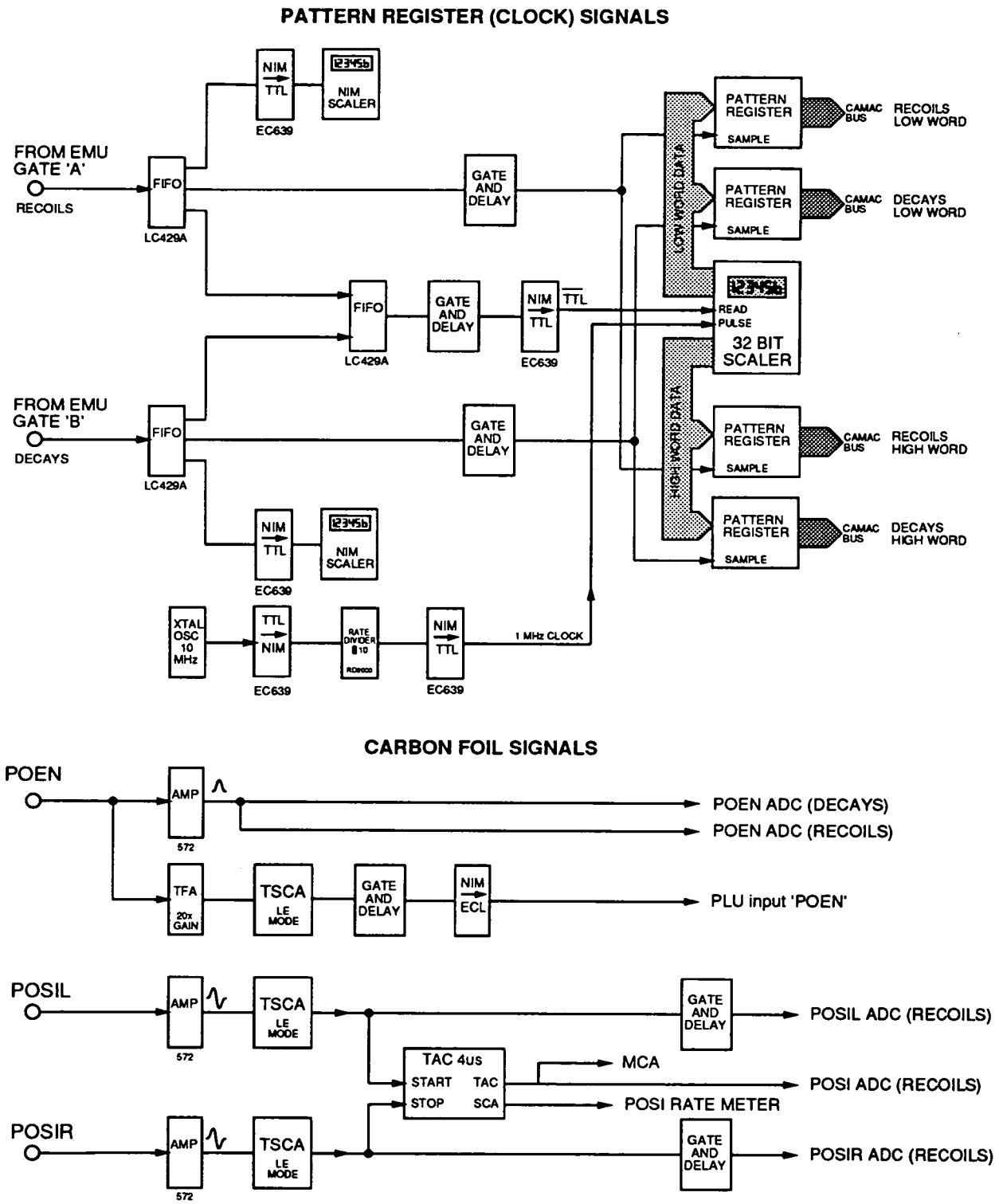

Figure 3.10: *Block diagram of the clock circuitry and the carbon foil electronics*

dose. This scaler continues counting whether or not the event manager is going, and is unaffected by event manager dead time.

3.4 Preamplifiers

3.4.1 The Edinburgh/RAL preamplifiers

The preamplifier is the first stage in the chain of data processing electronics connected to the detector. In general the physical event within the detector releases an amount of charge proportional to the deposited energy of the particle or photon. The preamplifier acts as the interface between these small, fast pulses and the following signal amplification stages. Preamplifiers used with solid state detectors are generally charge-sensitive, which avoids any non–linearity in the detector–preamplifier response due to variations in the detector capacitance. In a typical charge–sensitive preamplifier the magnitude of the output signal is proportional to the total time–integrated charge across the input.

The Edinburgh group's continuing interest in silicon strip detectors has required the development of a new design of preamplifier unit [Dav90]. In collaboration with the SERC Rutherford Appleton Laboratory, the group has recently developed a compact and cost–effective charge sensitive preamplifier to allow instrumentation of up to several hundred detector channels. The compact modular design is constructed using a thick–film hybrid technique, resulting in a 12–pin single–in–line (SIL) card measuring only 33mm by 12mm. For this thesis project it was necessary to design and build a motherboard (see section 3.4.2) into which 96 of the new preamplifier cards would be connected, making an extremely compact multi–channel preamplifier unit. This work was the first application of the new preamplifier cards in a multi–channel system.

In order to process the negative and positive polarity signals produced from a

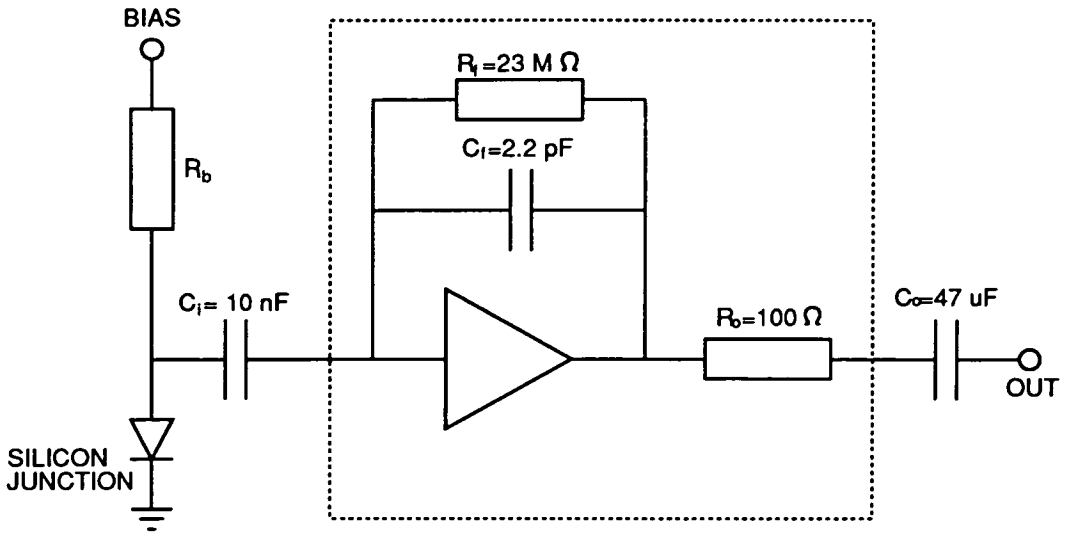

Figure 3.11: *Block diagram of the preamplifier hybrid circuitry. The circuit shown within the box is contained on the hybrid chip, whilst the other discrete components are contained on the motherboard*

double–sided strip detector, two versions of the preamplifier cards are used. These are denoted type A for negative input signals (from the detector's rear face) and type B for positive input signals (from the detector's front face). Both circuit types produce output signals of an opposite polarity to their inputs. The circuit is very similar in function for each design, and is shown schematically in figure 3.11. Several separate parts of the circuit can be identified, namely the amplification stage, the signal output driver, and the feedback components; a detailed description of the circuit design and operation is given by S. Thomas *et al.* [Tho90]. The output resistance R_o is fixed equal to the 100 Ω impedance of the twisted pair cables connecting the motherboard to the shaping amplifiers. The amplifiers also have an input impedance of 100 Ω, resulting in a factor of 2 attenuation in the preamplifier signal at the shaping amplifier input.

The feedback circuit R_f and C_f determine the circuit gain and the signal rise and fall time. Tolerance in the feedback components results in a spread of values for the circuit characteristics such as rise time, decay time and amplitude. These are minimised by using ±1% resistors for R_R and ±10% capacitors for C_f. Typical

Sensitivity	73 nV/electron 20 mV/MeV in silicon
Noise Noise slope	< 3 keV FWHM ($C_d = 0$ pF) < 90 eV/pF
Input capacitance	$0 - 300$ pF
Rise time ($10 - 90\%$)	< 20 ns ($C_d = 0$ pF) < 40 ns ($C_d = 100$ pF)
Fall time ($0 - 63\%$)	50 μs
Dynamic range	$0 - 200$ MeV (± 4 V)
Output impedance	100 Ω

Note: Type A takes a negative input, type B takes a positive input. Both circuits invert the output signal

Table 3.3: *Specification of Edinburgh/RAL preamplifier cards*

characteristics are given in table 3.3. Figure 3.12 shows the pin–out and package arrangements for the two card packages. All eight ground pins are connected to the rear earth plane, which ensures maximum circuit grounding, and also provides a path to remove the heat generated from the hybrid. This is of particular importance when the motherboard is positioned in the vacuum, since simple convective cooling of the cards is no longer possible. In this work the preamplifiers are positioned externally on the separator end plate, and are cooled by an adjacent fan unit.

3.4.2 Preamplifier motherboard

A 96 channel preamplifier motherboard was designed and built as part of this project, to incorporate the new Edinburgh preamplifier cards. The circuit was

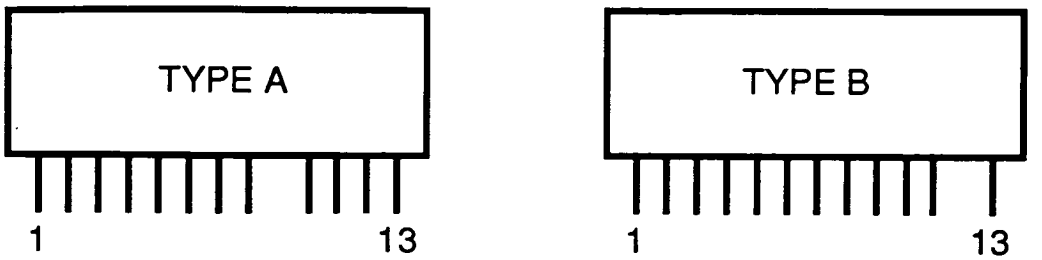

PIN	FUNCTION
1	INPUT (-ve)
2-8	GND
9	no connection
10	+13 V
11	GND
12	-13 V
13	OUTPUT (+ve)

PIN	FUNCTION
1	INPUT (+ve)
2-8	GND
9	-13 V
10	+13 V
11	GND
12	no connection
13	OUTPUT (-ve)

Figure 3.12: *Details of the pin layout for type A and type B preamplifier cards*

based on a 32 channel test board which had been supplied by the Rutherford Appleton Laboratory. Figure 3.13 shows a photograph of the finished board, which measures approximately 415 mm by 155 mm.

The printed circuit board layout was designed using a commercial computer aided design package called PCAD, running on IBM–AT microcomputers. This package allows the user to interactively position the copper tracks, pads and holes on the screen, and can handle multi–layer boards, special component configurations, text layers etc. The final design can then be plotted out on a large format A0 pen plotter for visual checking. The disk file containing the details of all the layers is then supplied to the manufacturing contractor, who uses a computer–driven photoplotter to directly generate the etching masks for the board. The board used two copper layers, front and back, plus additional layers for text printing and the solder resist mask. Manufacture of two copies of the board was carried out by a local company, Zot of Musselburgh [Zot], whilst soldering of the board's components was done by myself in Edinburgh (see figure 3.14).

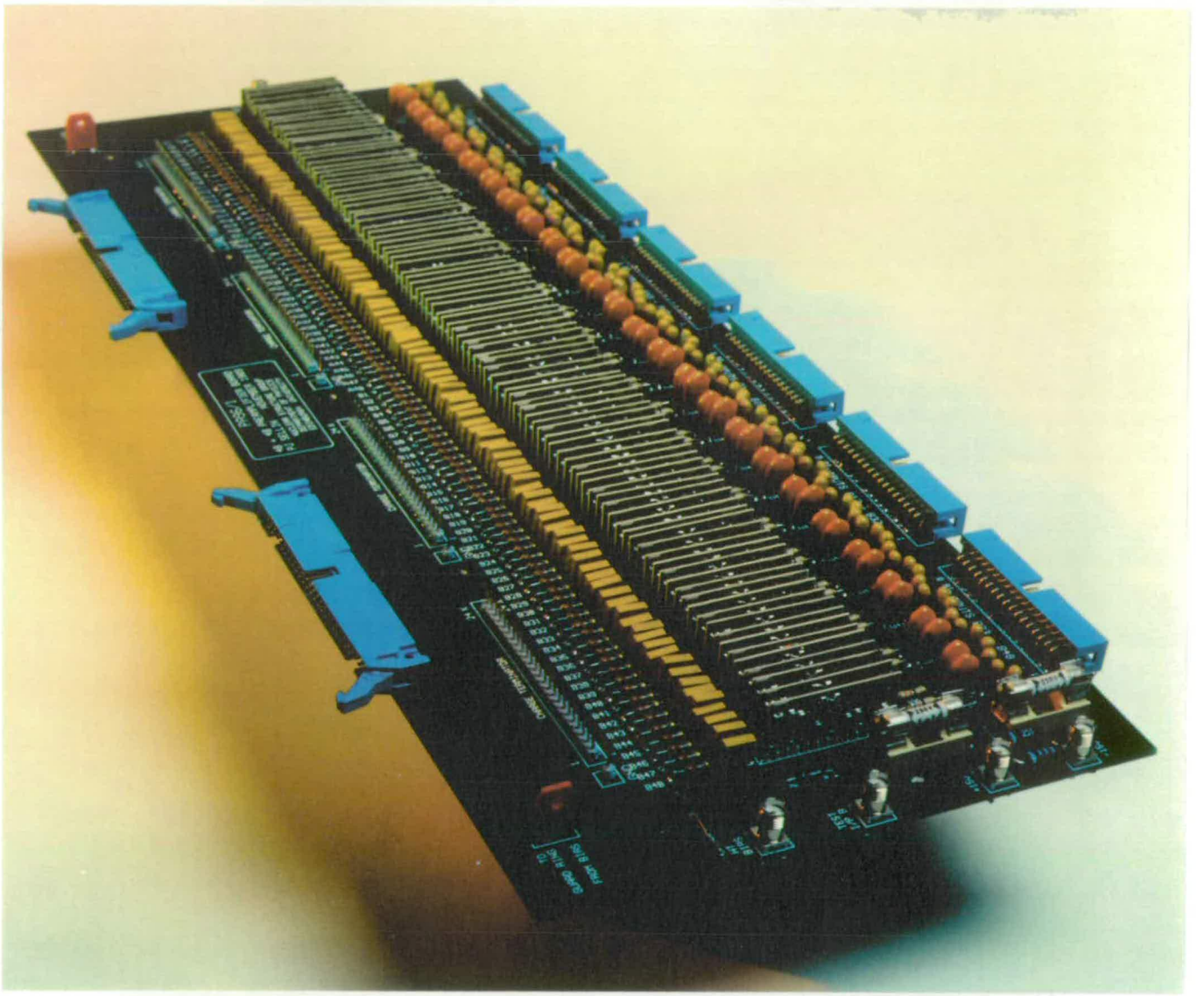

Figure 3.13: *Photograph of the 96 channel preamplifier motherboard*

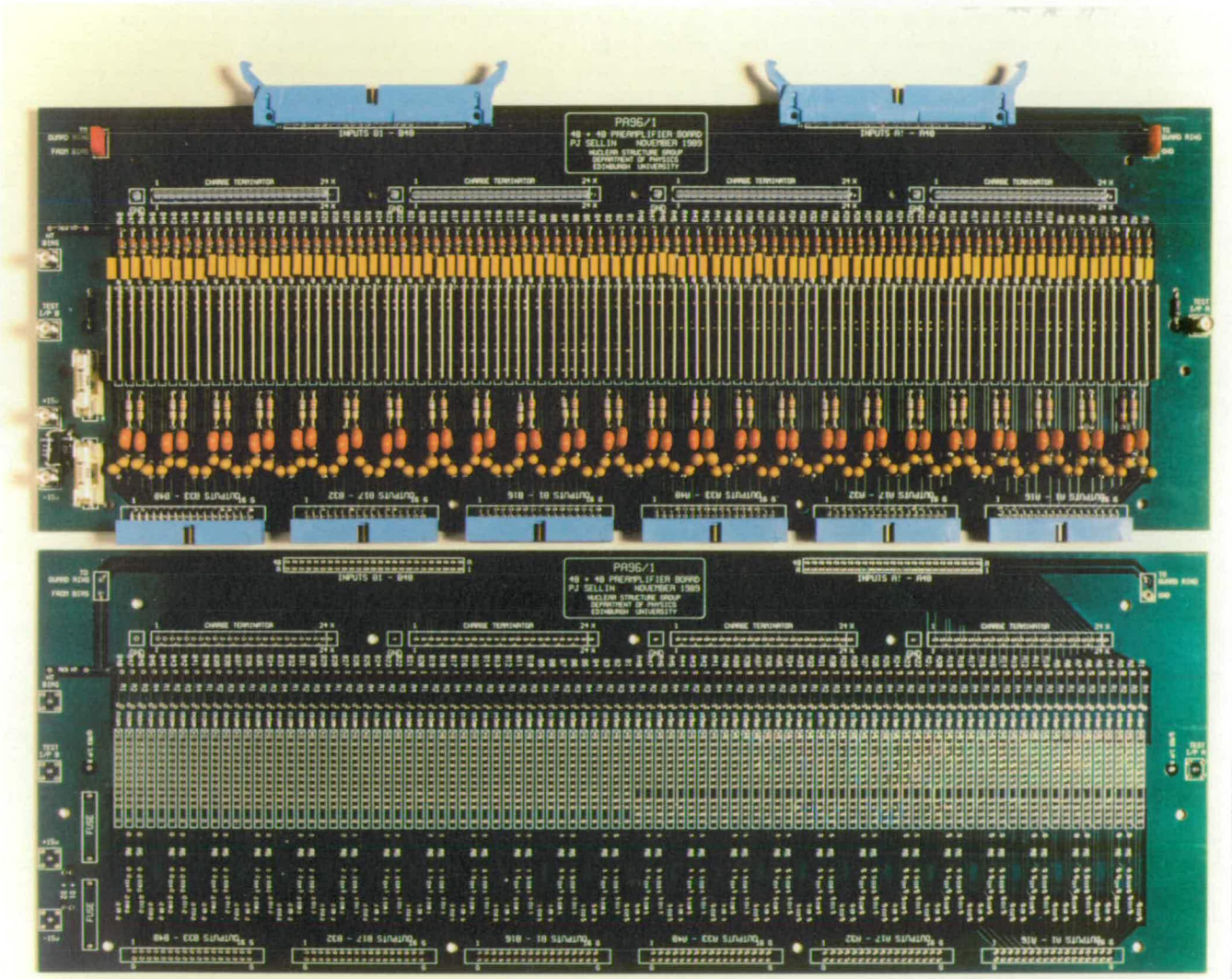

Figure 3.14: *Photograph of the preamplifier printed circuit board showing (upper) the finished board, and (lower) the board without components*

Due to lack of space inside the vacuum vessel at the focal plane of the recoil separator, the preamplifier unit was designed to be attached externally, directly onto the end plate containing the detector system. The board is mounted inside a standard 19 inch case, which is bolted vertically onto the flange plate (figure 3.15). A pair of short 50–way ribbon cables connect the preamplifiers' inputs to the end plate cable feed–throughs immediately below the unit. DC power, detector bias and pulser signals connect to BNC sockets on the side of the case. The lid of the case is mainly cut away and covered with a metal mesh which allows the adjacent cooling fans to blow air directly onto the cards. Approximately 20 W are consumed by a 96–channel board, and considerable heat is generated around the tightly packed cards.

The motherboard circuit provides a test input which is used to supply pulses to each preamplifier channel. The use of pulser signals simulates real events coming from the detector, and are used during setting up to test the total circuit continuity and logic. Additional inputs for test probes into each separate channel are provided for the use of a 'charge terminator' (an RC circuit) to inject a standard amount of charge into any particular preamplifier input in order to provide a calibration peak for strip gain matching.

Five external connectors are provided on the board to connect the supply lines, bias line and test input lines to the case–mounted BNC sockets. These use miniature SMA screw connectors which provide a robust and mechanically sound connection. Signal inputs are through two 50–way IDC ribbon cable connectors at the bottom of the board, each carrying 48 signal lines plus one guard ring connection. For the front face the guard ring is connected to the bias supply via a removable link on the board. The rear face guard ring connection is linked similarly to ground. The output signals are connected through six 34–way IDC connectors to the twisted pair cableways running to the control room.

The noise characteristics of a preamplifier are an important measure of its qual-

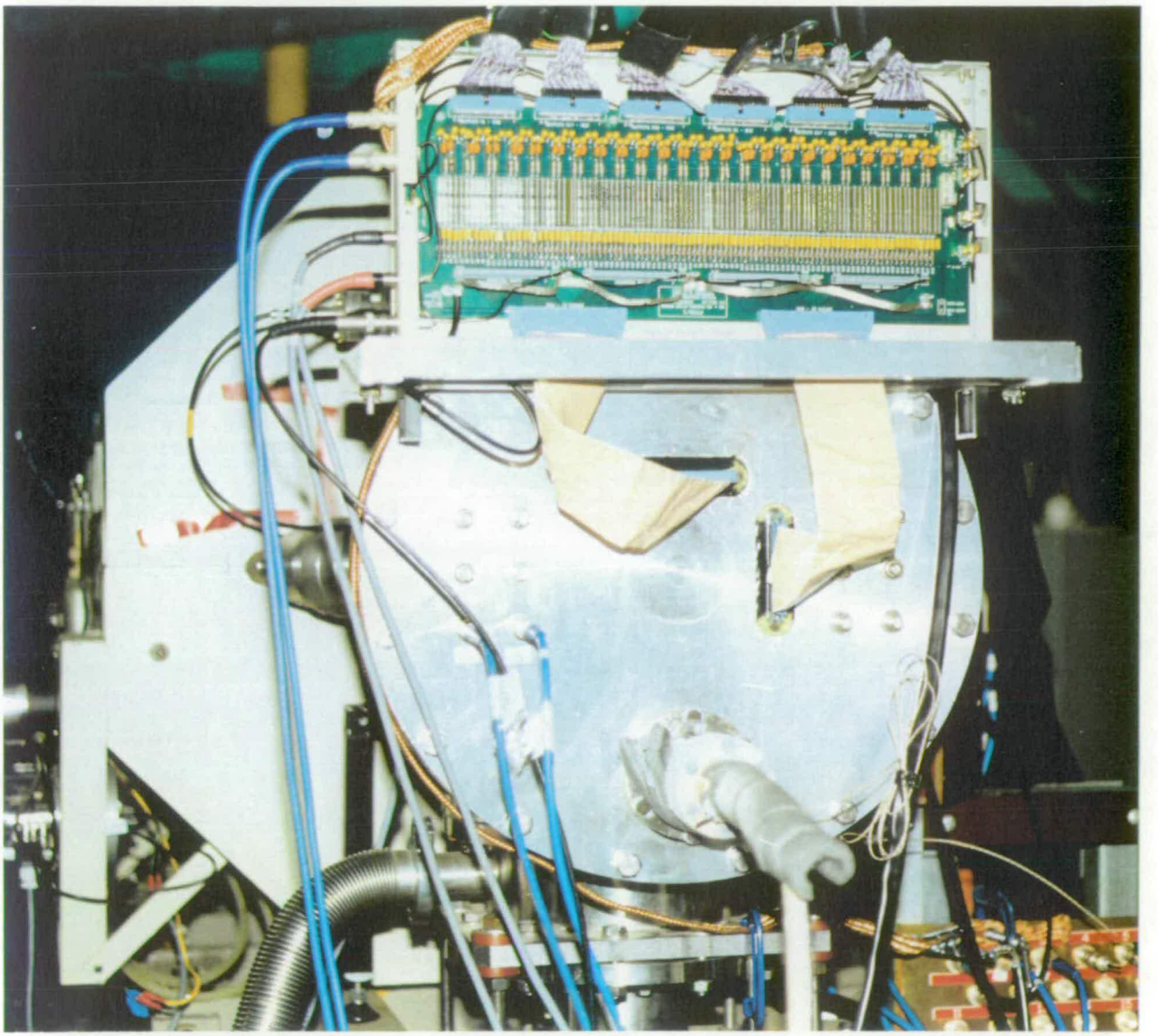

Figure 3.15: *Photograph of the end of the recoil separator, showing the preamplifier unit bolted to the vacuum end plate*

ity of performance. Whilst the sources of noise that are generated in a detector/preamplifier system are varied and complex, the noise function does have a strong dependence on the input capacitance. This capacitance is due to both the capacitance of the detector, and that of the interconnecting cables. Little can be done to minimise the detector contribution, since invariably the type and geometry of the detector is determined by the nature of the experiment, however it is usually possible to minimise the length of the connecting cables. This often leads to positioning the preamplifier circuits within the confines of the vacuum vessel, which is partly the motivation behind this compact preamplifier design. In this case the motherboard is positioned as close to the cable feed–throughs as possible, and connections are made with short lengths of specially screened cable.

A further consideration in preamplifier design is the connection of bias supply to the detector. In the context of silicon detectors where the bias is rarely more than a few hundred volts, the supply is connected through a bias resistor to a point just before the preamplifier input coupling capacitor (see figure 3.8). To minimise inherent thermal noise in the bias resistor R_b [Del80], its value should be as high as reasonably possible, within the limitation that any bias leakage current I_b will drop a potential across R_b and so reduce the actual bias on the detector. In practice, providing the values of R_b and I_b are known, the bias supply voltage can be increased to compensate for any voltage drop. Only in the most serious stages of a detector's radiation damage to a detector can the leakage current rise so rapidly as a function of applied bias that the system 'runs away' and the actual detector bias cannot be increased.

3.5 Shaping Amplifiers

The shaping amplifier accepts low amplitude signals from the preamplifier and processes them into pulses with a shape and amplitude suitable for input into the analogue–to–digital converters (ADCs). The shaping amplifier gain is chosen to

produce the required dynamic range, typically from 20 MeV full scale to 200 MeV full scale, using a 20 mv/MeV sensitivity preamplifier. The amplifier shapes the long–tailed input signal to produce a skewed–gaussian shaped pulse, with a shaping time of typically 0.5 μs on the rising edge and a tail extending over several microseconds.

Shaping	CR–$(RC)^2$
Shaping time constant	0.5 μs
Input polarity	positive or negative
Input impedance	100 Ω
Pole–zero cancellation	50 $\pm$ 10 μs
Gain[1]	maximum 50 (20 MeV = 10 V) minimum $\simeq$5 (200 MeV = 10 V)
Noise	< 1 mV rms at output (maximum gain)
Output dynamic range	0–10 V into 1 kΩ (positive polarity)
Discriminator threshold[2]	adjustable from 20 MeV to $\simeq$ 400 keV (maximum gain)
Time walk	< 20 ns over full dynamic range
Minimum resolving time	200 ns
ECL logic output width	adjustable from 50 ns to 200 ns

1) Includes 2x attenuation of preamplifier signal at shaping amplifier input stage
2) After circuit changes to improve base line restoration performance

Table 3.4: *Specification of Edinburgh/RAL shaping amplifier modules*

The amplifiers described here were designed and manufactured by the Edinburgh group and the SERC Rutherford Appleton Laboratory [Tho90], and were designed to be compatible with the hybrid preamplifier units (section 3.4.2). In order to instrument systems of several hundred channels, the amplifiers needed to achieve a high density and low cost per channel. Surface mount techniques are used to manufacture each circuit on a plug–in module measuring 77 mm by 42 mm. Eight

modules are mounted onto a double height Eurocard motherboard, up to 16 of which can be housed in a standard 19 inch rack. This project was the first time that these amplifiers were used together to form a multi–channel system.

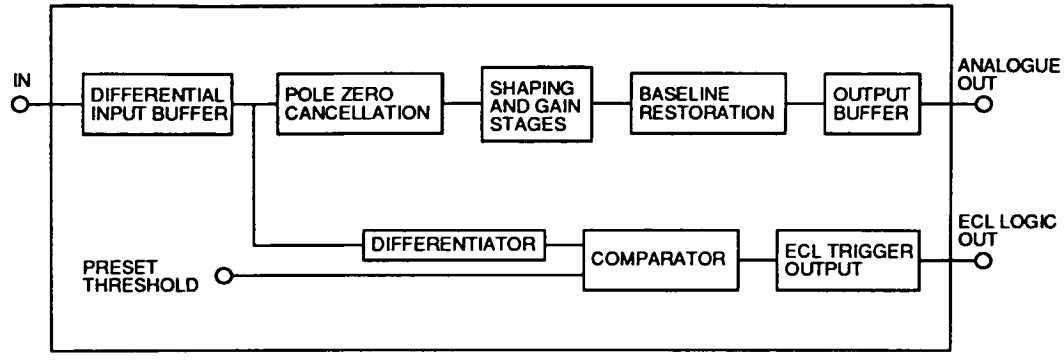

Figure 3.16: *Block diagram of the shaping amplifier circuitry*

A block diagram of the component parts of the amplifier is shown in figure 3.16 and is described in detail by S. Thomas *et al.* [Tho90]. The differential input buffer accepts signals from the twisted pair cable, and is designed to reject any pickup and electrical noise common to both input conductors. The pole–zero cancellation circuit removes the long–tailed decay of the preamplifier signal, and controls the shape of the amplifier output pulse as it returns to base line. Each module contains two adjustable potentiometers, one for pole–zero adjustment and the other to vary the DC offset. A shaping and gain stage follows, with plug–in resistors on the card allowing the dynamic range to be set to between 20 MeV and $\simeq$ 220 MeV. Table 3.5 shows typical values of amplifier gain for given resistor packages, which simultaneously fix the gain for all eight channels. A final amplification stage in the output buffer produces a signal suitable to drive the ADCs via short ribbon cables.

Each amplifier module also produces a logic signal, output from a built–in leading edge discriminator. The discriminator circuit takes its signal from the differential buffer output, which retains the fast leading edge of the preamplifier signal, and outputs an ECL (Emitter Coupled Logic) logic pulse. The threshold voltage level is set for all eight modules by a potentiometer mounted on the card front panel.

Resistor	100 pF	120 pF	150 pF
1 kΩ	55	80	100
1.2 kΩ	75	100	125
1.5 kΩ	100	130	170
1.8 kΩ	140	170	210
2.0 kΩ	165	200	250
2.2 kΩ	190	220	280
2.4 kΩ	200	240	300

ECL logic pulse widths (ns)

Gain resistor	System gain* (V/MeV)	Energy equal to 10 V (MeV)
0 Ω	0.5	20
22 Ω	0.489	20.4
1 kΩ	0.25	40
2.2 kΩ	0.156	64.1
10 kΩ	0.045	222

*gain = 0.5/(1+gain resistor in kΩ)

System gain

Table 3.5: Shaping amplifier pulse width and gain settings

The output pulse width for each logic channel can be changed by one of eight plug–in capacitors mounted on the card, within the range of 55 – 200 ns (see table 3.5). The discriminator threshold has a minimum level of 5 – 10 mV at the buffer input, corresponding to energies of 200 – 300 keV.

The original design specification for this circuit was drawn up several years before this project work and consequently did not anticipate the stringent requirements of this particular application. The most important additional feature of this work is the need for the amplifiers to handle, and recover from, highly over–loaded input pulses. This occurs when high energy (50 – 100 MeV) signals from implantation events are sent through the high gain (0 – 20 MeV) amplifiers. Although these signals do not cause an event trigger and so are not read by the ADCs, it is vital that the high gain amplifiers can recover quickly from saturation. Too long a recovery time would make the system insensitive to any low energy decay signals which occurred quickly after an implantation event. The baseline restoration circuit has a fixed maximum restoration rate, which governs how quickly a signal undershoot can recover to baseline. Any decay signals arriving during this undershoot will be recorded with a reduced amplitude and will consequently experience some degradation of energy resolution.

Several alterations were made to the amplifier modules after they were delivered, in order to improve the overload recovery performance. Since saturation was occurring in the input buffer stage, the buffer gain was reduced by a factor of 2, which was compensated for by a 2× gain increase in the output driver. As the discriminator threshold voltage remained unaffected, this caused an increase in the minimum discriminator threshold energy to approximately 450 keV. The buffer output signal was offset negatively, in order to allow a greater positive dynamic range and reduce saturation in the later gain stages. Following the commissioning experiment several further improvements were made to the baseline recovery performance (see section 4.2.1).

3.6 Trigger logic and control signals

The logic circuitry is used to generate the two event manager trigger signals, one for implantation events (recoil trigger RT) and the other for decay events (decay trigger DT). The final logic decision is made by the programmable logic unit (PLU) which is connected as shown in figure 3.9. The PLU contains two independent sections (denoted '0' and '1'), with section '0' used for the trigger signals and section '1' used for the MALU control signals. Each section contains a 256–byte look–up table which maps any of the eight inputs onto any of the eight outputs. In this way the user programs each section to define the output bit pattern associated with each combination of input bits. The use of a look–up table minimises the propagation time for signals through the unit, which is typically $\leq$ 10 ns.

The event manager trigger signals DT and RT are generated from the 5 input signals AOR, BOR, RENA, RENB and POEN (described in section 3.3). The logic conditions and timing relations for each trigger type are shown in figure 3.17. Signals AOR and BOR indicate that at least one strip has fired in each face of the detector, and are used as the basic indicator of an event within the strip detector. Both trigger types require an AND between AOR and BOR in order to reject spurious triggers generated from pickup or other electrical noise. Signals RENA and RENB indicate that a high energy ($>$ 15 MeV) event has occurred in either face of the detector, and POEN records a particle passing through the carbon foil detector. The recoil trigger RT therefore requires any of RENA, RENB or POEN in addition to the AND of AOR and BOR. Accordingly the decay trigger (DT) requires that none of RENA, RENB or POEN are present.

The timing of the signals is carefully set so that each of RENA, RENB and POEN (the 'veto' signals) completely overlap both AOR and BOR. The widths of AOR and BOR are adjusted from the 48–way OR logic units and are set as short as possible whilst still ensuring a consistent overlap between the two signals (typically

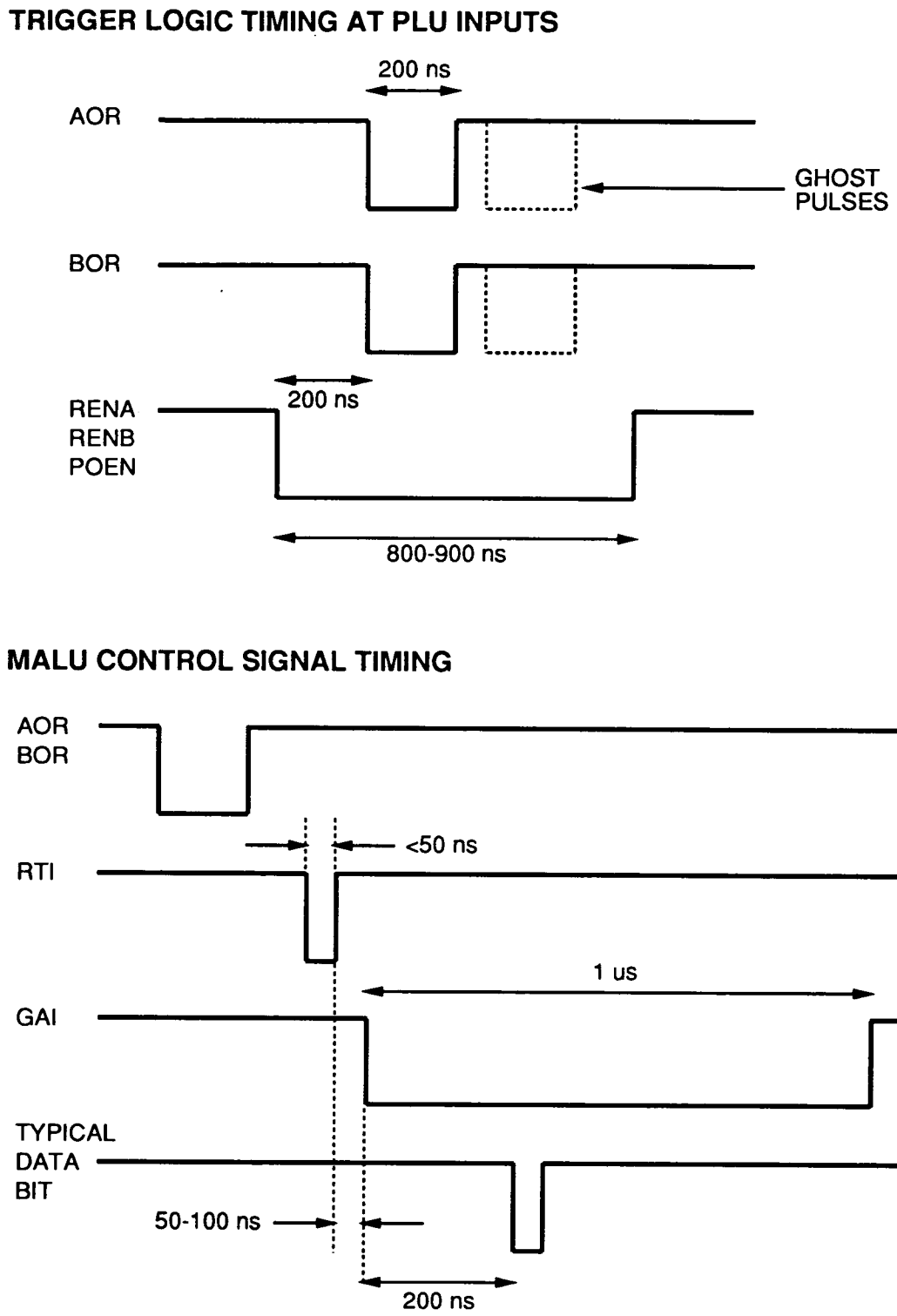

Figure 3.17: *Timing relations for trigger logic (upper diagram) and MALU control signals (lower diagram)*

```
C          INPUTS 0:          OUTPUTS 0:
C      1   AOR (DELAYED)    8  INPUT #5
C      2   BOR (DELAYED)    7  INPUT #4
C      3   RENA             6  INPUT #3
C      4   RENB             5  INPUT #2
C      5   POEN             4  INPUT #1
C      6                    3  AOR .OR. BOR (use for QTERM only)
C      7                    2  TRIGGER B (RECOILS)
C      8                    1  TRIGGER A (DECAYS)
      LOGICAL INPUT( 8 ), OUTPUT( 8 )
      OUTPUT( 1 ) = INPUT( 1 ) .AND. INPUT( 2 ) .AND.
     *              .NOT.( INPUT(3) .OR. INPUT(4) .OR. INPUT(5) )
      OUTPUT( 2 ) = INPUT( 1 ) .AND. INPUT( 2 ) .AND.
     *              ( INPUT(3) .OR. INPUT(4) .OR. INPUT(5) )
      OUTPUT( 3 ) = INPUT( 1 ) .OR. INPUT( 2 )
      OUTPUT( 4 ) = INPUT ( 1 )
      OUTPUT( 5 ) = INPUT ( 2 )
      OUTPUT( 6 ) = INPUT ( 3 )
      OUTPUT( 7 ) = INPUT ( 4 )
      OUTPUT( 8 ) = INPUT ( 5 )
      RETURN
      END
```

Figure 3.18: *Program file for trigger signal logic*

```
C          INPUTS 1:          OUTPUTS 1:
C      1   AOR (pin 10)     8  INPUT #3
C      2   BOR (pin 10)     7  INPUT #2
C      3   EMU VETO         6  INPUT #1
C      4                    5
C      5                    4
C      6                    3
C      7                    2
C      8                    1  MALU GAI/RTI
      LOGICAL INPUT( 8 ), OUTPUT( 8 )
      OUTPUT( 1 ) = ( INPUT( 1 ) .OR. INPUT( 2 ) )
     *              .AND. .NOT.(INPUT (3))
      OUTPUT( 2 ) = .FALSE.
      OUTPUT( 3 ) = .FALSE.
      OUTPUT( 4 ) = .FALSE.
      OUTPUT( 5 ) = .FALSE.
      OUTPUT( 6 ) = INPUT( 1 )
      OUTPUT( 7 ) = INPUT ( 2 )
      OUTPUT( 8 ) = INPUT ( 3 )
      RETURN
      END
```

Figure 3.19: *Program file for MALU control signal logic*

100–200ns). It is found that for implantation events 'ghost' AOR and BOR pulses follow the main signals, approximately 300–400ns after the prompt signal's leading edge and at a much reduced rate. These arise from cross talk in the cableways, which induces bipolar signals in the conductors adjacent to the channel containing the high energy pulse. Consequently the veto signals are stretched to completely cover such additional AOR and BOR signals.

The delay in each signal line is minimised as far as possible, whilst still maintaining the shown relative timing. Since the trigger pulses are used to gate the ADCs , they must be sufficiently prompt to ensure that the resulting gate pulse can straddle the peak of the analogue signals. The promptness of the trigger pulses relative to the analogue signals is limited by the RENA/RENB pulses, which are derived from slow rise time signals. This delay is minimised by using high band width linear amplifiers after the mixer units, connected to leading edge discriminators.

The second section of the PLU is used to generate the control signals for the majority logic units (MALUs). These units record the strip hit pattern of each implantation event, which is later used to reconstruct the event's x,y coordinates. The units require an external gate signal (GAI) and reset signal (RTI), which must be carefully timed in relation to the data bits (see figure 3.17). The narrow reset signal clears the data inputs of any spurious data and is immediately followed by a wide gate pulse. In order for the data bits to be latched onto the inputs, they must arrive whilst the gate signal is held high. The pulse shaping and relative timing for the RTI and GAI signals are performed by a dual gate and delay generator (LeCroy 2323A), fed from the PLU output. The PLU logic function used to produce the control signals is shown in figure 3.19, essentially an OR between prompt unshaped AOR and BOR signals with a veto signal supplied from the input stage of the event manager. The veto signal is set high for the time between a recoil trigger arriving and the event manager having finished processing the event. This prevents a second valid gate signal being generated whilst the existing MALU data bits are waiting to be read. In addition the gate signal is fed back

into the reset 'blanking' input in the gate and delay generator to prevent spurious reset signals being generated during the length of the gate pulse.

It is crucial that the MALU data bits are delayed sufficiently so that they all arrive after the leading edge of the gate pulse. This required the construction of new delay boards prior to the main experiment with a $0 - 500$ ns delay range, to replace the original 100 ns boards used unsuccessfully in the commissioning experiment.

3.7 The Charissa event manager

3.7.1 Overview

The event manager records the experimental parameters for each event and packages them into a format suitable for writing to magnetic tape. The Daresbury Charissa event manager is able to record both analogue and digital parameters, and package them together into combined events. Analogue signals are connected to ADCs, which digitise the pulses under the control of a gate pulse supplied by the event manager. Within the Charissa system this digitised ADC data is referred to as 'FERA data', derived from the name of the ADC FERA data bus. The non–analogue event parameters (eg. strip hit patterns and clock values) are recorded by a variety of CAMAC data units, which are also strobed by a gate pulse from the event manager.

For this work the number of available FERA channels was expanded from the previous limit of 48 [Bro90] up to 104, requiring thirteen 8–channel ADCs. An additional 16 CAMAC channels are used, producing a maximum event size of 120 channels. Charissa operates in 'indirect trigger' mode whereby a trigger signal causes all ADCs to convert irrespective of whether each channel has an analogue signal present. Any zero data words are then stripped from the event package

by the event manager before writing to tape. This simultaneous conversion of all channels simplifies the ADC control signals, at the expense of a longer event manager deadtime.

The standard Charissa system only allows the input of a single type of event trigger. For this application the system was expanded to allow the independent and simultaneous processing of signals from two independent triggers, one from each event type. This was necessary in order to have zero relative deadtime between the processing of the two event types. In practice a minimum relative delay of $\simeq$ 10 μs is imposed by the recovery time of the decay signal amplifiers after saturation by implantation events. Dual trigger processing was achieved by the addition of a two–channel signal multiplexor to the trigger input stage of the event manager. This new unit, the Edinburgh Multiplexor Unit (EMU), was designed and built for the project by Mr Dick Hunt of the Oxford University Nuclear Electronics group. The EMU accepts two independent trigger signals, and stacks one into a queue for subsequent processing if they arrive simultaneously. In principle Charissa is capable of handling events with a total of 256 channels, although this project was the first use of more than 96 total channels.

3.7.2 Outline of the Charissa event manager

The Charissa event manager was designed to be a simpler and more flexible system than the existing Daresbury event managers, able to cope with a large number of mixed ADC and CAMAC channels. The structure of Charissa consists of new 'front–end' units connected to an output stage compatible with the existing event managers. The structure of the Charissa data is therefore of the same format as the other systems, and the resulting tapes can be analysed with existing Daresbury software routines.

The event controller (EC) is the key part of the Charissa system, and is responsible for controlling the operation of the ADCs and CAMAC data units (see figure 3.20).

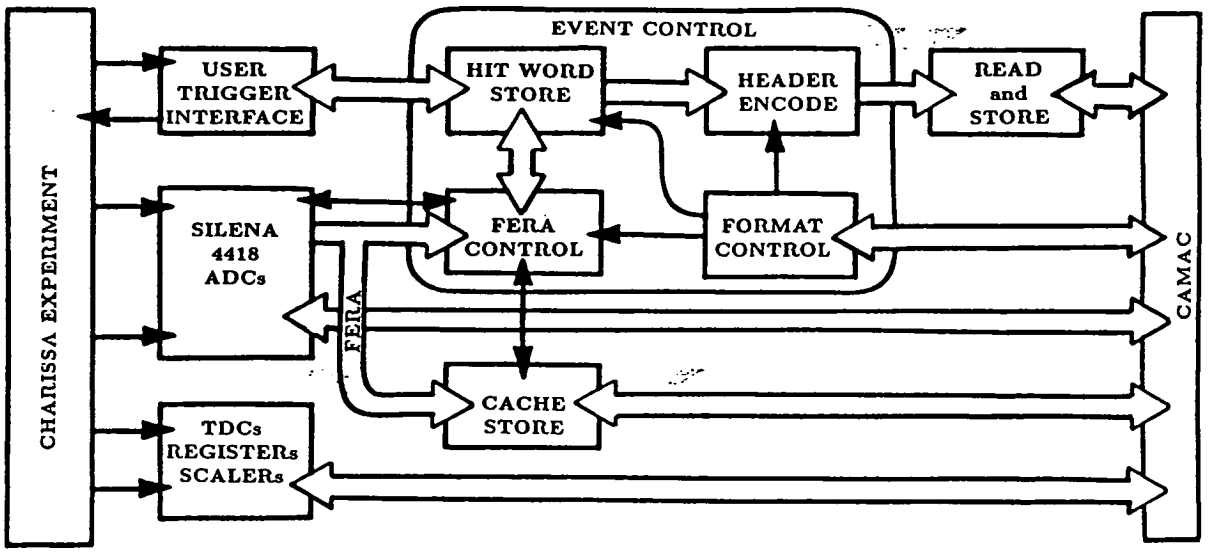

Figure 3.20: *Schematic diagram of the Charissa event manager (from [Bro89])*

In a normal Charissa configuration the single event trigger is supplied directly to the EC, which then sends a gate pulse to all the ADCs and CAMAC data units. In this application the trigger pulse is received from the EMU, and the gate pulse sent back through the EMU to the ADCs. The EC also handles the ADCs' control signal bus, which requires sending and receiving a complex sequence of handshaking signals. After each sequence of ADC conversions the resulting FERA data is passed into the data stack. The EC then communicates with the read and store module (RSM), passing it hit pattern information in the form of header words and hit pattern words (see appendix A). The RSM is common to both types of Daresbury event manager, and is responsible for grouping the data values from each event into an event block. Within Charissa the RSM rebuilds each event block with reference to the data stack, and stores the resulting event blocks in its

output buffer. When the buffer is full the resulting RSM block is output to the acquisition computer to be written to tape.

A typical sequence of operations following an event trigger is as follows:

- The event trigger arrives at the EC, which sends a gate pulse to the ADCs to start their conversion process. The gate signal also strobes the inputs of the CAMAC units.
- ADCs finish conversion and send their data words sequentially down the FERA data bus to the Data Stack (DS) and the EC.
- The DS stores each data word into a 256 word sequential buffer. The EC constructs a header word plus words containing the channel hit patterns for valid FERA and CAMAC channels.
- The EC passes the header word and hit pattern words to the RSM.
- The RSM builds the total event from the header/hit pattern words, followed by FERA data words from the DS then CAMAC data words read from the CAMAC data units. The whole event is then stored in an output buffer and all ADCs and CAMAC data units are cleared ready for the next event.
- When the current output buffer fills beyond a certain level (the High Water Mark or HWM) the RSM swaps to start filling the alternative output buffer. The full buffer then empties its data down the CAMAC serial link to the A–machine.

The detailed structure of the data format for events of length up to 128 channels is given in appendix A.

3.7.3 The Edinburgh Multiplexor Unit (EMU)

The EMU acts as a front–end unit, accepting two triggers inputs and sending out control signals to each of two sets of ADCs. Dual trigger processing is vital in this case, since with only a single trigger the event manager would be dead for approximately 150 μs after an implantation event. With dual triggers, each trigger type controls, via the EMU, a separate set of ADCs and CAMAC units; the same ADCs cannot be shared by two trigger types. If one trigger arrives whilst the other is being processed, the later group of ADCs are held until the first group have finished reading out to the EC. No more triggers are accepted by the EMU until both triggers have cleared. For triggers arriving in coincidence, one is queued until the other has finished processing, with each trigger being given equal priority so that the queuing order alternates between successive coincidences.

The use of a trigger queue means that the time at which the ADCs or CAMAC units are read by the event manager is no longer a fixed time interval after the originating EMU trigger signal. Care has to be taken for those CAMAC units which record the real time for each event (the clock pattern registers) to ensure that they are strobed by a non–delayed trigger signal from the EMU. The rear panel of the EMU provides four output signals; GATEA and GATEB which follow the trigger input signals, and READA and READB which show the group which is being processed at any time by the EC. An inhibit signal is also output which are set high for the time between the GATE and the READ for recoil triggers.

Chapter 4

Detection system performance

4.1 Overview of the commissioning experiment

The first experiment using a double–sided silicon strip detector was carried out in April 1990 on the Daresbury recoil separator. For this commissioning experiment the reaction $^{58}Ni + {}^{54}Fe \rightarrow {}^{112}Xe^{*}$ was studied, which produces the known proton emitter ^{109}I with a relatively large cross section of $\simeq 50$ μb. This proton transition has been convincingly but indirectly assigned to the decay of ^{109}I [Fae84, Gil87] by a combination of excitation function measurements and Q–value systematics. The proton decay has been previously measured with an energy of 813 ± 5 keV [Hof88] and a half–life of 109 ± 17 μs [Gil87], and therefore provided an excellent test of the performance of the new detection system. In particular, due to the short half–life of the proton transition, this reaction provided a sensitive test of the overload recovery performance of the amplifiers.

Prior to this experiment the strip detector's performance with heavy ions over the required wide range of particle energies was unknown. The susceptibility of the detector to radiation damage was also unknown within the context of this particularly damaging type of application. The effect of radiation damage as a

function of dose rate was uncertain for incident high energy heavy ions, and it was important that there was not a catastrophic drop in energy resolution and a corresponding rise in leakage current.

In addition there was the possibility of problems within the detector caused by inter–strip charge sharing, particularly from high energy implantation events. Such events distribute the deposited energy over two or more strips, and are subsequently rejected in software. It is therefore important that an acceptably low proportion of events (eg. $< 10\%$) show a multiplicity greater than one. The strip multiplicity performance and effects of radiation damage are summarised in section 4.3. The new preamplifier and amplifier electronics were being used for the first time in this experiment to process signals from a total of 120 channels. This represented the largest number of channels of any Daresbury experiment and required the use of the Charissa data acquisition system in a novel configuration (see section 3.7).

The commissioning experiment used a beam of ^{58}Ni ions incident on targets of 500 μg cm^{-2} thick 97% isotopically enriched ^{54}Fe. The beam energy was 240 MeV, producing the compound nucleus ^{112}Xe* with an excitation energy of approximately 52 MeV. This excitation energy was chosen to maximise the yield of ^{109}I produced via the p2n evaporation channel. Typical beam rates were 70 enA, producing implantation rates of approximately 3 kHz in the detector. The recoil separator was set to position A=109 residues with charge state $Q = 27^+$ onto the centre of the focal plane.

4.2 Radioactivity observed from ^{112}Xe*

In the reaction ^{58}Ni + ^{54}Fe $\rightarrow$ ^{112}Xe* the compound nucleus ^{112}Xe* produces, in addition to the proton emitter ^{109}I, the strong alpha emitting tellurium isotopes ^{108}Te (E_α = 3314 $\pm$ 5 keV [Hei91], b_α = 68%) and ^{109}Te (E_α = 3107 $\pm$ 5 keV

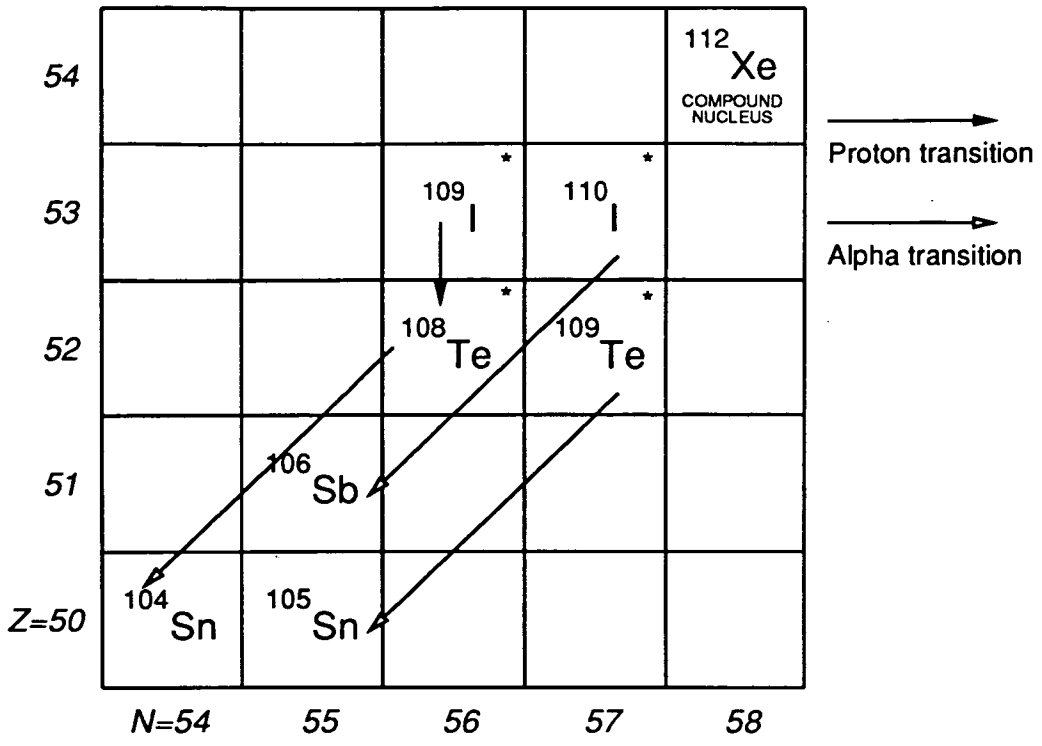

Figure 4.1: *Proton and alpha transitions observed from the compound nucleus* $^{112}Xe^{*}$. *Isotopes marked '*' are produced directly from the compound nucleus*

[Hei91], b_α = 4%) summarised in figure 4.1. The tellurium alpha decays have been well documented, originally by Macfarlane *et al.* [Mac65a] and more recently by Schardt *et al.* [Sch79] and Heine *et al.* [Hei91]. Since ^{108}Te is the daughter of ^{109}I, it should be possible with sufficient sensitivity to identify the correlated decay sequence

$$^{109}\mathrm{I} \xrightarrow{p} {}^{108}\mathrm{Te} \xrightarrow{\alpha} {}^{104}\mathrm{Sn}$$

which would be characterised by the occurrence of ^{108}Te decay events within the A=109 region of the detector.

The decay energy spectrum obtained from this reaction is shown in figure 4.2. The energy signal is derived from the average of the two signals from the strip detector's front and rear faces (see section 4.3.2) after requiring that only one strip per face contains a valid signal. The spectrum clearly shows the proton peak from

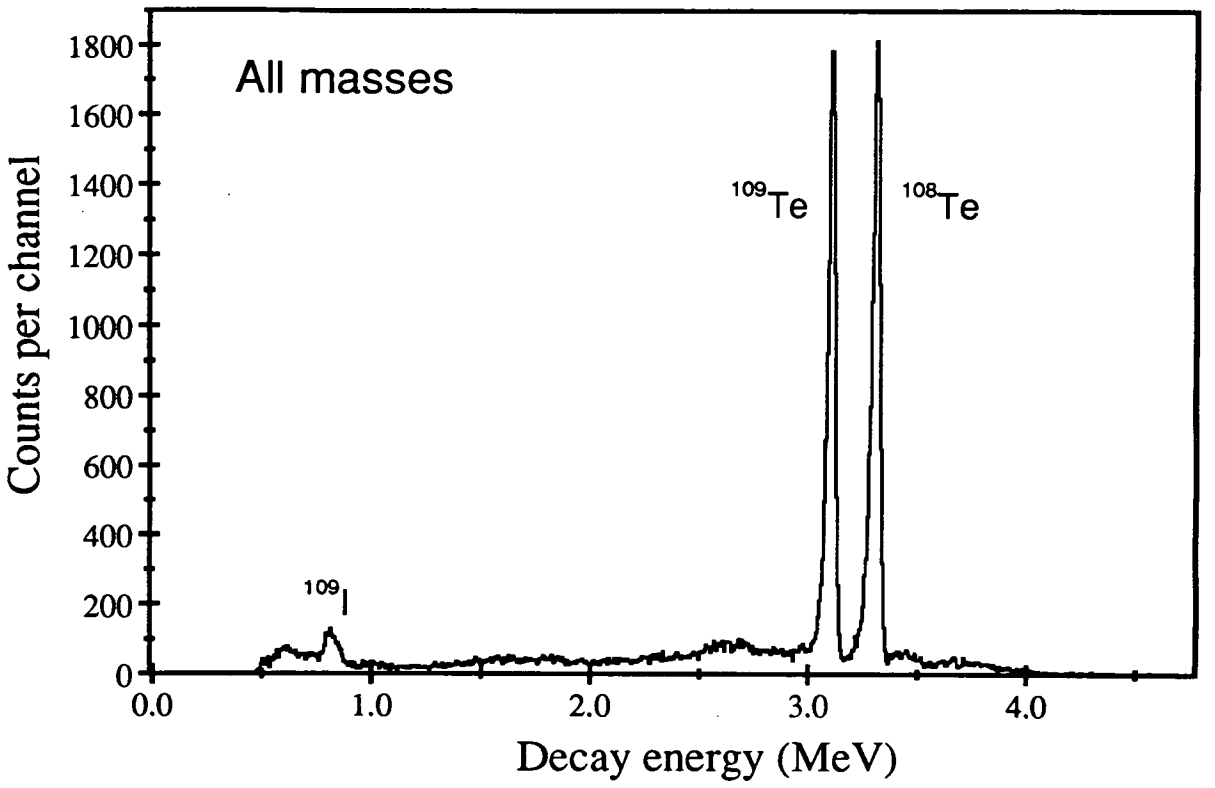

Figure 4.2: *Energy spectrum for all decay events from* $^{112}Xe^{*}$

^{109}I at an energy of 0.81 MeV, which contains approximately 900 proton events, and the two alpha peaks due to ^{109}Te (3.11 MeV) and ^{108}Te (3.31 MeV). The energy resolution of the alpha lines in figure 4.2 is approximately 40 keV FWHM, whilst that of the proton line is slightly degraded (the reasons for this are discussed in section 4.2.1). The peaks are on top of a low-lying continuum of events which is made up of various components (see section 4.2.3), but is mainly due to the β^{+}–delayed proton spectrum of ^{109}Te [Bog73]. The discriminator thresholds of the decay amplifiers impose a low energy cutoff of the continuum at approximately 500 keV. The threshold levels in this experiment were kept fairly high to prevent detector pickup causing false decay event triggers.

The mass separation achieved with the recoil separator is demonstrated in figure 4.3 which shows the same data in a two dimensional plot of decay energy versus horizontal position x. The horizontal position for each event is taken di-

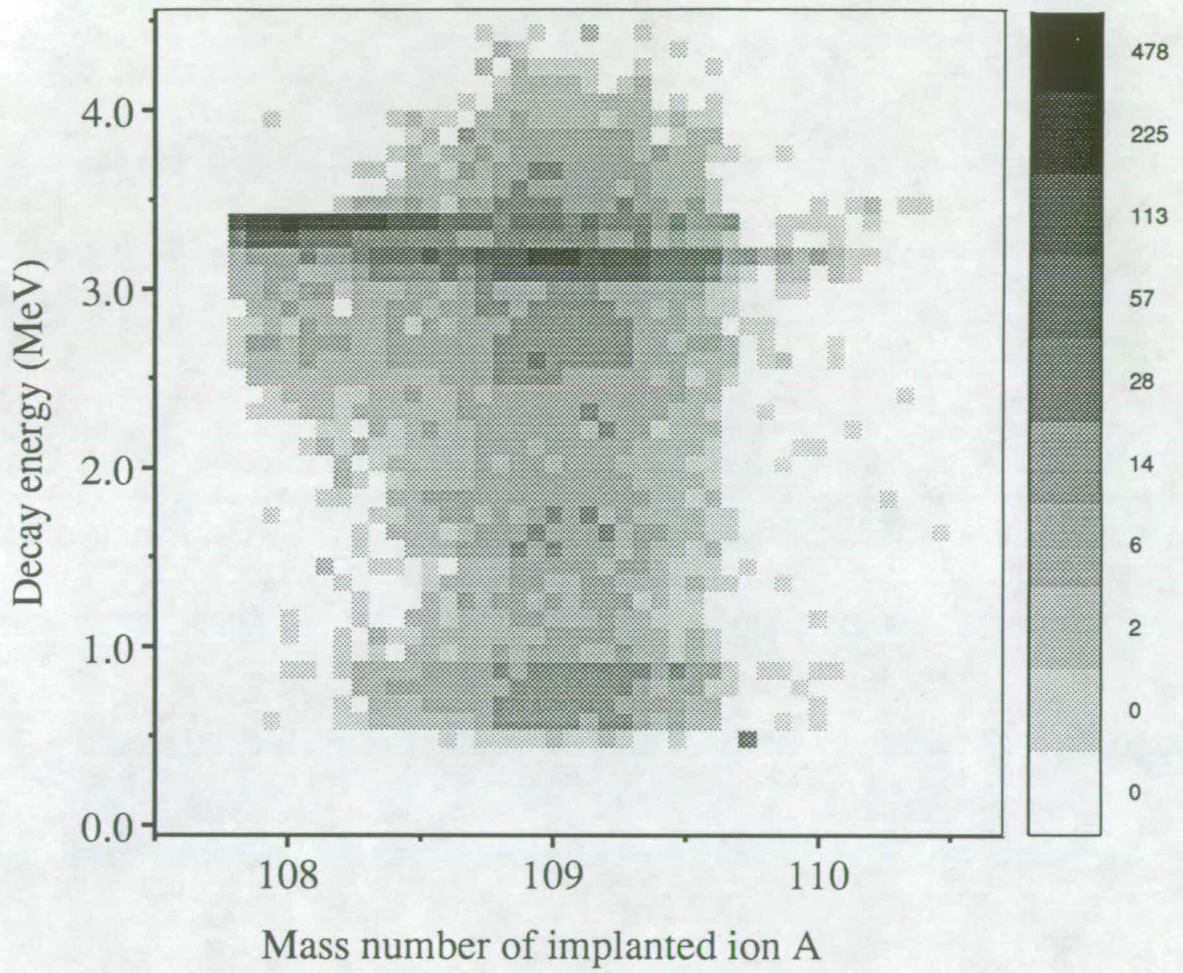

Figure 4.3: *Plot of decay energy versus the mass number of the implanted ion, for decay events from $^{112}Xe^{*}$, showing each of the A=108 and A=109 alpha peaks. The proton peak from ^{109}I is not resolved in this spectrum, and is contained within the region of A=109 events below 1 MeV*

rectly from the number of the vertical (front) strip in which the event occurs, and is proportional to the $^{A}/_{Q}$ of the implanted ion. Figure 4.3 has been calibrated on the x-axis for charge state $Q = 27^{+}$, and mass 109 is located near the centre of the detector. The strong alpha lines from ^{108}Te and ^{109}Te can be clearly seen in the A=108 and A=109 regions respectively, and the broad peak containing the proton peak from ^{109}I is clearly visible in the A=109 region. Mass windows are applied to this spectrum during software analysis to generate mass-gated decay energy spectra. The mass resolution shown in figure 4.3 is worse than that normally achieved with the separator, caused by the focal plane being slightly displaced from the plane of the strip detector. This was due to the new detector mounting on the separator end plate, which positioned the strip detector slightly further down the separator beam axis than the normal detector position.

Figure 4.4 shows the corresponding decay energy spectra gated on the A=108, A=109 and A=110 regions of the detector. It can be seen that the proton line occurs predominantly in the A=109 spectrum, which also contains the 3.11 MeV alpha line from ^{109}Te. This data provides the first direct mass assignment of the proton events to an A=109 nucleus. Each spectrum contains some contamination from the strong peaks in adjacent mass groups, caused by the reduced mass resolution. The lower plot in figure 4.4 also shows a small peak at an energy of 3.44 MeV. This is from the alpha decay of ^{110}I (E_{α} = 3457 $\pm$ 10 keV [Hei91], $t_{\frac{1}{2}} = 690 \pm 40$ ms [Kir77], $b_{\alpha} < 10\%$ [Roe78]), and shows clearly how mass-gating can suppress background events and so highlight weak decay lines.

4.2.1 The proton peak from ^{109}I

The spectrum in figure 4.5 shows decay events mass gated around A=109, with the proton peak clearly visible. The peak has an energy resolution of approximately 70 keV FWHM, which is significantly degraded in comparison to the alpha peaks. The additional width of the proton peak is a purely experimental feature, caused

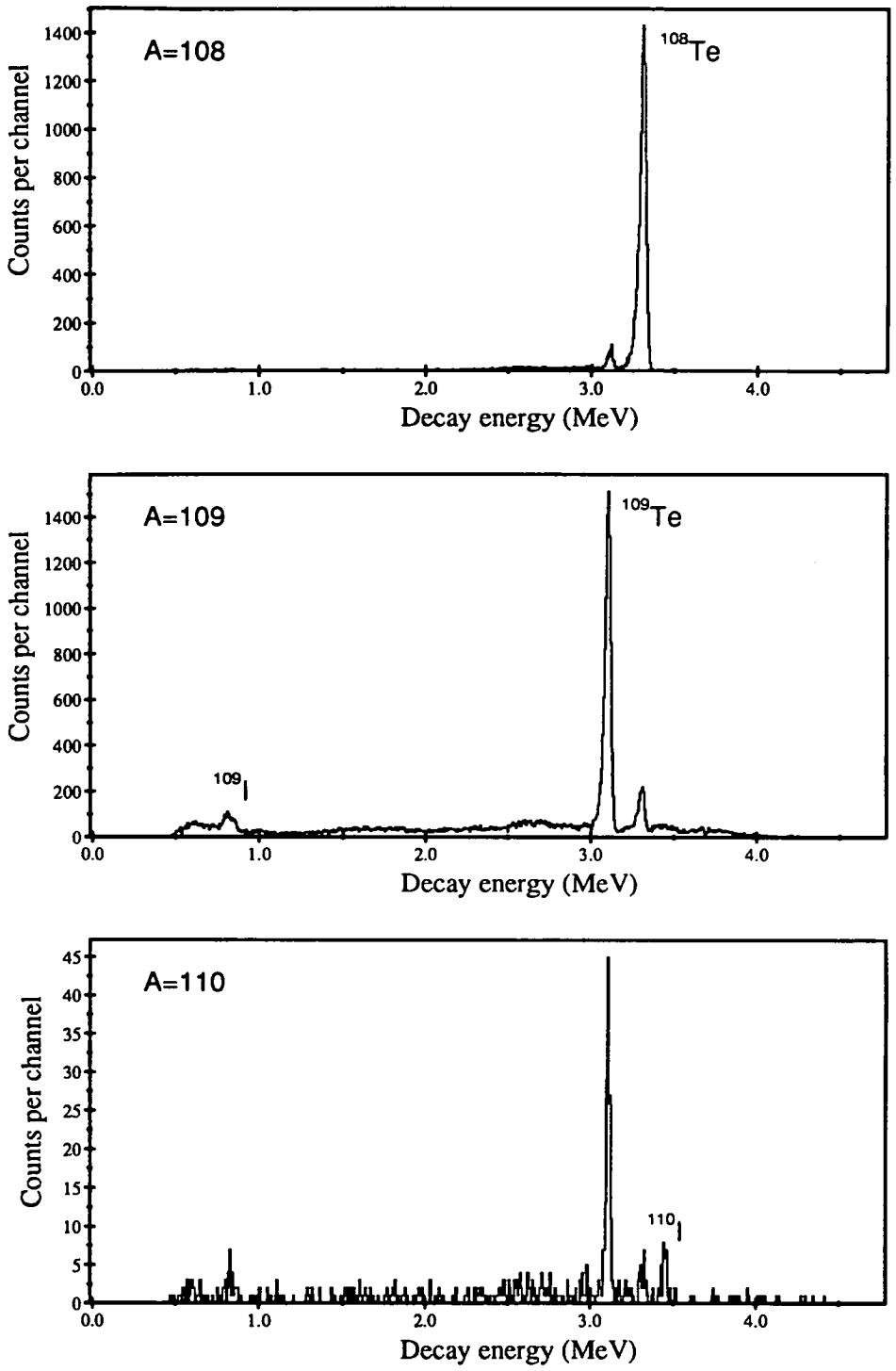

Figure 4.4: *Mass gated energy spectra for decay events from $^{112}Xe^{*}$, gated on A=108, A=109 and A=110. The proton peak at 0.81 MeV is clearly visible in the A=109 spectrum. The poor mass resolution of this data causes some contamination in each spectrum from strong peaks in adjacent mass groups*

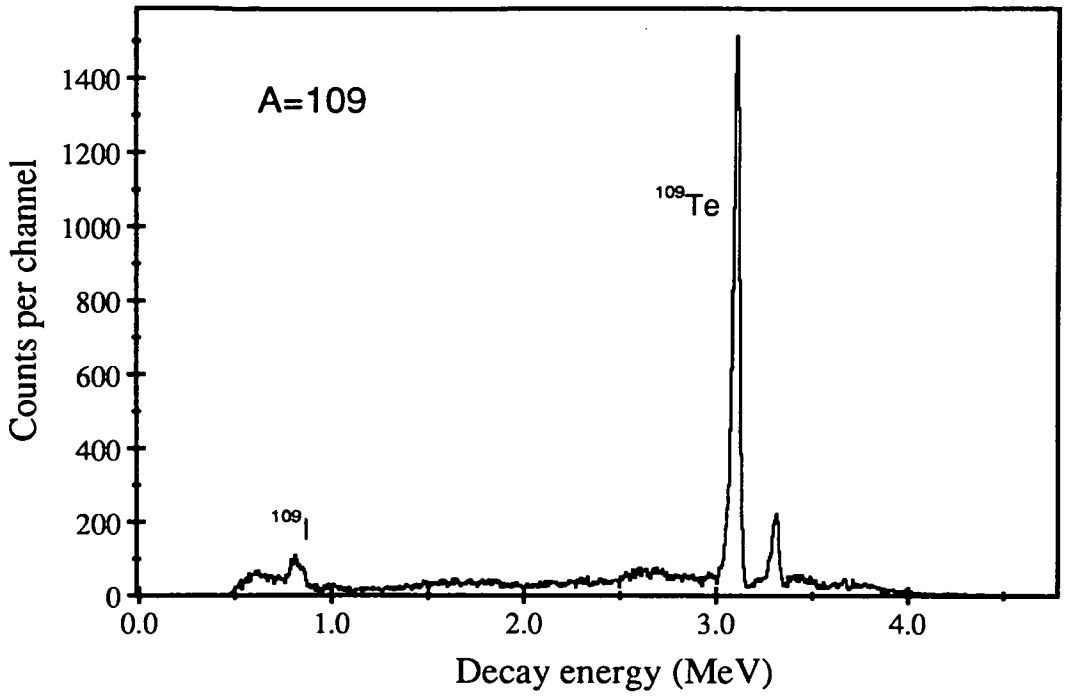

Figure 4.5: *Mass gated A=109 decay energy spectrum from $^{112}Xe^{*}$. The proton peak from the decay of ^{109}I is clearly visible at an energy of 0.8 MeV*

by the finite baseline recovery time of the decay amplifiers after saturation from an implantation event. Any decay event pulse which occurs whilst the baseline is below zero volts will be recorded with a reduced energy. In this way very fast decay lines will exhibit a time–dependent shift in their peak centroid during the baseline recovery period.

Figure 4.6 shows the energy spectra of mass gated A=109 decay events from $^{112}Xe^{*}$, gated on the time difference between each decay event and the preceding implantation event. The short–lived proton line appears much more strongly in the $0 - 100$ μs gated spectrum, and has virtually disappeared in the $400 - 500$ μs spectrum (after approximately five half–lives). The resolution of the proton peak in each of the time difference gated spectra is now the same as that of the alpha peaks.

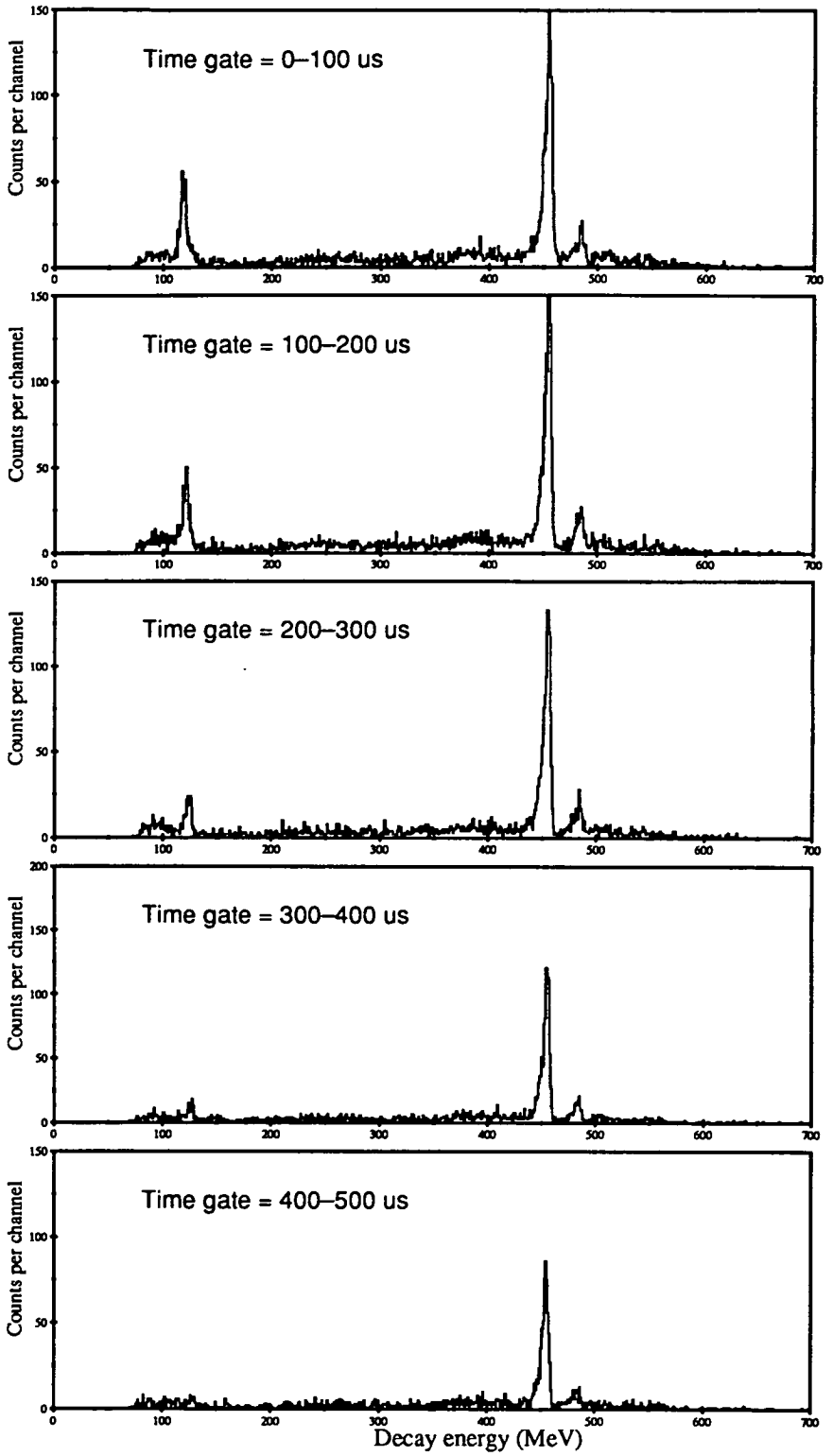

Figure 4.6: *Mass gated A=109 energy spectra of decay events from $^{112}Xe^{*}$, gated on increasing time difference between each decay event and the previous implantation event (without position correlations)*

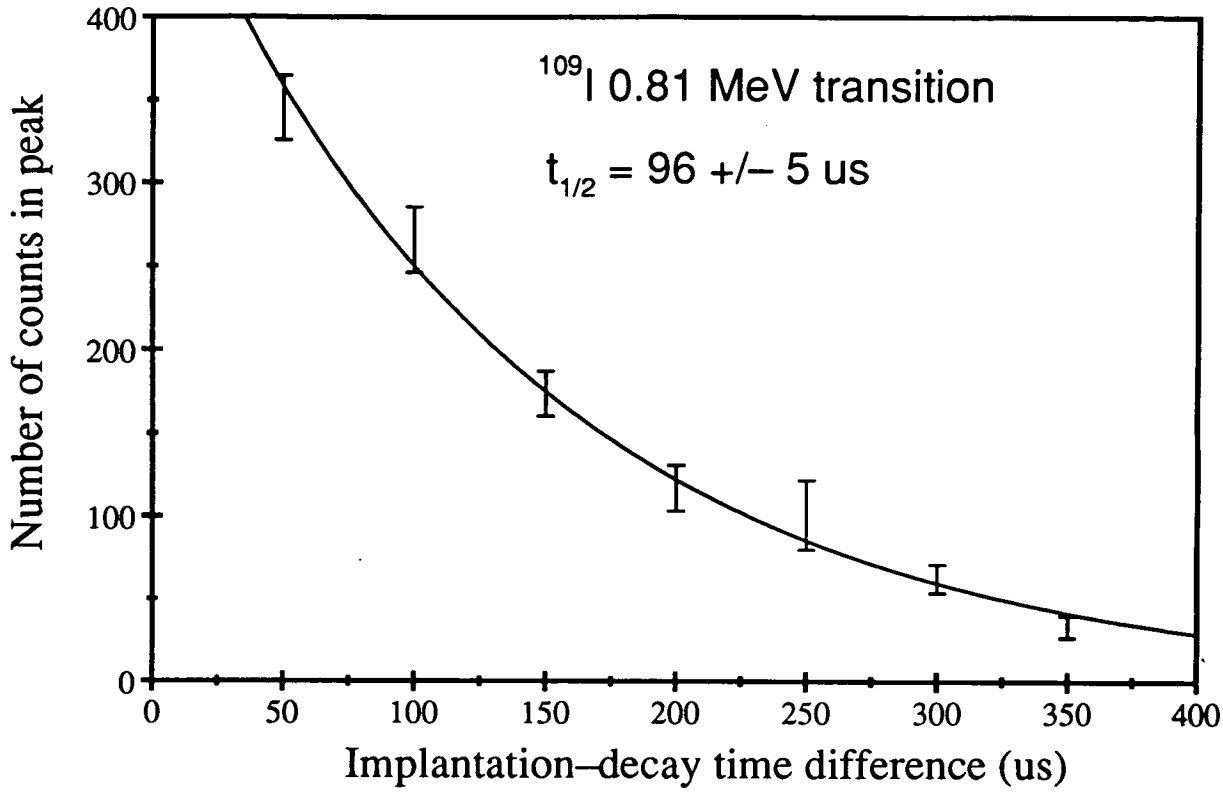

Figure 4.7: *Integrated counts of the ^{109}I proton peak after background subtraction, as a function of implantation–decay time difference. The decay curve is an exponential function fitted to the data*

The half–life of ^{109}I can be calculated from the decreasing yield of the proton peak in this sequence of time–gated spectra. Figure 4.7 shows the background–subtracted yield for the proton peak over a range of time differences from 50 μs to 450 μs. The error bars on each point include the error in estimating the background counts under the peak. The resulting least–squares exponential fit gives a half–life value of $t_{\frac{1}{2}} = 96 \pm 5$ μs which substantially improves on the accuracy of the previous value (110 ± 17 μs [Hof88]).

Figure 4.8 shows a plot of the proton peak centroid position as a function of implantation–decay time difference. This clearly shows the peak centroid with a reduced energy at short time differences. The centroid position approaches a steady value at time differences longer than approximately 350 μs. Oscilloscope

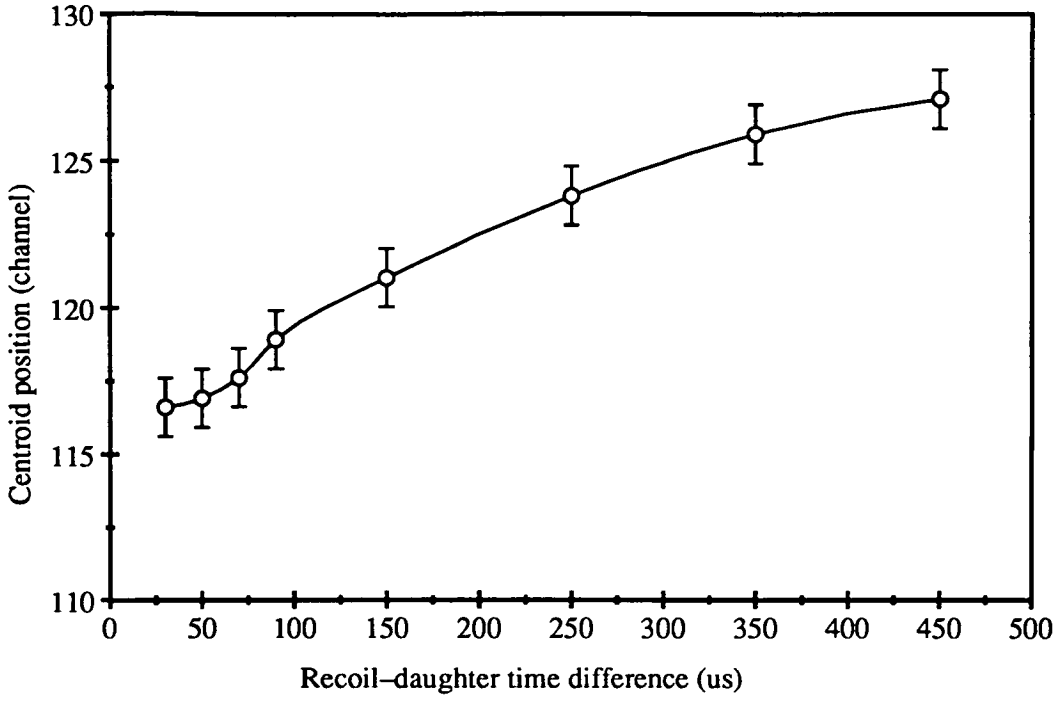

Figure 4.8: *Plot of proton peak centroid position as a function of implantation–decay time difference*

measurements taken during the experiment from saturated decay amplifier output signals showed an undershoot lasting for a corresponding time. The magnitude of the undershoot could be minimised by correct adjustment of each amplifier's pole–zero potentiometer. This lengthy procedure could not be done accurately using pulser signals, and so had to be carried out for each decay amplifier using real events at the beginning of the experiment.

Following this experiment computer simulations were carried out at the Rutherford–Appleton Laboratory [Tho90a] to model the a.c. coupling between the preamplifier and amplifier. This indicated that the magnitude of the undershoot is inversely proportional to the size of the preamplifier output coupling capacitor. Consequently each of the 96 coupling capacitors on the preamplifier board was changed from 10 μF to 100 μF prior to the main experiment. In addition the magnitude of the undershoot was found to be dependent on the size of the overloading

signal. Therefore during the main experiment degrading foils were positioned in front of the strip detector (typically 600 $\mu g\,cm^{-2}$ aluminium) which reduced the residue's energy to around 50 MeV. The combination of these two modifications reduced any undershoot effect in the main experiment to a level which was undetectable above the signal noise.

4.2.2 Correlation analysis of the decay chain $^{109}I \rightarrow {}^{108}Te \rightarrow {}^{104}Sn$

The correlated proton and alpha events from the decay of ^{109}I and ^{108}Te respectively are identified using an energy gate around the proton peak within the A=109 mass gated energy spectrum. When a decay event occurs within the proton energy gate it is stored into a one–dimensional array, which records the events' time, energy and x,y position. For each subsequent decay event a search is made in reverse chronological order through the array to locate the last parent event which occurred within the given detector pixel. A correlated sequence is established if the parent decay event lies within a specified window of parent–daughter time difference. An exponential curve is fitted to the parent–daughter time difference spectrum, which gives the daughter nucleus half–life after correcting for any background effects.

Figure 4.9 shows the resulting correlated energy spectra for the parent proton decay events from ^{109}I (upper plot) and the daughter alpha decay events from ^{108}Te (lower plot). The lower plot contains the full energy alpha peak, plus a distribution of lower energy events caused by backward emitted alpha particles escaping out of the detector. Figure 4.10 show the x,y distribution for these correlated decay events, and the corresponding horizontal (mass) projection. The projection clearly shows a symmetric mass distribution within the A=109 mass window, confirming that the ^{108}Te nuclei are produced from the proton emission of ^{109}I and are not merely leaking through from the adjacent mass region. This data

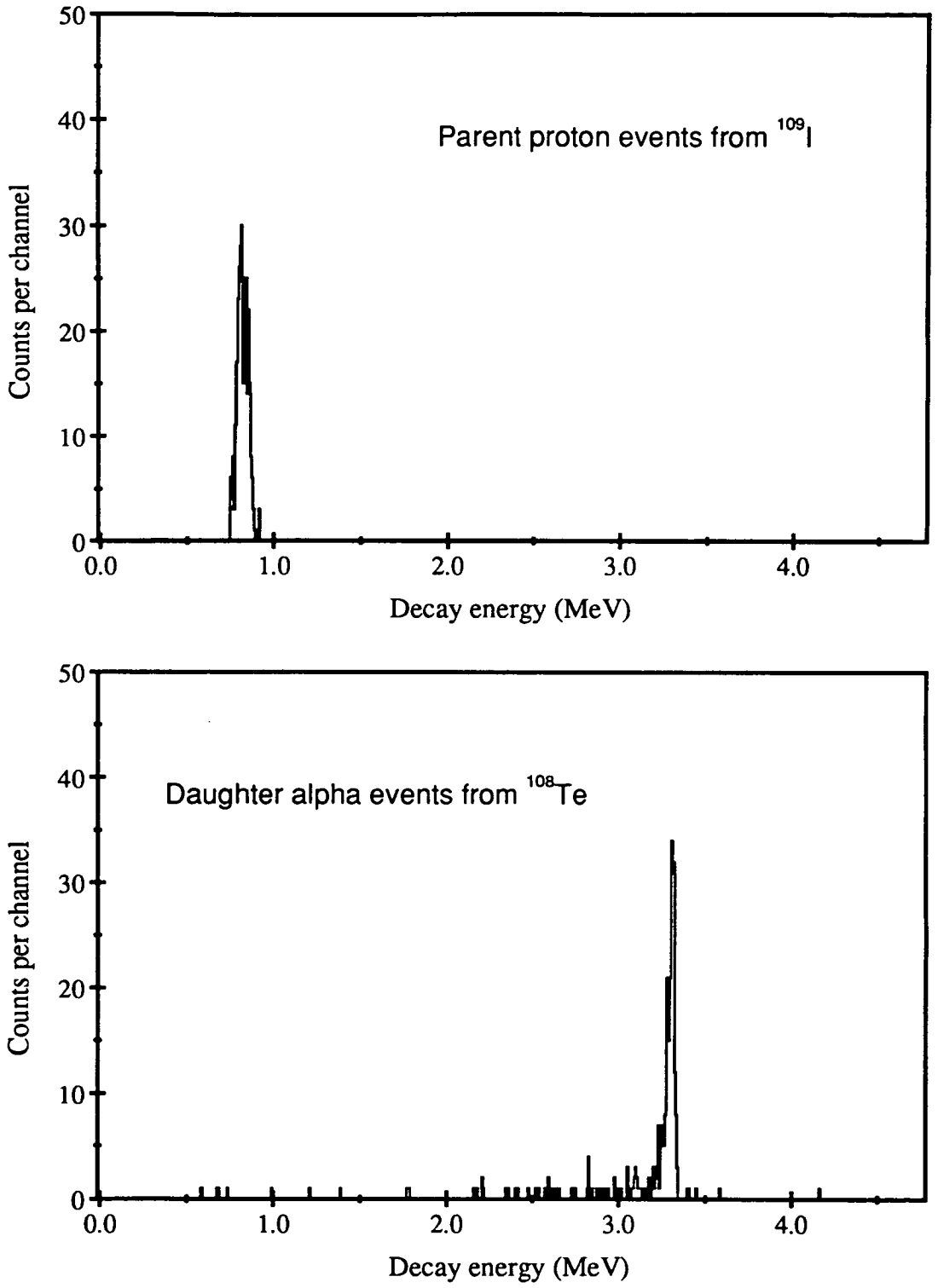

Figure 4.9: *Correlated decay events from the proton decay of* ^{109}I *(upper spectrum) and the alpha decay of* ^{108}Te *(lower spectrum)*

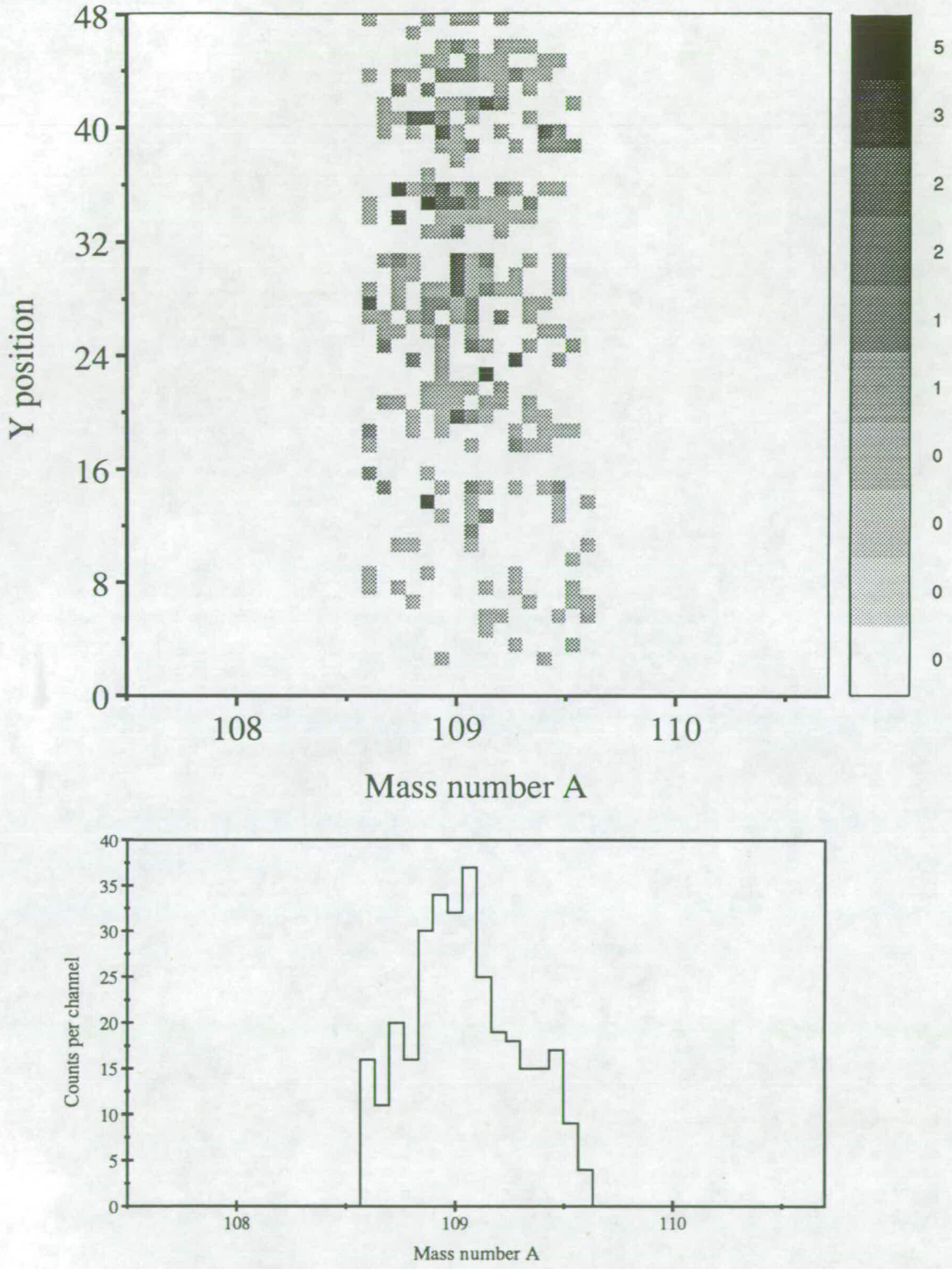

Figure 4.10: *Two–dimensional plot of x versus y position for correlated decay events from ^{109}I and ^{108}Te. The lower spectrum shows the mass distribution of the same data, which has abrupt edges imposed by the width of the mass window*

provides the first direct assignment of the 0.81 MeV proton peak to the nucleus ^{109}I.

4.2.3 The β^+–delayed proton continuum

The A=109 mass gated decay energy spectrum shows a substantial continuum of events ranging in energy from the discriminator threshold level of approximately 500 keV up to about 5 MeV. This is mainly due to β^+–delayed protons from ^{109}Te which are emitted as a competing decay mode to the alpha peak, with a ratio $\frac{b_{\beta p}}{b_\alpha} = 2.4 \pm 0.4$ [Tid85]. The energy spectrum of the β^+–delayed protons has been measured by Bogdanov *et al.* [Bog73] at the JINR cyclotron using the reaction ^{96}Ru(^{16}O,3n).

The efficiency of the strip detector for measuring this type of spectrum is a complex function of proton energy, since the range of protons in silicon varies from approximately 8 μm at 0.5 MeV to approximately 200 μm at 5 MeV. The protons are emitted isotropically from the implanted nucleus, which has an implantation depth in this data of approximately $12 - 15$ μm. Consequently a proportion of them will escape from the front face (emitted 'backwards') and only deposit a fraction of their total energy in the strip detector. Similarly for this 85 μm detector a smaller fraction will escape from the rear face (emitted 'forwards'). Forward emitted protons will be stopped in the PIPS detector, so that the total energy of these events can be reconstructed later from the sum of the strip detector and PIPS energy signals. Furthermore the PIPS signal can be used to tag these forward escaping events, allowing them to be subtracted from the strip detector energy spectrum and so suppress the background continuum.

A Monte Carlo simulation of the strip detector performance has been developed, which has been used to model the strip detector response to protons and alpha particles over a range of energies. The program allows either single peaks or predetermined energy spectra to be input, and the resulting modelled decay energy

spectra can be combined to allow comparison to the real data. The simulation tracks the path of each particle through the strip detector using an energy loss look–up table from the data of Ziegler [Zie80]. Particles which cross into an adjacent 'strip' are rejected, simulating the single multiplicity gate imposed in the analysis software. The effective boundary between adjacent strips within the volume of the silicon is modelled as an abrupt interface, without any interstrip dead region. Each effective pixel therefore consists of an active volume of silicon 335 $\times$ 335 μm with a user defined depth equal to the thickness of the detector. The nominal implantation depth of the residue is supplied from 'DEDX' codes, and a gaussian straggling function is used to model the slight variation in the final residue depth (typically $\pm$5%). This variation in implantation depth models the combined effects of heavy ion straggling in the silicon, and the variation in residue energy due to beam energy fluctuations and target straggling.

Figure 4.11 shows the results from the Monte Carlo modelling of the ^{109}Te β^+–delayed proton spectrum from Bogdanov *et al.* [Bog73]. The top plot simulates a hypothetical 500 μm thick strip detector where the residues are implanted at a depth of 250 μm. With this thickness of silicon the protons would be stopped within the detector, and the simulation calculates that 75% of the events are contained within a single pixel. The dark shaded 'picket fence' pattern of this spectrum is due to the finite step size within the Monte Carlo, which causes rounding approximations in the calculated deposition energy of particles with a long path length. The remaining two spectra in figure 4.11 show the same simulation but for an 85 μm thick strip detector with a nominal implantation depth of 16 μm. The middle spectrum shows the resulting strip detector energy spectrum, which contains a large tail at low energy ($\lesssim$ 0.7 MeV) due to backward emitted protons emerging from the front face of the detector. The lower plot shows the strip detector energy spectrum gated in coincidence with PIPS events, which identifies forward emitted protons as the main source of continuum events over the region from 1.0 MeV to around 2.0 MeV. For energies greater than $\simeq$ 2 MeV

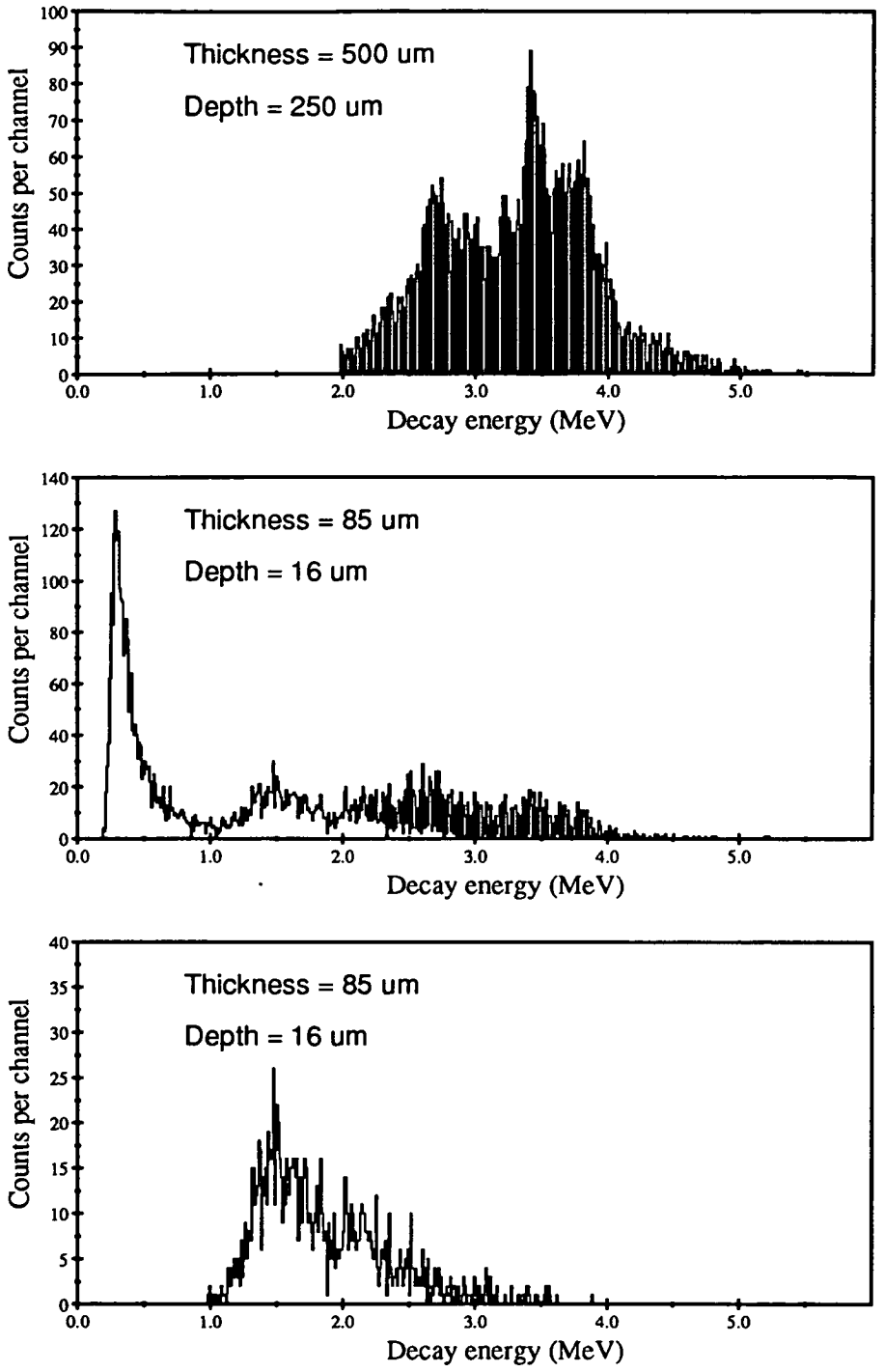

Figure 4.11: *Monte Carlo simulation of the strip detector response to the β^+-delayed proton spectrum of ^{109}Te. The upper plot simulates a thick detector which stops all the proton events, whilst the middle plot shows the energy spectrum from an 85 μm strip detector. The lower plot shows the same spectrum gated in coincidence with signals from the PIPS detector*

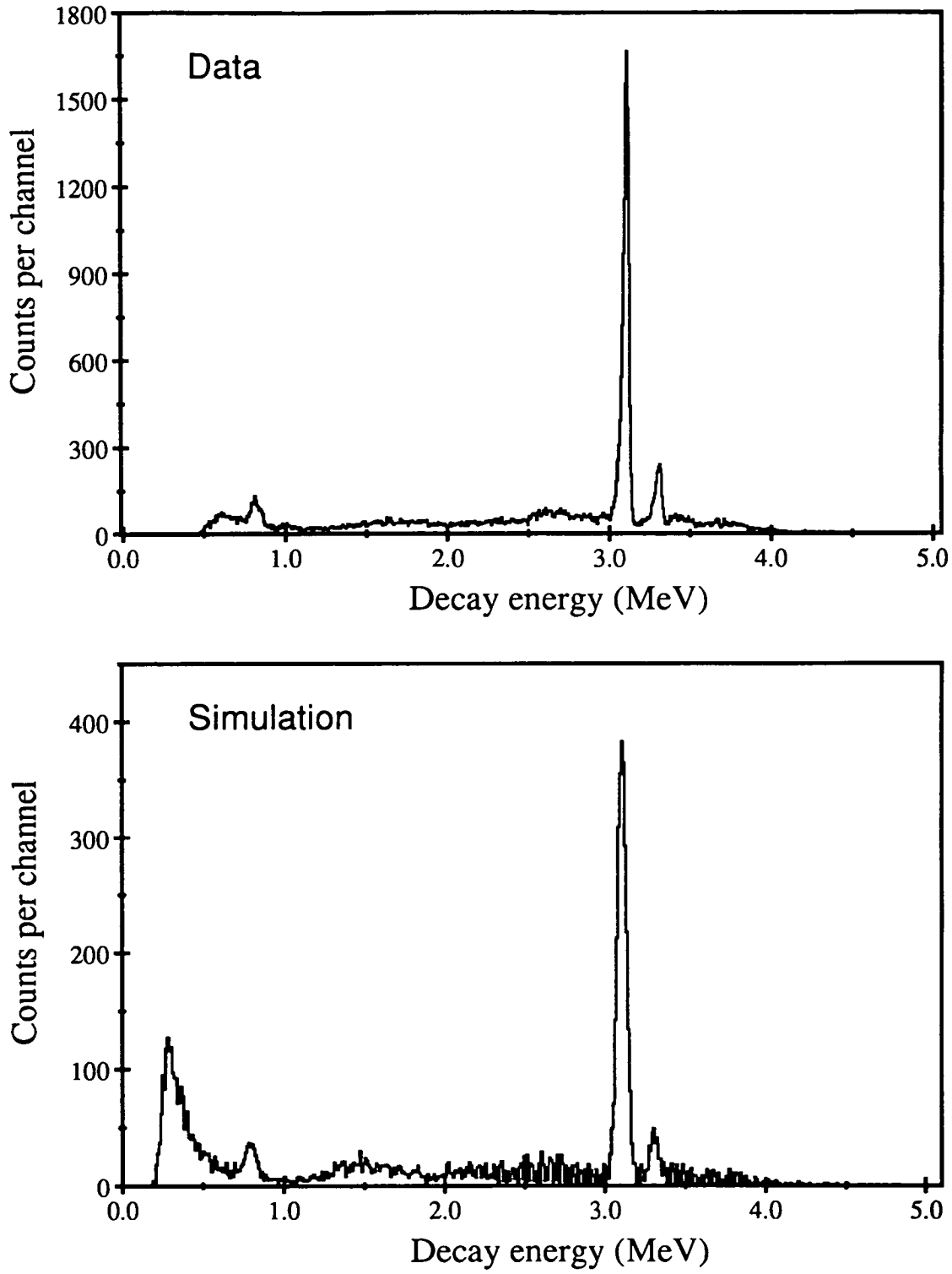

Figure 4.12: *Comparison between the A=109 mass gated decay energy spectrum (upper plot) and the Monte Carlo simulation (lower plot). The low energy escape peak in the simulation is below the discriminator threshold ($\simeq$ 0.5 MeV), and so does not appear in the data spectrum*

the continuum is increasingly caused by proton events stopped within the strip detector.

The Monte Carlo simulation was used to model the complete A=109 mass gated decay energy spectrum, with the result shown in figure 4.12. The simulation used the three discrete peaks in the same relative yields as recorded in the data spectrum. The magnitude of the β^+-delayed proton continuum was scaled from the area of the ^{109}Te alpha peak using the ratio $\frac{b_{\beta p}}{b_\alpha}$. The energy resolution of the simulated peaks was also taken from the data, which in this case was approximately 70 keV FWHM for both the alpha and the proton peaks. The simulated implantation depth was 16 μm, which was greater than the range in silicon of either 0.81 MeV protons (13 μm) or 3.31 MeV alpha particles (15 μm). Consequently there were no escape events from the discrete lines, and no additional contribution to the continuum. It can be seen that the simulated spectrum accurately reproduces the various features of the experimental data.

The use of the strip detector to provide a ΔE signal for long range particles enables particle identification between protons and positrons to be made for those events reaching the PIPS detector. Figure 4.13 shows a two dimensional plot of decay energy from the PIPS detector versus decay energy from the strip detector. The separation between protons and positrons can be clearly seen from the data, with the higher energy protons towards the top of the spectrum depositing less energy in the strip detector than the lower energy protons. The positrons deposit typically $\lesssim$ 1.5 MeV in the strip detector, and an approximately equal amount in the PIPS detector.

The continuum under the ^{109}I proton peak can therefore be identified as a combination of backward emitted protons and forward emitted positrons. By gating this spectrum in anticoincidence with the PIPS energy signal, the part of the continuum due to forward emitted particles can be largely removed. This is illustrated in figure 4.14 which shows the A=109 decay energy spectrum from the strip

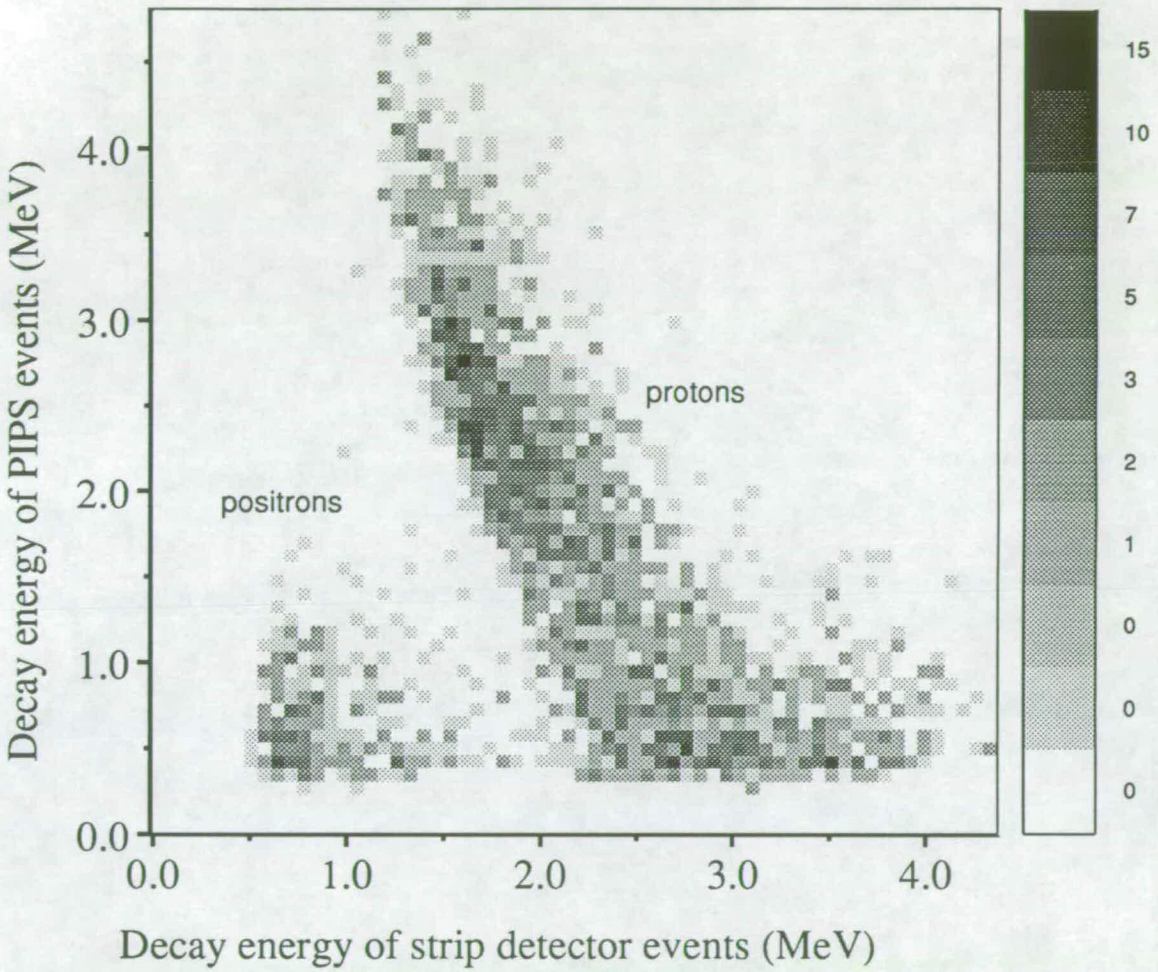

Figure 4.13: *Plot showing PIPS energy versus strip detector energy for those decay events from $^{112}Xe^{*}$ which produce signals in both detectors. The separation between protons and positrons can be clearly seen*

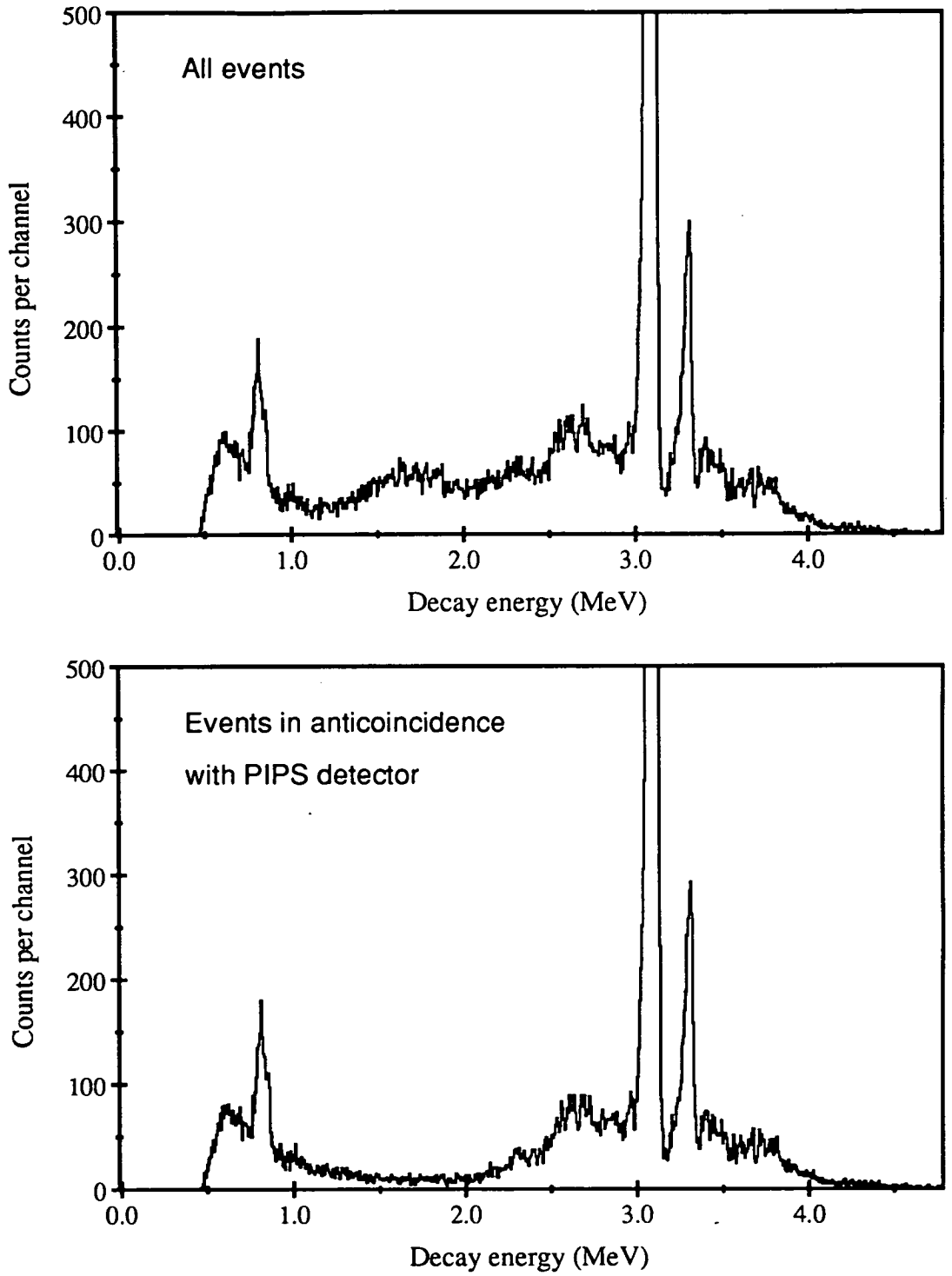

Figure 4.14: *Energy spectra of A=109 mass gated decay events from* $^{112}Xe^{*}$ *recorded in the strip detector, before and after subtraction of events coincident with events in the PIPS detector. The subtracted spectrum shows a substantially reduced event continuum between 1.0 and 2.5 MeV*

detector before and after removal of the PIPS–coincident events. This technique can be used to reduce background events in the strip detector energy spectrum, and so enhance low energy weak proton lines.

4.3 Performance of the double–sided strip detector

4.3.1 Strip multiplicity

The double–sided strip detector provides two energy signals for each event, derived from the strips from each of the front and rear faces. In general the energy signal from each face is generated in software by summing the energy signals from each valid strip on that face. Usually a single strip multiplicity condition is required for each face, and the energy signal is merely that of the single valid strip.

High multiplicity events in the strip detector could be caused either by inter–strip charge sharing effects or from particles tracking through two or more strips. In the reaction studied only positrons and high energy protons have sufficient range in silicon to produce a significant proportion of two strip events. This fraction has been calculated as $< 12\%$ of the total events for a typical A=109 decay energy spectrum (eg. figure 4.2) using the Monte Carlo simulation described in section 4.2.3. Over 90% of these multi–strip events originate from the β^+–delayed protons. Table 4.1 lists the actual strip multiplicities for implantation and decay events measured for each of the strip detector faces. It can be seen that $\simeq 85\%$ of decay events produce a signal in only one strip per face. The zero multiplicity 'implantation events' are due to pickup in the energy signals from the mixer boards which cause false recoil triggers. If these signals are discarded, the proportion of single multiplicity recoil events rises to approximately 96% of the total. As the range of the heavy ions in silicon is only $\lesssim 15$ μm at 100 MeV, this proportion of

high multiplicity events reflects the fraction of events affected by charge sharing between adjacent strips.

Strip multiplicity (recoils)	Front face events	Rear face events
0	16%	17%
1	83%	79%
2	1%	3%
3	0	1%
Strip multiplicity (decays)	**Front face events**	**Rear face events**
0	0	0
1	89%	83%
2	7%	12%
3	3%	3%
4	1%	1%

Table 4.1: *Typical strip multiplicities for implantation and decay events from each face of the strip detector*

4.3.2 Energy signals and resolution

To derive an energy signal from each face of the strip detector, each of the 48 strips from the detector face are gain matched relative to themselves within software. This corrects for the variations in the fixed gain of each set of preamplifier, amplifier and ADC. Relative gain matching is achieved by first calculating a gain and offset value for each strip channel using a pulser 'walk through' spectrum and a charge terminator peak, then scaling each channel gain to a common value. The energy resolution of peaks after gain matching can be as low as 15 keV FWHM for a new detector, caused mainly by the combined electronic noise from the detector, cables and amplifiers. The data taken during the commissioning experiment followed a lengthy setting up period, during which time the detector took beam for

a period of approximately 36 hours. The energy resolution of the early recorded data is therefore approximately 35 keV FWHM. The energy resolution obtained during the main experiment was $\lesssim$ 20 keV FWHM.

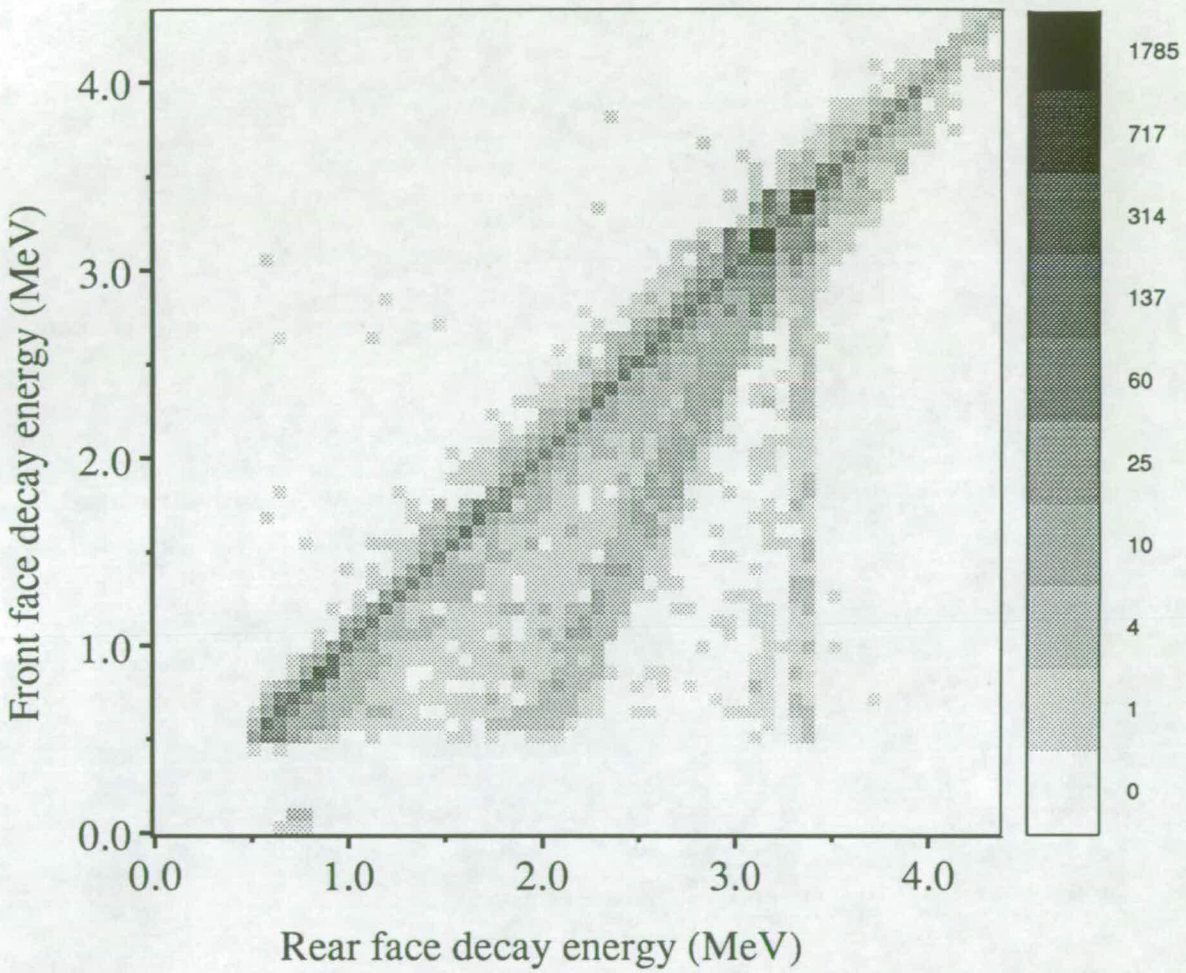

Figure 4.15: *Two dimensional plot of front face decay energy versus rear face decay energy. The 'equal energy' events form a strong central diagonal ridge, and clearly show the two intense alpha peaks from* ^{108}Te *and* ^{109}Te

A significant improvement in the energy resolution can be subsequently achieved in software by deriving the decay energy signal from the calculated mean of the two energy signals from each face. The front and rear face signals are first gain matched relative to each other, so that a two dimensional plot of front face energy versus rear face energy gives a 45° line through the origin. This is shown in

figure 4.15, where the central diagonal ridge contains > 90% of the total events, and represents those with equal front and rear face energy signals. The data is projected through an 'equal energy' gate on the $y = -x$ axis, which requires that the front and rear energies are equal to within ± 10 keV. The mean of the two energy signals is then calculated, and the resulting decay energy spectrum shows an improvement in the alpha peak FWHM energy resolution of $8 - 12\%$ compared to each of the individual faces' energy signals. This indicates some degree of correlation between the noise in the two signals, due to the component of noise which originates from within the detector.

Figure 4.16 shows two dimensional plots of front face decay energy versus rear face decay energy, before and after imposing a single strip multiplicity condition. The upper plot shows all decay events from $^{112}Xe^*$, with the two tellurium alpha decay peaks clearly visible in the central diagonal band of events. For decay events the single multiplicity gate substantially reduces the off-diagonal event background, particularly the grid–like structure to the left–hand side of the upper spectrum, which is due to detector pickup. A noticeable feature in this data is the steep diagonal line which drops down from the strong alpha peaks. The intensity of this region is not reduced by the single strip condition, and represents events with a reduced energy from both front and rear face signals. However these events represent less than 7% of the yield of the full energy alpha peaks, and are rejected by the equal energy gate. Yorkston *et al.* [Yor87] propose a charge trapping mechanism which causes reduced charge collection for those particles depositing energy close to the front face inter–strip region. The resulting deficit in the charge collected at the front face is half of that in the charge collected at the rear face, which would account for the observed line in these spectra.

Figure 4.17 shows the equivalent spectra for implantation events. The upper spectrum shows all events, whilst the lower spectrum shows single multiplicity events only. The central diagonal band contains the majority of events, and has a large width due to the poor energy resolution of the mixer board energy signals.

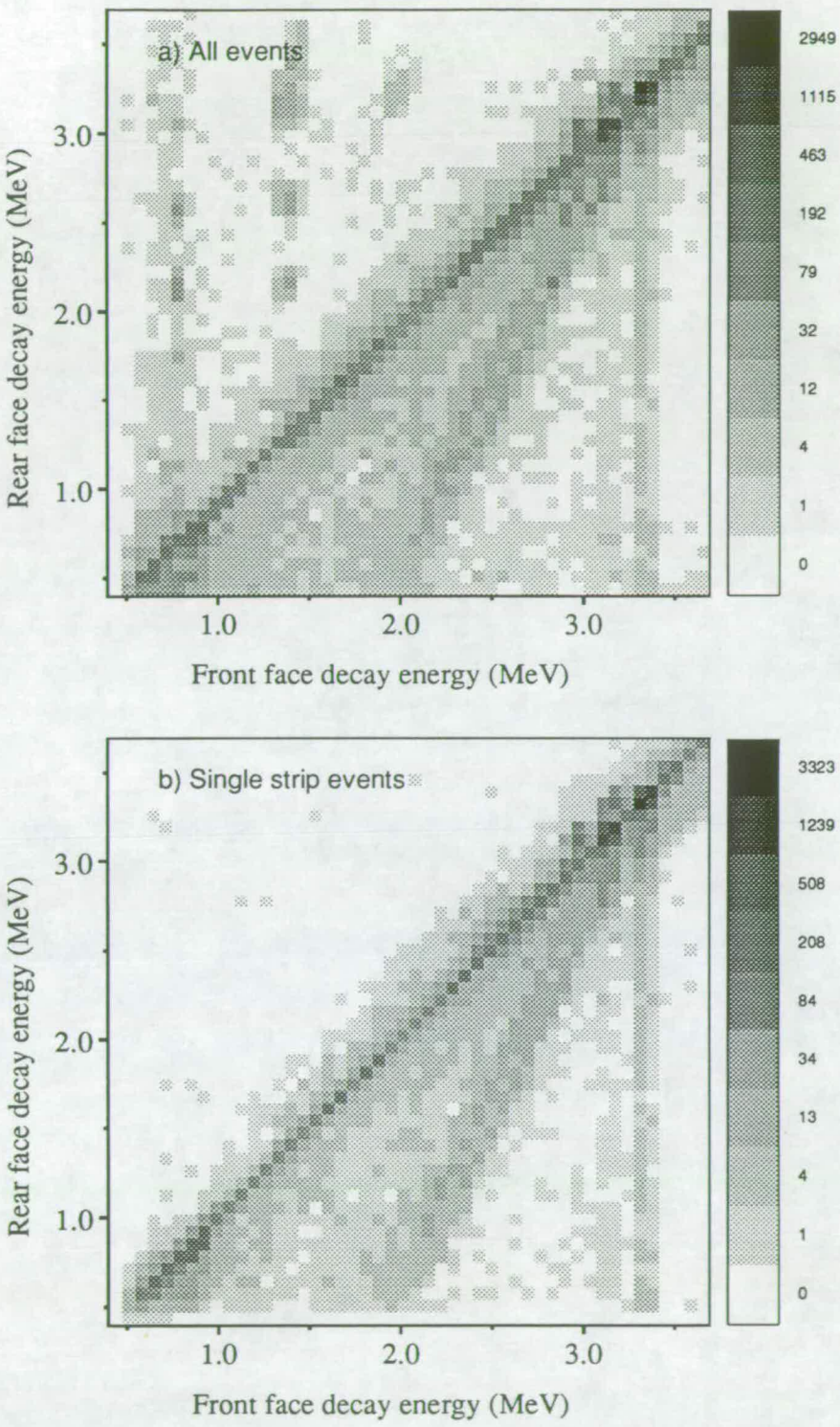

Figure 4.16: *Plots showing front face energy against rear face energy for decay events. Spectrum (a) shows all decay events whilst spectrum (b) only contains decay events with a single strip multiplicity from both each faces*

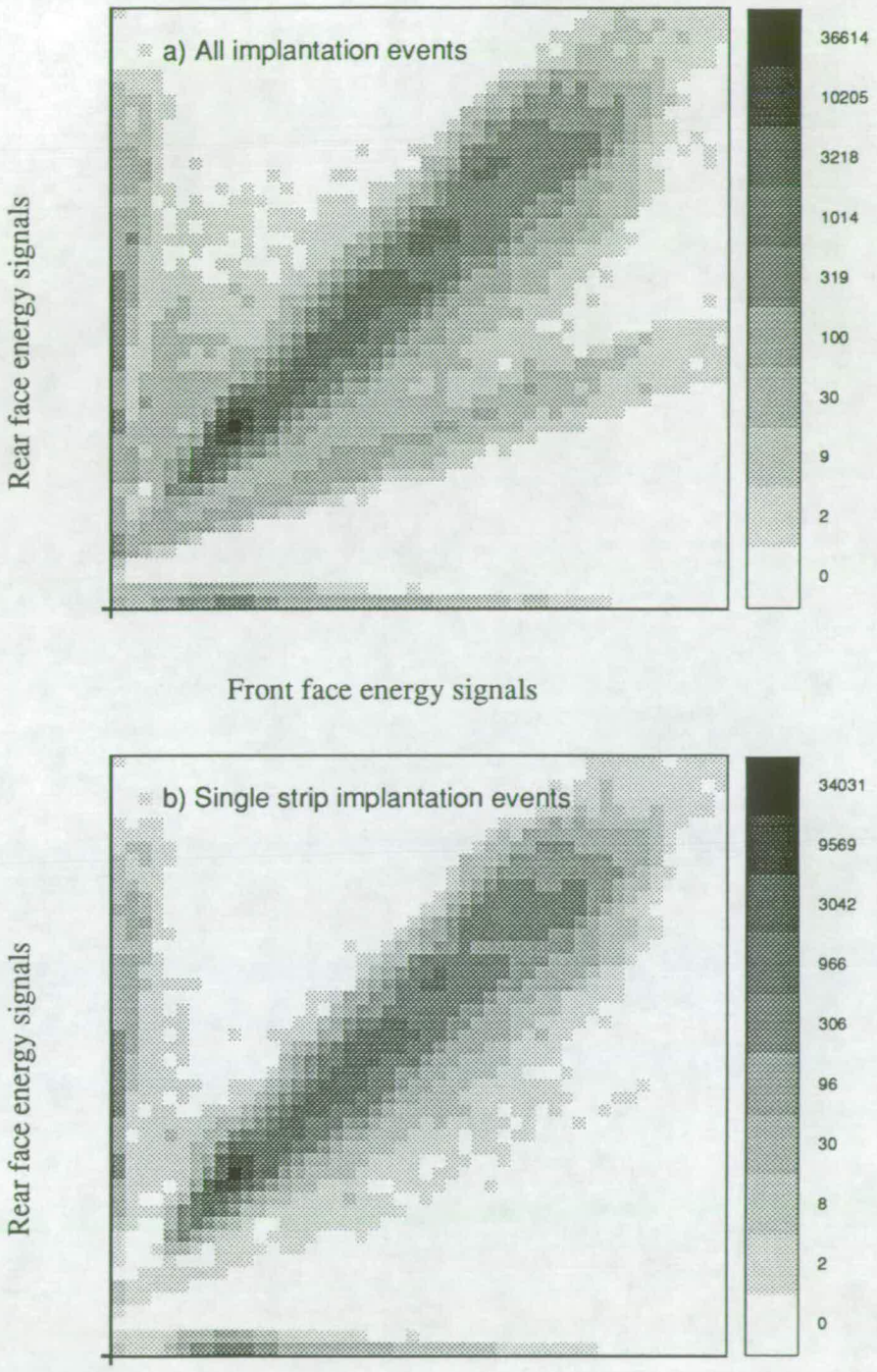

Figure 4.17: *Plots showing front face energy against rear face energy for implantation events. Spectrum (a) shows all events whilst spectrum (b) only contains events with a single strip multiplicity*

The ungated spectrum also shows a less steep diagonal band which contains events with a reduced rear face energy. These events are most likely caused by charge sharing between the rear strips, and the number of these events is reduced by applying the single multiplicity condition from approximately 7000 (1% of the total implantation events) to approximately 700.

4.3.3 Radiation damage effects

During the commissioning experiment the first strip detector was replaced after receiving a total dose of 1.1×10^8 implantation events. At this stage the detector had become sufficiently damaged that the ^{108}Te and ^{109}Te alpha decay peaks were noticeably skew. Figure 4.18 shows the decay energy spectra (a) through to (f) for this data accumulated during each successive run file during the lifetime of the detector. The alpha resolution degrades from approximately 35 keV FWHM after 2.3×10^7 implantation events (21% of the detector total dose) to approximately 70 keV FWHM after 9.1×10^7 events (81% of the total) corresponding to a local dose of approximately 6.1×10^7 heavy ions cm^{-2}. Since the total dose varies in different regions of the detector, radiation damage tends to be localised in those strips which receive the highest beam rate. After the run corresponding to spectrum (f) in figure 4.18, the recoil separator was adjusted to move the mass groups over by half a mass unit. This moved the centroids of the mass distributions onto less damaged regions of the detector and extended the detector lifetime.

Figure 4.19 shows a plot of leakage current against detector dose over the same time period. The graph also shows the average beam rate in arbitrary units. At a total dose of nearly 3×10^6 events the beam rate was increased and the implantation rate rose from approximately 6 events cm^{-2}s^{-1} to 28 events cm^{-2}s^{-1}. This corresponded to the end of the setting up period and the start of data taking to tape, and the resulting increase in gradient of the leakage current function can be clearly seen. The total dose received by this strip detector (1.1×10^8 events)

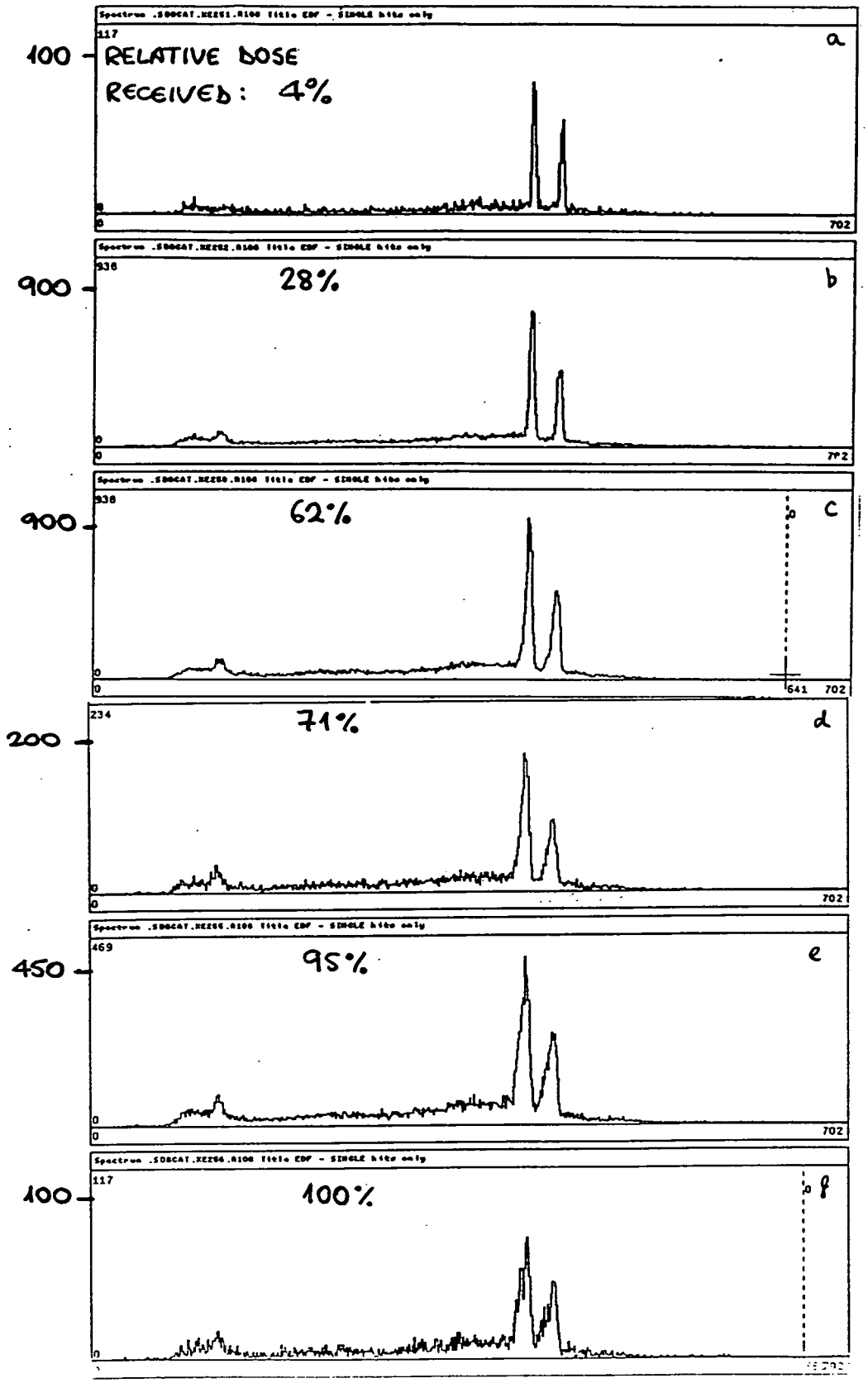

Figure 4.18: *Energy spectra showing decay events from $^{112}Xe^{*}$ during the lifetime of the detector*

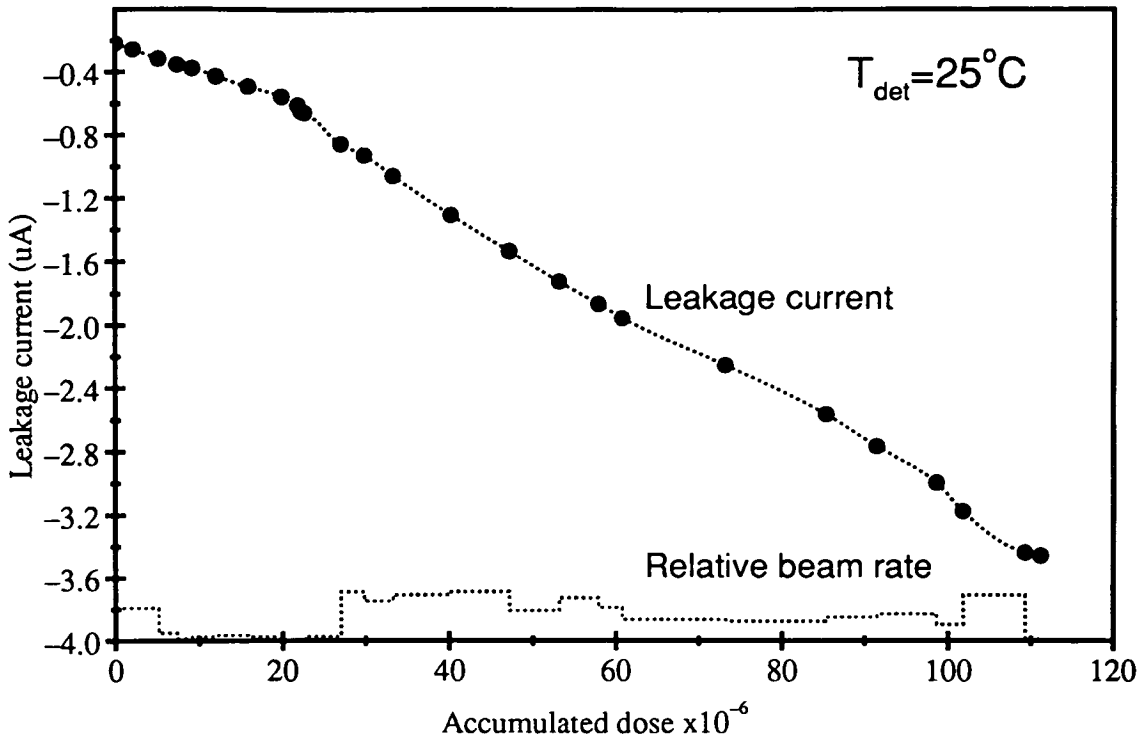

Figure 4.19: *Plot of leakage current against total dose for the first strip detector used in the commissioning experiment. Also shown is the average beam rate in arbitrary units*

was greater than for subsequent devices, with the second detector used in this experiment receiving a total of 4.9×10^7 implantation events.

During the main experiment the strip detector and mount was cooled to approximately 0°C in order to minimise the leakage current. Figure 4.20 shows the leakage current plotted as a function of detector temperature, which shows a reduction in current of approximately 40% for a drop in temperature from 19°C to 10°C. The PIPS detector had a minimum operating temperature of 0°C which prevented the detector mount from being cooled below zero.

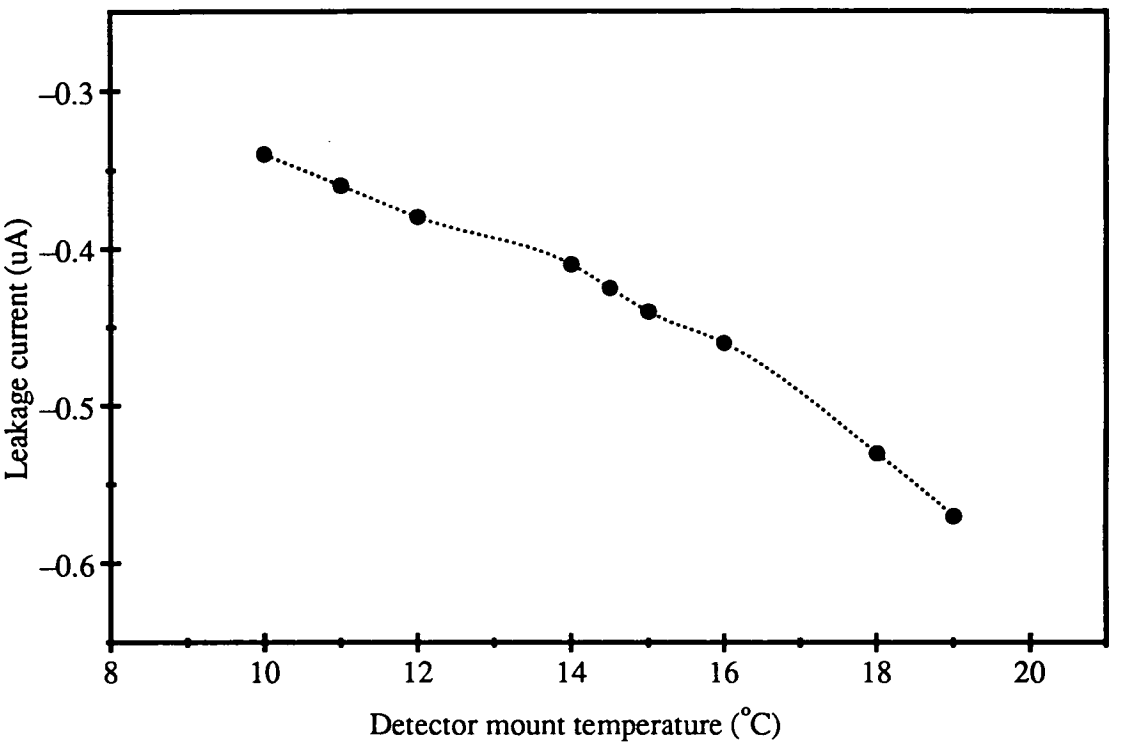

Figure 4.20: *Plot of strip detector leakage current against temperature*

Chapter 5

Proton radioactivity measurements around ^{147}Tm and ^{151}Lu

5.1 Experimental details

In April 1991 the main experiment for this work was carried out, which investigated proton radioactivity from around ^{147}Tm and ^{151}Lu. Two consecutive runs were performed on the Daresbury recoil separator over a period of 72 hours, using the reactions ^{58}Ni + ^{92}Mo $\rightarrow$ ^{150}Yb* and ^{58}Ni + ^{96}Ru $\rightarrow$ ^{154}Hf*. For the first reaction 500 μg cm^{-2} thick self-supporting foils of isotopically enriched ^{92}Mo were irradiated with a beam of ^{58}Ni ions. This produced the compound nucleus ^{150}Yb* with a mean excitation energy of 50 MeV, designed to maximise the yield of ^{147}Tm produced via the p2n evaporation channel.

The second reaction used 400 μg cm^{-2} thick foils of isotopically enriched ^{96}Ru mounted on 700 μg cm^{-2} thick aluminium, which were irradiated with a beam of ^{58}Ni ions. The reaction was carried out in two parts using beam energies

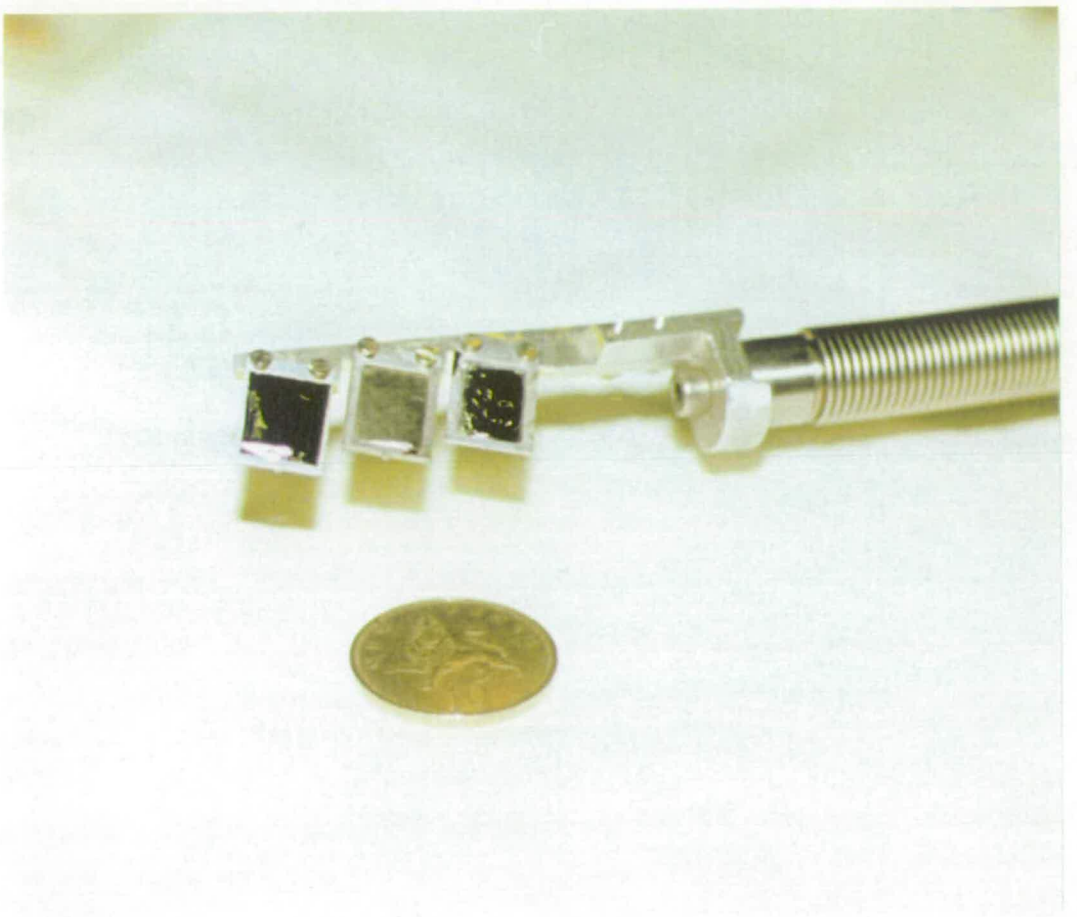

Figure 5.1: *Photograph of three ^{96}Ru targets mounted on the recoil separator target ladder*

of 300 MeV amd 311 MeV, and producing the compound nucleus $^{154}Hf^*$ with mean excitation energies of 61 MeV and 69 MeV respectively. The two excitation energies covered the range of excitation energies used by Hofmann for this reaction at GSI. This range of excitation energies was designed to maximise the production of ^{150}Lu, produced via the p3n channel. The ^{96}Ru targets were mounted onto the target ladder with the aluminium 'backing' facing the beam (see figure 5.1). In this way the evaporation residues did not suffer additional scattering from the aluminium backing, so maximising their acceptance by the recoil separator. Other ^{96}Ru targets were tried with backings of molybdenum and gold, but they were too fragile to take beam for more than a few minutes.

In the first reaction the recoil separator was set to position A=147 evaporation residues onto the centre of the detector, with charge state $Q = 27^+$. The beam rate was maintained at approximately 80 enA (4.4 pnA) over a total period of 36 hours, with average implantation and decay event rates of 700 Hz and 450 Hz respectively. In the second reaction the recoil separator was adjusted to position A=150 residues onto the centre of the detector, with charge state $Q = 29^+$. Data was taken over a period of 24 hours with a beam energy of 300 MeV, followed by a further 8 hours with a beam energy of 311 MeV. A beam current of 80 enA was maintained, with implantation and decay event rates of approximately 1.5 kHz and 500 Hz respectively.

Two detectors were used for the experiment, with the changeover occurring at the end of the $^{58}Ni + {}^{92}Mo \rightarrow {}^{150}Yb^*$ reaction. Both detectors were virtually identical to those used during the commissioning run. containing 48 strips per face amd an active area of approximately 16 mm $\times$ 16 mm. The first detector (serial number MSL 556-1) contained a 65 μm thick wafer, and the second (MSL 556-7) contained a 67 μm thick wafer. Both detectors suffered considerably less radiation damage than those used in the commissioning run, due to these reactions producing a substantially reduced flux of evaporation residues transmitted by the recoil separator.

5.2 Results

5.2.1 Proton emission observed from ^{147}Tm

The decay energy spectrum produced from the compound nucleus ^{150}Yb* is shown in figure 5.2. The spectrum clearly shows the proton peak from the decay of ^{147}Tm, at an energy of 1.05 MeV. An additional weaker proton peak can also be seen at an energy of 1.11 MeV. The two proton peaks are clearly resolved, with an energy resolution of approximately 25 keV FWHM. A number of strong alpha peaks also occur within a range of energies from 3.9–5.3 MeV. The majority of these originate from nuclei with mass numbers in the range A=150–154, which are produced from contaminant ^{94}Mo in the target.

Figure 5.3 shows the decay energy plotted against the mass of the implanted ion ($Q = 27^+$), and shows a low energy line at about 1.0 MeV in the A=147 mass group. This line contains the two proton peaks from ^{147}Tm, which are not resolved in this spectrum. A number of alpha lines are also visible at higher energies, which mostly reach the separator focal plane as charge state ambiguities ($Q = 28^+$). The resulting mass distribution for these residues is displaced from the main $Q = 27^+$ distribution by about half a mass unit.

Figure 5.4 shows the A=147 mass gated decay energy spectrum for this data. The mass gate also accepts some alpha events from ^{152}Er, ^{153}Er and ^{153}Tm, emitted from $Q = 28^+$ residues. In addition the spectrum contains the alpha peak from ^{149}Tb, which has a 4.1 hour half-life and was implanted into the detector in a preceding experiment. The continuum of events ranging from $\simeq$ 0.5 MeV up to $\geq$ 5 MeV is mainly due to backward emitted alpha particles escaping from the front face of the strip detector. Alpha particles with energies between 4.0 MeV and 5.5 MeV have ranges in silicon of between 20 μm and 30 μm. As degrading foils were used in this reaction the average implantation depth is only $6 - 8$ μm, deduced by comparison with Monte–Carlo simulations. A small contribution to

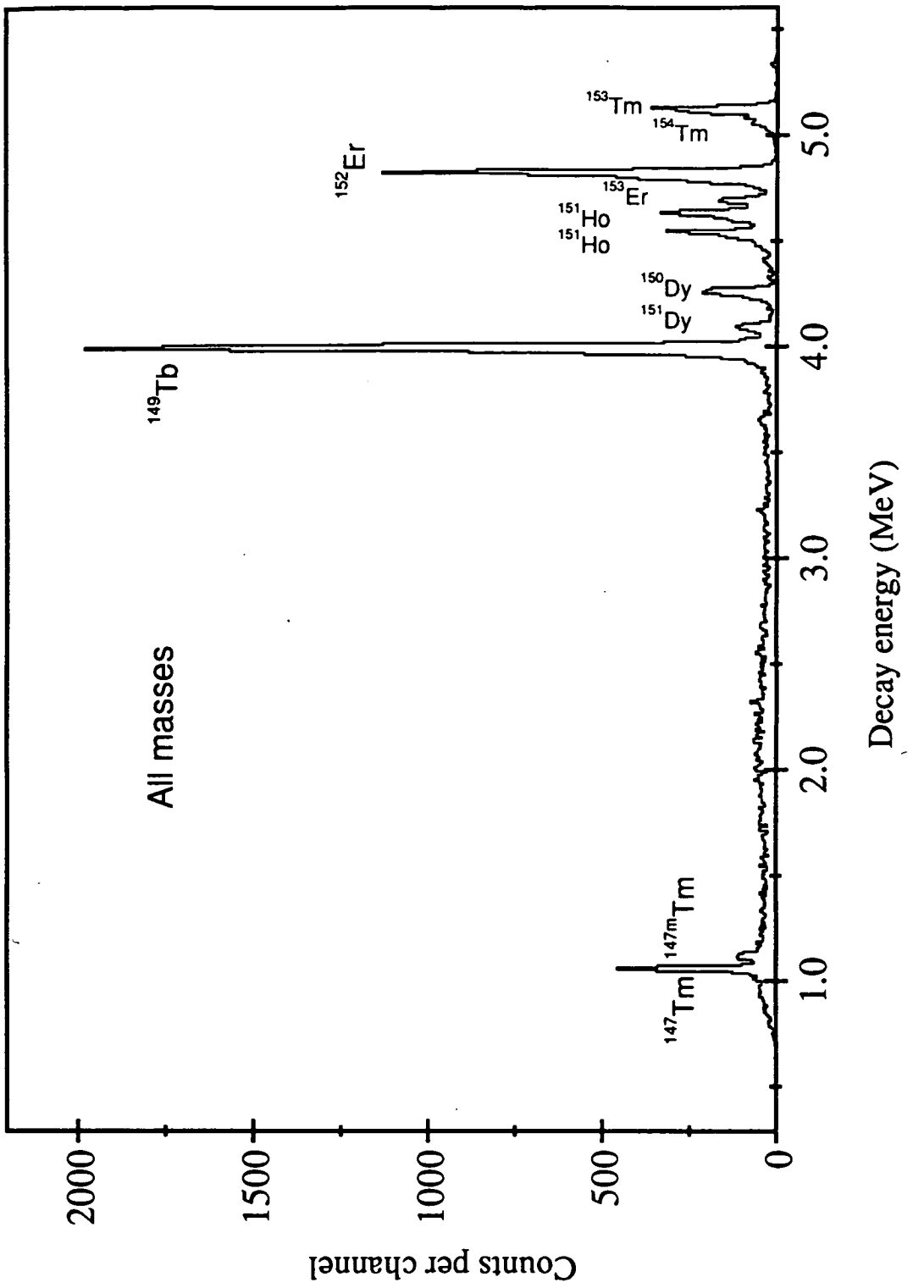

Figure 5.2: *Decay energy spectrum for all events from $^{150}Yb^{*}$. The two proton transitions from ^{147}Tm are clearly visible at energies just above 1.0 MeV, and a variety of alpha lines are present at higher energies*

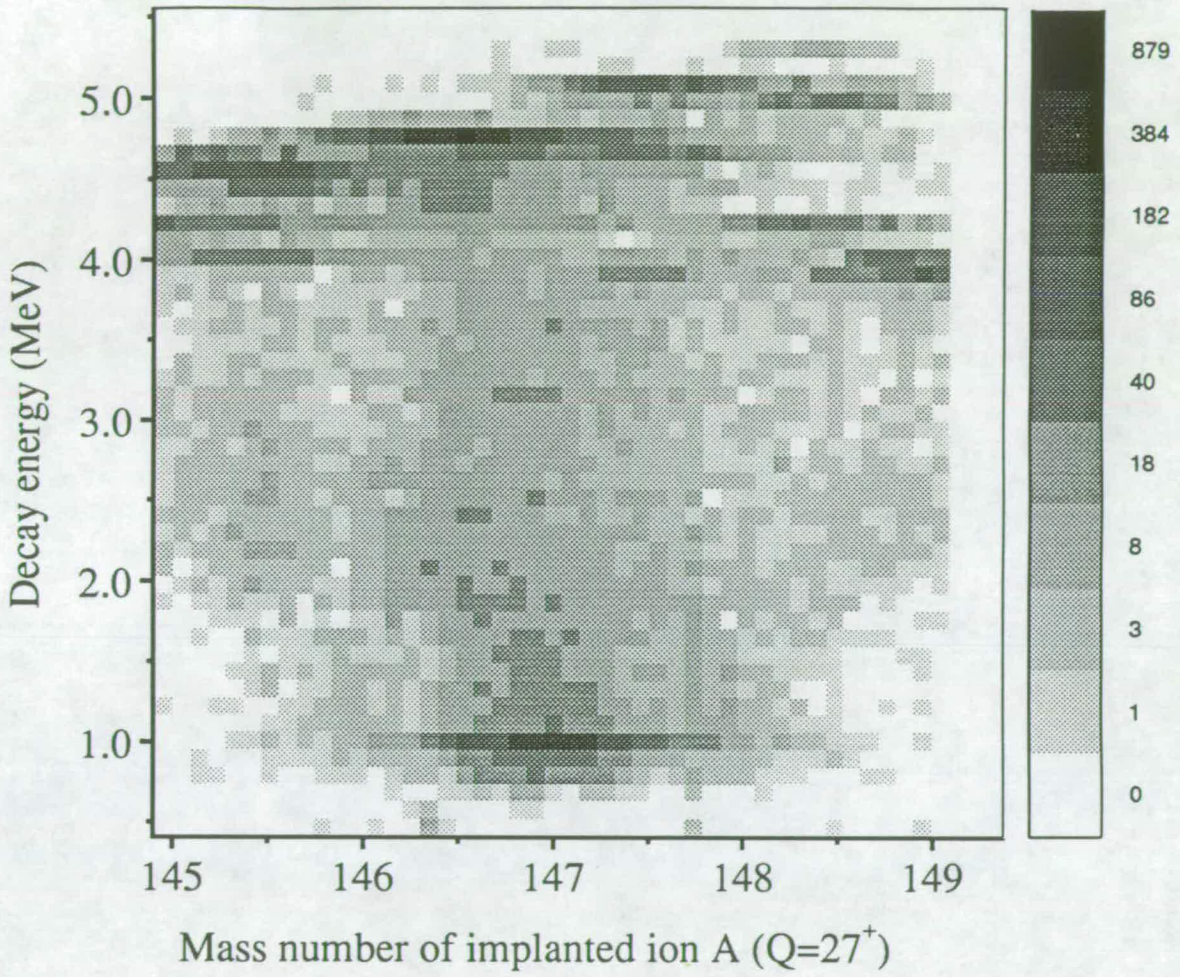

Figure 5.3: *Plot of decay energy versus mass number of the implanted ion, for events from $^{150}Yb^{*}$. The two proton transitions are contained within the low energy line in mass group A=147*

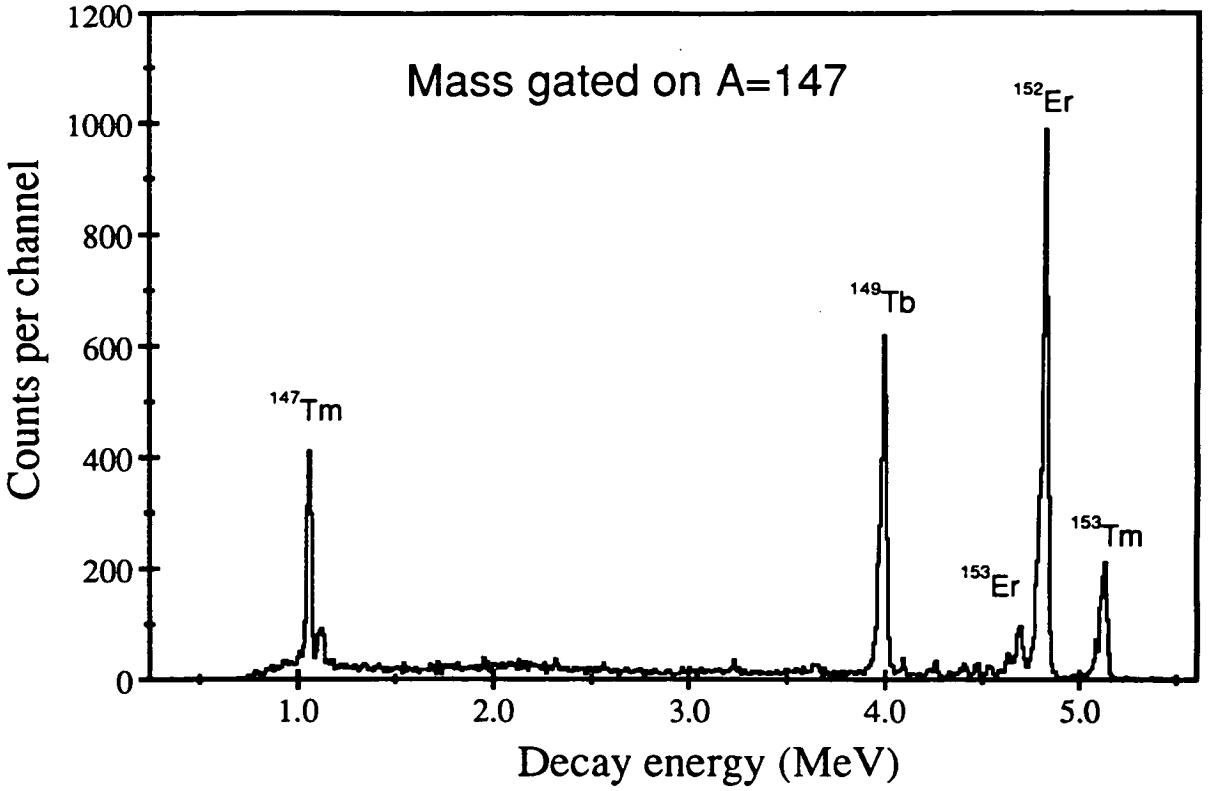

Figure 5.4: *Mass gated A=147 decay energy spectrum for events from $^{150}Yb^{*}$. This identifies both proton peaks as originating from A=147 nuclei. The mass gate also partly accepts events from A=152,153 ($Q= 28^{+}$) nuclei and the contaminant alpha peak from ^{149}Tb.*

the continuum is due to the β^{+}–delayed proton spectrum of ^{149}Er [Fir89], produced via the β^{+}–decay of ^{149}Tm ($t_{\frac{1}{2}} = 0.9 \pm 0.2$ s [Tot87]).

The two proton peaks are both visible in the A=147 mass gated spectrum of figure 5.4. As was discussed in section 2.4.2, the only A=147 nucleus with a calculated positive Q_p value is ^{147}Tm, which is produced from ^{150}Yb* via the p2n channel. This data therefore confirms the assignment of the 1.05 MeV proton transition to the ground state decay of ^{147}Tm, and is only the second direct mass identification of this decay. The spectrum also provides the first unambiguous assignment of the 1.11 MeV proton peak to the decay of an A=147 nucleus. This transition is therefore identified as proton emission from a low-lying excited state

in ^{147}Tm.

Nucleus	^{147m}Tm	^{150}Lu	(^{147}Tm)
E_{det} [a]	1110.6 ± 3.8	1261.1 ± 3.8	947.4 ± 5.0
ER [b]	7.7	8.5	6.6
ER - ΔER [c]	1.5 ± 0.8	1.7 ± 0.9	1.3 ± 0.7
ΔE_p [d]	1.5	1.6	1.3
E_{sc} [e]	13.1	13.7	13.1
E_p [f]	1110.6 ± 3.9	1261.0 ± 3.9	947.4 ± 5.0
Q_p [g]	1118.3 ± 3.9	1269.5 ± 3.9	954.0 ± 5.0
$Q_{p,nuc}$ [h]	1131.4 ± 3.9	1283.2 ± 3.9	967.1 ± 5.0

Note: All energies are in keV

[a] Energy of peak centroid

[b] Energy of recoil nucleus

[c] ΔER energy deficit of recoil nucleus in silicon [Hof88]

[d] Energy deficit of proton in silicon [Pai81]

[e] Energy of proton screening correction [Hof88]

[f] $E_p = E_{det}$ - (ER - ΔER) + ΔE_p

[g] $Q_p = E_p$ + ER

[h] $Q_{p,nuc} = Q_p + E_{sc}$

Table 5.1: *Summary of measured proton decay energies from ^{147m}Tm and ^{150}Lu. Tentative assignments are in brackets*

The energy of the proton peak from the excited state transition was measured from this data, using the ^{151,151m}Ho alpha peaks and the ground state ^{147}Tm peak as calibration points. The ground state transition energy has been measured by Hofmann at SHIP using the alpha lines from ^{151}Ho, ^{151m}Ho and ^{152}Er plus the proton line from ^{151}Lu as calibration energies. The energy of the excited state transition in ^{147}Tm measured from this data is E_p = 1110.6 ± 3.9 keV. This is

obtained from the measured energy in the detector after correcting for the pulse height defect of protons in silicon [Pai81] and the deficit–corrected recoil energy of the daughter nucleus (see table 5.1). This value is consistent with that obtained by Hofmann (1118.5 $\pm$ 5.3 keV) and has an improved accuracy, which is mainly due to the good peak/background ratio obtained from this data.

Total yields obtained for the proton peaks are 1300 for the ground state peak and 400 for the excited state peak. Assuming a measured cross section of 30 μb for the ground state peak [Hof88], this corresponds to a cross section of 10 μb for the excited state.

Figure 5.5 shows a set of A=147 decay energy spectra expanded about the two proton peaks. The four spectra show decay events back–correlated to a preceding implantation event within the given implantation–decay time difference. The correlation procedure searches for the implantation event which occurred in the same pixel position as the decay event, and so rejects random correlations from background events over an extremely long range of time differences. The change in relative intensity of the two proton peaks with increasing time difference is clearly shown in the spectra. The 10 ms time difference spectrum contains virtually all the yield of the 1.11 MeV peak whereas the intensity of the 1.05 MeV peak increases through the sequence of spectra. Figure 5.6 shows the implantation–decay time difference curves for the 1.11 MeV peak (upper spectrum) and the 1.05 MeV peak (lower spectrum). The good statistics available from these decay curves allow new independent half–life measurements to be made for each of the two lines. The resulting half–lives values, deduced from exponential fits to the decay curves, are $t_{\frac{1}{2}} = 376 \pm 38$ μs for the excited state transition (previous value $t_{\frac{1}{2}} \simeq$ 360 μs [Hof84]) and $t_{\frac{1}{2}} = 546 \pm 18$ ms for the ground state transition (previous value $t_{\frac{1}{2}} \simeq 560$ ms [Lar83]). It can be seen that both the half–life values obtained from this data significantly improve the accuracy of the previous measurements.

A third new proton transition has also been observed from the reaction

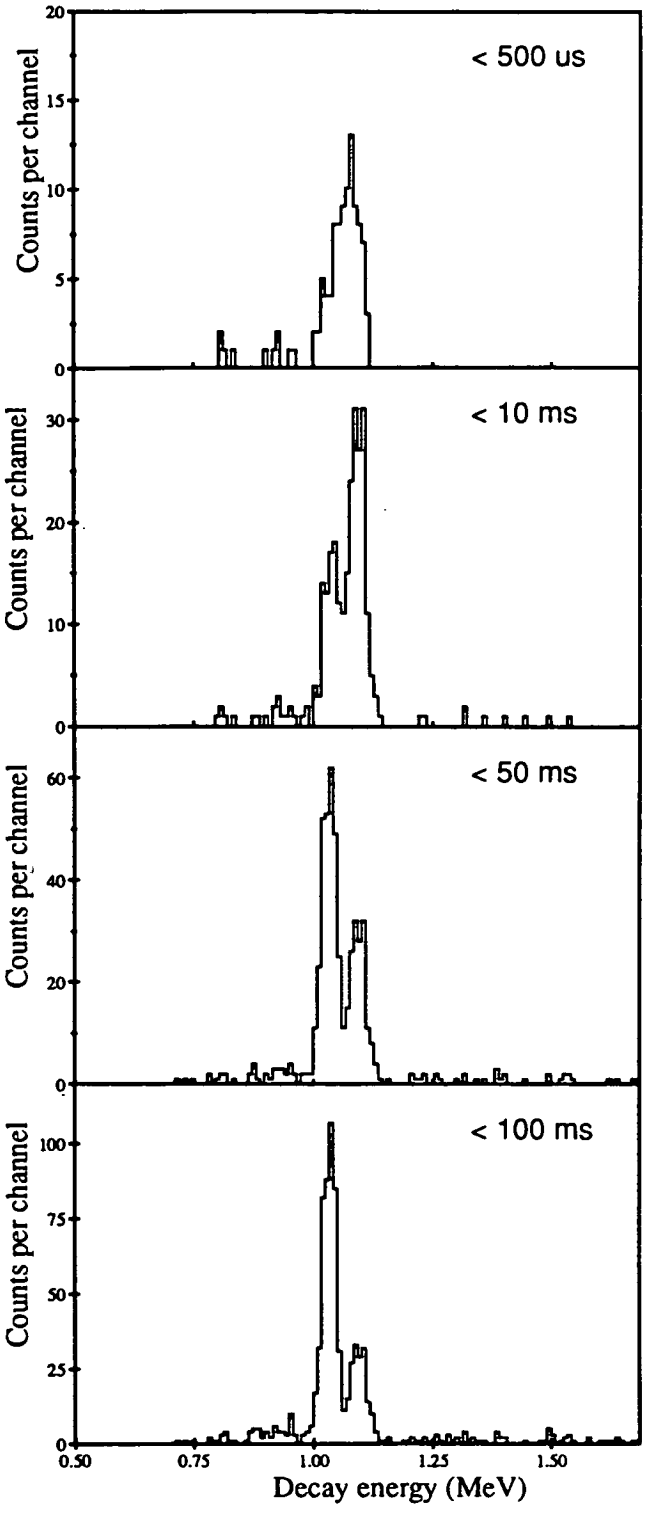

Figure 5.5: *Sequence of A=147 position–correlated decay energy spectra showing the two proton transitions from ^{147}Tm, gated on increasing implantation–decay time difference.*

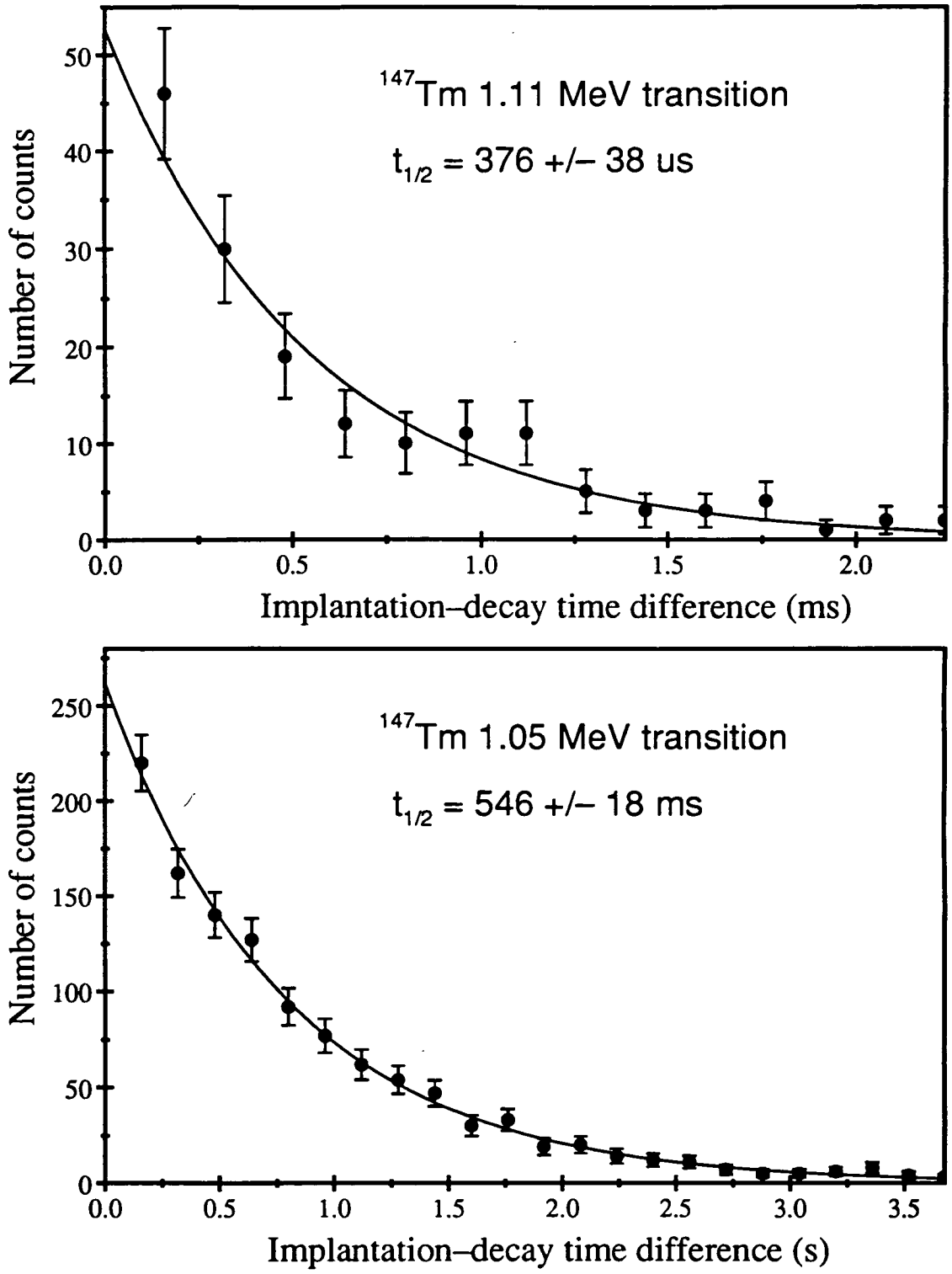

Figure 5.6: *Implantation–decay time difference spectra for the ground state proton transition (lower spectrum) and the excited state proton transition (upper spectrum) from ^{147}Tm. The decay curves are exponential functions fitted to the data*

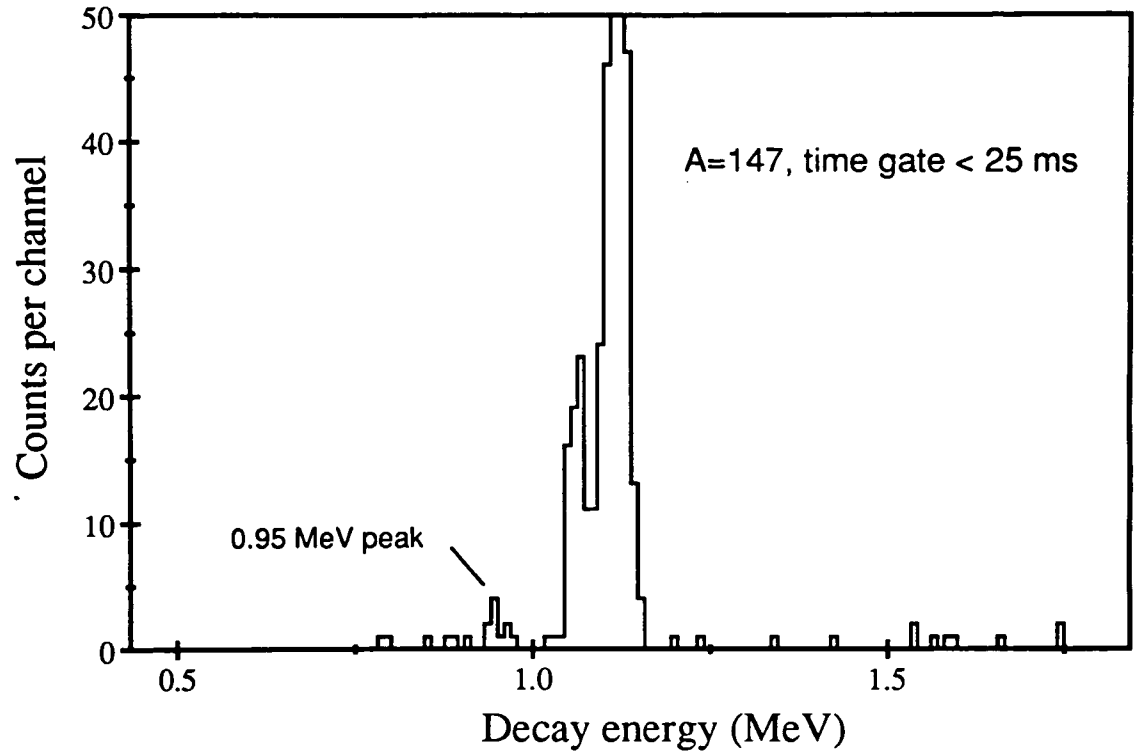

Figure 5.7: *Time gated A=147 decay energy spectrum for events from $^{150}Yb^*$, showing the weak proton transition at 0.95 MeV*

$^{58}Ni + {}^{92}Mo \rightarrow {}^{150}Yb^*$. This weak line is shown in figure 5.7 with a measured energy of 947.4 ± 5.0 keV in mass group A=147. The peak contains 10 counts, and is only clearly visible in decay energy spectra time gated within the interval 0–25 ms. Spectra with longer time gates contain a significant level of long–lived background events which swamp the prompt peak.

The validity of this transition was confirmed by incrementing a time difference spectrum gated around the energy of the 0.95 MeV peak. This was compared with a similar spectrum which was generated using an energy gate just below the observed peak. These two spectra are shown in figure 5.8, with horizontal scales of 1 channel per 16 ms. The upper plot, gated around the peak, clearly shows short–lived activity in the first two channels over and above the long–lived background of events. The first channel contains seven counts, which is more than five standard deviations above the level expected from the background distribution

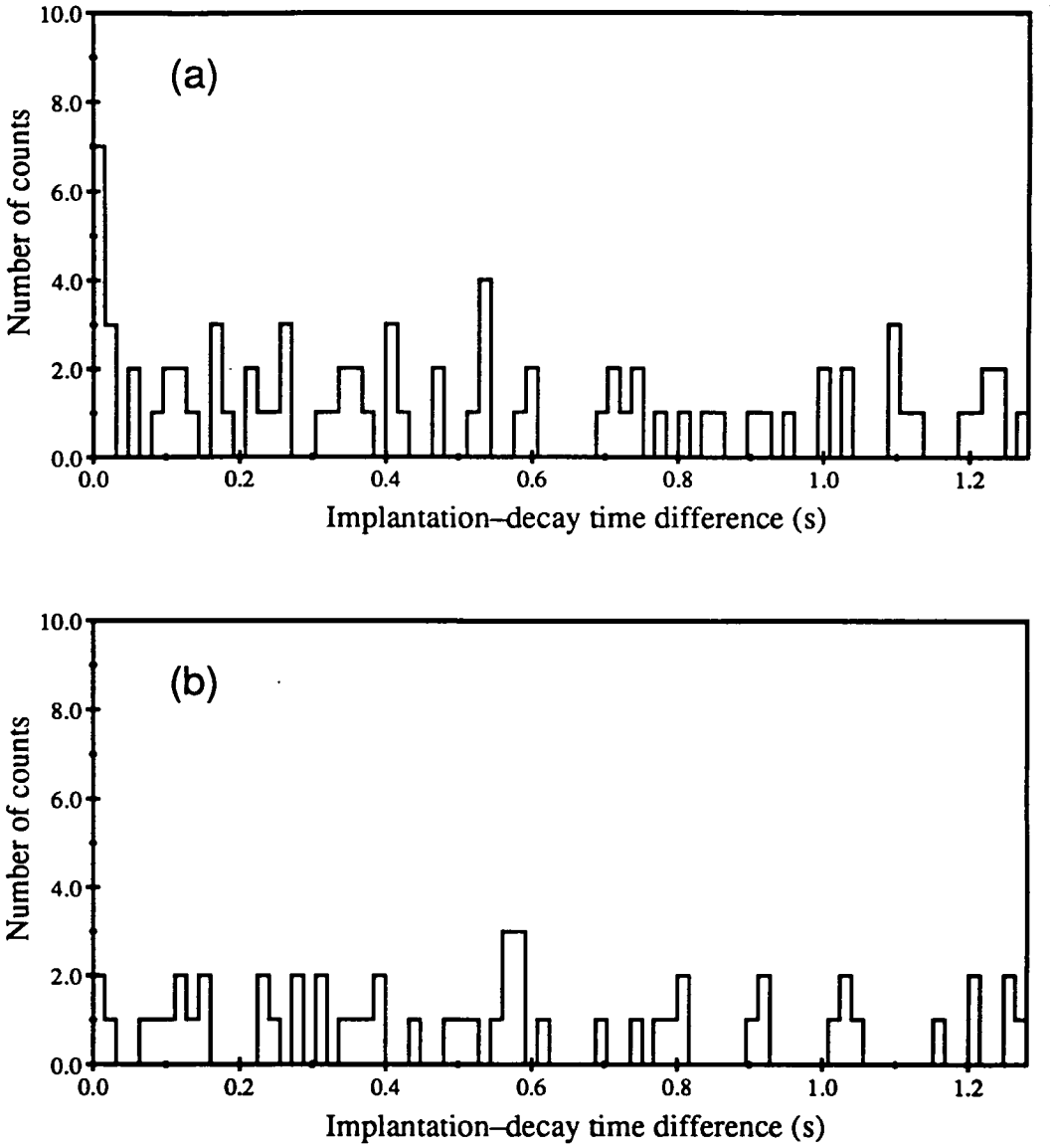

Figure 5.8: *Time difference spectra gated around (a) the 0.95 MeV proton peak, and (b) below 0.95 MeV. The upper spectrum shows short lived activity in the first two channels, which is not seen in the lower spectrum*

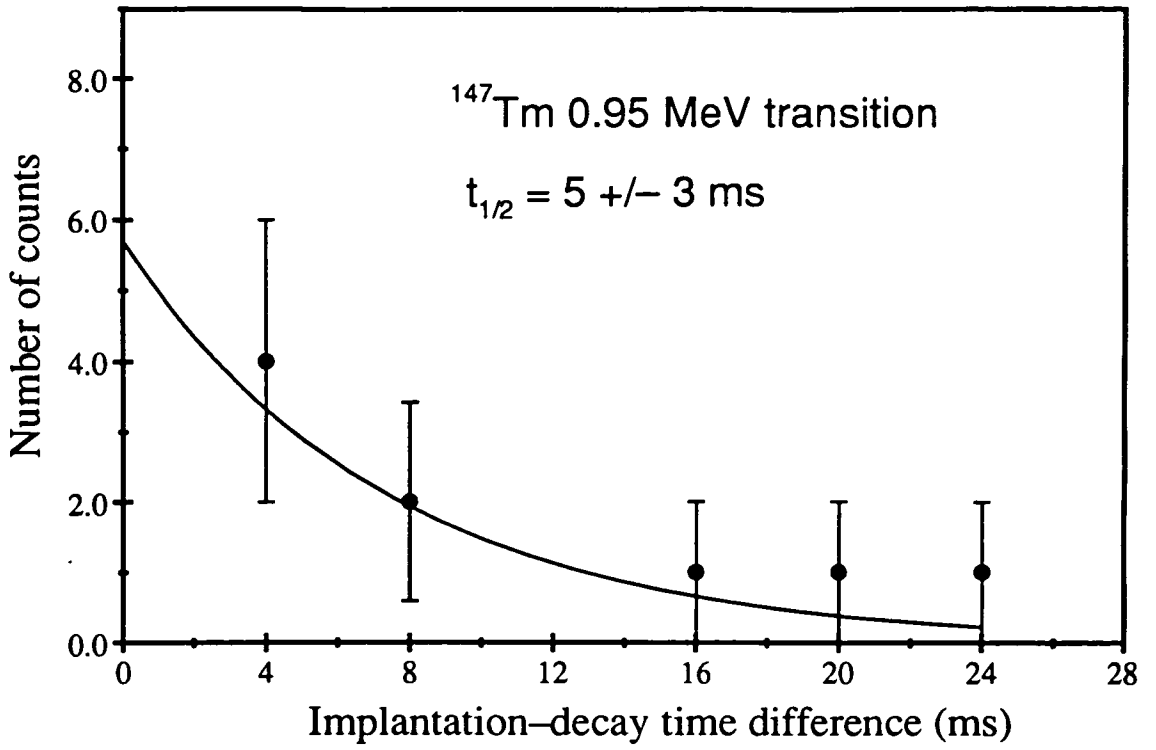

Figure 5.9: *Time difference spectrum for events from the 0.95 MeV proton peak. The decay curve is an exponential function fitted to the data*

alone. The lower spectrum, gated below the peak, shows no short–lived activity. This therefore rules out the possibility of the peak being caused by escape events from the strong proton lines, which would appear in both time difference spectra. Figure 5.9 shows the resulting time difference spectrum produced from these events. A exponential curve is shown fitted to this data by a least–squares method, which gives the half–life value $t_{\frac{1}{2}} = 5 \pm 3$ ms.

Table 5.2 summarises the results of half–life calculations for each of the three A=147 proton transitions, calculated assuming a spectroscopic factor of unity. The WKB code [Pag90] uses each of the two optical model potentials of Bechetti and Greenlees, and Perey and Perey. As was discussed in section 2.4.2, the difference in calculated half–lives arising from the choice of potential is not significant in comparison with the sensitivity of the half–life to the proton l–value. The existing assignment of the 1.05 MeV proton peak to an l=5 transition from an $h_{\frac{11}{2}}$

Nucleus	^{147}Tm		^{147m}Tm		(^{147}Tm)	
Energy E_p [a]	(1051.0 ± 3.3)		1110.6 ± 3.9		947.4 ± 5.0	
$Q_{p,nuc}$	(1071.4 ± 3.3)		1131.4 ± 3.9		967.1 ± 5.0	
Measured half-life $t_{\frac{1}{2}}^{exp}$	546 ± 18 ms		376 ± 38 μs		5 ± 3 ms	
Proton branch b_p [b]	21 ± 10%		≃ 100%		≃ 100%	
Partial half-life $t_{\frac{1}{2},p}^{exp}$	$2.6^{+2.4}_{-0.8}$ s		376 ± 38 μs		5 ± 3 ms	
$t_{\frac{1}{2},p}^{calc}$ [c]	B+G	P+P	B+G	P+P	B+G	P+P
$3s_{\frac{1}{2}}$	180 μs	140 μs	24 μs	19 μs	6.8 ms	5.3 ms
$2d_{\frac{3}{2}}$	1.6 ms	1.3 ms	220 μs	170 μs	62 ms	49 ms
$1h_{\frac{11}{2}}$	5.0 s	1.9 s	670 ms	260 ms	210 s	80 s

Notes: All energies are in keV

[a] E_p for ^{147}Tm from [Hof88], used as calibration point

[b] b_p calculated using β^+-decay half-life estimates from Takahashi [Tak73], taken from [Lar83] for ^{147}Tm

[c] WKB calculations [Pag90]; B+G - Bechetti and Greenlees potential; P+P - Perey and Perey potential. Calculation assumes a spectroscopic factor of unity

Table 5.2: *Summary of half-life calculations for the three measured A=147 proton transitions. Energy values in brackets are taken from [Hof88]*

orbital is clearly confirmed by this additional half-life measurement. The reduced error in the new half-life measurement of the 1.11 MeV transition adds further evidence to support an l=2 transition from a $d_{\frac{3}{2}}$ proton level in ^{147}Tm. This assignment was originally suggested by Hofmann *et al.* [Hof84] but subsequent authors (eg. [Tot87, Kor89, Ako90]) have labelled the transition from an $s_{\frac{1}{2}}$ level. Table 5.2 also shows partial proton half-lives calculated for the new 0.95 MeV proton peak. These values are clearly consistent with an unhindered l=0 transition. It might appear reasonable to assign this transition to proton emission from the $s_{\frac{1}{2}}$ single proton level in ^{147}Tm, thereby identifying the $s_{\frac{1}{2}}$ level as the ground state in ^{147}Tm. However this explanation cannot account for the observed population of the $d_{\frac{3}{2}}$ level in ^{147}Tm, which would decay in this scenario by a fast ($<$ 100 ns) E2 transition to the $s_{\frac{1}{2}}$ level. A discussion of the possible alternative explanations for this transition is given in section 5.3.3.

An additional aim of this experiment was to search for the four discrete lines seen by Hofmann from ^{150}Yb* (see section 2.4.2). The upper plot in figure 5.10 shows the decay energy spectrum from the GSI data, accumulated during the 5 ms beam–on period (followed by a 15 ms beam–off period). The four lines have energies of approximately 2467 keV (σ = 10 μb), 2851 keV (σ = 20 μb), 2935 keV (σ = 5 μb) and 3277 keV (σ = 5 μb). The lower plot in figure 5.10 shows the position–correlated decay energy spectrum from this data, with an implantation–decay time gate $\leq$ 50 ms. There is no evidence for any peaks above the background events at any energy between that of the ^{147}Tm peaks, and the alpha peak from ^{149}Tb at 3.99 MeV.

The two sets of data appear incompatible, since peaks of such an apparently large cross section should be easily seen in the Daresbury data. A Monte Carlo simulation was used to calculate an estimate of the strip detector efficiency for protons at these energies, which indicates that $>$ 30% of events will be recorded with a full energy signal. Taking account of this factor, substantial peaks would still be expected in the lower spectrum of figure 5.10, which should contain between

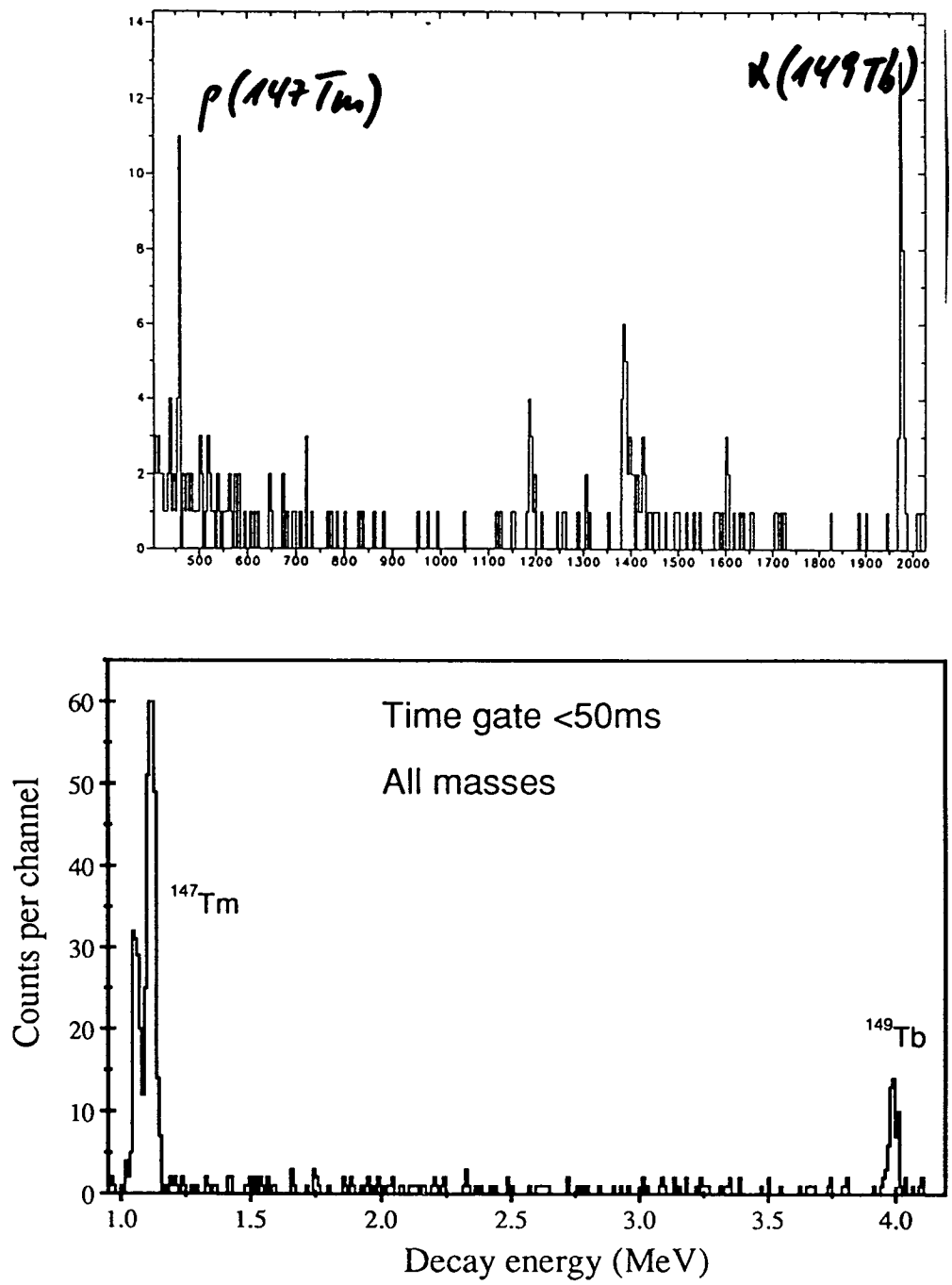

Figure 5.10: *Time gated energy spectra showing decay events from* $^{150}Yb^{*}$. *The upper spectrum is of data taken from GSI [Hof91] showing four peaks at energies ranging from 2.5 MeV–3.3 MeV. The lower spectrum shows decay events for all mass groups from this experiment, with no sign of any peaks in this energy range*

10 and 50 counts. Some reduction in yield could be expected due to a slight difference in the excitation energy of the ^{150}Yb* compound nucleus in the GSI and Daresbury experiments, however the excitation energy in this data covers the range 48 MeV to 52 MeV due to beam energy loss in the target. It is therefore implausible that a difference in excitation energy could reduce the yield sufficiently to account for the complete lack of peaks.

The RIDS experiments are noticeably more sensitive than the previous work carried out at SHIP. In the Daresbury data the presence of $Q = 28^+$ residues means that the recoil separator accepted masses over a continuous range from A=145 to A=154. It is therefore possible to exclude as the source of this activity all nuclei in the given mass range which are expected to have observable production cross sections. This eliminates the thullium isotopes $^{146-151}$Tm, plus the remaining two and three nucleon channel residues ^{147}Ho, ^{147}Er and ^{148}Er. It is possible that the activity could be due to transitions between high–lying isomeric states in nuclei lying closer to stability. Such nuclei would have proton bound ground states, and could have been populated in the GSI data via isotopic impurities in the target material. Alternatively of course the apparent proton activity could be due to some experimental artifact.

5.2.2 The new proton emitter ^{150}Lu

The latter part of the main experiment studied the reaction ^{58}Ni + ^{96}Ru $\rightarrow$ ^{154}Hf* with beam energies of 300 MeV ($E_x \simeq$ 61 MeV) followed by 311 MeV ($E_x \simeq$ 69 MeV). Figure 5.11 shows the decay energy spectrum for all events from the combined data of both these runs. A variety of intense alpha lines are present, mainly due to isotopic contamination of the target, and the spectrum is plotted with a logarithmic vertical scale to enhance the weaker peaks. The proton peak shows clearly at an energy of 1.23 MeV, and contains a slight asymmetry on the high energy side. The spectrum in figure 5.12 contains the same data, expanded

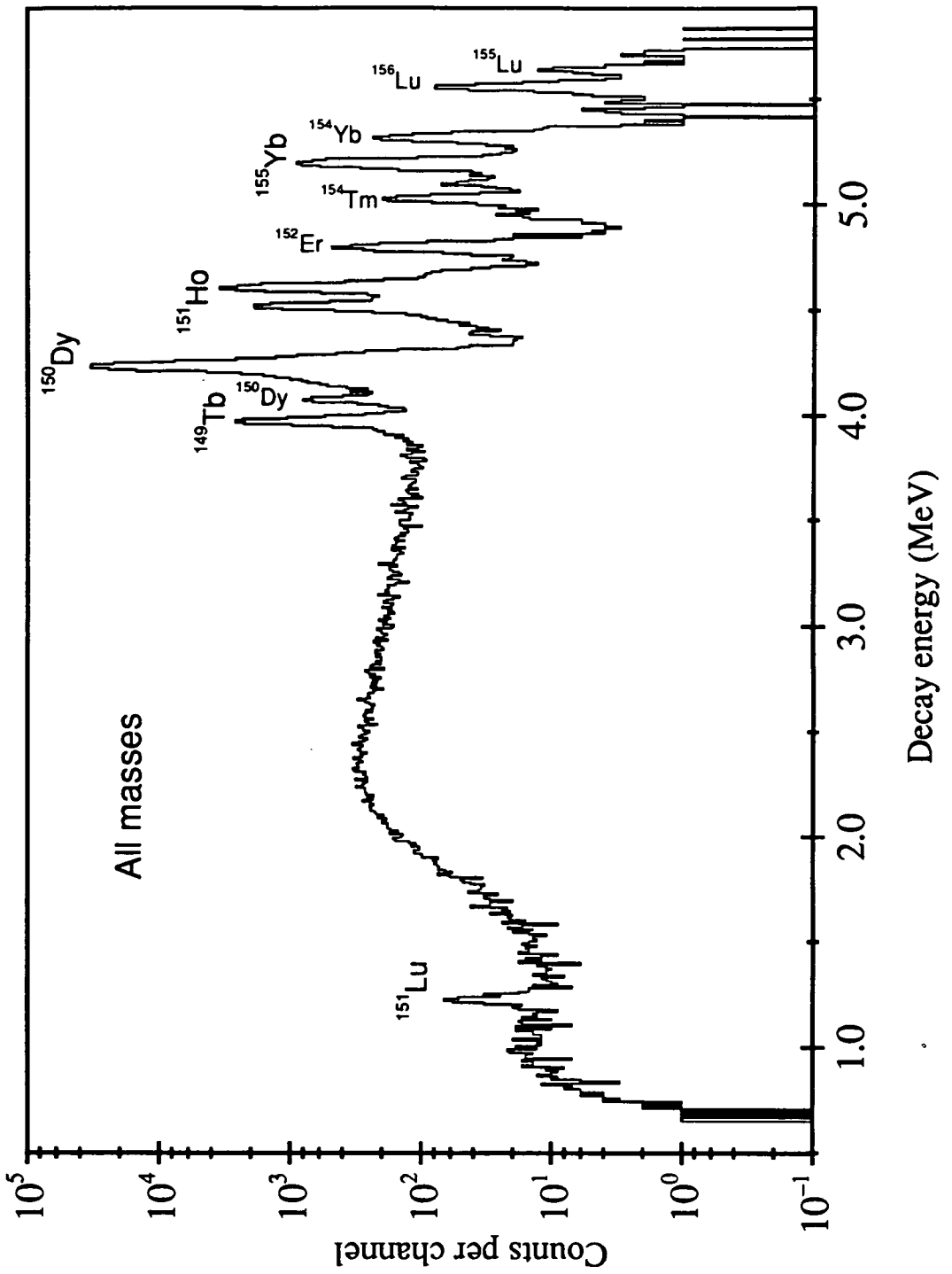

Figure 5.11: *Decay energy spectrum for all events from $^{154}Hf^*$. The proton peak from ^{151}Lu is clearly visible at an energy of approximately 1.2 MeV*

about the low energy region, and shows an additional weaker peak partially resolved at an energy about 30 keV above the centroid of the main peak. This is the 1.26 MeV proton transition seen previously only by Hofmann, and discussed in section 2.4.2.

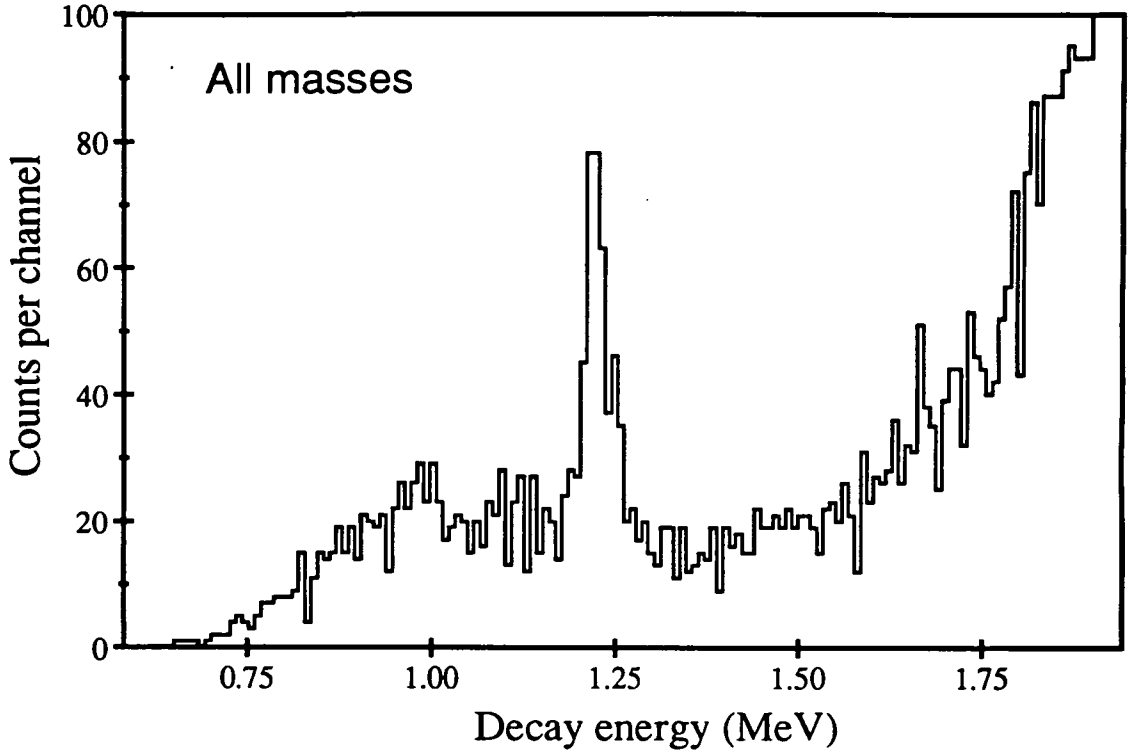

Figure 5.12: *Decay energy spectrum for events from $^{154}Hf^{*}$, without mass gating. The spectrum is expanded about the proton peak from ^{151}Lu, which contains a partially resolved high energy component*

Figure 5.13 shows this data plotted as a two dimensional spectrum of decay energy versus mass number of the implanted ion. The strip detector covers approximately $3\frac{1}{2}$ mass units, ranging from A=149 to the edge of A=152 ($Q = 29^{+}$). Residues produced from reactions with target contaminant are also present with charge state $Q = 30^{+}$ in the mass range A=154–156.

The proton line is weakly visible at an energy of approximately 1.2 MeV in the A=151 region of the detector, however the vertical scale of this spectrum is unable to resolve the second peak. The mass and energy structure of this line can be

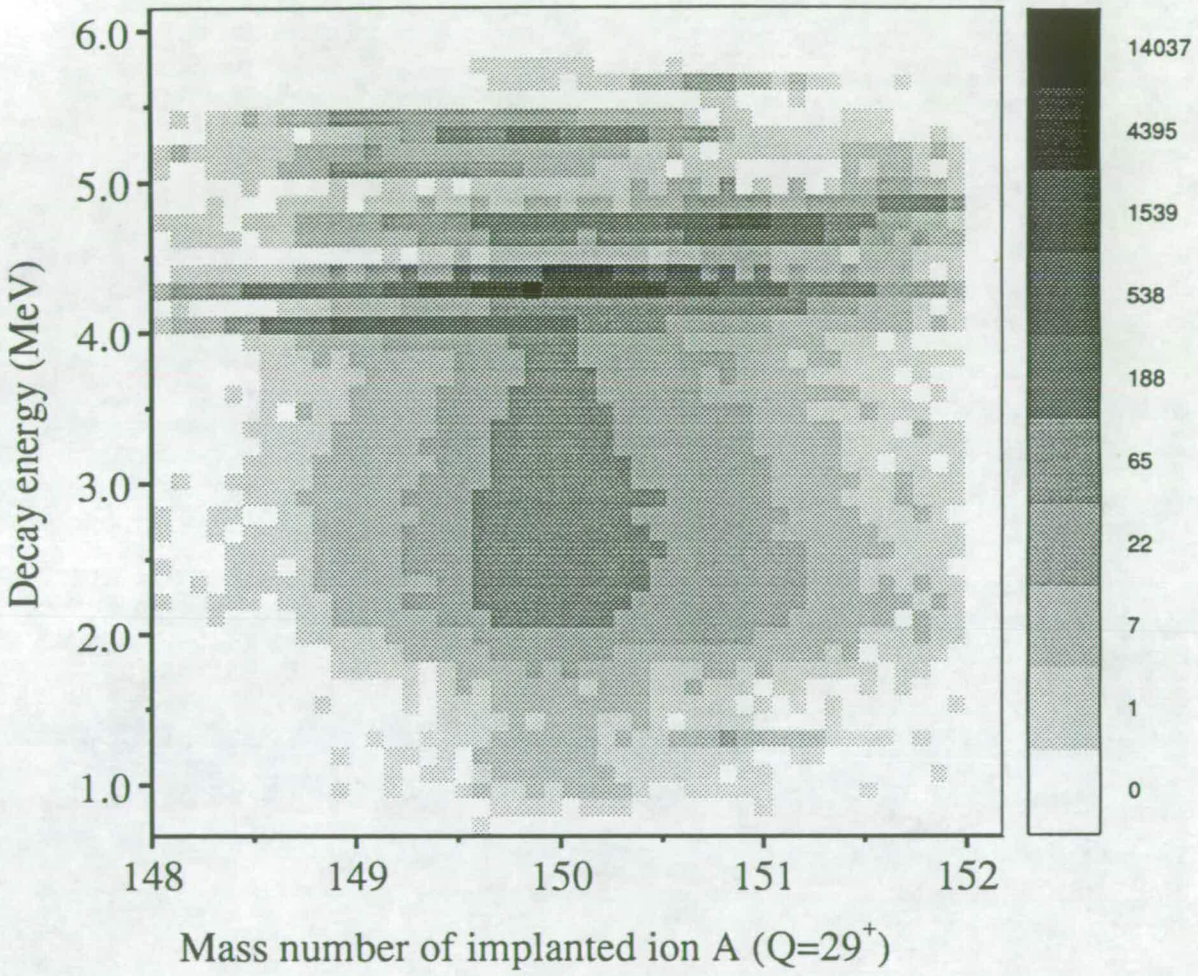

Figure 5.13: *Decay energy versus mass number for decay events from $^{154}Hf^{*}$. The stronger proton line is just visible at an energy of 1.2 MeV in the A=151 region of the detector*

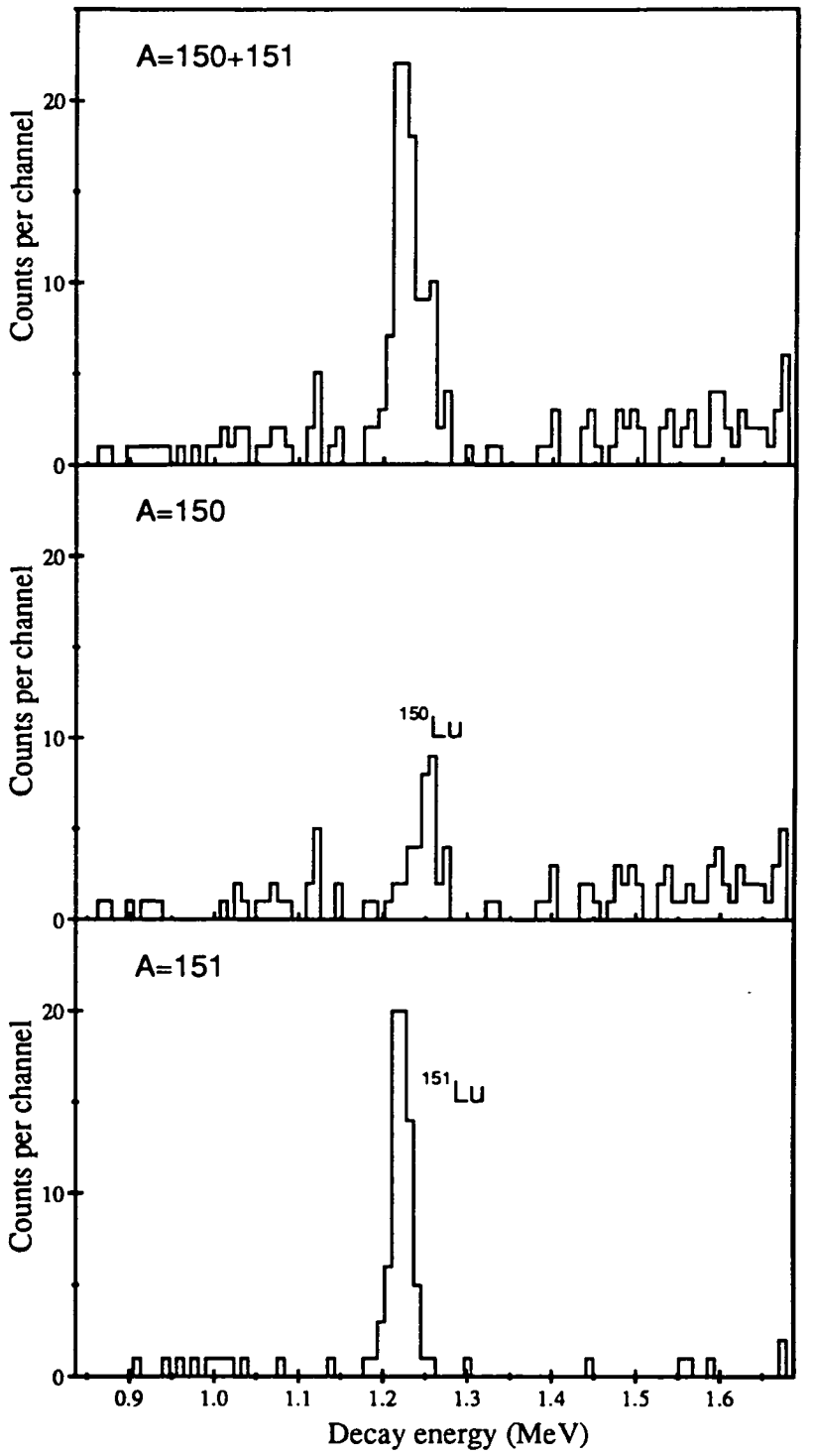

Figure 5.14: *Mass gated energy spectra showing decay events from $^{154}Hf^{*}$ position correlated within 50 ms. The A=151 spectrum (lower) shows the 1.23 MeV peak from ^{151}Lu and the A=150 spectrum (middle) shows the weaker 1.26 MeV peak, assigned to the proton decay of ^{150}Lu*

identified in figure 5.14, which contains mass gated decay energy projections from the two dimensional spectrum. The three spectra in figure 5.14 contain decay events which are position correlated to the preceding implantation event within a 50 ms time window. The upper spectrum is mass gated on A=150 and A=151, and clearly shows the higher energy component on the side of the 1.23 MeV peak. The lower spectrum is gated on A=151 and shows the 1.23 MeV proton peak from ^{151}Lu without the higher energy component. This provides the first direct assignment of the 1.23 MeV transition to ^{151}Lu. The middle spectrum is gated on A=150 and clearly shows the weaker proton peak at an energy of 1.26 MeV. This transition is therefore unambiguously assigned to the decay from an A=150 nucleus. Of the A=150 nuclei produced from ^{154}Hf*directly, ^{150}Hf, ^{150}Yb and ^{150}Er can be excluded on Q–value arguments (Q_p= −0.1 MeV, −2.0 MeV and −3.6 MeV respectively [Mol88]). ^{150}Tm has a small positive Q–value (Q_p= 0.3 MeV [Mol88]) but would be produced via the 3pn channel with a yield of about an order of magnitude greater than ^{151}Lu via the p2n channel. The 1.26 MeV peak is therefore identified as the proton decay of ^{150}Lu, most likely from the ground state level. This becomes the fifth known proton radioactive nucleus, and the only known odd–odd example.

The energy of the ^{150}Lu peak was measured from this data, using the proton peak from ^{151}Lu and the alpha peaks from ^{151,151m}Ho as calibration energies. The transition energy obtained after corrections (see table 5.1) was E_p = 1261.0 ± 3.9 keV, which is in excellent agreement with the previous value measured by Hofmann of 1262.7 ± 3.6 keV.

The combined data taken from the runs at the two beam energies contains a total of $\simeq$ 40 counts in the ^{150}Lu peak and $\simeq$ 160 counts in the ^{151}Lu peak. Figure 5.15 shows the decay curves obtained from this data for ^{150}Lu and ^{151}Lu, with exponential functions fitted to the data. The first half–life measurement of ^{150}Lu was made from this data, giving a value of $t_{\frac{1}{2}}$ = 30 ± 5 ms. The half–life was also calculated for ^{151}Lu giving $t_{\frac{1}{2}}$ = 89 ± 8 ms which is comparable with the

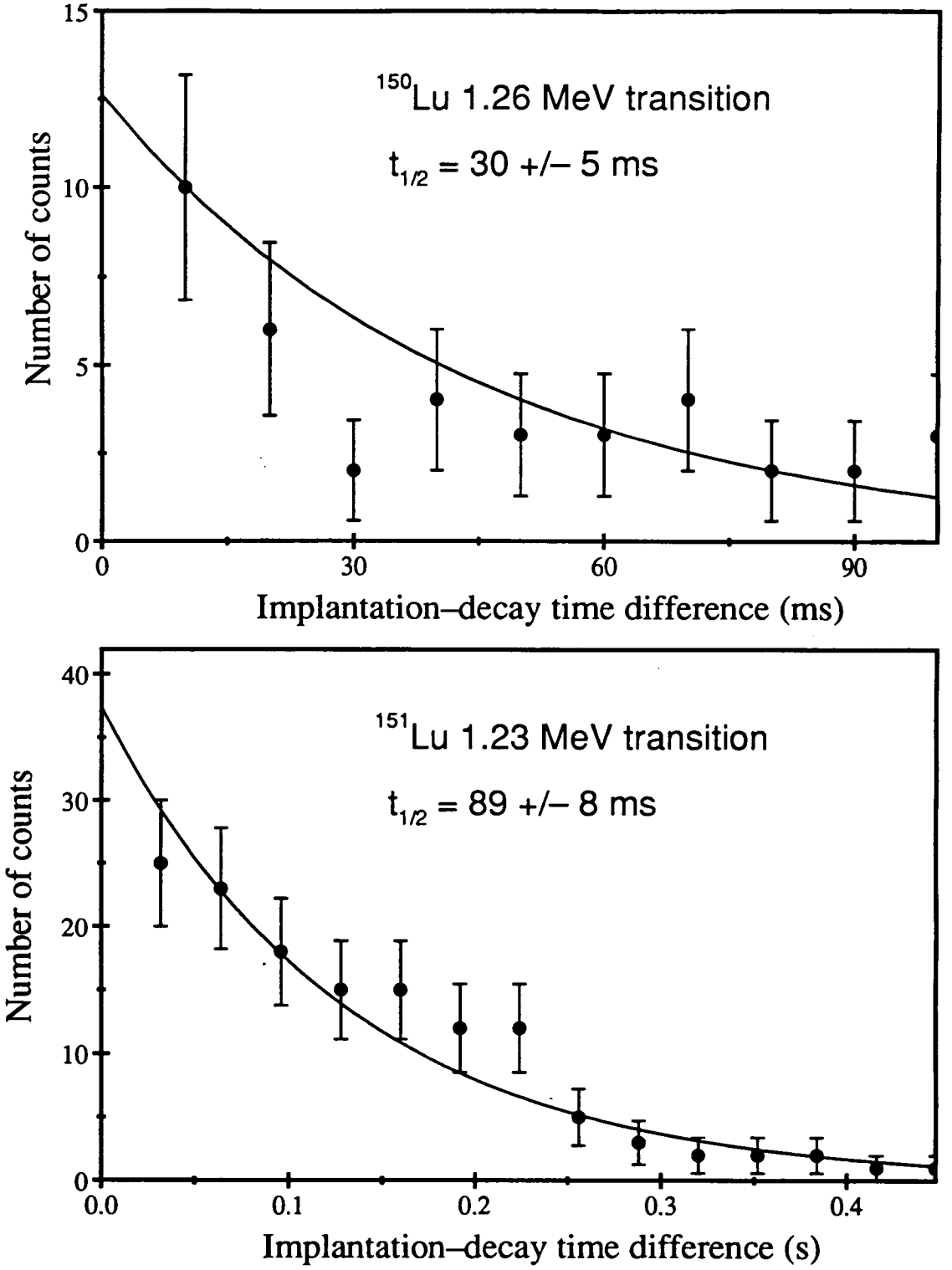

Figure 5.15: *Implantation–decay time difference spectra from ^{150}Lu (upper spectrum) and ^{151}Lu (lower spectrum). The decay curves are exponential functions fitted to the data*

previously measured value ($t_{\frac{1}{2}} = 85 \pm 10$ ms).

Table 5.3 shows a summary of proton partial half-life calculations for ^{150}Lu and ^{151}Lu, covering the three proton orbitals in the major shell closure between $50 < Z \leq 82$. Partial proton half-lives are calculated using the WKB model assuming a spectroscopic factor of unity, with the real part of the optical model potentials from Bechetti and Greenlees, and Perey and Perey. The proton branching ratio b_p is deduced using calculated β partial half-lives from Takahashi *et al.* [Tak73]. The new half-life measurement of ^{150}Lu clearly identifies an l=5 transition, suggesting that the proton fermi level is the $h_{\frac{11}{2}}$ state for the ground state of ^{150}Lu. This continues the trend of the $h_{\frac{11}{2}}$ proton state occupying the fermi level in ^{151}Lu and ^{153}Lu [McN89].

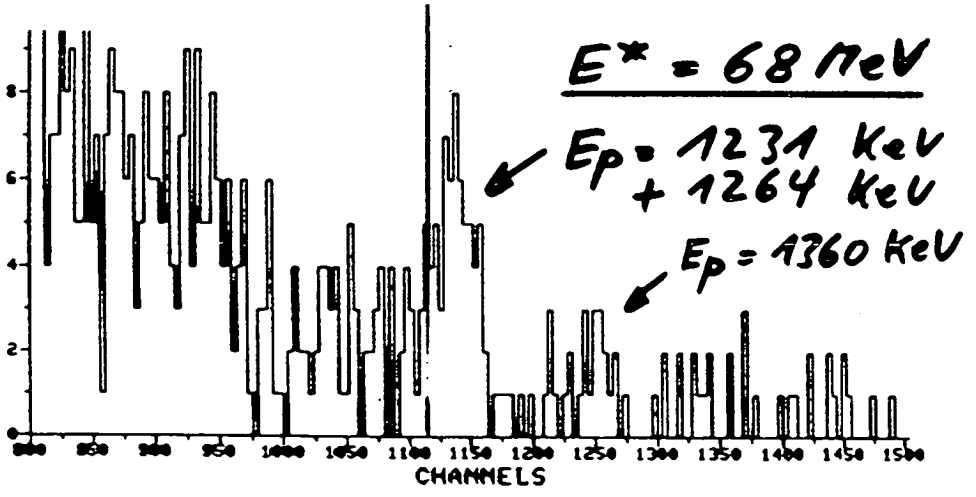

Figure 5.16: *Energy spectrum of decay events from $^{154}Hf^*$, from data taken at GSI [Hof91]. A possible weak peak is shown at an energy of 1.36 MeV.*

An additional aim of this part of the experiment was to search for the weak 1.36 MeV proton line tentatively reported by Hofmann (see section 2.4.2). The

Nucleus	^{150}Lu		^{151}Lu	
Energy E_p [a]	1261.0 ± 3.9		(1232.8 ± 2.8)	
$Q_{p,nuc}$	1283.2 ± 3.9		(1254.8 ± 2.8)	
Measured half-life $t_{\frac{1}{2}}^{exp}$	30 ± 5 ms		89 ± 8 ms	
Proton branch b_p [b]	80 ± 20%		70 ± 35%	
Partial half-life $t_{\frac{1}{2},p}^{exp}$	40^{+70}_{-35} ms		120^{+120}_{-40} ms	
$t_{\frac{1}{2},p}^{calc}$ [c]	B+G	P+P	B+G	P+P
$3s_{\frac{1}{2}}$	2.3 μs	1.8 μs	4.8 μs	3.7 μs
$2d_{\frac{3}{2}}$	2.7 ms	2.0 ms	5.5 ms	4.1 ms
$1h_{\frac{11}{2}}$	53 ms	20 ms	107 ms	42 ms

Notes: All energies are in keV

[a] E_p for ^{151}Lu from [Hof88], used as reference for ^{150}Lu energy

[b] b_p calculated using β^+–decay half-life estimates from Takahashi [Tak73]

[c] WKB calculations [Pag90]; B+G - Bechetti and Greenlees potential; P+P - Perey and Perey potential. Calculation assumes a spectroscopic factor of unity

Table 5.3: *Summary of half-life calculations for the proton transitions from ^{150}Lu and ^{151}Lu. Energy values in brackets are from [Hof88]*

original GSI spectrum is given in figure 5.16 [Hof91], produced from $^{154}Hf^{*}$ at an excitation energy $E_x \simeq 68$ MeV. The spectrum suggests a very weak peak at 1.36 MeV with an approximate cross section of 1 μb and a deduced lower half-life limit of 2 ms. By comparison with the yield of the ^{150}Lu peak, the Daresbury data would be expected to contain approximately 10 counts at 1.36 MeV. The decay energy spectra from this data (see figures 5.12, 5.14) show no evidence in any mass group for a peak at this energy. Due to the poor event statistics in the GSI spectrum, it must be concluded that the suggested peak is actually due to statistical fluctuations in the event background .

5.2.3 Summary of the experimental measurements

The combined experiments from this work measured five of the six previously observed proton transitions, which have been assigned to the nuclei ^{147}Tm, ^{150}Lu, ^{151}Lu and ^{109}I. The resulting data provides direct mass assignments for all of these proton transitions which, with the exception of the ground state decay from ^{147}Tm, had only previously been indirectly identified. In addition a new weak proton transition was observed from A=147 residues produced from $^{150}Yb^{*}$, with a decay energy of 947.4 $\pm$ 5.0 keV. The half-life of this transition and that from ^{150}Lu were measured for the first time, and those of the four other transitions were measured with a substantially improved accuracy. Energy measurements were also made for the proton peaks from ^{147m}Tm and ^{150}Lu, using the proton lines from ^{147}Tm and ^{151}Lu respectively as internal calibration energies. These two new measurements provide the first independent comparison with the energies measured at SHIP, and were in excellent agreement with these values.

The resulting Q_p values for the four observed nuclei are shown in figure 5.17, together with predicted proton Q-values calculated using the mass models of Möller Nix [Mol88], and Liran and Zeldes [Lir76]. The lower plot shows the new data point from ^{150}Lu, which has a Q_p value consistent within 120 keV with either

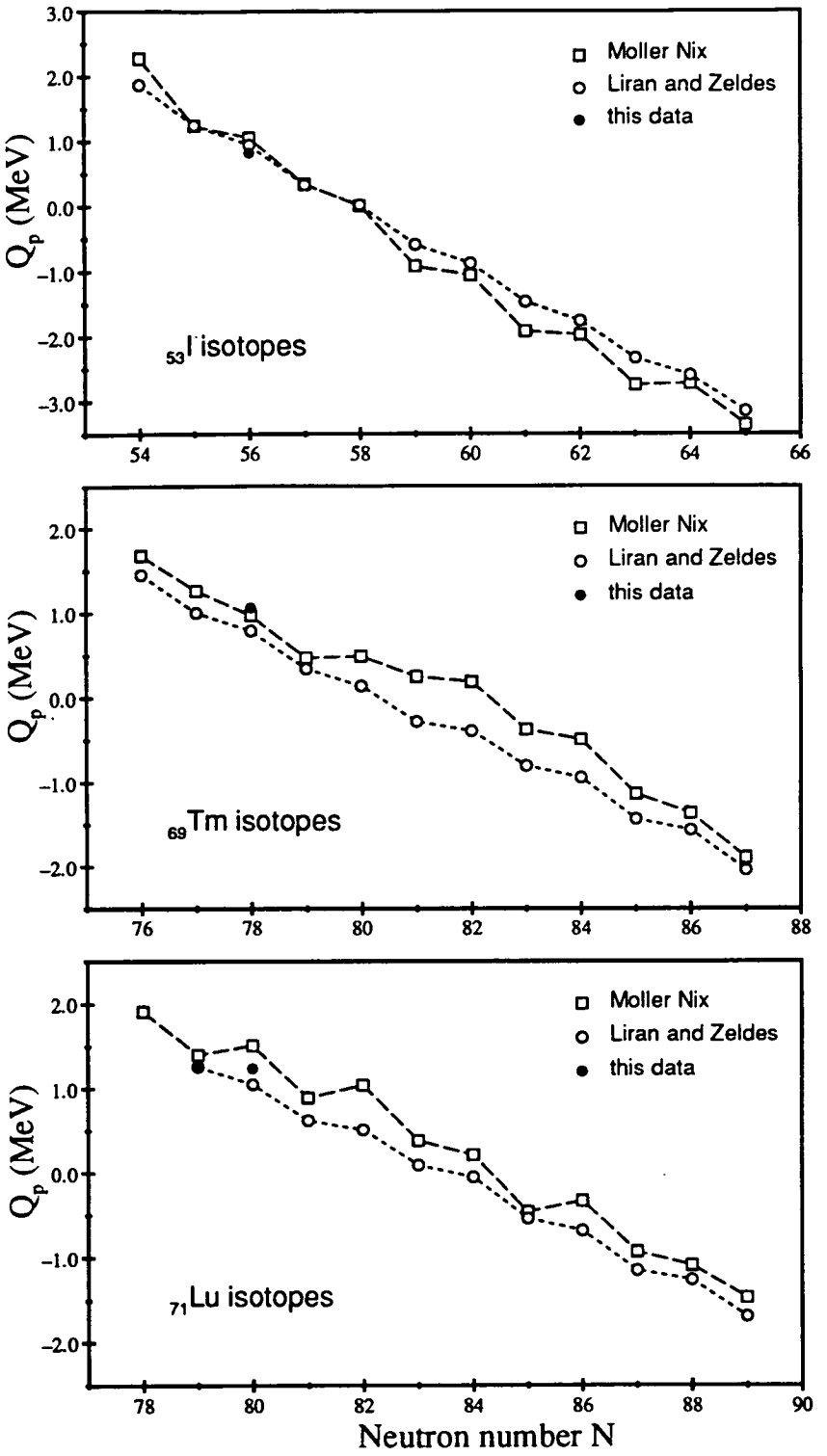

Figure 5.17: *Q_p values for isotopes of iodine, thullium and lutetium. Calculated values are from the mass models of Möller Nix [Mol88], and Liran and Zeldes [Lir76]*

Parent nucleus	E_p (keV)	Previous $t_{\frac{1}{2}}^{exp}$	New $t_{\frac{1}{2}}^{exp}$	Δl
^{147}Tm	1051.0 ± 3.3 [a]	560 ± 40 ms [b]	546 ± 18 ms	5
^{147m}Tm	1110.7 ± 3.2	360 ± 80 μs [c]	376 ± 38 μs	2
(^{147}Tm)	947.4 ± 5.0	− − −	5 ± 3 ms	
^{150}Lu	1261.0 ± 3.9	$\geq$ 10 ms [c]	30 ± 5 ms	5
^{151}Lu	1232.8 ± 2.8 [a]	85 ± 10 ms [c]	89 ± 8 ms	5
^{109}I	812.6 ± 4.0 [a]	110 ± 17 μs [d]	96 ± 5 μs	2

Notes: Measurements taken from this work except as given below

[a] [Hof88] [b] [Lar83] [c] [Hof84] [d] [Gil87]

Table 5.4: *Summary of all proton half-life and energy measurements from this work. Tentative assignments are in brackets*

mass model calculation. Both models give values which are in good agreement with all the known data points, which are all at least four isotopes away from the nearest known mass measurements. This is particularly impressive for the Liran and Zeldes model which was calculated before any of the direct proton transitions were observed. However it must be remembered that the Möller Nix model only uses five free parameters and still achieves an accuracy comparable with those containing several hundred adjustable values. Both models appear to behave well in both the shell model and transitional regions, although the Möller Nix values suffer from an apparently over-strong odd-even staggering in the lutetium isotopes. The new data point from ^{150}Lu suggests that this pairing effect is weaker than the Möller Nix values predict, indicating that the new pairing correction term (altered prior to the 1988 mass evaluation) requires some further adjustment. It is

interesting to note that the recently measured Q_p value of ^{146}Tm (see section 5.4) is approximately 70 keV greater than that of ^{147}Tm. This follows the trend of shallow odd–even staggering seen between ^{150}Lu and ^{151}Lu.

Table 5.4 summarises the new half–life and energy measurements made from this work, with the previously published half–life values given for comparison. The measured half–lives allow the emitted proton orbital angular momentum Δl to be deduced, assuming transitions between pure shell model states. The validity of this assumption will be discussed in the following sections.

5.3 Discussion

The sensitivity of the proton emission decay mode to the proton Q–value and orbital angular momentum can be used to deduce detailed nuclear structure information about the parent and daughter nuclei involved. The relationship between the measured transition energy and the parent and daughter nuclear masses allows comparisons to be made between the experimental Q_p values and different calculated mass predictions. The simplicity of the proton decay mode, without the need for a cluster preformation factor, allows direct comparisons to be made between measured half–lives and calculated single–particle transition probabilities. In most cases the parent and daughter levels associated with the transition can be uniquely assigned, so identifying the level ordering of low–lying states in nuclei far from stability. In this way information on level ordering and separation can be gained for nuclei which are often several isotopes further from stability than the nearest isotopes with a known level scheme. In the following sections it will be shown that the measured proton transitions from nuclei close to the N=82 closure can be well described in terms of shell model states. In particular the proton transitions from the nuclei ^{147}Tm and ^{150}Lu will be considered, and the resulting level assignments will be compared with the known level systematics in this region.

5.3.1 Summary of shell model states around Z $\geq$ 64, N $\leq$ 82

The low-lying level schemes of nuclei in the quadrant $Z \geq 64$ and $N \leq 82$ are well described by spherical shell model states involving the valence nucleons outside the ^{146}Gd core. These nucleons are protons occupying the $3s_{\frac{1}{2}}$, $2d_{\frac{3}{2}}$ and $1h_{\frac{11}{2}}$ proton orbitals, and neutron holes in the $3s_{\frac{1}{2}}$, $2d_{\frac{3}{2}}$ and $1h_{\frac{11}{2}}$ neutron orbitals. The resulting level schemes consist of a combination of low-lying single-particle levels together with two and three particle states at higher energies. In the following discussion the level schemes of odd-even nuclei (eg. ^{147}Tm) and odd-odd nuclei (eg. ^{150}Lu) will be summarised separately.

The single proton level scheme of odd-even nuclei below N=83 is only known for the N=82 isotones, for which the partial level schemes are known up to ^{151}Tm [Ako90] (see figure 2.3). The level schemes of these isotones above the Z=64 sub-shell closure are characterised by low energy single-particle proton states due to the $h_{\frac{11}{2}}$, $s_{\frac{1}{2}}$ and $d_{\frac{3}{2}}$ orbitals, with the $h_{\frac{11}{2}}$ level occupying the ground state in ^{149}Ho and ^{151}Tm. In addition there is a $\pi h_{\frac{11}{2}}{}^{n}$ seniority three level sequence ending with a $\frac{27}{2}^{-}$ isomer at an energy of $\lesssim$ 3 MeV, and a $(\pi h_{\frac{11}{2}})(\pi d_{\frac{3}{2}})(\pi s_{\frac{1}{2}})$ $\frac{15}{2}^{-}$ state at approximately 0.7 MeV. No level scheme information is currently known for the Tb, Ho and Tm N=78 and N=80 isotones, apart from the levels in ^{147}Tm measured in this work. The currently known partial single-particle level schemes for $78 \leq N \leq 86$ are summarised in figure 5.18, and show states close together in energy which follow systematic trends across each set of odd-Z isotopes. Whilst it might appear reasonable to extrapolate the known level schemes into the lighter isotopes, the possible effect on the level ordering of crossing below the N=82 shell closure makes any such estimates prone to uncertainty.

The low-lying level schemes of odd-odd nuclei with N=79 or N=81 contain two β^{+}-emitting isomers very close together in energy. In each case one of the isomers has J^{π}=1^{+} due to an $s_{\frac{1}{2}}$ or $d_{\frac{3}{2}}$ proton coupling with a neutron hole, and the

N=78	N=80	N=82	N=84	N=86
$^{149}_{71}$Lu	^{151}Lu	^{153}Lu	^{155}Lu	^{157}Lu
			$h_{\frac{11}{2}}$ 69 c	$h_{\frac{11}{2}}$ 32 d
	$h_{\frac{11}{2}}$ 0 a	$h_{\frac{11}{2}}$ 0 b	$s_{\frac{1}{2}}, d_{\frac{3}{2}}$ 0 c	$s_{\frac{1}{2}}$ 0 d
$^{147}_{69}$Tm	^{149}Tm	^{151}Tm	^{153}Tm	^{155}Tm
		$d_{\frac{5}{2}}$ 474+x f	$d_{\frac{5}{2}}$ 505 h	
$s_{\frac{1}{2}}$?		$d_{\frac{3}{2}}$ 108+x g	$d_{\frac{3}{2}}$ 135 h	
67 a				
$d_{\frac{3}{2}}$?		$s_{\frac{1}{2}}$ x=50? f	$s_{\frac{1}{2}}$ 43 h	$s_{\frac{1}{2}}$ 41 h
$h_{\frac{11}{2}}$ 0 a	$h_{\frac{11}{2}}$ 0 e	$h_{\frac{11}{2}}$ 0 g	$h_{\frac{11}{2}}$ 0 h	$h_{\frac{11}{2}}$ 0 h
$^{145}_{67}$Ho	^{147}Ho	^{149}Ho	^{151}Ho	^{153}Ho
		$d_{\frac{5}{2}}$ 564 k	$d_{\frac{5}{2}}$ 398 l	
		$d_{\frac{3}{2}}$ 221 k	$d_{\frac{3}{2}}$ 142 l	
		$s_{\frac{1}{2}}$ 49 k	$s_{\frac{1}{2}}$ 41 m	$s_{\frac{1}{2}}$ 68 n
$h_{\frac{11}{2}}$ 0 i	$h_{\frac{11}{2}}$ 0 j	$h_{\frac{11}{2}}$ 0 k	$h_{\frac{11}{2}}$ 0 m	$h_{\frac{11}{2}}$ 0 n
$^{143}_{65}$Tb	^{145}Tb	^{147}Tb	^{149}Tb	^{151}Tb
		$d_{\frac{5}{2}}$ 354 m	$d_{\frac{5}{2}}$ 207 q	$h_{\frac{11}{2}}$ 99 r
		$d_{\frac{3}{2}}$ 253 m	$d_{\frac{3}{2}}$ 101 q	$d_{\frac{5}{2}}$ 72 r
		$h_{\frac{11}{2}}$ 51 m	$h_{\frac{11}{2}}$ 36 q	$d_{\frac{3}{2}}$ 23 r
$h_{\frac{11}{2}}$ 0 p	$h_{\frac{11}{2}}$ 0 j	$s_{\frac{1}{2}}$ 0 m	$s_{\frac{1}{2}}$ 0 q	$s_{\frac{1}{2}}$ 0 r

Notes: All energies are in keV

a	[Hof88]	g	[Tot86]	m	[Lia87]
b	[McN89]	h	[Kor89]	n	[Neu87]
c	[Tot91]	i	[Vie89]	p	[Oll89]
d	[Lew91]	j	[Nol82]	q	[NDS85]
e	[Tot87c]	k	[Fir89]	r	[Kem78]
f	[Ako90]	l	[Bar88]		

Figure 5.18: *Summary of the experimentally determined proton single-particle levels in odd-Z even-N nuclei with* $Z > 64$, $78 \leq N \leq 86$

other state has J^{π}=5$^-$ or 6$^-$ due to an $h_{\frac{11}{2}}$ proton coupling with either an $s_{\frac{1}{2}}$ or a $d_{\frac{3}{2}}$ neutron hole. The 1$^+$ level has been observed in the odd–odd $N < 82$, $Z > 64$ isotopes ^{146}Tb, ^{148}Ho [Nol82], and the high spin isomer in ^{148}Tm [Nol82], ^{146}Tb [Bro89], ^{148}Ho [Tot88], ^{150}Tm [Nol82, Tot87a] and ^{152}Lu [Tot87]. The high spin isomer has been assigned to a 6$^-$ state in ^{148}Tm, ^{148}Ho and ^{150}Tm, to a 5$^-$ state in ^{146}Tb and to a state with J^{π}=(4,5,6$^-$) in ^{152}Lu. In addition a millisecond $\pi h_{\frac{11}{2}} \nu^{-1} h_{\frac{11}{2}}$ 10$^+$ isomer has been observed in the N=81 isotones ^{146}Tb, ^{148}Ho and ^{150}Tm, which decays through a variety of $\pi h_{\frac{11}{2}} \nu^{-1} d_{\frac{3}{2}}$ and $\pi h_{\frac{11}{2}} \nu^{-1} s_{\frac{1}{2}}$ levels to terminate in the high spin β^+–decaying state.

The negative parity high spin states are populated when these odd–N nuclei are produced via heavy ion fusion–evaporation reactions, whereas only the 1$^+$ isomer is observed from β^+–decaying precursors [Bro90]. The relative separation of the two isomeric levels is therefore generally unknown, although Nitschke *et al.* [Nit88] place the 6$^-$ state in ^{148}Ho and ^{150}Tm approximately 100 keV above the 1$^+$ state.

5.3.2 Assignment of the proton transitions from ^{147}Tm

Figure 5.19 summarises the estimated partial level schemes of the N=78 isotones ^{147}Tm and ^{146}Er and the N=79 isotones ^{150}Lu and ^{149}Yb extrapolated from the systematics of levels in neighbouring $N \leq 82$ $Z > 64$ nuclei. The assignment of the 1.18 MeV proton transition from ^{147}Tm to a $d_{\frac{3}{2}}$ level implies a 60 keV excitation energy of this level from the $h_{\frac{11}{2}}$ ground state. The energy systematics of the $d_{\frac{3}{2}}$ and $s_{\frac{1}{2}}$ levels in thullium isotopes (see figure 5.18) show the $s_{\frac{1}{2}}$ orbital occupying the first excited state in $N > 82$ isotopes, with an excitation energy of approximately 40 keV. The $d_{\frac{3}{2}}$ level in ^{153}Tm is above the $s_{\frac{1}{2}}$ level with an excitation energy of 135 keV. Disregarding the level scheme of ^{151}Tm given in figure 5.18, there is no further information available on these levels until reaching ^{147}Tm.

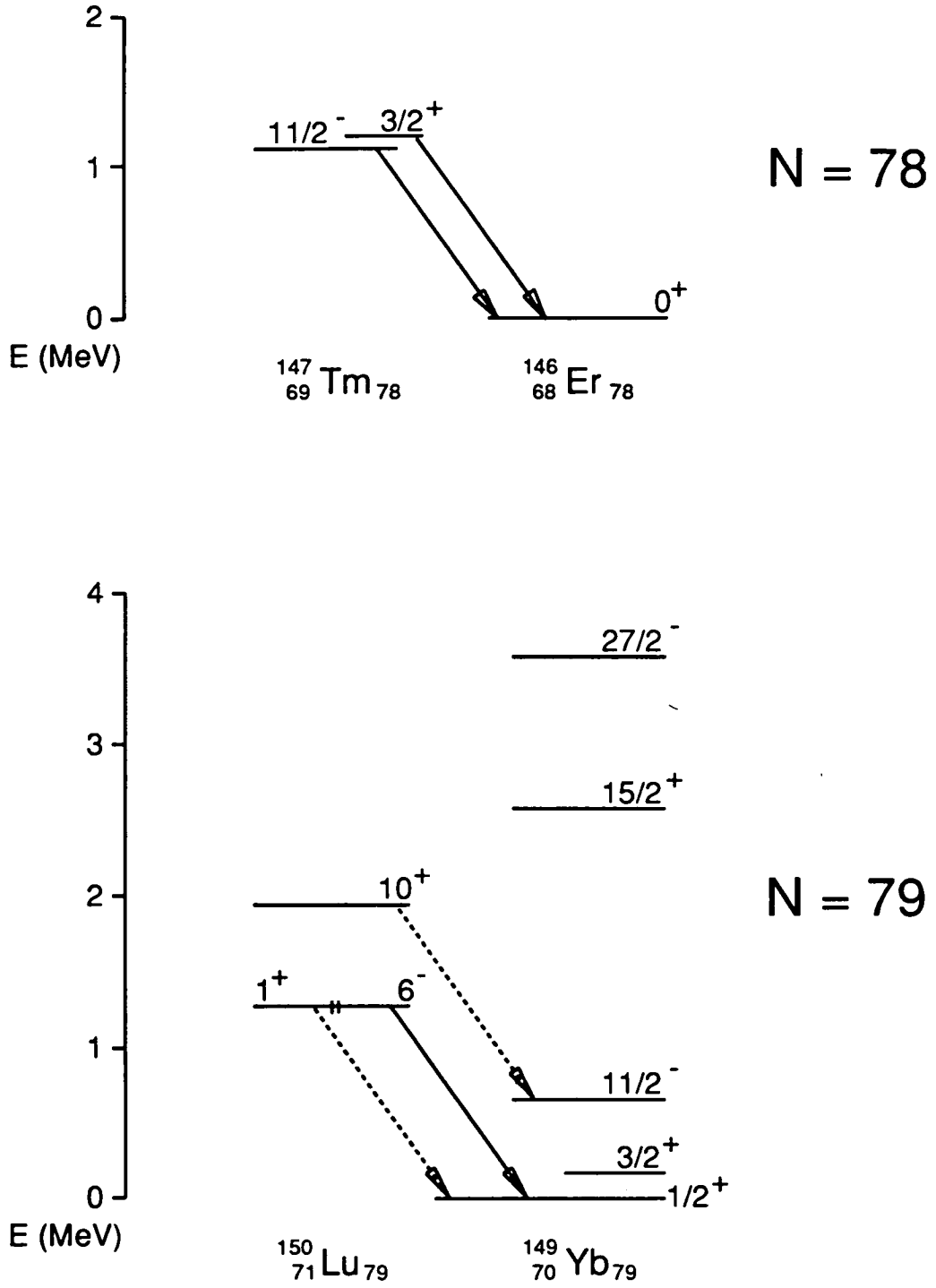

Figure 5.19: *Extrapolated partial level schemes of ^{147}Tm, ^{146}Er and ^{150}Lu, ^{149}Yb from [Hof88]. The three identified proton transitions are shown with solid arrows. Two additional possibilities for the 1.26 MeV transition from ^{150}Lu are shown, which are energetically allowed without additional configuration hindrance*

Therefore the assignment of the $d_{\frac{3}{2}}$ level to an excited state immediately above the $h_{\frac{11}{2}}$ level in ^{147}Tm requires that in isotopes below the N=82 closure either the $d_{\frac{3}{2}}$ and $s_{\frac{1}{2}}$ levels cross each other, or that the $s_{\frac{1}{2}}$ level drops below the $h_{\frac{11}{2}}$ level. Placing the $s_{\frac{1}{2}}$ level below the $h_{\frac{11}{2}}$ orbital can be ruled out due to the observed population of the $d_{\frac{3}{2}}$ state (discussed in the following section). The calculated single–particle level schemes of Akovali *et al.* [Ako90] for $Z > 64$ $N = 82$ isotones predict that the $s_{\frac{1}{2}}$ hole state lies just above the $h_{\frac{11}{2}}$ ground state in ^{149}Ho and ^{151}Tm. However it is pointed out [Tot85] that the precise level ordering calculated by this code is extremely sensitive to the input parameters used.

It is more likely that the $d_{\frac{3}{2}}$ and $s_{\frac{1}{2}}$ levels cross over below N=82, considering that in the even–N isotones shown in figure 5.18 the $d_{\frac{3}{2}}$ level energy is falling with increasing Z, whilst that of the $s_{\frac{1}{2}}$ level is remaining approximately constant. The positioning of the $d_{\frac{3}{2}}$ level below the $s_{\frac{1}{2}}$ level in nuclei below N=82 is also suggested by the decay studies of ^{145}Dy to levels in ^{145}Tb [Tot91].

It can be seen that the low–lying level schemes of ^{149}Tm and ^{151}Tm are crucial to this proposed trend. Unfortunately the published scheme for ^{151}Tm [Ako90] measured only the $g_{\frac{7}{2}}$–$d_{\frac{3}{2}}$ sequence without an absolute energy above the $h_{\frac{11}{2}}$ ground state. The position of the $s_{\frac{1}{2}}$ level below the $d_{\frac{3}{2}}$ level was deduced by Akovali *et al.* assuming that the $s_{\frac{1}{2}}$ orbital occupied the first excited state in ^{147}Tm. The energy of this level in ^{151}Tm (denoted 'x' in figure 5.18) was similarly estimated by interpolating from the 67 keV excitation in ^{147}Tm and the 43 keV excitation in ^{153}Tm. The proposed interchange in the ordering of the $s_{\frac{1}{2}}$ and $d_{\frac{3}{2}}$ levels throws doubt on the published level scheme of ^{151}Tm, and prevents any reasonable estimate of the absolute energies of the single–particle levels. At present there is no data available on the level scheme of ^{149}Tm, apart from the assignment of the ground state to the $h_{\frac{11}{2}}$ level [Tot87c].

5.3.3 The new A=147 0.95 MeV proton decay

The 0.95 MeV peak was observed from evaporation residues from ^{150}Yb* within mass group A=147. The measured half-life of 5 ± 4 ms is consistent (see table 5.2) with an unhindered l=0 proton transition. However it is not possible, for the reasons discussed below, to make an unambiguous of this decay to a level in ^{147}Tm.

The most straightforward explanation would be to assign this transition to the decay of a single-particle state in ^{147}Tm. Comparing the measured half-life to those of the two known ^{147}Tm proton transitions, it is clear that each of the three decays occurs from separate states in the parent nucleus. This therefore excludes the assignment of this peak to a $d_{\frac{3}{2}} \rightarrow 2^+$ transition from ^{147}Tm to ^{146}Er.

The more obvious explanation of a transition from the $s_{\frac{1}{2}}$ single proton state in ^{147}Tm to the 0^+ ground state of ^{146}Er requires that the $s_{\frac{1}{2}}$ proton level occupies the ground state in ^{147}Tm. This is not consistent with the observed proton emission from the $d_{\frac{3}{2}}$ level in ^{147}Tm, since in this scenario the $d_{\frac{3}{2}}$ level would be approximately 160 keV above the $s_{\frac{1}{2}}$ ground state and would decay to this level by a fast E2 transition. Single particle estimates for this gamma transition calculate a half-life of approximately 30 ns, which would reduce the proton branch to $<<$ 0.1%. Moreover all the known nuclei in this region show only one low-lying isomeric state, caused by either the $s_{\frac{1}{2}}$ or $h_{\frac{11}{2}}$ proton, and sequences of prompt transitions from higher states into these levels are well documented.

An additional possibility is that the 0.95 MeV transition could be due to proton emission from one of the remaining A=147 isobars produced from ^{150}Yb*. Predicted Q_p values for the nuclei ^{147}Yb, ^{147}Tm, ^{147}Er and ^{147}Ho were discussed in section 2.4.2, calculated from the Möller Nix model. These show that only ^{147}Tm is proton unbound (Q_p= 1.0 MeV), whilst ^{147}Yb, ^{147}Er and ^{147}Ho have substantially negative Q_p values (Q_p= -0.4 MeV, -2.1 MeV and -0.3 MeV respectively).

Calculated Q_p values from the shell model of Liran and Zeldes give similar results. In the case of the odd–Z isotope ^{147}Ho, which is expected to have an $h_{\frac{11}{2}}$ ground state, a possible $s_{\frac{1}{2}}$ excited state would need to be at an energy 1.3 MeV above the ground state in order to decay with the observed energy. Systematics of single–particle levels in this region clearly exclude this possibility.

Considering the even–N A=147 nuclei, it is possible to rule out ^{147}Er immediately on Q_p value arguments. The nucleus ^{147}Yb, produced via the 3n channel, might be produced at the very limit of sensitivity for this experiment. This would be consistent with the ten counts observed in this proton peak. The $s_{\frac{1}{2}}$ proton level would be expected to occupy the ground state in ^{147}Yb as it does in ^{151}Yb [Tot86], with the $h_{\frac{11}{2}}$ level forming a low–lying isomer. Although the accuracy of predicted Q_p values for even–Z nuclei is uncertain, it is difficult to conclude that the Möller Nix Q_p value is too low by 1.3 MeV. Since the Liran and Zeldes calculations give the same Q_p value for ^{147}Yb, the required Q–value difference cannot be put down to an over strong even–odd staggering effect within the Möller Nix model. Therefore in the absence of any new mass data in this region, the assignment of this decay to proton emission from either ^{147}Ho or ^{147}Yb must be ruled out.

The remaining possibility is to assign the 0.95 MeV line to a transition between high–lying multi–particle isomeric states in parent and daughter nuclei. Odd–even nuclei in this region are known to possess a $\frac{15}{2}^-$ $(\pi h_{\frac{11}{2}})(\pi d_{\frac{3}{2}})(\pi s_{\frac{1}{2}})$ state and a $\frac{27}{2}^-$ $(\pi h_{\frac{11}{2}})^3$ isomer, at energies of about 0.7 MeV and 3 MeV respectively. The $\frac{15}{2}^-$ level decays rapidly ($<$ 1 ns) via an E2 transition to the $h_{\frac{11}{2}}$ single–particle level. Proton decay from the $\frac{27}{2}^-$ isomer to the 10^+ $(\pi h_{\frac{11}{2}})^2$ isomer in the even–even daughter could be energetically allowed, and would not involve any additional configuration hindrance. β–decay has been observed from $\frac{27}{2}^-$ isomers in N=83 nuclei [Bar88] with half–lives of up to 0.5 seconds, and millisecond isomers have been measured from the corresponding 10^+ state in N=81 nuclei [Bro89]. The l=3 $\frac{27}{2}^- \rightarrow 10^+$ proton transition has a calculated proton partial half–life of approximately 250 ms, so that a 5 ms isomeric state would exhibit a 2% proton

branch. This could provide an explanation for the 0.95 MeV activity, from the isomeric state in ^{147}Tm. The existence of a low spin isomeric two–proton state (eg. $(\pi d_{\frac{3}{2}})(\pi s_{\frac{1}{2}})$) immediately above the $s_{\frac{1}{2}}$ proton level in ^{147}Tm could also explain the observed transition, by decaying to the 2^+ state in ^{146}Er. Such a level is not known however, and the resulting transition would suffer from some degree of configuration hindrance.

In conclusion therefore the 0.95 MeV transition is most likely due to an unhindered proton transition from ^{147}Tm. Although the measured half–life is consistent with an l=0 transition, the decay from a groundstate $s_{\frac{1}{2}}$ single–particle level in ^{147}Tm can be excluded due to the observed population of the $d_{\frac{3}{2}}$ level. The decay is therefore tentatively assigned to proton emission from the $\frac{27}{2}^-$ isomer in ^{147}Tm. Further spectroscopic information will be required on nuclei in this region before a more positive assignment can be made.

5.3.4 The proton decay of ^{150}Lu

The extrapolated partial level scheme of ^{150}Lu is also shown in figure 5.19, together with that of its daughter N=79 nucleus ^{149}Yb. The 1^+ and 6^- isomers in ^{150}Lu are shown degenerate, since their relative ordering and energy separation are unknown. For convenience these levels will be referred to in this discussion as the ground state levels. The 10^+ isomeric state at the bottom of the $\pi h_{\frac{11}{2}} \nu^{-1} h_{\frac{11}{2}}$ band is shown approximately 700 keV above the ground state levels. Both the transitions from the 1^+ or 6^- levels in ^{150}Lu to the $s_{\frac{1}{2}}$ neutron hole state in ^{149}Yb have the correct energy to account for the observed 1.26 MeV proton line, however only the $6^- \rightarrow s_{\frac{1}{2}}$ transition gives rise to a proton with the required l=5 orbital angular momentum. Proton emission from the 1^+ state can be ruled out on half–life grounds, since the emitted proton would have l=0 or l=2 which imposes an upper half–life limit of $\lesssim$ 15 μs. Any possibility of an observable proton transition originating from the 1^+ state would depend critically on the relative energy

separation of these two ground state levels in ^{150}Lu.

Also shown in this level scheme is the Δl=5 transition from the 10^+ isomer in ^{150}Lu to the $h_{\frac{11}{2}}$ neutron hole state in ^{149}Yb. This transition could have an energy around 1.26 MeV since both these excited state have similar predicted excitation energies above their respective ground states. Decays from the 10^+ isomers in the N=81 isotones ^{146}Tb, ^{148}Ho and ^{150}Tm have been measured [Bro89] as E3 transitions with half-lives in the range 1–5 ms. It is probable that an assignment of this transition to the 10^+ state can be excluded, since the low cross section expected for the p3n channel would require a 100% proton branch to account for the observed yield. In conclusion therefore the 1.26 MeV proton transition is assigned to the transition between the 6^- level in ^{150}Lu and the $s_{\frac{1}{2}}$ neutron hole state in ^{149}Yb.

5.3.5 Comparison of half-life predictions in the shell model and transitional proton emitters

Results from this study of proton radioactivity have measured the half-lives of six proton transitions, producing first measurements for the decay of ^{150}Lu and the new A=147 transition. Experimental half-life values now exist for seven direct proton transitions, occurring from nuclei in two distinct regions of the nuclear chart. It is therefore of interest to compare the data from both these shell model and transitional regions with the various theoretical calculations.

Table 5.5 shows a selection of calculated proton partial half-lives for all the known proton transitions. The theoretical values are calculated using the WKB model [Pag90] with the potential of Perey and Perey [Per72], the quasi-stationary model of Buck *et al.* [Buc91], and the single-particle calculations of Bugrov and Kadmenskiĭ [Bug85]. In each case the half-lives have been calculated using the quoted value of the emitted proton orbital angular momentum Δl. The Bu-

Nucleus	$t_{\frac{1}{2},p}^{exp}$	Δl	$t_{\frac{1}{2}}^{calc}$ (b)		
			P+P	Buck	Bugrov
^{147}Tm	$2.6^{+2.4}_{-0.8}$ s	5	1.9 s	1.0 s	1.9–5.1 s
^{147m}Tm	376 ± 38 μs	2	170 μs	140 μs	210–340 μs
(^{147}Tm)	5 ± 3 ms	(0)	5.3 ms	8.1 ms	– – –
^{150}Lu	40 ± 10 ms	5	20 ms	11 ms	19–47 ms
^{151}Lu	130^{+100}_{-40} ms	5	42 ms	21 ms	40–110 ms
^{109}I	96 ± 5 μs	4	2.4 ms	1.5 ms	2.3–2.8 ms (c)
		2	5.5 μs	6.4 μs	30–190 μs (d)
^{113}Cs	33 ± 7 μs (a)	4	110 μs	72 μs	16-41 μs (e)
		2	0.3 μs	0.4 μs	0.3–6.8 μs (f)

Notes:

(a) from [Gil87]

(b) $t_{\frac{1}{2}}^{calc}$ assuming a spectroscopic factor of unity

Half-lives are calculated from spherical potentials, except as noted below

(c) $\beta_2 \simeq 0.05 - 0.10$, $\frac{3}{2}^+[421]$

(d) $\beta_2 \simeq 0.05 - 0.10$, $\frac{1}{2}^+[420]$

(e) $\beta_2 \simeq 0.1 - 0.15$, $\frac{3}{2}^+[421]$

(f) $\beta_2 \simeq 0.1 - 0.15$, $\frac{1}{2}^+[420]$

Table 5.5: *Comparison of calculated partial proton half-lives with the new measurements for the six known $Z > 50$ proton transitions, with tentative assignments shown in brackets. Calculations for the 0.95 MeV A=147 transition have assumed Δl=0 with a 100% proton branch for comparison purposes*

grov and Kadmenskiĭ calculations for ^{109}I and ^{113}Cs are from their multi–particle model [Bug89] which calculates proton wave functions from shell model basis states within an axially deformed Woods Saxon potential. All the remaining theoretical values use a spherical potential with an assumed spectroscopic factor of unity.

Nuclei close to the N=82 shell closure are generally spherical in shape, and proton half–lives measured from ^{147}Tm, ^{150}Lu and ^{151}Lu are expected to be described well by transitions between spherical shell model states. Table 5.5 shows that each of the models gives good agreement within a factor of two to the measured half–lives for these transitions. It is possible to exclude any calculated values which are significantly longer than the experimental partial half–life. In each case the calculated value is equal or shorter than the experimental half–life, which would be expected since a spectroscopic factor of unity has been used in the calculations. Therefore the over all impression is that the transitions are consistent with a spherical shell model description of these nuclei.

However the position is different for the two lighter nuclei ^{109}I and ^{113}Cs. The predicted shell model states around the fermi level in these nuclei are the $2d_{\frac{5}{2}}$ and the $1g_{\frac{7}{2}}$ levels, above the ^{100}Sn core. None of the shell model calculations for either the Δl=2 or Δl=4 transitions are in agreement with the measured half–lives, with the Δl=2 single–particle transitions requiring hindrance factors of $20 - 100\times$ to reproduce the data. This apparent failure of the shell model description can be understood by considering the trend in nuclear deformation in the region $50 \leq (N, Z) \leq 82$. Figure 5.20 summarises the β_2 deformation calculated for this region by Möller Nix [Mol81]. The dotted straight line connects the two regions of known proton radioactivity. There is a marked variation in β_2 along this line, with the deformation rising rapidly from zero at $(N, Z) = 50$, reaching a maximum around Z=60, and then decreasing slowly back to zero at N=82. Both the nuclei ^{109}I and ^{113}Cs are predicted to exhibit substantial prolate deformation, typically $\beta_2 \simeq 0.15$ [Ben84]-0.20 [Mol81] for ^{109}I and $\beta_2 \simeq 0.20$ [Ben84]-0.25 [Mol81] for

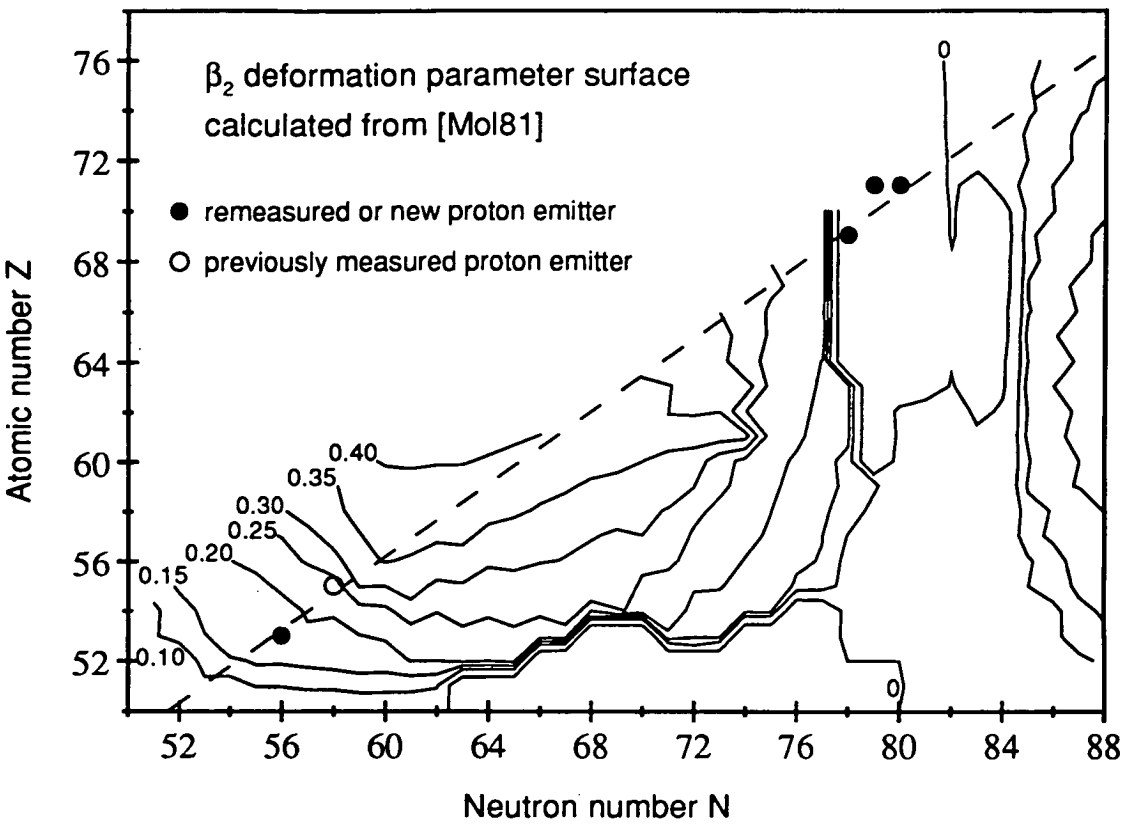

Figure 5.20: *Plot of nuclear deformation in the region* $Z \geq 50$, $50 \leq N \leq 88$, *calculated by the model of Möller Nix [Mol81]*

^{113}Cs.

The model of Bugrov and Kadmenskiĭ [Bug89] produces calculated half-lives in good agreement with the measured values. This model calculates the proton transition probability from a deformed odd-even nucleus into low-lying rotational states in the daughter nucleus. The resulting proton partial half-lives for ^{109}I and ^{113}Cs are calculated as a function of deformation for the Nilsson orbitals $\frac{3}{2}^+[421]$ (from the $1g_{\frac{7}{2}}$ shell model state) and $\frac{1}{2}^+[420]$ (from the $2d_{\frac{5}{2}}$ shell model state). The values given in table 5.5 use the deformation values $\beta_2 \simeq 0.05 - 0.10$ for ^{109}I and $\beta_2 \simeq 0.10 - 0.15$ for ^{113}Cs to best fit the experimental half-lives. Bugrov *et*

al. therefore assign the proton decays of ^{109}I and ^{113}Cs to the orbitals $\frac{1}{2}^+[420]$ and $\frac{3}{2}^+[421]$ respectively. It is found in each case that increasing mixtures of the low spin shell model states ($3s_{\frac{1}{2}}$ in ^{109}I and $2d_{\frac{3}{2}}$ in ^{113}Cs) cause a shortening of the calculated half-life as a function of increasing deformation. It would appear therefore that it is inappropriate to describe the proton transitions from these two deformed nuclei in terms of shell model states and spectroscopic factors.

5.3.6 Proton tunnelling and spectroscopic factors in shell model nuclei

It has been shown in section 5.3.5 that proton emission half-lives of spherical shell model nuclei are consistent with theoretical estimates using simple single-particle calculations. This approach has dominated the various theoretical studies of proton radioactivity (eg. [Hof82, Fei83, Gil87, Bug89] which have modelled the decay process using a variety of spherical nuclear potentials. In such cases the simplicity of the proton decay mechanism allows the measured half-lives to be used as a sensitive probe of the low energy region of the potential barrier, where variations in the calculated transmission probabilities are dominated by changes in the barrier tunnelling length.

Several authors have used a shell model spectroscopic factor S_{jl} (eg. [Gil87, Bug89]) to model the occupancy of the proton fermi orbital. Assuming the normal order of filling for the proton levels above Z=50 ($1g_{\frac{7}{2}}$, $2d_{\frac{5}{2}}$, $1h_{\frac{11}{2}}$, $2d_{\frac{3}{2}}$ and $3s_{\frac{1}{2}}$), the spectroscopic factors are S_{jl} = 0.67 for ^{147}Tm, 0.5 for ^{150,151}Lu and 1.0 for ^{147m}Tm. The calculated single-particle partial half-lives (denoted $t_{\frac{1}{2}}^{sp}$) are divided by the quoted spectroscopic factors, to give the adjusted calculated value using

$$t_{\frac{1}{2}}^{calc} = t_{\frac{1}{2}}^{sp} S_{jl}{}^{-1} \tag{5.1}$$

Table 5.6 gives $t_{\frac{1}{2}}^{calc}$ values for the four uniquely assigned shell model transitions. The 0.95 MeV transition assigned to ^{147}Tm is omitted since the partial proton

Nucleus	S_{jl}	$t^{exp}_{\frac{1}{2},p}$	$t^{calc}_{\frac{1}{2}}$ (a)			
			B+G	P+P	Buck (b)	Buck (c)
^{147}Tm $\frac{11}{2}^-$	0.67	$2.6^{+2.4}_{-0.8}$ s	7.5 s	2.8 s	1.5 s	3.6 s
^{147m}Tm $\frac{3}{2}^+$	1.0	376 ± 38 μs	220 μs	170 μs	140 μs	270 μs
^{150}Lu $\frac{11}{2}^-$	0.5	40 ± 10 ms	106 ms	40 ms	22 ms	56 ms
^{151}Lu $\frac{11}{2}^-$	0.5	130^{+100}_{-40} ms	214 ms	84 ms	42 ms	116 ms

Notes:

(a) $t^{calc}_{\frac{1}{2}} = t^{sp}_{\frac{1}{2}} {S_{jl}}^{-1}$

(b) Variable depth potential [Buc91] (see text)

(c) Fixed depth (70 MeV) Woods Saxon potential [Buc91]

Table 5.6: *Comparison of calculated partial proton half–lives for proton transitions from shell model nuclei, with corrections made for spectroscopic factors*

half–life is uncertain. All the values in table 5.6 are derived from single–particle calculations using a spherical potential.

The first conclusion to make from table 5.6 is that the use of shell model spectroscopic factors produces a better agreement between the single–particle calculated values and the experimental partial half–lives. In nearly all cases apart from the Bechetti and Greenlees WKB values the $t^{calc}_{\frac{1}{2}}$ values are equal to, or slightly shorter than, the measured values.

In comparing the calculations, some variation between the different potentials can be established. The WKB values calculated using the Bechetti and Greenlees potential tend to be consistently too long for high Δl transitions, in particular for ^{147}Tm and ^{150}Lu. For small Δl transitions the calculated values become closer to those produced with the potential of Perey and Perey. Overall the Perey and

Perey potential provide half–lives which are closest to the measured values. There are known problems with the Bechetti and Greenlees optical model parameterisation [Fei83] which is derived from proton scattering and reaction experiments concentrated in the 30–40 MeV proton energy range. The alternative parameter set compiled by Perey and Perey [Per72] are more suitable at lower proton energies below 20 MeV.

Two sets of half–life values are shown from Buck *et al.*, which are both calculated by varying the nuclear radius to produce a resonant state exactly the measured proton energy. The first set uses the parameters of Bechetti and Greenlees for the the depth of the real potential, and are systematically too low by a factor of approximately two. The second set of half–lives are calculated with a fixed depth (70 MeV) Woods Saxon potential, and tend to slightly exceed the measured values.

In conclusion therefore the four measured proton partial half–lives for nuclei close to N=82 are described well using various forms of spherical potentials. The inclusion of a shell model spectroscopic factor into the calculated single–particle values produces half–lives with a more consistent fit to the data. The best set of calculated values are produced with the real optical potential of Perey and Perey, after adjusting for the spectroscopic factor. All of the calculated values tend to underestimate the partial half–life of the ^{147m}Tm decay, suggesting that some additional configuration hindrance is required to correctly model this transition. It will be interesting to see whether further examples of proton emission half–lives, particularly from nuclei just above N=82, can be similarly described in terms of transitions between simple shell model states.

5.4 The search for further examples of proton radioactivity

The set of proton transitions which have been measured in this work has established the success of the new technique in detecting low cross section short-lived proton transitions. The measurement of ^{150}Lu is the first identification of a proton emitter produced via the p3n evaporation channel. This sensitivity to p3n residues with cross sections $\simeq$ 1 μb is a breakthrough in the search for further examples of proton radioactivity. Many more examples of proton emitting nuclei are predicted at medium and heavy masses which can be produced via the p3n channel using the currently available combinations of stable beams and targets.

Several odd-Z proton emitting nuclei are predicted in the heavier mass region immediately above the N=82 closure. Recent experiments have used the technique develope in this thesis work, and have identified the new proton emitters ^{156}Ta (N=83) and ^{160}Re (N=85) [Pag92]. Half-life measurements from these proton transitions assign the emitted proton to the $d_{\frac{3}{2}}$ orbital in each case. In ^{160}Re the $d_{\frac{3}{2}}$ level can be unambiguously assigned to the ground state, indicating a reversal of the $h_{\frac{11}{2}}$,$d_{\frac{3}{2}}$ level ordering in this region. This may suggest the onset of slight deformation above the N=82 closure. A further experiment studying the p3n channel from ^{150}Yb* has identified two proton peaks from ^{146}Tm [Liv92]. These results complete a sequence of four proton emitting odd-odd nuclei, namely ^{146}Tm, ^{150}Lu, ^{156}Ta and ^{160}Re.

It would be of interest to continue this study up to and beyond the Z=82 proton shell closure. A previous study of the reaction ^{74}Se + ^{106}Cd $\rightarrow$ ^{180}Pb* looked for the proton decay of ^{177}Tl produced via the p2n channel from ^{180}Pb* [Sel91]. No evidence was found for the decay of this nucleus with a sensitivity limit of $> 10^{+10}_{-5}$ nb, which was most likely due to the half-life of ^{177}Tl being less than 1 μs. For the remaining odd-Z isotopes in this region, ^{165}Ir and ^{172}Au offer

the best chance of decaying by dominant proton emission. The alpha decay of ^{166}Ir has been observed [Hof81a] and subsequent searches for the proton branch at Daresbury have proved negative. However since only 3 hours of beam were required to observe the ^{166}Ir alpha peak produced via the p3n channel, it should be possible to search for the p4n nucleus ^{165}Ir over several days of beam time. Amongst the gold isotopes alpha decay has been observed from ^{173}Au [Sch83]. Production of ^{172}Au is possible via the p3n channel using a beam of ^{84}Sr on a target of ^{92}Mo. At higher masses the proton drip line has not yet been accessed above Pb, and fusion–evaporation experiments in this region will require higher beam energies to overcome the larger coulomb barrier of heavier target nuclei.

The more immediate aim for this experimental programme is to search for proton radioactivity in the light rare earth region around $57 \leq Z \leq 67$. Previous experimental searches for proton emission in this region were unsuccessful due to insensitivity either to short half-lives [Lar83, Kar70] or to the p3n channel cross section [Hof84]. As has been discussed in section 5.3.5, deformation calculations predict that drip line nuclei in this area exhibit substantial deformation ($\beta_2 \simeq 0.4$), which remains constant between parent and daughter nuclei. It will be of particular interest to identify proton radioactivity in this region, which would form a link between the two existing areas of known proton emission.

Work is also under way to search for proton radioactivity from new deformed nuclei in the N=Z region from $A \simeq 80$ up to below ^{100}Sn. Below A=80 the location of the proton drip line has important implications for certain astrophysical processes, particularly around the nuclei ^{65}As and ^{69}Br. N=Z nuclei in this region are also expected to exhibit unusually large ground state deformations. Nuclei in this region can be best accessed using fragmentation reactions, with new exotic beams such as ^{78}Kr [Moh91] providing new opportunities to extend the known limit of the proton drip line.

The sensitivity of this technique will also allow additional measurements to be

made of the more intense proton emitters such as ^{109}I and ^{147}Tm. A proposed experiment is to combine the RIDS detection system with the high efficiency gamma ray detection available from the Eurogam array at Daresbury. Using the RIDS signals as a 'smart trigger' it should be possible to identify some of the low–lying gamma transitions in these nuclei.

In the more distant future the possibility of radioactive ion beams at high energies will open up access to a vast range of new proton emitting nuclei. In particular it should be possible to access the proton drip line for even–Z nuclei, with the prospect of observing direct two–proton radioactivity. In addition the production of much heavier proton unstable nuclei could establish a further region of proton radioactivity at high masses. This thesis work has provided the essential first steps on which can be based the ultimate goal of locating, and crossing, the proton drip line along its entire length.

Appendix A

Data structures within the Charissa event manager

Event–by–event data is processed through the Charissa event manager using a variety of data formats. In general as the data passes from the front end of the event manager through to the tape drives, it is stored in blocks which are bundled into groups of increasing size. Three key groups within the data processing sequence can be identified, namely

- The Event Block, the most basic unit of data produced from the Event Controller and Data Stack. Generation of one or more event block is initiated by each trigger signal applied to the event manager.
- The Read–and–Store Module (RSM) block, produced by the RSM from typically 100 event blocks. Each RSM block is sent down the CAMAC serial loop to the acquisition computer.
- The Tape block, generated by the acquisition computer which bundles several RSM blocks together to form a tape block. The tape block is written directly to the magnetic tape drive.

The basic data structure used by Charissa in a GEC environment is the 16–bit *word*. All the subsequent data blocks are built up from groups of such words, whether they contain data values (data words) or special reserved information (eg. header words, hit pattern words). However confusion can arise since other naming systems are used, particularly within GEC literature where 16–bit words are referred to as *half*–words. The following conventions are used in this discussion

- Words contain bits 1 to 16, where bit 1 is the least significant bit (lsb). Words are shown from bit 16 to bit 1 going from left to right.
- The symbol @ denotes a hexadecimal number, with the hex form of a word written sequentially left–to–right. In terms of 8–bit bytes, the word @A1F9 contains the two bytes @A1 (byte 1) and @F9 (byte 2).

Note that GEC conventions for bit labelling are different (ie. bit0 → bit15). Care is also required when dealing with GEC tape routines, which treat all tape block lengths in terms of *bytes*, even though handling data as words.

Event blocks

Each physical event produces one or more event blocks, depending on the number of parameters produced in the event. The event block contains three distinct word types, which are subsequently recognised by the event unpacking software.

1. The header word

The header word has a standard format of the form

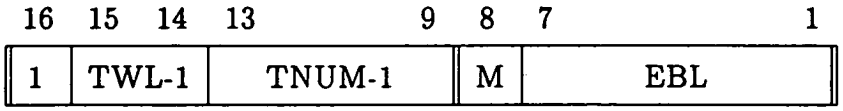

- TWL trigger word length, defines how many hit words are to follow the header word (from 1 to 4).

- TNUM trigger number, usually set to either 25 or 26 for Charissa data.
- M, the *more* flag used as a continuation marker for events containing more than 64 channels (see below).
- EBL event block length, inclusive of the header word.

2. The hit pattern word

One or more hit pattern words follow the header word, consistent with the value of TWL above. The hit pattern words define the channels containing valid data, and are used by the RSM to calculate how many data words to read from either the Data Stack (for ADC data) or the CAMAC units. Bit 1 of the first hit pattern word is set for valid data in channel 1, through to bit 16 in the fourth hit pattern word for channel 64.

3. The data word

The data values follow the hit pattern words, with one data word present for each bit set in the hit pattern words.

The total sequence of header word, hit pattern words and data words makes up an event block. Since the header word only allows TWL a maximum value of 4, this limits the number of channels allowed per event block to 64. In order to process data from larger events the *more* flag is used to join two or more event blocks together. For an event requiring two event blocks the first header word sets M=1 to show that more event blocks are associated with this event, whilst the second header word contains M=0. In the second event block the hit pattern words signify valid data from channels 65 to 128. By convention the trigger number is incremented for each event block joined in this way, so that the first event block's header word has TNUM=25 the second has TNUM=26 and so on.

In this application the EMU unit is used in front of the EC to accept two separate trigger types. Whilst each trigger has its own separate ADCs and CAMAC units, from the point of view of the data processing one event type is not differentiated

from the other. In practice most of the events originate from B triggers (implantation events), interspersed occasionally by events due to A triggers (decay events). The two types can be distinguished by using the CAMAC channels participating in each event type (channels 105–116), which are defined within the last two hit pattern words in the second event block. The event manager trigger panel is wired during the experiment to define channels 105–110 plus 113–114 for trigger type B, and only CAMAC channels 111–112 and 115–116 for trigger type A. In this way these hit pattern words always have the values shown below.

For type A events:

```
HPW 3, event block 2:  1 1 0 0   0 0 0 0   x x x x   x x x x     @C0xx
                       112           105 104           97

HPW 4, event block 2:  0 0 0 0   0 0 0 0   0 0 0 0   1 1 0 0     @000C
                       128                       116   113
```

For type B events:

```
HPW 3, event block 2:  0 0 1 1   1 1 1 1   0 0 0 0   0 0 0 0     @3F00
                       112           105 104           97

HPW 4, event block 2:  0 0 0 0   0 0 0 0   0 0 0 0   0 0 1 1     @0003
                       128                       116   113
```

The data structure of a typical type B event is given in figure A.1, consisting of two joined event blocks. In this event type there are 6 valid ADCs (in channels 1–5 and 7) plus the 8 CAMAC channels discussed above. In principle, events of up to 256 channels can be handled in this way with four event blocks coupled together. However at present the memory size of the RSM limits the maximum channel number to 128.

RSM blocks

The RSM produces the event blocks from the data passed to it from the event controller and the data stack, and groups up to about 100 event blocks to form a

Header word 1	1 1 1 1	1 0 0 0	1 0 0 0	1 0 1 1	@F88B
HPW 1	0 0 0 0	0 0 0 0	0 1 0 1	1 1 1 1	@005F
HPW 2	0 0 0 0	0 0 0 0	0 0 0 0	0 0 0 0	@0
HPW 3	0 0 0 0	0 0 0 0	0 0 0 0	0 0 0 0	@0
HPW 4	0 0 0 0	0 0 0 0	0 0 0 0	0 0 0 0	@0
Data 1	0 0 0 0	0 0 1 1	0 1 1 1	1 0 1 1	@037B
Data 2	0 0 0 0	0 0 1 1	1 0 0 0	1 0 1 0	@038A
Data 3	0 0 0 0	0 1 1 1	0 0 0 0	1 1 0 1	@070D
Data 4	0 0 0 0	0 0 0 1	1 0 1 0	1 1 0 0	@01AC
Data 5	0 0 0 0	0 0 1 0	0 1 1 1	0 1 1 0	@0276
Data 6	0 0 0 0	0 0 0 0	0 1 0 1	1 1 1 1	@005F
Header word 2	1 1 1 1	1 0 0 1	0 0 0 0	1 1 0 1	@F90D
HPW 1	0 0 0 0	0 0 0 0	0 0 0 0	0 0 0 0	@0
HPW 2	0 0 0 0	0 0 0 0	0 0 0 0	0 0 0 0	@0
HPW 3	0 0 1 1	1 1 1 1	0 0 0 0	0 0 0 0	@3F00
HPW 4	0 0 0 0	0 0 0 0	0 0 0 0	0 0 1 1	@0003
Data 1	1 1 0 1	1 1 0 0	0 1 0 1	1 1 1 1	@DC00
Data 2	0 0 0 0	0 0 0 0	0 0 0 0	0 0 0 1	@0001
Data 3	0 0 0 0	0 0 0 0	0 0 0 0	0 0 0 0	@0
Data 4	0 0 0 0	0 0 0 0	0 0 0 0	0 0 0 0	@0
Data 5	0 1 1 1	1 1 1 1	1 0 0 0	0 0 0 0	@7F80
Data 6	0 0 0 0	0 0 0 0	0 0 0 0	0 0 0 0	@0
Data 7	1 1 0 0	1 1 0 0	0 0 1 1	0 1 0 1	@CC35
Data 8	1 0 1 1	1 1 1 1	0 0 1 1	0 1 1 0	@BF36

Figure A.1: *Example data structure of the two event blocks produced by a typical trigger B event*

RSM block. The total length of the block is 2011 words, consisting of a reserved header word (@8020) denoting the start of the RSM block, followed by the event blocks. The RSM contains two output buffers, into one of which it stores the current RSM block. When the buffer is nearly full the RSM switches to filling the alternative buffer, and the completed RSM block is downloaded from the full buffer to the acquisition computer. A system parameter called the highwater mark (HWM) defines the boundary within each buffer, which when exceeded by the start of the next event block causes the buffer to switch over. It is set by the user to a value at least four event blocks below the 2011 limit. In this way the last event in each RSM block will avoid having the second event block truncated.

Any extra vacant words in the RSM block after the last event block are padded by the RSM with zeros. The HWM used in this application was generally 1940.

Word	Contents	Comments
1	BLEN	block length in bytes
2	NUM	block number
3	@FBA	incl. length of data block (4026 bytes)
4	@0	reserved null value
5	@8020	start of RSM block 1
|		|
2015		|
2016	@FBA	
2017	@0	
2018	@8020	start of RSM block 2
|		|
4028		|
4029	@FBA	
4030	@0	
4031	@8020	start of RSM block 3
|		|
6041		|
6042	@FBA	
6043	@0	
6044	@8020	start of RSM block 4
|		|
8054		|

Note:

1. BLEN contains the length of the block in bytes for a tape data block. It contains a coded value in the range 0–3 for special (non–data) tape blocks

2. Tape data blocks are numbered in order from the beginning of each each tape, and are generally preceded by 4 special blocks at the start of each volume.

Figure A.2: *Example data structure of a tape data block*

Tape data blocks

The acquisition computer bundles several RSM blocks into a single tape block, which is written to tape as a tape data block. The format of the tape data block consists of several reserved words, followed by typically four RSM blocks. This produces a tape data block of length 8054 words (16108 bytes), with the structure shown in figure A.2.

The GEC event–by–event tape format also uses special non–data blocks written in a reserved format. Figure A.3 shows the structure of these additional tape blocks, listed below. Three special blocks are used only once at the start of the tape, to identify the volume name etc. In each case the 'block number' in word 2 of these blocks contains a reserved value to identify the block type.

- Volume Header Block (NUM=@0), contains the tape volume name etc.
- Volume User Label Block (NUM=@1), contains a text string supplied by the user when the tape is initialised.
- Reserved Block (NUM=@2), not used.

In addition a file label block is used to mark the start of each file on the tape. At the end of the tape an end–of–information (EOI) block marks the limit of readable data. These two block types are identified by coded values of BLEN in word 1.

- File Label Block (BLEN=@1), contains the file name etc.
- End Of Information (EOI) block (BLEN=@2).

During the course of this project, software was developed to pre–sort the event–by–event data tapes. Typical data tapes produced from these experiments can contain as few as $\simeq$10% residue and decay events, the remainder being implantation events

caused by beam particles and other reaction products. The pre–sorting program was used in such cases to transfer the valid events onto new data tapes, which could then be sorted significantly (up to 8x) faster. Additional software was developed to check the data tapes for errors in the tape data block format. This was used during initial commissioning to help debug Charissa.

Volume header block

Word	Byte	Contents	
1	1-2	@0000	BLEN not used
2	3-4	@0000	NUM with special value @0
3-6	5-12		volume name (8 bytes)
7-42	13-84		unused

Volume user label block

Word	Byte	Contents	
1	1-2	@0000	BLEN not used
2	3-4	@0001	NUM with special value @1
3	5-6		inclusive length of user text
4	7-8		default tape blocksize (bytes)
5-41	9-82		user information
42			initialisation date

Reserved block

Word	Byte	Contents	
1	1-2	@0000	BLEN not used
2	3-4	@0002	NUM with special value @2
3-9	5-18		unused

File label block

Word	Byte	Contents	
1	1-2	@0001	BLEN with special value @1
2	3-4		NUM (>@2)
3-6	5-12		file name (8 bytes)
7-14	13-28		reserved
15	29-30	@01xx	file type where xx denotes @00 = text @02 = binary @FF = catalogue
16-40	31-80		reserved
41	81-82		default file blocksize (bytes)
42	83-84		write date

Data block

Word	Byte	Contents	
1	1-2		BLEN (>@11)
2	3-4		NUM (>@3)
3	5-6	@0FBA	inclusive length of data block
4	7-8	@0	reserved
5	9-10	@8020	start of RSM data block
6-8054	12-16108		etc...

EOI block

Word	Byte	Contents	
1	1-2	@0002	BLEN with special value @2
2	3-4		NUM (>@2)
3-41	5-82		reserved
42	83-84		write date

Figure A.3: *Block structure of GEC event–by–event tapes*

References

[Ako90] Y.A. Akovali, K.S. Toth, A.L. Goodman, J.M. Nitschke, P.A. Wilmarth, D.M. Moltz, M.N. Rao and D.C. Sousa, Phys. Rev. **C41** (1990) 1126

[Ars69] D. A. Arseniev, A. Sobiczewski and V.G. Soloviev, Nucl. Phys. **A126** (1969) 15

[Bar88] R. Barden, A. Plochocki, D. Schardt, B. Rubio, M. Ogawa, P. Kleinheinz, R. Kirchner, O. Klepper and J. Blomqvist, Z. Phys. **A329** (1988) 11

[Bec69] F.D. Becchetti and G.W. Greenlees, Phys. Rev. **182** (1969) 1190

[Ben84] R. Bengtsson, P. Möller, J.R. Nix and Jing–ye Zhang, Physica Scripta **29** (1984) 402

[Ber87] G. Berthes, Ph.D. thesis 1987, GSI report GSI–87–12

[Bet37] H.A. Bethe, Rev. Mod. Phys. **9** (1937) 69

[Bjø80] S. Bjørnholm and J.E. Lynn, Rev. Mod. Phys. **52** (1980) 725

[Bog73] D.D. Bogdanov, V.A. Karnaukhov and L.A. Petrov, Yad. Fiz. **17** (1973) 457, (Sov. J. Nucl. Phys. **17** (1973) 233)

[Bor91] V. Borrel, J.C. Jacmart, F. Pougheon, R. Anne, C. Détraz, D. Guillemaud–Mueller, A.C. Mueller, D. Bazin, R. Del Moral, J.P. Dufour, F. Hubert, M.S. Pravikoff and E. Roeckl, Nucl. Phys. **A531** (1991) 353

[Bro89] R. Broda, P.J. Daly, J.H. McNeill, Z.W. Grabowski, R.V.F. Janssens, R.D. Lawson and D.C. Radford, Z. Phys. **A334** (1989) 11

[Bro90] J.D. Brown, R.A. Hunt, W.D.M. Rae, S.J. Bennett, M. Freer and B.R. Fulton, Nuclear Physics Laboratory, Oxford University **OUNP-90-12**

[Bru81] C. Bruske, K.H. Burkard, W. Hüller, R. Kirchner, O. Klepper and E. Roeckl, Nucl. Instr. and Meth. **186** (1981) 61

[Bol72] M. Bolsterli, E.O. Fiset, J.R. Nix and J.L. Norton, Phys. Rev. **C5** (1972) 1050

[Buc91] B. Buck, A.C. Merchant and S.M. Perez, private communication 1991

[Bug85] V.P. Bugrov, S.G. Kadmenskiĭ, V.I. Furman and V.G. Khlebostroev, Yad. Fiz. **41** (1985) 1123, (Sov. J. Nucl. Phys. **41** (1985) 717) and V.P. Bugrov, V.E. Bunakov, S.G. Kadmenskiĭ and V.I. Furman, Yad. Fiz. **42** (1985) 57, (Sov. J. Nucl. Phys. **42** (1985) 34)

[Bug89] V.P. Bugrov and S.G. Kadmenskiĭ, Yad. Fiz. **49** (1989) 1562, (Sov. J. Nucl. Phys. **49** (1989) 967)

[Cer70] J. Cerny, J.E. Esterl, R.A. Gough and R.G. Sextro, Phys. Lett. **33B** (1970) 284

[Com88] E. Comay, I. Kelson and A. Zidon, Phys. Lett. **210B** (1988) 31

[Con82] K.A. Connell and M.M. Przybylski, Daresbury Laboratory Technical Memorandum, **DL/NUC/TM575E** (1982)

[Dav90] T. Davinson, A.C. Shotter, E.W. Macdonald, S.V. Springham, P. Jobanputra, A.J. Stephens and S.L. Thomas, Nucl. Instr. and Meth. **A288** (1990) 245

[Del80] C.F.G. Delaney, Electronics for the Physicist with Applications, Chapter 11, Ellis Horwood Ltd 1980

[Dét86] C. Détraz, Proc. of the International Nuclear Physics Conference, Harrogate, IOP Conference Series **86** vol 2 (1986) 495

[Dét90] C. Détraz, R. Anne, P. Bricault, D. Guillemaud–Mueller, M. Lewitowicz, A.C. Mueller, Yu Hu Zhang, V. Borrel, J.C. Jacmart, F. Pougheon, A. Richard, D. Bazin, J.P. Dufour, A. Fleury, F. Hubert and M.S. Pravikoff

[Fae84] T. Faestermann, A. Gillitzer, K. Hartel, P. Kienle and E. Nolte, Phys. Lett. **137B** (1984) 23

[Fei83] W. Feix and E. Hilf, Phys. Lett. **120B** (1983) 14

[Fir89] R.B. Firestone, J.M. Nitschke, P.A. Wilmarth, K. Vierinen, J. Gilat, K.S. Toth and Y.A. Akovali

[Gam28] G. Gamow, Z. Phys. **51** (1928) 204

[Gil87] A. Gillitzer, T. Faestermann, K. Hartel, P. Kienle and E.Nolte, Z. Phys. **A326** (1987) 107

[Gui89] D. Guillemaud–Mueller, Yu. E. Penionzhkevich, R. Anne, A.G. Artukh, D. Bazin, V. Borrel, C. Détraz, D. Guerreau, B.A. Gvozdev, J.C. Jacmart, D.X. Jiang, A.M. Kalinin, V.V. Kamanin, V.B. Kutner, M. Lewitowicz, S.M. Lukyanov, A.C. Mueller, N. Hoai Chau, F. Pougheon, A. Richard, M.G. Saint–Laurent and W.D. Schmidt–Ott, Z. Phys. **A332** (1990) 189

[Gur28] R.W. Gurney and E.U. Condon, Nature (1928), and Phys. Rev. **33** (1929) 127

[Hau88] P.E. Haustein, Atomic Data and Nuclear Data Tables **39** (1988) 185

[Hag79] E. Hagberg, P.G. Hansen, P. Hornshøj, B. Jonson, S. Mattsson and P. Tidemand–Petersson, Nucl. Phys. **A318** (1979) 29

[Hag87] E.Hagberg et al., Proc. of the 5th. Int. Conf. on Nuclei far from Stability, Lake Rosseau, AIP Conference Proceedings, **164** (1987) 41

[Hax49] O. Haxel, J.H.D. Jensen, H.E. Suess, Phys. Rev. **75** (1949) 1766

[Hei91] H. Heine, T. Faestermann, A. Gillitzer, J. Homolka, M. Köpf and W. Wagner, Z. Phys. **A340** (1991) 225

[Hof81] S. Hofmann, G. Münzenberg, W. Faust, W. Faust, F. Heβberger, W. Reisdorf, J.R.H. Schneider, P. Armbruster, K. Güttner and B. Thuma, Proc. of the 4th. Int. Conf. on Nuclei far from Stability, Helsingør 1981

[Hof81a] S. Hofmann, G. Münzenberg, F.P. Heβberger, W. Reisdorf, P. Armbruster and B. Thuma, Z. Phys. **A299** (1981) 281

[Hof82] S. Hofmann, W.Reisdorf, G. Münzenberg, F.P. Heβberger, J.R.H. Schneider and P. Armbruster, Z. Phys. **A305** (1982) 111

[Hof83] S. Hofmann, Kerntechnik **42** (1983) 157

[Hof84] S. Hofmann, Y.K. Agarwal, P. Armbruster, F.P. Heβberger, P.O. Larsson, G. Münzenberg, K. Poppensieker, K. Reisdorf, J.R.H. Schneider and H.J. Schött, Proc. 7^{th} Int. Conf. on Atomic Masses and Fundamental Constants, AMCO–7 Darmstadt 1984, Ed. O. Klepper, THD– Schriftenreihe Wissenschaft und Technik, **26** (1984) 184

[Hof88] S. Hofmann, Particle Emission from Nuclei, Eds. M. Ivascu and D.N. Poenaru, CRC Press, Boca Raton, FL 33431 USA

[Hof91] S. Hofmann, private communication 1991

[Hou89] E. Hourani, F. Azaiez, Ph. Dessagne, A. Elayi, S. Fortier, S. Gales, J.M. Mason, P. Massolo, Ch. Miehe and A. Richard, Z. Phys. **A334** (1989) 277

[Jac70] K.P. Jackson, C.U. Cardinal, H.C. Evans, N.A. Jelley and J. Cerny, Phys. Lett. **33B** (1970) 281

[Jam88] A.N. James, T.P. Morrison, K.L. Ying, K.A. Connell, H.G. Price and J. Simpson, Nucl. Instr. and Meth. **A267** (1988) 144

[Kad75] S.G. Kadmenskiĭ and V.I. Furman, Fiz. Elem. Chastis At. Yadra **6** (1975) 469 (Sov. J. Part. Nucl. **6** (1975) 189)

[Kar64] V.A. Karnaukhov and G.M. Ter–Akopyan, Phys. Lett. **12** (1964) 339

[Kar70] V.A. Karnaukhov, D.D. Bogdanov and L.A. Petrov, Proc. Int. Conf. on the Properties of Nuclei far from the Region of Beta–Stability, Leysin, Switzerland, 1970, p.457

[Kem78] P. Kemnitz, L. Funke, F. Stary, E. Will, G. Winter, S. Elfström, S.A. Hjorth, A. Johnson and Th. Lindblad, Nucl. Phys. **A311** (1978) 11

[Kem80] J. Kemmer, Nucl. Instr. and Meth. **169** (1980) 499

[Kem84] J. Kemmer, Nucl. Instr. and Meth. **226** (1984) 89

[Kir77] R. Kirchner, O. Klepper, G. Nyman, W. Reisdorf, E.Roeckl, D. Schardt, N. Kaffrell, P. Peuser and K. Schneeweiss, Phys. Lett. **70B** (1977) 150

[Kir81] R. Kirchner, K.H. Burkard, W. Hüller and O. Klepper, Nucl. Instr. and Meth. **186** (1981) 295

[Kle82] O. Klepper, T. Batsch, S. Hofmann, R. Kirchner, W. Kurcewicz, W. Residorf, E. Roeckl, D. Schardt and G. Nyman, Z. Phys. **A305** (1982) 125

[Kor89] M.O. Kortelahti, K.S. Toth, K.S. Toth, K.S. Vierinen, J.M. Nitschke, P.A. Wilmarth, R.B. Firestone, R.M. Chasteler and A.A. Shihab–Eldin, Phys. Rev. **39** (1989) 636

[Kra79] H.J. Krappe, J.R. Nix and A.J. Sierk, Phys. Rev. **C20** (1979) 992

[Lar83] P.O. Larsson, T. Batsch, R. Kirchner, O. Klepper, W. Kurcewicz, E. Roeckl, D. Schardt, W.F. Feix, G. Nyman and P. Tidemand-Petersson, Z. Phys. **A314** (1983) 9

[Lew91] M. Lewandowski, A.W. Potempa, V.I. Fominikh, K.Ya. Gromov, M. Janicki, Ju.V. Juschkevich, V.G. Kalinnikov, N.Ju. Kotovskij, V.V. Kuznetsov, N. Raschkova, Ja.A. Sajdimov and J. Wawryszczuk, Z. Phys. **A340** (1991) 107

[Lia87] C.F. Liang, P. Paris, P. Kleinheinz, B. Rubio, M. Piiparinen, D. Schardt, A. Plochocki and R. Barden, Phys. Lett. **191B** (1987) 245

[Lir76] S. Liran and N. Zeldes, Atomic Data and Nuclear Data Tables **17** (1976) 431

[Liv92] K. Livingston, private communication 1992

[Mac65] R.D. Macfarlane, Phys. Rev. **137/6B** (1965) 1448

[Mac65a] R.D. Macfarlane and A. Siivola, Phys. Rev. Lett. **14** (1965) 114

[Mad88] D.G. Madland and J.R. Nix, Nucl. Phys. **A476** (1988) 1

[McN89] J.H. McNeill, J. Blomqvist, A.A. Chishti, P.J. Daly, W. Gelletly, M.A.C. Hotchkis, M. Piiparinen, B.J. Varley and P.J. Woods, Phys. Rev. Lett. **63** (1989) 860

[Mic] Micron Semiconductor Ltd, Lancing, UK

[Moh91] M.F. Mohar, D. Bazin, W. Benenson, D.J. Morrissey, N.A. Orr, B.M. Sherrill, D. Swan, J.M. Winger, A.C. Mueller and D. Guillemaud-Mueller, Phys. Rev. Lett. **66** (1991) 1571

[Mol74] P. Möller, S.G. Nilsson and J.R. Nix, Nucl. Phys. **A229** (1974) 292

[Mol81] P. Möller and J.R. Nix, Nucl. Phys. **A361** (1981) 117

[Mol81a] P. Möller and J.R. Nix, Atomic Data and Nuclear Data Tables **26** (1981) 165

[Mol88] P. Möller and J.R. Nix, Atomic Data and Nuclear Data Tables **39** (1988) 214

[Mor86] T.P. Morrison, Nucl. Instr. and Meth. **A251** (1986) 337

[Mun79] G. Münzenberg, W. Faust, S. Hofmann, P. Armbruster, K. Güttner and H. Ewald, Nucl. Instr. and Meth. **161** (1979) 65

[Mye70] W.D. Myers, Nucl. Phys. **A415** (1970) 387

[Naz90] W. Nazarewicz, M.A. Riley and J.D. Garrett, Nucl. Phys. **A512** (1990) 61

[NDS85] Nuclear Data Sheets **46** (1985)

[NDS87] Nuclear Data Sheets **50** (1987)

[Neu87] R. Neugart, E. Arnold, W. Borchers, W. Neu, G. Ulm and K. Wendt, Proc. of the 5th. Int. Conf. on Nuclei far from Stability, Lake Rosseau, AIP Conference Proceedings, **164** (1987) 126

[Nil55] S.G. Nilsson, Mat. Fys. Medd. Dan. Vid. Selsk. **29** (1955) No.16

[Nit88] J.M. Nitschke, P.A. Wilmarth, J. Gilat, K.S. Toth and F.T. Avignone, Phys. Rec. **C37** (1988) 2694

[Nix72] J.R. Nix, Annu. Rev. Nucl. Sci. **22** (1972) 81

[Nol82] E. Nolte, S.Z. Gui, G. Colombo, G. Korschinek and K. Eskola, Z. Phys. **A306** (1982) 223 part 2

[Oll89] T. Ollivier, R. Béraud, A. Charvet, R. Duffait, A. Emsallem, M. Meyer, N. Idrissi, A. Gizon and J. Tréherne, Z. Phys. **A320** (1985) 695

[Pag90] R.D. Page, PhD thesis, University of Birmingham 1990

[Pag91] R.D. Page, P.J. Woods, S.J. Bennett, M. Freer, B.R. Fulton, R.A. Cunningham, J. Groves, M.A.C. Hotchkis and A.N. James, Z. Phys. **A338** (1991) 295

[Pag92] R.D. Page, T. Davinson, N.J. Davis, K. Livingston, S. Hofmann, A.N. James, P.J. Sellin, A.C. Shotter and P.J. Woods, Phys. Rev. Lett., in press

[Pai81] G. Paić, K. Kadija, B. Ilijaš and K. Kovačević, Nucl. Instr. and Meth. **188** (1981) 119

[Per72] C.M. Perey and F.G. Perey, Nuclear Data Tables, **10** (1972) 539

[Pou87] F. Pougheon, J.C. Jacmart, E. Quiniou, R. Anne, D. Bazin, V. Borrel, J. Galin, D. Guerreau, D. Guillemaud–Mueller, A.C. Mueller, E. Roeckl, M.G. Saint–Laurent and C. Détraz, Z. Phys. **A327** (1987) 17

[Pra73] H.C.Pradhan, Y. Nogami and J. Law, Nucl. Phys. **A201** (1973) 357

[Ras59] J.O. Rasmussen, Phys. Rev. **113/6** (1959) 1593

[Rei89] J.E. Reiff, M.A.C. Hotchkis, D.M. Moltz, T.F. Lang, J.D. Robertson and J. Cerny, Nucl. Instr. and Meth. **A276** (1989) 228

[Roe78] E. Roeckl, R. Kirchner, O. Klepper, G. Nyman, W. Reisdorf, D. Schardt, K. Wein, R. Fass and S. Mattsson, Phys. Lett. **78B** (1978) 393

[Sch79] D. Schardt, R. Kirchner, O. Klepper, W. Reisdorf, E. Roeckl, P. Tidemand–Petersson, G.T. Ewan, E. Hagberg, B. Jonson, S. Mattsson and G. Nyman, Nucl. Phys. **A326** (1979) 65

[Sch82] C. Schiessl, W. Wagner, K. Hartel, H.J. Körner, W. Mayer and E. Rehm, Nucl. Instr. and Meth. **192** (1982) 291

[Sch83] J.R.H. Schneider, S. Hofmann, F.P. Heβberger, G. Münzenberg, W. Reisdorf, and P. Armbruster, Z. Phys. **A312** (1983) 21

[Sel91] P.J. Sellin, P.J. Woods, R.D. Page, S.J. Bennett, R.A. Cunningham, M. Freer, B.R. Fulton, M.A.C. Hotchkis and A.N. James, Z. Phys. **A338** (1991) 245

[Sel92] P.J. Sellin, P.J. Woods, D. Branford, T. Davinson, N.J. Davis, D.G. Ireland, K. Livingston, R.D. Page, A.C. Shotter, S. Hofmann, R.A. Hunt, A.N. James, M.A.C. Hotchkis, M.A. Freer and S.L. Thomas, Nucl. Instr. and Meth. **A311** (1982) 217

[Str67] V.M. Strutinsky, Nucl. Phys. **A95** (1967) 420

[Str68] V.M. Strutinsky, Nucl. Phys. **A122** (1967) 1

[Tai84] N.S.R. Tait, Nucl. Instr. and Meth. **220** (1984) 54

[Tak73] K. Takahashi, M. Yamada and T. Kondoh, Atomic Data and Nuclear Data Tables **12** (1973) 101

[Tal56] J.D. Talman, Phys. Rev. **102** (1956) 455

[Tho90] S.L. Thomas, T. Davinson and A.C. Shotter, Nucl. Instr. and Meth. **A288** (1990) 212

[Tho90a] S.L. Thomas, Private Communication 1990

[Tid85] P. Tidemand–Petersson, R. Kirchner, O. Klepper, E. Roeckl, D. Schardt, A. Płochocki and J. Zylicz, Nucl. Phys. **A437** (1985) 342

[Tot84] K.S. Toth, D.M. Moltz, E.C. Schloemer, M.D. Cable, F.T. Avigone and Y.A. Ellis–Akovali, Phys. Rev. **C30** (1984) 712

[Tot85] K.S. Toth, Y.A. Ellis–Akovali, F.T. Avignone, R.S. Moore, D.M. Moltz, J.M. Nitschke, P.A. Wilmarth, P.K. Lemmertz, D.C. Sousa and A.L. Goodman, Phys. Rev. **C32** (1985) 342

[Tot86] K.S. Toth, Y.A. Ellis–Akovali, J.M. Nitschke, P.A. Wilmarth, P.K. Lemmertz, D.M. Moltz and F.T. Avignone, Phys. Lett. **B178** (1986) 150

[Tot87] K.S. Toth, J.M. Nitschke, P.A. Wilmarth, Y.A. Ellis–Akovali, D.C. Sousa, K. Vierinen, D.M. Moltz, J. Gilat and N.M. Rao, Proc. of the 5th. Int. Conf. on Nuclei far from Stability, Lake Rosseau, AIP Conference Proceedings, **164** (1987) 718

[Tot87a] K.S. Toth, D.C. Sousa, J.M. Nitschke and P.A. Wilmarth, Phys. Rev. **C35** (1987) 310

[Tot87b] K.S. Toth, D.C. Sousa, J.M. Nitschke and P.A. Wilmarth, Phys. Rev. **C35** (1987) 620

[Tot87c] K.S. Toth, J. Gilat, J.M. Nitschke, P.A. Wilmarth, K. Vierinen and F.T. Avignone, Phys. Rev. **C36** (1987) 826

[Tot88] K.S. Toth, D.C. Sousa, J.M. Nitschke and P.A. Wilmarth, Phys. Rev. **C37** (1988) 1196

[Tot91] K.S. Toth, Private Communication 1991

[Vie89] K.S. Vierinen, J.M. Nitschke, P.A. Wilmarth, R.M. Chasteler, A.A. Shihab–Eldin, R.B. Firestone, K.S. Toth and Y.A. Akovali, Phys. Rev. **C39** (1989) 1972

[Wap77] A.H. Wapstra and K. Bos, Atomic Data and Nuclear Data Tables **19** (1977) 175

[Wap88] A.H. Wapstra, G. Audi and R. Hoekstra, Atomic Data and Nuclear Data Tables **39** (1988) 281

[Woo54] R.D. Woods and D.S. Saxon, Phys. Rev. **95** (1954) 577

[Woo89] P.J. Woods, S.J. Bennett, M. Freer, B.R. Fulton, R.D. Page, K. A. Connell, R.A. Cunningham, J. Groves, A.N. James, M.A.C. Hotchkis and W.D.M. Rae, Nucl. Instr. and Meth. **A276** (1989) 195

[Yor87] J. Yorkston, A.C. Shotter, D.B. Syme and G. Huxtable, Nucl. Instr. and Meth. **A262** (1987) 353

[Zie80] J.F. Ziegler, Handbook of Stopping Powers of Energetic Ions in all Elements (Vol. 5 of The Stopping Powers and Ranges of Ions in all Elements, Ed. J.F¿ Ziegler), Pergamon Press 1980

[Zot] Zot Engineering Ltd, Inveresk Industrial Estate, Musselburgh, East Lothian